공학박사 학위논문

Form-Stabilized Phase Change Material Composites and their Applications to Thermoelectric Energy Harvesting

열전 에너지 하베스팅 응용 가능한 형상 유지 상전이 복합재료

2019년 2월

서울대학교 대학원

재료공학부

유 정 빈

Doctoral Dissertation in Engineering

Form-Stabilized Phase Change Material Composites and their Applications to Thermoelectric Energy Harvesting

by

Chengbin Yu

Advisor: Prof. Jae Ryoun Youn

February 2019

Department of Materials Science and Engineering

Graduate School

Seoul National University

Form-Stabilized Phase Change Material Composites and their Applications to Thermoelectric Energy Harvesting

열전 에너지 하베스팅 응용 가능한 형상 유지 상전이 복합재료

지도 교수 윤 재 륜

이 논문을 공학박사 학위논문으로 제출함

2018 년 12 월

서울대학교 대학원

재료공학부

유 정 빈

유정빈의 박사 학위논문을 인준함

2018 년 12 월

위 원 장 서 용 석 (인)

부위원장 윤 재 륜 (인)

위 원 김 장 주 (인)

위 원 안 철 희 (인)

위 원 송 영 석 (인)

Abstract

Energy storage plays a considerable part in absorbing heat energy for thermoelectric energy conversion. Thermal energy storage (TES), one of the most popular systems for recycling energy, generally employs a phase change material (PCM) as a working material due to its high latent heat, appropriate phase transition temperature range, and high thermal stability. The latent heat thermal eneergy storage (LHTES) is a good example of PCMs applications and the energy storage density can be improved by combing these PCMs with thermoelectric devices. The PCMs can absorb or release a great deal of thermal energy isothermally during the heating and cooling process. However, have a leakage problem during the melting and cooling process, the field applications are restricted. To manufacture the form stable PCMs, some supporting materials are required to improve the dimensional stability of PCMs. Utilizing 3D porous materials as a supporting material has been reported and comparing with conventional supporting materials, the 3D porous materials have larger pore volume than other materials to be filled up by the pure PCMs. Therefore, graphene aerogel has been investigated as a supporting material to prevent the leakage of PCMs due to its large surface area and complicated internal structure. As for thermoelectric effect, the Seebeck effect induces electrons to move from hot side to cold side of the energy harvesting device and form stable PCMs are placed on the side of PN cells to achieve the thermoelectric energy harvesting during melting and coolng process.

Chapter I provides an descriptions of phase change materials (PCMs) and organic PCMs which has been widely utilized in the energy storage. The goal of work and the advanced portion of this study is generally employed. The two different PCMs are placed on the sides of PN cells and the theory of this combination is fully mentioned. The Seebeck effect is utilized for the thermoelectric energy harvesting and the functions of PCMs are discussed sufficiently. The multiple energy harvesting, arriving phase transitions concept, and the optimum couple of PCMs are introduced and the novelty of each part is examined in this chapter. In addition, the modified supporting material is a new method to improve the energy storage and subsequently contribute to the thermoelectric energy harvesting. The goal of this work related to the supporting

materials are briefly described.

Chapter II introduces the form stable phase change materials (PCMs) by using microencapsulation method which can exhibit a smart response to the heating and cooling steps. The encapsulated form stable PCM composites sustain their intrinsic solid state upon melting process. The pure PCM inside the microcapsule started to solid-liquid phase transition upon heating and recovered from liquid to the solid state after removing the heat source. Therefore, the form stable PCM microcapsules lead to the volume expansion and shrinkage on the melting and crystallization process. The volume change of PCM composites gave rise to the degree of filler arrangement which sufficiently increased the electrical conductivity. The graphene and carbon nanotube (CNT) powders are generally utilized as excellent fillers for obtaining the electrical conductivity under the temperature variation. The temperature is initially increased from 25 °C to final 90 °C and decreased to the room temperature after removing the heat source. After that, the electrical conductivity of both graphene and CNT showed large magnitude modification and further demonstrated the volume expansion of PCM microcapsules are effectively changed the internal electrical resistivity under the phase transition process.

Chapter III demonstrates the single PN cell energy harvesting system with two different PCMs and measure the induced current under heating and cooling process. The current is generated due to the temperature difference between the two sides of PN cell and maintained when the hot side temperature is higher than that of cold side. Based on the result of single PN cell energy harvesting system, two different PCMs are selected for the energy harvesting based on the Seebeck effect. Normally, the PN junction is blocking the current movement on the reverse bias which results in the electric energy that is measured merely when the temperature of the hot side is higher than that of cold side. The energy barrier is existed and hard to detect the induced current when the temperature of the cold side exceeds that of the hot side of PN cell semiconductors. Thus, the additional energy harvesting system needs to be introduced and the multiple energy harvesting system is mentioned effectively. The harvested current is obtained two times as the change of temperature on the PCMs. After achieving the multiple energy harvesting based on reversed temperature difference, it needs to increase rate of arriving phase transition field on both melting and cooling process. To address this problem, the

supporting material is modified by increasing the filler weight fraction and form stable PCMs consist multiple energy harvesting system exhibits the expected result upon phase transitions. The conductive filler can perform as a thermal carrier and the harvesting system is carried out sufficiently. The optimum component of two PCMs are proved by utilizing different filler embedded PCMs. The multiple current is obtained and the optimum energy harvesting system could exhibit the largest peak area for thermoelectric energy conversions. To predict the temperature difference between the two PCMs, the numerical analysis is calculated during the heating and cooling cycles, and the Seebeck effect is demonstrated by employing a finite element method (FEM). The numerical calculation showed the energy harvesting system is controllable in a systematic manner and useful for practical applications.

In Chapter IV, the modified supporting material is applied to manufacture the form stable phase change material (PCM) and the one section is infiltrated some of PDMS to emerge a flexible properties. Due to the combination of the skeleton under the aerogel structure, the modified PDMS/aerogel can prevent the shrinkage under the infiltrating process and filled up more working material into the pore space. The fabricated PCMs with PDMS shows larger temperature gradients and current peaks upon melting and cooling process. The energy harvesting system is able to store and release more thermal energy by utilizing modified PCMs and increase the thermoelectric energy conversion efficiencies. Furthermore, the other section for increasing the harvesting efficiency is modified the supporting material by chemical cross-linking method. To solve the shrinkage problem more effectively, the supporting material is dealt with the cross-linker and enhanced its mechanical properties to sustain the initial structure. The cross-linked supporting material could infiltrate more pure PCMs than that of raw materials and mechanically stable to prevent the disruption under the melting process. The stable form stable PCMs are certainly placed on the multiple PN cells to construct a new energy harvesting system and observe a harvested current during the phase transition process. As a result, the system is produced more electrical current under the solar simulator and hold a thermal stable properties during melting and cooling cycles.

In Chapter V, the pyroelectric effect by combining with the PCM composites is a new approach for thermoelectric energy harvesting. The pyroelectric film is more and

more attracted because of simple control, and electrical polarization. In this field, pyroelectric electrodes enable convert thermal to electrical energy conversion as occurring the pyroelectric effect. Unlike the PN junction modules that depend on the temperature difference, pyroelectric energy harvesters demand continuous temperature variations induced by the heat source in order to generate the electrical current. In this work, the phase change materials (PCMs) act as a thermal energy absorber and reservoir to generate the induced voltage upon heating and cooling. The glass transmission including pyroelectric device demonstrates a new thermal energy applications and further indicates the optimum pyroelectric system under the phase transition process.

In Chapter VI, the conclusion of this doctoral dissertation is described. The goal of this work is presented under a combination of previous Chapter II and Chapter IV. The single PN cell based energy harvesting system, multiple energy harvesting system, arriving phase transition applications, and the optimum component PCMs are generally proved and the final results are also mentioned in order to suggest the practical applications. In addition, the restiction of these PN cell energy harvesting system is described and the upcoming research about the thermoelectric energy conversion is developed in this chapter.

Keywords: Phase change material, microencapsulation, PCM microcapsule, volume expansion, PN cells, energy harvesting system, thermoelectric energy harvesting, multiple energy harvesting system, Seebeck effect, finite element method, PDMS/aerogel, cross-linked, shrinkage problem, harvesting efficiency, pyroeelctric effect, electrical polarization, continuous temperature variations.

Student Number: 2013-23814

Contents

List of Figures

List of Tables

Chapter I.

Introduction

1.1. What is a phase change material?

The phase change material (PCM) which can absorb or release a great deal of thermal energy isothermally during the heating and cooling process. Since PCMs have the advantage of high latent heat, they have been applied to the energy field systems including solar cell utilization, smart textiles, energy storage building materials, and wasted heat energy utilization. A calssification of PCMs is given in (**Fig. 1.2.1**)[1].

There are a large number of organic and inorganic chemical materials, which can be identified as PCM from the point of view melting temperature and latent heat of fusion as present in **Fig. 1.2.2**[2, 3]. However, except for the melting point in the operating range, majority of phase change materials does not satisfy the criteria required for an adequate storage media as discussed earlier. As no single mateiral can have all the required properties for an ideal thermal-storage media, one has to use the available materials and try to make up for the poor physical property by an adequate system design [4, 5]. For example metallic fins can be used to increase the thermal conductivity of PCMs, supercooling may be suppressed by introducing a nucleating agent or a 'cold finger' in the storage material and incongruent melting can be inhibited by use of suitable thickness [6, 7]. In general inorganic compounds have almost double volumetric latent heat storage capacity (250-400 kg/dm^3) than the organic compounds (128-200 kg/dm^3). For their very different thermal and chemical behavior, the properties of each subgroup which affects the design of latent heat thermal energy storage systems using PCMs of that subgroup are discussed in various researches as shown in **Fig.1.2.3**[8].

Organic materials are further described as paraffin and non-paraffin[9]. Organic materials include congruent melting means melt and freeze repeatedly without phase

segregation and consequent degradation of their latent heat of fusion, self-nucleation means they crystallize with little or no super-cooling and usually non-corrosive paraffin wax consists of a mixture of mostly straight chain n-alkanes, the crystallization of the main chain release a large amount of latent heat [10, 11]. Both the melting point and latent heat of fusion increase with chain length [12, 13]. Paraffin qualifies as heat of fusion storage materials due to their availability in a large temperature range [14, 15]. Due to cost consideration, however, only technical grade paraffins may be used as PCMs in latent heat storage system [16-19]. Paraffin is safe, reliable, predictable, less expensive and non-corrosive[20, 21]. They are chemically inert and stable below 300 °C, show little volume changes on melting and have low vapor pressure in the melt form [22-24]. For these properties of the paraffins, system-using paraffins usually have very long freeze-melt cycle [25, 26]. The melting point of alkane increase with the increasing number of carbon atoms [27]. Apart from some several favorable characteristic of paraffins, such as congruent melting and good nucleating properties [28-30]. They show some undesirable properties such as: (i) low thermal conductivity[31], (ii) non-compatible with the plastic container and (iii) moderately flammable [32]. All these undesirable effects can be partly eliminated by slightly modifying the wax and the storage unit [33-35].

The non-paraffin organic are the most numerous of the phase change materials with highly varied properties [36, 37]. Each of these materials will have its own properties unlike the paraffin's, which have very similar properties [38-40]. This is the largest category of candidate's materials for phase change storage [41]. Abhat et al.[10] and Buddhi and Sawhney [42] have conducted an extensive survey of organic materials and identified a number of esters, fatty acids, alcohol's and glycol's suitable for energy storage [43-45]. These organic materials are further subgroups as fatty acids and other non-paraffin organic [46-48]. These materials are flammable and should not be exposed to excessively high temperature, flames or oxidizing agents. Some of the features of these organic materials are as follows: (i) high heat of fusion, (ii) low thermal conductivity, (iii) inflammability, (iv) low flash points, (v) varying level of toxicity, and (vi) instability at high temperatures. Fatty acids have high heat of fusion values comparable to that of paraffin's. Fatty acids also show reproducible melting and freezing behavior and freeze

with no super-cooling. The general formula describing all the fatty acid is given by carbon chains incorporating carboxyl groups and hence, qualify as good PCMs.

Inorganic materials are further classified as salt hydrate and metals [49]. These phase change materials do not super-cooling and their heats of fusion do not degrade with cycling at the melting point the hydrate crystals breakup into anhydrous salt and water, or into a lower hydrate and water. One problem with most salt hydrates is that of incongruent melting caused by the fact that the released water of crystallization is not sufficient to dissolve all the solid phase present. Due to density difference, the lower hydrate settles down at the bottom of the container. They are not very corrosive, compatible with plastics and only slightly toxic. Many salt hydrates are sufficiently inexpensive for the use in storage.

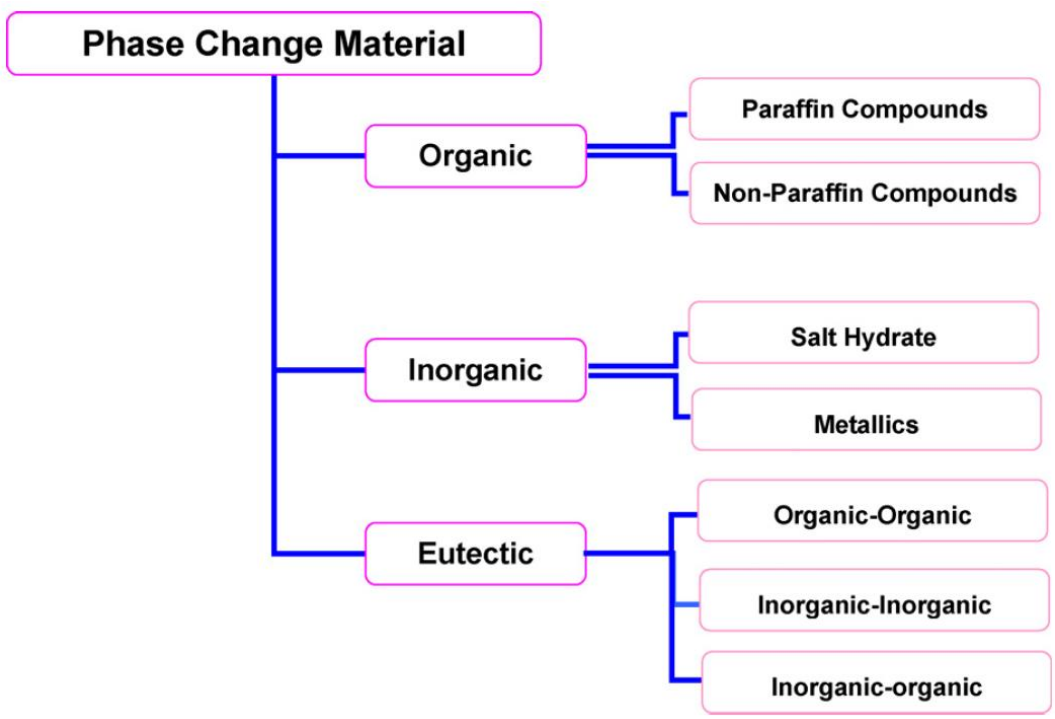

Figure 1.2.1. Classification of PCMs.

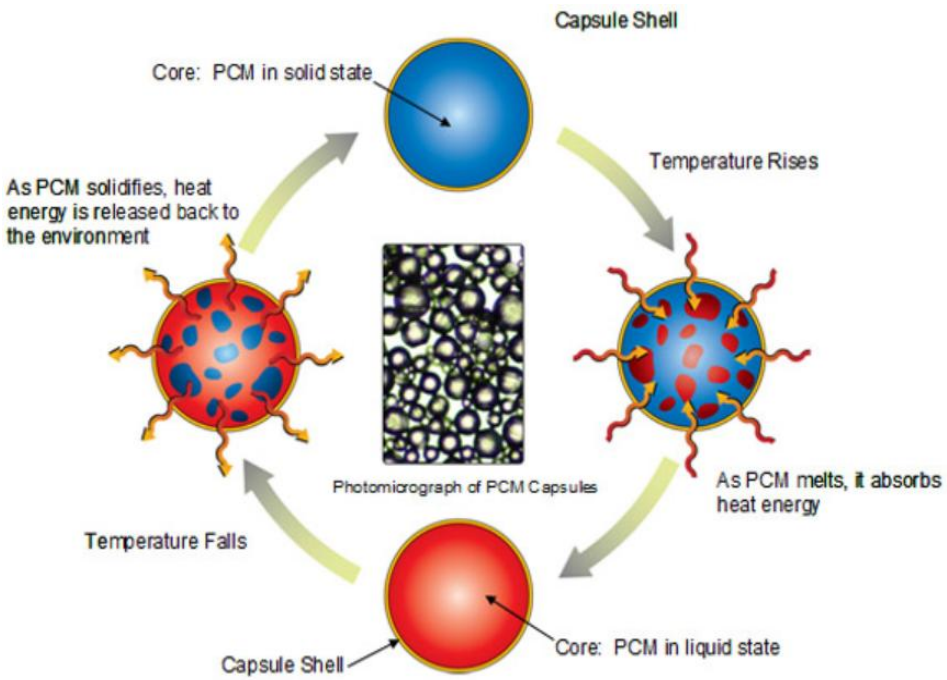

Figure 1.2.2. The principle of PCMs during the phase transition process.

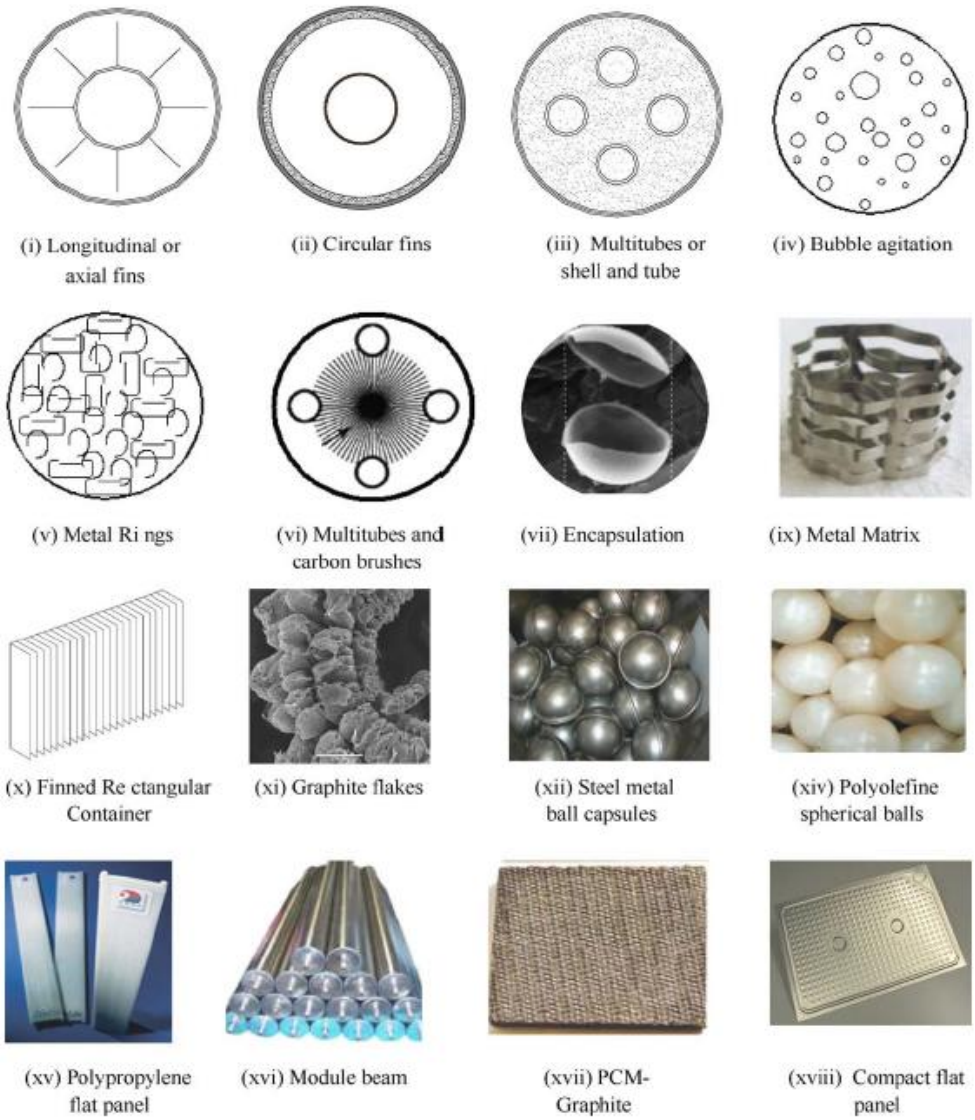

Figure 1.2.3. Heat transfer enhancement methods employed in phase change material research.

1.2. Research background

1.2.1. Form stable phase change materials

Since solid-liquid PCMs, however, have a leakage problem during the melting and cooling process, the field applications are restricted. To manufacture the form stable PCMs, some supporting materials are required to improve the dimensional stability of PCMs, some supporting materials are required to improve the dimensional stability of PCMs. In recent decades, various supporting materials such as urea-formaldehyde (UF), polyurethane (PU) [50], polyethylene (PE) [51], and polyaniline (PANI) have been used to retain PCMs with a core-shell composite structure as given in **Fig. 1.2.4** [52]. Since a large portion of the working material has been replaced with the supporting shell material, the overall latent heat of the composite is reduced. As a result, the conventional PCM composites have smaller energy storing capacity than the pure PCMs during the phase transition [53, 54]. The principle of using the phase change material is simple, as the heat supplies, the material changes its phase from solid to liquid with phase transitions at constant temperature until it completely converts into solid [55]. Similarly, when heat is released, the material changes phase from liquid to solid. Again at constant temperature until it solidifies completely. The matrix with a traditional structure have a large thermal inertia (sensible heat storage) and supply natural air conditioning in the rooms. In the commercial sector, the trend is to decrease the wall thickness to reduce the weight, material consumed, the transport costs and the construction time. The latent hat storage by incorporating a phase change material (PCM) into some typical materials is an attractive way to compensate for the small storage capacity of most existing modern applications as well as the advanced materials [56]. The main disadvantage of light weight PCMs is the low thermal mass tending to the large temperature fluctuations due to external heating or cooling load. Using PCM material in such fields can decrease the temperature fluctuation, particularly due to incident solar radiations loads as proved in several numerical studies.

The microencapsulation technology is the prominent for use of PCM in the form stable energy storage utilization. With the advent of PCM implemented in gypsum board, plaster, concrete and other shell covering materials, thermal storage can be part of the main structure even for light weight applications. Several forms of bulk encapsulated PCMs have been developed for active and passive solar applications in building including direct heat gain. However, the surface area of most encapsulated commercial products has been inadequate to deliver heat to the shell materials after the PCM melted by the solar radiation or thermal transformation. One problem to solve in some PCM applications is the liquid migration, using some kinds of packing. Microcapsules consist of little containers, which pack a core material with a hard shell. Microencapsulating PCM brings some more important advantages like that microcapsules can handle phase change materials as core, as far as, they tolerate volume changes.

It is the process by which individual particles or droplets of solid or liquid material (the core) are surrounded or coated with a continuous film of polymeric material (the shell) to produce capsules in the micrometer to millimeter range, known as microcapsules. Microcapsules may be spherically shaped, with a continuous wall surrounding the core, while others are asymmetrically and variably shaped, with a quantity of smaller droplets of core material embedded throughout the microcapsule. All three states of matter (solids, liquids, and gases) may be microencapsulated. This allows liquid and gas phase materials to be handled more easily as solids, and can afford some measure of protection in handling hazardous materials. Microencapsulation may be achieved by a myriad of techniques, with several purposes in mind. Microcapsules are tiny little containers which pack the core material individually with a hard shell. Microcapsules can therefore handle even liquids as solid material. They tolerate phase change materials as core. Microcapsules maybe processed as aqueous dispersion or powder and improve the formulation of phase change materials as many working materials go through a powder state during processing. Phase change temperatures between room temperature to less than 80 °C are available to manufacture with microcapsules. Several physical and chemical methods have been developed for production of microcapsules. The description of microcapsules depends mainly on the core material and the deposition process of the shell as below: (i) Mononuclear microcapsules contain the shell around the core. (ii)

Poly-nuclear capsules have many cores enclosed within the shell. (iii) Matrix encapsulation in which the core material is distributed homogeneously into the shell material.

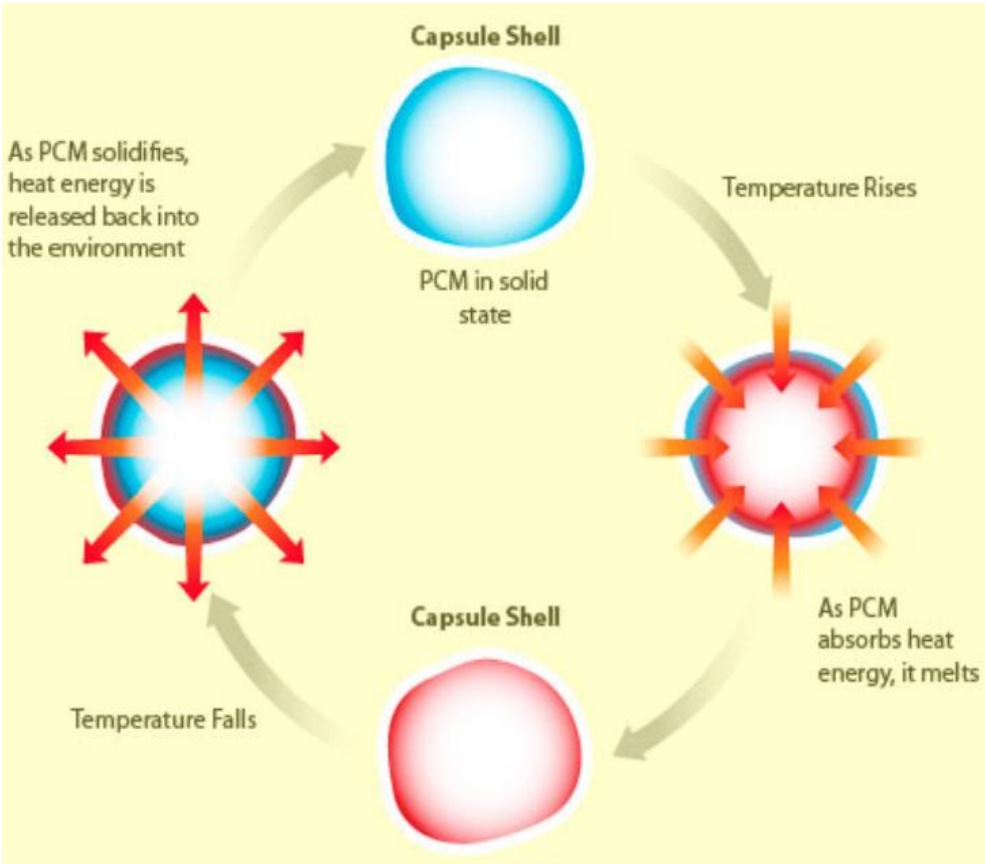

Figure 1.2.4. The schematic of form stable PCM microcapsule.

1.2.2. Microencapsulated phase change materials

Materials with tunable electrical conductivities can be widely used for various applications such as thermal sensing, thermal switching control, and wireless devices. The polymer nanocomposites, especially phase change materials (PCMs) exhibit high latent heat upon melting and crystallization method, excellent thermal stability and

reliability which could be utilized effectively in this field. However, the leakage problem restricts the applications and needs some supporting materials to entangle the working materials [57]. To address the leakage problem, the present research has developed a family of polyaniline (PANI)/PCM microcapsules for sustaining their intrinsic shape on both heating and cooling process [58]. The electrical conductivities of these form stable PCM composites containing conductive nano-fillers typically decrease with temperature variation and even exhibit a rapid drop near the melting point (T_m). Flexible responsive materials, such as graphene embedded phase change material (PCM), can exhibit a smart response to the heating and cooling steps and be utilized for the thermal sensing applications. The electrical conductivity is varied during the phase transition due to volume change of the working material. However, the leakage is one of the serious problems and restricts the PCM from applications.

Phase change material is encapsulated in the present work to prevent the leakage problem. Polyaniline (PANI) is selected as the supporting material to surround the pure phase change material and thus the fabricated PCM composite could sustain the shape under the phase transition process. Herein, the polyaniline encapsulated phase change material is produced and the graphene powder is added to increase the electrical property of the PCM composite. The graphene embedded PCM composite shows excellent electrical performance when the temperature is increased to the isothermal phase transition state. The pure PCM inside the microcapsules begin to melt and the liquid state lead to the volume expansion of the PCM composite. Therefore, the reversible form stable phase transition is achieved and the electrical conductivity is increased as the distance between conductive graphene fillers is reduced with volume expansion of the PCM. This study suggests that the microencapsulated PCM composite should provide new applications for thermal sensing and flexible thermoelectric devices like smart photodetectors.

Thermo-responsive materials can be employed for temperature sensing systems. In this study, we demonstrate a carbon nanotube (CNT) incorporated form stable phase change material (FSPCM) that exhibits over 3 orders of magnitude variation in the electrical resistivity during the phase transition process. The manipulation of electrical resistivity is made by the volume change induced by the thermal energy due to the phase

transformation. The phase change material (PCM) is encapsulated by polyaniline (PANI) and maintained the solid state during the melting and cooling processes. The form stable microcapsules underwent the volume expansion and shrinkage according to temperature. The CNT embedded phase change material (PCM) showed remarkable electrical reversibility and thermal stability in the melting/cooling cycles. We foresees that the CNT/PCM nanocomposite can be applied to flexible electronics and thermal sensing probes.

1.2.3. Phase change materials for energy harvesting

The key challenges in thermoelectric power conversion are creating a significant temperature difference and obtaining more heat energy through a thermoelectric device. Herein, graphene/polyethylene glycol composites (G-PEGs) are proposed as a heat supply for thermoelectric devices [59, 60]. The G-PEGs not only afford a lot of conductive pathways for heat transfer but also act as highly thermally conductive reservoirs to hold phase change materials for thermal energy collection, storage and release. The concept described in this study holds great promise in designing multifunctional composites for heat collection, transport, and supply in thermoelectric power conversion.

An important physical law of heat is that heat always flow from an area of high temperature to an area of low temperature. Therefore, according to this phenomenon, heat is easily lost and consumed, from the perspective of conserving heat energy. The collection and storage of surplus heat for further utilization elsewhere is significant with respect to the conservation of heat energy. In the past, convectional single-phase functionally thermal fluids (such as water and ethylene glycol) exhibited the ability to transport heat energy from high temperature regions to low temperature regions by means of a tube and a pump. Furthermore, the latent functionally thermal fluid is established, wherein phase change materials (PCMs) are microencapsulated and suspended in a conventional single-phase heat transfer fluid. The thermal fluid can collect, store, and transfer a larger apparent specific heat than conventional single-phase fluids during the phase change period. It would now be useful if other materials, besides functionally thermal fluids, which can effectively collect, store and convey heat energy, could be

developed. This would offer many possibilities for the use of heat energy in the conversion of thermal energy [60].

A novel architecture of a 3D interconnected net like graphene assembled in the phase change material (PCM), especially polyethylene glycol (PEG) matrix is proposed. Single-layer graphene with a high specific surface area (>2600m2g^{-1}) is superior to other carbon based materials as a thermal conductor [61]. The thermal conduction of carbon materials mainly relies on their electrically conductive surfaces; graphene with extremely high thermal conductivity (5100 W/mK) and electrical conductivity is considered to be an ideal material to replace metal, graphite parts, graphene oxide (GO) or reduced graphene oxide in the thermal management systems of electronic devices, e.g., the heat sinks of light-emitting diodes (LED). Phase change materials can absorb or release large amount s of latent heat during the phase transformation period and have been extensively applied in solar energy storage, waste heat recovery, smart air conditioning in buildings, and homo-thermal clothing [62]. Therefore, based on the advantages of graphene and PCMs, G-PEGs contain an interconnected graphene framework, which can act as a medium for directing thermal transport. The G-PEGs possess numerous small phase change units with unit interior reversible phase transformation, resulting in efficient collection/storage of heat. G-PEGs not only afford a lot of conductive pathways for heat transfer but also act as a highly thermally conductive reservoir to hold phase change materials for thermal energy collection, storage and release. Furthermore, demonstrating for the first time that the heat collection and storage abilities of the G-PEGs can provide a heat source for thermoelectric devices. The concept described in this study holds great promise in designing multifunctional composites for heat collection, transport, and supply in thermoelectric power conversion.

Herein, by taking PEG6000 as an example of a PCM, we clarified in detail the fabrication mechanism and processing of G-PEGs for thermal management by polyethylene glycol (PEG) reversible phase transformation [63]. The synthesis of G-PEGs is simple and is using an impregnation method. Firstly, PEG is melted at 80 °C and then a graphene aerogel is emerged into the melted PEG under vacuum state. After 8 hours and removing the vacuum state the PEG infiltrated PEG/graphene PCM composite is formed by solidification method.

Thermoelectric energy harvesting system which is composed of the shape-stabilized PCMs and semiconductors has shown a great potential in various applications [64, 65]. For the energy harvesting system, N and P type semiconductors are required to connect the PCMs for construction of an electrical circuit [66, 67]. The N and P type semiconductors including thermo-couples utilize two different effects for energy harvesting; Seebeck effect and Peltier effect [68]. The Seebeck effect induces electrons to move from hot side to cold side of the energy harvesting device by absorbing the heat energy and the Peltier effect results in a temperature difference between two side planes by using the supplied electric power. Recently, Jiang et al, [68] prepared an energy harvesting system to generate the electric current by placing PCMs on the hot side and a heat sink (e.g., ice water) on the cold side of N and P type semiconductor. However, the electric current is obtained only during the cooling stage after removing the heat source, i.e., when releasing the stored energy from the PCM. On the basis of former research, modified the energy harvesting system with two different form stable PCMs placed on the sides of N and P type semiconductor to achieve the thermoelectric energy harvesting during the phase transition process. The environmental temperature is only adjusted to examine the harvested energy and efficiency.

In the current study, we devised an advanced thermoelectric energy harvesting system with two different phase change materials (i.e., PEG and 1-TD), and N and P type thermoelectric generators (PN TEGs). By using the temperature difference between two PCM composites during heating and cooling processes, the enhanced energy harvesting is achieved. Graphene nano-platelet (GNP) is employed as a filler in the graphene aerogel to prevent the fracture and sustain the 3D porous internal structures. After fabricating the graphene based form stable PCMs, the PEG and 1-TD are placed on the two sides of PN TEGs for inducing thermoelectric energy harvesting. The electric current is measured during the phase transition process with respect to the temperature difference between two sides of semiconductors. An LED lamp is turned on by using the harvested electric energy. Besides, the thermoelectric energy conversion is numerically calculated to understand the energy harvesting mechanism.

1.2.4. Modified Phase change materials for energy harvesting

The phase change materials (PCMs) incorporate nano-fillers for thermal energy storage applications, where nano-fillers are included as minor components (< 10wt% in general), have been normally investigated to reinforce the utilization due to the nanoscale effect on surface area and internal structures [69]. Consider the volume ratio and realize the full functionality potential of expensive and heavy inorganic fillers used as little as possible for low cost lightweight and functional materials. In sharp contrast to the traditional understanding of mechanical integrity and functionality of polymer nanocomposites, the researcher often offers different strategies for materials design. For instance, nacre contains 95wt% of hard ceramics (aragonite) combined with 5wt% of soft organic materials (proteins and polysaccharides), which act as "mortar" rather than a matrix "brick" [70, 71]. Such a composition (hierarchically architecture in a manner opposite to that for synthetic polymer nanocomposites; these will hereinafter be referred to as inversed nanocomposites) is believed to resolve the bottleneck associated with mechanical properties by a simultaneous enhancement of the material tensile strength and toughness.

Having been inspired by biomimetic materials, strong composites obtained by the integration of graphene or similarly layered 2D nano-sheets (used as major hard building blocks) with soft organic materials have been recently demonstrated to achieve synergistic toughening through the interfacial interaction between the basal planes of the nano-sheets and the organic components. Such integrated graphene based composites are fabricated by various methods including layer by layer assembly, vacuum filtration, ice-templating, and sintering. Unfortunately, interactions along the lateral direction of nano-sheets cannot often improve the mechanical integrity of three-dimensional (3D) graphene aerogels (Gas), in which the edge-to-edge interactions at nano-sheet joints are more critical for reinforcing the crack propagation points of inner-sheet junctions. As has been previously reviewed by the authors and other researchers, 3D macroscopic graphene aerogel materials possess prominent features such as low densities, highly exposed surface areas, low mass and ion transport resistance, percolation-type electrical conductivity, and good chemical stability; these make them potentially suitable for

various applications including electrodes, catalytic supports, absorbents, separators, and chemical/bio-sensors. However, weak van der Waals interactions at the graphene sheet junctions result in mechanical integrity issues.

For the purpose of overcoming these challenges, various attempts have been performed, such as edge-to-edge assembly, introduction of a carbon linker, 3D printing technique, and addition of polymeric segments (e.g. polypyrrole (PPy), poly(vinyl alcohol) (PVA), poly(acrylic acid) (PAA), poly(dimethylsiloxane) (PDMS), etc.) [72]. Several approaches demonstrated impressive achievements in mechanical properties. However, there still remains a challenge to further develop high performance 3D graphene aerogels which can simultaneously ensure mechanical and electrical properties. For instance, excessive addition of polymers onto the basal planes of nano-sheets can inherently produce detrimental effects on their recovery rates due to the timescale of polymer relaxation as well as on electrical conductivity because of the polymer insulating properties. The selective insertion of soft segments exclusively into graphene inner-sheet joints is more desirable for the 3D macroscopic graphene aerogels since it creates an effective load transfer pathway throughout the interconnected graphene networks by delocalizing the applied stress.

Herein, the cartilage-inspired designs of 3D super-elastic and ultra-durable graphene aerogels that sustain their intrinsic structures. Consider the inversed nanocomposite composition, which is found in the human body at the macroscale level, the presence of small amounts of soft cartilage in joints is essential for connecting stiff (or hard) but hollow backbones and building an effective load-bearing system. Such bio-inspired cartilage architecture can be obtained inside the 3D internetworked graphene aerogels by selectively gluing the inter-sheet joints with soft materials and is completely different from the previously studied graphene nano-sheet based artificial nacres with different interactions [73].

Since graphene is first successfully fabricated from the graphite, it has been widely used in a variety of fields because of its remarkable physical and chemical properties, such as high thermal conductivity, great mechanical strength and high theoretical surface area [74, 75]. In particular, this “miracle material” has shown great potential in the purification of wastewater with contaminants such as metal ions, organic compounds, and

oil and has acted as a super absorbent material. However, the aggregation and potential risk of graphene nano-sheets extremely limits its applications in the environment. The assembly of two-dimensional (2D) graphene nano-sheets into a three-dimensional (3D) graphene aerogel structure can preserve the original properties of graphene and prevent the aggregation of graphene layer. Hence, many kinds of graphene aerogels have been prepared via various approaches, such as chemical reduction methods, hydrothermal reduction method, template-directed methods, and 3D printing, and the aerogels have shown fascinating performance in pollution control, energy storage, and catalytic transformation [76, 77].

The hierarchical porous network structure contains micro, meso, and macropores, which is the most remarkable characteristic of graphene aerogels and greatly promotes internal transmission and increases its recycling potential. Moreover, the π-π stacking between graphene nano-sheets can also be reduced to some extent to increase the exposure of the adsorption active sites [78]. However, the 3D porous network structure is generally formed through the random weak connections between the graphene oxide (GO) nano-sheets, such as H-bonding, and π-π stacking. The fragile morphology of graphene aerogels is generally too weak to withstand practical application conditions, resulting in irreversible collapse or deformation of the porous structure. The unstable structure greatly affects the durability and recyclability of graphene aerogels as adsorbents. Therefore, development of graphene aerogels with a high stability, good recyclability, and powerful adsorption capability is of vital importance for emerging requirements in environmental applications.

Various cross-linkers, such as polymers, metal ions, biomolecules, or small organic molecules have been employed to improve the structural stability of graphene aerogels through tuning the interactions between the GO nano-sheets. These interactions can be divided into two basic categories: weak non-covalent bonding (π-π stacking, hydrogen bonding and electrostatic interactions) and strong covalent bonding. Generally, graphene aerogels originating from non-covalent interactions are relatively unstable and cannot withstand mechanical pressures or other harsh environmental conductions. Compared to non-covalent interactions, cross-linking via covalent bonding between nano-sheets can substantially enhance the structural stability of graphene aerogels. However, studies of

covalently cross-linked graphene aerogels are limited, and the preparation processes, such as hydrothermal reduction and the introduction of other additives as hydrothermal reduction and the introduction of other additives as reducing agents, are generally complicated and expensive. Furthermore, the stability, porosity, compressibility and adsorption are key characteristics of graphene aerogels for their practical application.

Cysteamine is a small molecule with active thiol group and amine group at each end of carbon chain, which makes it a suitable binder to connect the graphene nano-sheets. Many previous works have chosen cysteamine as the functionalizing agent to form thiol functionalized graphene oxide. However, to the best of our knowledge, the incorporation of cysteamine with GO to form the graphene aerogels have not been reported. Here, graphene/cysteamine aerogels (GCA) are synthesized using the small organic molecule of cysteamine as a covalent cross-linker under a mild heating process at high temperature and compared with neat graphene oxide aerogel, GCA showed excellent porosity and stability, which are characteristic of a good supporting material for various infiltration method. As predicted, the GCA is improved significantly for the mechanical properties and sustained the intrinsic solid state via over melting point and resisting the external pressure. The GCA embedded PCM composites can absorb the thermal or light energy more stable for the thermoelectric energy harvesting.

1.2.5. Phase change materials for pyroelectric energy harvesting

Converting thermal energy into the electrical energy has been received large attention and become a new smart research field. Since the solar energy and wasted thermal energy is nearly boundless and useful to the human life. Harvesting energy from the large amount of solar or wasted thermal energy should be a great environment and vital for the low power consumptions. Pyroelectric materials which have the opportunity to convert thermal energy into the electrical energy, regarding as a smart power generator or thermal energy harvester [79]. Unlike thermoelectric generator (TEG) that depends on the temperature difference, pyroelectric energy harvesters require the continuous temperature variation by the external heat source in order to develop an electrical current [80].

According to the pyroelectric device, poly(vinylidene difluoride) (PVDF) is selected an excellent material for thermal and mechanical energy harvesting [81].

Since the pyroelectric effect is generated to the fluctuations of thermal energy, and enlarge the practical applications such as wind, sun light, heat flux, and cooling sources. Pyroelectric effect depends on the change of polarization as given by the charge separation between two opposite electrode. The phase change materials (PCMs) are able to absorb or release the thermal energy due to the high latent heat. In addition, the stored thermal energy provides to an opportunity of the change of temperature difference and lead to a pyroelectric effect upon heating and cooling process. Based on the nearly isothermal field during the phase transitions, the single or multiple PCMs utilized to design a new concept in the pyroelectric effect and generate the electrical voltage and current. In this part, summarize to the PCM composite in the PN cell energy harvesting applications, the polyethylene glycol (PEG) utilized as a working material at the hot side of the pyro-electrode when the Aluminum heat sink combines at the opposite side as a cold side of pyro-electrode. Furthermore, the optimization of PEG and 1-TD composites are subsequently mentioned to the pyro-electrode and developed a multiple pyroelectric energy harvesting system. The temperature difference causes the thermal polarization in the closed circuit and obtain the harvesting voltage during the melting and cooling process. In recent years, the wasted heat recovery applications are more attracted to increase the thermoelectric energy harvesting efficiency and contribute to the sustainable energy development. The heat flow especially vehicle gas is one of the serious social problems and utilized effectively in the energy harvesting become a new approach to solve the energy depletion and pollutions. Herein, the multiple energy harvesting system is placed at the various rate of heat flow to obtain the thermoelectric effect based on the pyro-electrode. In the different way of pyroelectric applications, the glass is widely used in the practical life and consider the sunlight transmits the window glass to generate the simple pyroelectric effect is a novelty of thermoelectric energy harvesting research. The different field of sunlight intensity is directly effect to the final temperature and even modify the degree of energy storage. To achieve the former problems, the PCM composite is act as a window blind to collect the solar energy and release the stored thermal energy after removing the heat source to obtain a pyroelectric energy harvesting.

As a result, the combination of PCM composites and pyro-electrode are well matched to generate the induced voltage and current upon heating and cooling, the glass transmission system demonstrates a new solar energy utilization and sufficiently applied to the thermoelectric energy harvesting.

1.3. Objectives of present work

In this Ph.D study, form stable phase change material (PCM) is manufactured successfully by using the microencapsulation method and vacuum impregnation method. In Chapter II, the pure PCM is well encapsulated to generate the microcapsules and utilized the volume expansion during the phase transition process. The volume change of microcapsules cause the filler modification and increase the electrical conductivities. The two different phase change materials polyethylene glycol (PEG), and 1-tetradecanolo (1-TD) are utilized as a working material and placed on the each side of PN TEG semiconductor. The single PN TEG energy harvesting system to further optimum components of two working materials are described in Chapter III, and further modified supporting materials to infiltrate the pure PCMs are generally illustrated in Chapter IV, the thermoelectric energy harvesting efficiency is correlated to the mass ratio of working material. It is indicated that the volume shrinkage during the vacuum infiltration method, the modified supporting materials are able to prevent the volume shrinkage and infiltrate more pure PCMs. Consider the pyroelectric effect under the temperature fluctuation, the form stable PCM composites are generally utilized to the pyroelectric system as described in Chapter V, and conclusion in the last Chapter VI.

The polyaniline (PANI) acts as a shell material due to the high thermal stability, and great flexibility. The polyethylene glycol (Mn= 20,000) is utilized in this study and manufactured the core-shell like PCM microcapsules via microencapsulation method. The graphene and carbon nanotube (CNT) powders are dispersed into the PCM microcapsules with different weight fractions (1wt%, 3wt%, 5wt%, 7wt%, and 10wt%) to measure the change of electrical conductivities during the phase transition process.

The different phase transition temperature causes the temperature difference at the two sides of PN TEG and generates the induced current in the circuit due to the Seebeck effect.

The PN junction (PN diode component) holds the forward direction and reverse bias and the electrical current could easily go through the depletion layer while the energy barrier is blocking the electron movement in the reverse bias. The multiple phase change materials based energy harvesting system is sufficiently overcome the PN TEG rectification property to generate excessive electrical energy from the thermal transformation. The thermal conductivity is directly affect to the thermoelectric energy harvesting efficiency and increase the filler of graphene nano-platelet (GNP) contents are essential to obtain a new result of thermoelectric effect.

After finding an optimum components, the modified supporting material is applied to manufacture the form stable PCM composites. The PDMS dispersed supporting material can forbid the volume shrinkage upon infiltration process and fill up more effectively into the porous internal space. Based on the volume stability, the cross-lined structure is upper increased the mechanical properties and resist external force at over the melting temperature. Hence, the cross-linked supporting material based PCM composites exhibit a great thermal to electrical transmission without any weight loss. Thus, the light absorption causes the temperature increase and produce the electrical current due to the temperature difference between two edges of PN TEGs.

From the PN cell energy harvesting applications, it is demonstrated that the form stable PCM composite with cross-linked supporting materials exhibits the most stable mechanical property and further utilizes in the new thermoelectric energy harvesting applications. The pyroelectric effect is one of the recent research especially in these 2 years, and design a pyro-electrode system with PCM composites suggest a new standard for temperature change at the external environment. The various design of pyroelectric energy harvesting system with PCM composites provide an opportunity to obtain the induced voltage and current during the phase transition process. In addition, the sunlight glass transmission become a practical application as using a pyro-film for energy harvesting. The PCM composites can act as a blind to collect the solar energy and even provide the stored energy for thermoelectric energy conversion. The last work indicates the solar energy irradiation to generate the pyroelectric effect and obtain the energy harvesting upon light-on and light-off process.

Chapter II.

Microencapsulated phase change materials

2.1. Overview

In this chapter, the form stable microencapsulated PCM composite is fabricated and utilized for a thermal flexible working materials. The graphene and CNT powders are well dispersed on the surface of PCM microcapsules and the electrical conductivities become rapidly changed during the phase transition process.

In Section 2.2, the pure PCM and shell materials are described and have an introduction in Section 2.2.1. The Section 2.2.2 shows the theoretical background such as the previous thermal sensing research and the importance of PCM microcapsules. The form stable PCM composite via microencapsulation method is then briefly described in Section 2.2.3, and the last Section 2.2.4 concludes the PCMs for microencapsulation applications.

The graphene powders/PCM composite for microencapsulation is mentioned in Section 2.3, and the objective of this work is shown in Section 2.3.1. The preparation of graphene powders are directly described in Section 2.3.2, and the preparation of PCM encapsulated composite is subsequently indicated in Section 2.3.3. The numerical simulation for predicting the volume expansion is well introduced in Section 2.3.4. After manufacturing the final graphene powders/PCM composite, the morphologies of PCM microcapsule is given in Section 2.3.5, and the last Section 2.3.6 shows the conclusion of graphene embedded form stable PCM microcapsules.

Consider the carbon nanotube (CNT) has better electrical conductivity than that of graphene powder due to the high aspect ratio. The PCM composite with CNT microcapsules are mentioned in Section 2.4, and the introduction of microencapsulation concept is described in Section 2.4.1. The preparation of PCM encapsulated composite is

briefly illustrated in Section 2.4.2, and the numerical simulation can further demonstrate the prediction of volume change in Section 2.4.3. The results and discussion of CNT embedded PCM composite is generally explained in Section 2.4.4, and the conclusion of this work is described in Section 2.4.5.

2.2. Review of PCM microcapsules

2.2.1. Introduction

The phase change materials (PCMs) are fully utilized to the thermal energy storage (TES) applications due to the high latent heat, high thermal density and thermal reliability. However, the common mentioned leakage problem restricts directly when the solid-liquid phase transition process. There are some of the supporting materials applied to prevent the leakage problem upon melting and cooling. The concept of utilizing the phase change materials (PCMs) are quite simple as providing or releasing a large amount of thermal energy and thus the system of PCMs existing the physical change among these phase transitions. The phase change material (PCM) composites with supporting materials can remain high heat of fusion without any leakage and the form stable phase change materials (PCMs) are generally used in the thermal sensor, buildings, and smart textiles.

The core-shell like PCM composites are the popular materials in the form stable solid-liquid PCMs which can sustain the solid state without weight loss or even leakage. The fabrication of sphere size of PCMs are microencapsulation method with rigorous stirring. It indicates the pure PCMs are hydrophobic and turn into the core structure at the DI water. In addition, the shell materials have great solubility at the conventional solvent and well dispersed in the aqueous solution. When the melted PCM and shell material are poured into the DI water with high rpm speed, the shell material become entangled around the sphere size of pure PCM. Finally, the PCM based microcapsules are generated by using the solvent evaporation method.

2.2.2. Theoretical background of microencapsulation

It is well realized that microencapsulation technology is normally utilized to

manufacture the form stable phase change materials (PCMs). Microencapsulation method is demand for little containers to pack the core working material sufficiently with a hard shell. The Microcapsules can handle the liquids as solid material without any leakage. The shell materials can sustain the intrinsic state and tolerate phase changes such as volume expansion in the internal core structures. Microencapsulation method is processed as aqueous dispersion with physical stirring. The microcapsules mainly depend on the core material and the degree of coating of shell materials.

The description of these microcapsules are required as the core-shell microcapsules include the shell materials around the sphere size of core shapes, and the microcapsules have plenty of cores enclosed within the shell materials. Furthermore, the core materials in the microencapsulation method is distributed homogeneously into the supporting materials. Thus, the microencapsulation of core-shell like structures are one of the practical ways to manufacture the form stable PCM composites.

2.2.3. Microencapsulation of PCMs

To fabricate the form stable PCM microcapsules are effective process to prevent the leakage problem. According to the concept of microcapsules, the pure PCMs are changed into the core shapes when the supporting materials are dispersed in the solvent. The core materials are already melted to the liquid state and stirring with over 6,000 rpm to generate the core-shell like structures. Some organic PCMs such as paraffin and polyethylene glycol (PEG) are getting more and more attention due to the high latent heat, great thermal stability, and chemical inertness. In this work, polyethylene glycol (PEG) with high molecular weight (Mn= 20,000) is selected as a working material and the polyaniline (PANI) is a shell materials to generate the PCM microcapsules. The PEG/PANI PCM composite is obtained by using microencapsulation method.

2.2.4. Conclusions

In this section, the microencapsulation method is an effective ways to fabricate the form stable phase change materials (PCMs) and obtain the sphere size of microcapsules. The polyaniline (PANI) encapsulated PCM composite is able to sustain the intrinsic solid

state during the phase transition process. Furthermore, the PCM microcapsules absorb or release high thermal energy due to the large portion of working materials. The PCM composite is expected to adopt at the thermal sensing, and photodetector by the internal volume change under the temperature variation.

2.3. Graphene powders/PCM for microcapsules

2.3.1. Introduction

In recent years, carbon based nanomaterials, e.g., graphene powders, carbon fibers, and carbon nanotubes (CNTs), have been widely used in the fields of electronics and thermoelectric due to their outstanding properties [82-84]. Graphene powders are selected as the filler to achieve novel electrical properties, and good electrical conductivity of the PCM composite is obtained in temperature variations [85]. Graphene powders can be dispersed in various polymer composites and attribute to the thermal and electrical properties in the polymer matrix [86, 87]. There have been previous studies on the electrical conductivity of composites with different amounts of graphene filler [88, 89]. However, the weight fraction of graphene powders must be controlled to achieve the optimum value by considering the percolation threshold [90].

Graphene embedded nanocomposites with higher electrical conductivity than pure polymer matrix have been widely reported [91, 92]. Combination of composite lattice is constructed by continuous honeycomb skeleton and layer by layer structure, which generated a favorable path for the electron movement [93]. However, it is hard to develop the desired sequence of fillers and the electrical property of the composite is even decreased with temperature rise [94, 95]. The phase change material is recommended to overcome the main problem because of its high thermal density and large enthalpy of phase transition [51, 96]. In comparison with previously reported thermal sensing materials based on graphene embedded nanocomposites, the graphene/PCM composites exhibit highly stable electrical conductivity and thermal reliability [53, 97]. Consideration of the change in PCM volume could contribute to the filler combination during the phase transition, and the electrical conductivity is gradually increased on heating of the PCM

composite. Thus, the phase change material is selected as a new flexible matrix to match the graphene filler in some typical researches [98, 99].

Although the PCM composite has an advanced thermal morphology, leakage of the PCM is one of the most conventional problems and restricts its application [96, 100-102]. To solve this leakage problem, some of the supporting materials such as polyethylene (PE) [103] and polyurethane (PU) are commonly utilized for sustaining the solid state during melting of the PCM [50]. These supporting materials are able to wrap the pure PCM to construct the form stable PCM composite and the final PCM composite could merely maintain the pristine shape during the phase transition [104-106]. However, these supporting materials are highly rigid and exhibit small volume changes during phase transition. Since the PCM composite needs a flexible supporting material which undergoes volume change without any leakage during melting of the PCM, polyaniline is selected as the supporting material for flexible and form stable properties [107, 108]. The encapsulated PCM composite exhibits form stable and thermally flexible morphologies, which contribute to the flexible electrical property.

In this study, we fabricate a PCM composite with electrical flexibility and dimensional stability by combining the polyethylene glycol (PEG) with polyaniline. The polyethylene glycol is a typical working material which can absorb or release a large amount of heat during phase transition and the pure PEG is encapsulated by polyaniline with the vigorous stirring method. The form stable PCM composite is produced by collecting polyaniline microcapsules containing the PEG. In addition, graphene powders are dispersed in the prepared PEG/PANI composite via ultrasonication method to generate a graphene embedded form stable PCM composite. Electrical performance of the resultant PCM composite is investigated by measuring the electrical conductivity with increasing temperature from 25 °C to 90 °C.

2.3.2. Preparation of graphene powders

The graphene oxide (GO) is generally synthesized by using the modified Hummers' method [109]. In order to increase the degree of oxidation, 3.0 g of graphite is gradually added into 12 mL sulfuric acid (H_2SO_4) for pre-oxidation. The graphite mixture is placed

in the hood for about 12 hours to remove the moisture. The pre-oxidized graphite and $KMnO_4$ (5 g) mixture is stirred in an oil bath at 35 °C for 2.5 hours. Then, 700mL deionized (DI) water is poured into the oxidized mixture and 20 mL H_2O_2 is added to the diluted mixture to remove excessive $KMnO_4$. The GO system turns bright yellow immediately and the GO solution is utilized after washing with 10% HCl solution to obtain the graphene oxide powder. Graphene oxide powders are obtained via freeze-drying method. After that, the 100 mg GO powder is subsequently diluted in 10 mL DI water and sonicated for about 30 min to produce a homogeneous GO solution. 90 ML DMF (dimethylformamide) is added into the GO solution to increase the solubility and ultrasonication is applied for more about 30 min. The DMF&GO solution is placed in a water bath at 80 °C for 24 h after dropping 1 mL hydrazine. Finally, the reduced graphene oxide (rGO) is obtained by filtering the solution.

2.3.3. Preparation of PCM encapsulated composite

To synthesize the polyaniline shell material, 4 g aniline monomer is added to the 150 mL DI water and 10 g PEG is melted at 80 °C. 150 mL DI water is poured into the melted PEG and the PEG solution is mixed with the aniline emulsion and 10 g APS (Ammonium peroxydisulfate) (mass ratio of 5:2 with respect to the aniline monomer). The PEG based aqueous mixture is rigorously stirred at 9,000 rpm for 4 hours to encapsulate the PEG with the polyaniline (PANI) chains. After evaporating the solvent and drying at a vacuum oven, the micro-sphere shaped PEG/PANI composite is obtained. Graphene powders are dispersed in the prepared PEG composite with different mass ratios, and ultrasonication is applied for 30 min to increase the degree of dispersion [110, 111]. The graphene embedded PCM composite is obtained finally by evaporating the solvent and drying in vacuum. The PCM composites with different weight fraction of rGO are labeled as 1wt%, 3wt%, 5wt%, 7wt%, and 10wt% PEG/PANI/rGO.

2.3.4. Numerical simulation

Numerical simulation is carried out by utilizing a finite element method (FEM) software, COMSOL Multiphysics, to predict the thermal expansion coefficient of the

PCM composite during the melting and crystallization processes. The finite element mesh is constructed based on the size of encapsulated PCM composite and properties of polyaniline are used for the surface shell material while properties of polyethylene glycol for the internal working material. Density, latent heat (ΔH), heat capacity, young's modulus, melting and crystalline temperatures are employed for the numerical simulation. The spherical PCM composite is initially placed at room temperature and the environmental temperature is increased from room temperature (25 °C) to 90 °C for melting to observe the volume change over the phase transition. The PCM composite is exposed to the air for cooling after removing the heat source. Temperature of the PCM composite is decreased to room temperature from 90 °C and volume shrinkage is induced due to solid transition of the PEG. Total number of finite elements for this numerical simulation is 17,384 except for 8,304 boundary elements and 1,368 edge elements.

Structural mechanics is selected for calculation of thermal stresses at the time dependent module in COMSOL Multiphysics. Volume expansion of the spherical cell with respect to the temperature variation is calculated by the solid mechanics and the basic governing equation is given as below.

$$\rho \frac{\partial^2 \mu}{\partial t^2} = \nabla \cdot \mathrm{S} + \mathrm{Fv} \tag{1}$$

where ρ is density of the PCM, μ is the rate of motion during volume change as a function of time t, v is the strain tensor, and F is the external force under the phase transitions. S is the Piola-Kirchhoff stress and the relation between thermal stress and strain is as follows.

$$\mathrm{S} = S_{ad} + \mathrm{C}: \epsilon_{el} \tag{2}$$

Where S_{ad} means the Cauchy stress for confirming the initial volume change, C is the fourth-order elasticity tensor of material, and ϵ_{el} is the linear elastic strain and expressed by the following combination of deformation.

$$\epsilon_{el} = \epsilon - \epsilon_{inel} \tag{3}$$

$$\epsilon_{inel} = \epsilon_0 + \epsilon_{th} \tag{4}$$

Change in the elastic strain can be defined by the structural changes from the equations (3) and (4). The linear elastic strain is correlated to the stress-strain ϵ and inelastic strain ϵ_{inel} from the Hooke's law. Hence, the inelastic strain is determined by the initial strain ϵ_0 and thermal strain ϵ_{th}. Both internal and external forces generate the shape deformation in addition to the volume change due to thermal expansion. The thermal strain caused by the volume change is described as below.

$$\epsilon_{th} = dL\ (T, T_{ref}) \tag{5}$$

where dL is the thermal strain with respect to temperature variation and directly related to the Young's modulus of the PCM composite. To evaluate the effect of the phase transition on the thermal strain during heating and cooling, the heat transfer equation in solids is employed and heat flow is identified for the phase transition. The governing equation of heat transfer is demonstrated as below.

$$\rho C_p \frac{\partial T}{\partial t} + \rho C_p u \cdot \nabla T + \nabla \cdot \boldsymbol{q} = Q \tag{6}$$

$$\boldsymbol{q} = -k \nabla T \tag{7}$$

where ρ is the mass density, C_p is heat capacity of the PCM, and $\boldsymbol{q}$ represents the heat transfer rate. From Equation (7), the heat transfer rate is related to the thermal conductivity k and temperature variation of the PCM composite. The governing equation on the heat capacity of the phase change material is expressed as below.

$$C_p = \frac{1}{\rho}\left(\theta \rho_{phase1} C_{p \cdot phase1} + (1-\theta)\rho_{phase2} C_{p \cdot phase2}\right) + L\frac{\partial \alpha_m}{\partial T} \tag{8}$$

Phase 1 is changed to phase 2 and fill-factor θ is generally related to the heat capacity, thermal conductivity, latent heat L, and mass coefficient α_m. In addition, the heat flux under the natural convection $\boldsymbol{q_0}$ is effectively correlated to the temperature difference and heat transfer coefficient h as below.

$$\boldsymbol{q_0} = h \cdot (T_{ext} - T) \tag{9}$$

The volume change ΔV is calculated by the thermal strain during melting and

crystallization processes after combining solid mechanics with heat transfer theories. Based on the numerical result, the volume expansion ratio $\Delta V/V$ is calculated and expressed as follows.

$$\frac{\Delta V}{V} = exp\left[\alpha_v\left(T_f - T_i\right)\right] - 1 \tag{10}$$

The thermal expansion coefficient α_V is a function of temperature difference between the final temperature T_f and initial temperature T_i with the volume expansion ratio. The basic governing equation of the electrical resistivity in the filler embedded composite is typically given as below [112].

$$\rho' = \rho_0[(p_V - p_C)/(1 - p_C)]^{-t} \tag{11}$$

The electrical resistivity of the composite ρ' is a function of filler resistivity ρ_0, filler volume fraction p_V, percolation threshold p_C, and conductivity critical exponent t. The percolation threshold indicates the optimum filler content in the composite due to the saturation of filler contacts. The electrical resistivity $\rho(T)$, is affected by the temperature variation and the thermal expansion causes the increase of electrical conductivity as described by the following equation [113].

$$\rho(T) = \rho'[1 + \alpha_V(T - T_i)] \tag{12}$$

2.3.5. Results and discussion

2.3.5.1. Confirmation of manufactured graphene and polyaniline

The spherical structure of the encapsulated PEG is illustrated and the volume change of the PCM composite during phase transition is also shown in **Fig. 2.3.1**. As shown in the schematic figure, the form stable PCM composite is well encapsulated by the shell material and thus sustain the solid state over the melting temperature. The polyethylene glycol works as a core material and volume change of the core-shell structure is induced by the phase transition during heating and cooling. In other words, the thermal expansion and contraction of the PCM lead to the volume change of the spherical system. The graphene powders are dispersed well on the surface of PCM microcapsules and move easily as the surface of the PCM composite is expanded or contracted. The contact between graphene fillers is promoted with respect to the volume expansion of the PCM composite and the electrical conductivity is increased accordingly. After removing the heat source, the system undergoes the crystallization process and recovers the initial volume. The volume shrinkage over the cooling process causes decrease of electrical conductivity. Before fabricating the encapsulated PCM composite, volume change of the pure PEG is observed by using an optical microscope as shown in **Fig. 2.3.2**. It is identified that the PEG structure turns into the liquid state as the temperature is increased up to 90 °C and the solid crystal structure is generated upon cooling.

The microscopic images demonstrate that the PEG is utilized effectively as a core material of the microcapsule with distinct volume changes. To assure that the reduced graphene oxide is obtained, the FTIR results are shown in **Fig. 2.3.3a** with different peals from those of the graphene oxide. The typical peaks in the GO generally appear at 1056cm^{-1} (C-O bond vibration), 1621cm^{-1} (C=C stretching vibration), 1717cm^{-1} (C=C bonding), and 3408cm^{-1} (–OH group). The above peaks for functional groups disappear in the case of the reduced graphene oxide except for the sp^2 C=C bonding at the 1598cm^{-1}. The FTIR result also shows that the rGO is successfully obtained from the prepared

graphene oxide. Furthermore, the synthesized polyaniline is identified by the H- NMR measurement as shown in **Fig. 2.3.3b**. The polyaniline is polymerized successfully from aniline monomer and the polyaniline salt is formed [114]. Thus, the PANI shows the NH proton signal and peaks of the aromatic protons [115]. The NH proton appears at 6.12 ppm and aromatic protons are illustrated from 7.2 ppm to 7.6 ppm with concentrated peak at 7.38 ppm. Generation of the PANI through the microencapsulation method is demonstrated by the H- NMR peak.

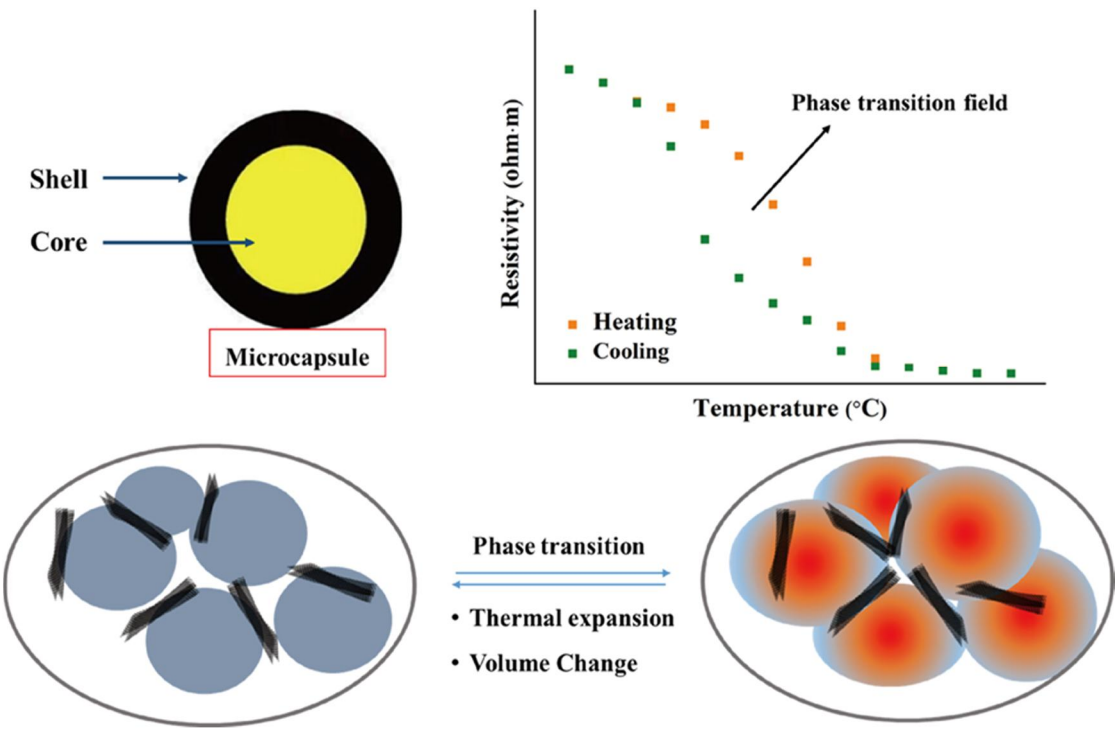

Figure 2.3.1. Schematic of core-shell microcapsule, volume change due to thermal expansion of the spherical PCM composite during phase transition, and electrical resistivity with respect to temperature.

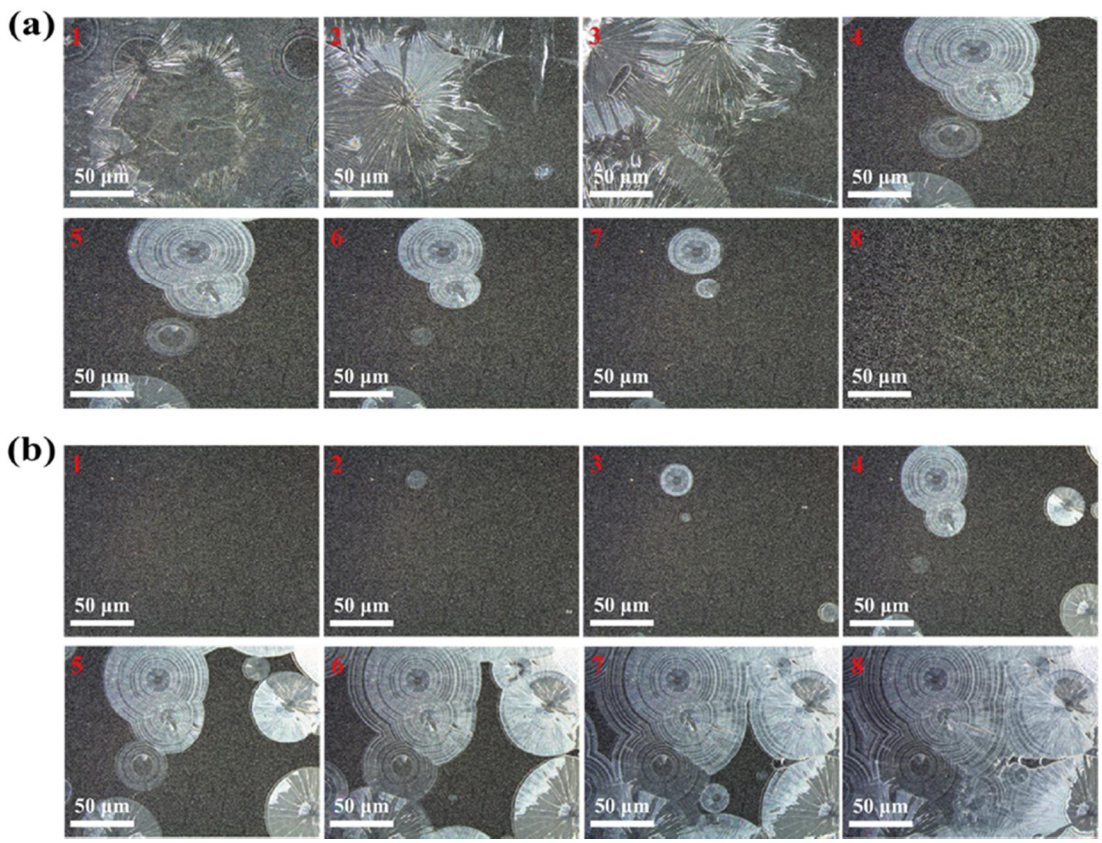

Figure 2.3.2. Structural change during (a) heating from 25 °C to 90 °C and (b) cooling from 90 °C to 25 °C.

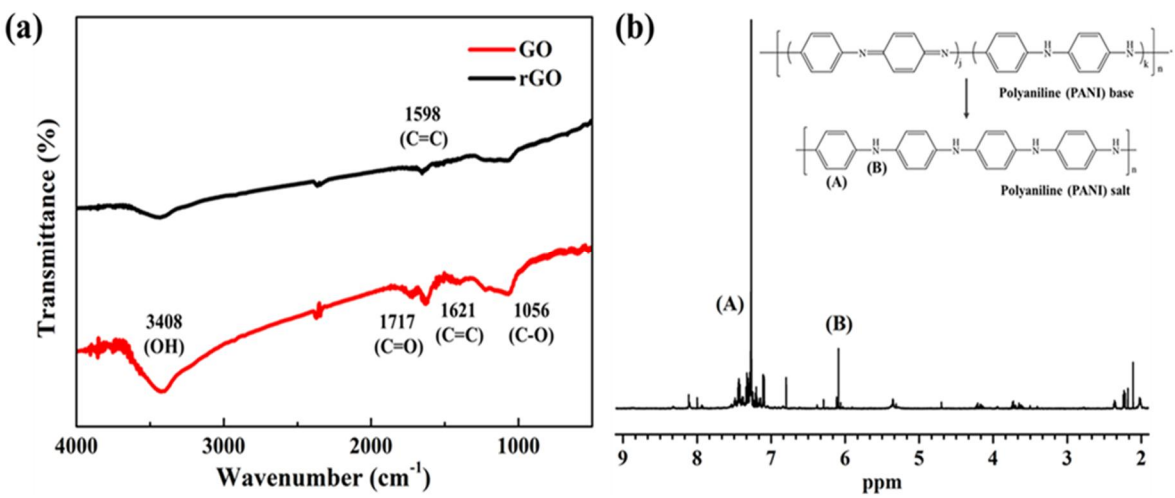

Figure 2.3.3. (a) FTIR patterns of graphene oxide (GO) and reduced graphene oxide (rGO), and the (b) H NMR peaks of polyaniline (PANI) chain.

2.3.5.2. Morphology of final PCM composite

The encapsulated PCM composite is placed on a hot plate to characterize the geometric stability as shown in **Fig. 2.3.4**. The pure PEG and PEG/PANI composites are placed on the hot plate to observe the leakage and the temperature is increased from 25 °C to 90 °C. The images of the composites are captured by using a digital camera and all samples sustain the solid state at the room temperature. When the temperature reaches 50 °C, the pure PEG begins to melt partially while the PEG/PANI and 5wt% PEG/PANI/rGO composites maintain the initial structure. The pure PEG is totally melted into the liquid state at the 90 °C and the PEG/PANI composites maintain the solid state without any weight loss or leakage. The images show that the PCM composites are able to prevent the leakage during the phase transition and even at over the melting temperature. Surface morphology of the pure PEG, and the graphene embedded PCM composite are examined by the SEM and TEM images as shown in **Fig. 2.3.5**. The pure PEG has the flat surface with some of wrinkles as shown in **Fig. 2.3.5a**, and the pure PEG is encapsulated by the PANI to produce a core shell like structure which is illustrated in **Fig. 2.3.5b**.

The PCM composite is composed of encapsulated spherical microcapsules and the pure PEG is wrapped by the spherical shell structure and the volume change occurs during phase transition. The graphene at the surface of PCM composite is observed clearly at the TEM image as shown in **Fig. 2.3.5c**. It is implied that the graphene powders are successfully attached to the surface of the encapsulated PCM which can be migrated with the volume change of these PCM microcapsules. The XRD peaks are obtained for the PCM composites as shown in **Fig. 2.3.6**. Diffraction peaks of the pure PEG are identified at $2\theta = 19.17°$ and $2\theta = 23.32°$ (Fig. 6a). The XRD results of the PANI indicate that the main structure appears around at $2\theta = 20°$ as shown in **Fig. 2.3.6b** and XRD peaks of the encapsulated PCM composites are shown in the **Fig. 2.3.6c**. Both of PEG/PANI and PEG/PANI/rGO samples exhibit nearly similar peaks to the pure PEG. The XRD peaks provide evidence that no chemical reaction occurs within the PEG, PANI, or graphene

powders. In order to estimate the size of microcapsules and graphene powders, the DLS results and average cell diameter of the microcapsules are shown in **Fig. 2.3.7**. Size of the graphene powder is distributed over the range of 750 ~ 950 nm and the average size is nearly close to 846.35 nm. The cell size distribution of the microcapsule is determined by the image processing as shown in **Fig. 2.3.7b** and its average diameter is about 1817.24 nm.

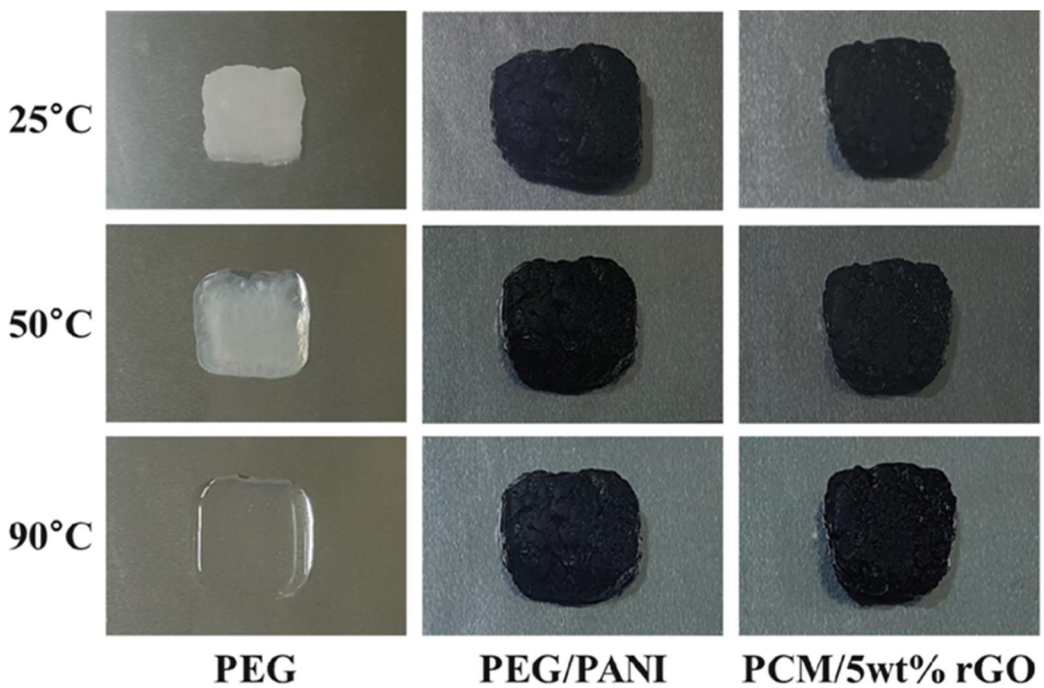

Figure 2.3.4. Form stable images of pure PEG, PEG/PANI, and 5wt% PEG/PANI/rGO composite with the temperature variation.

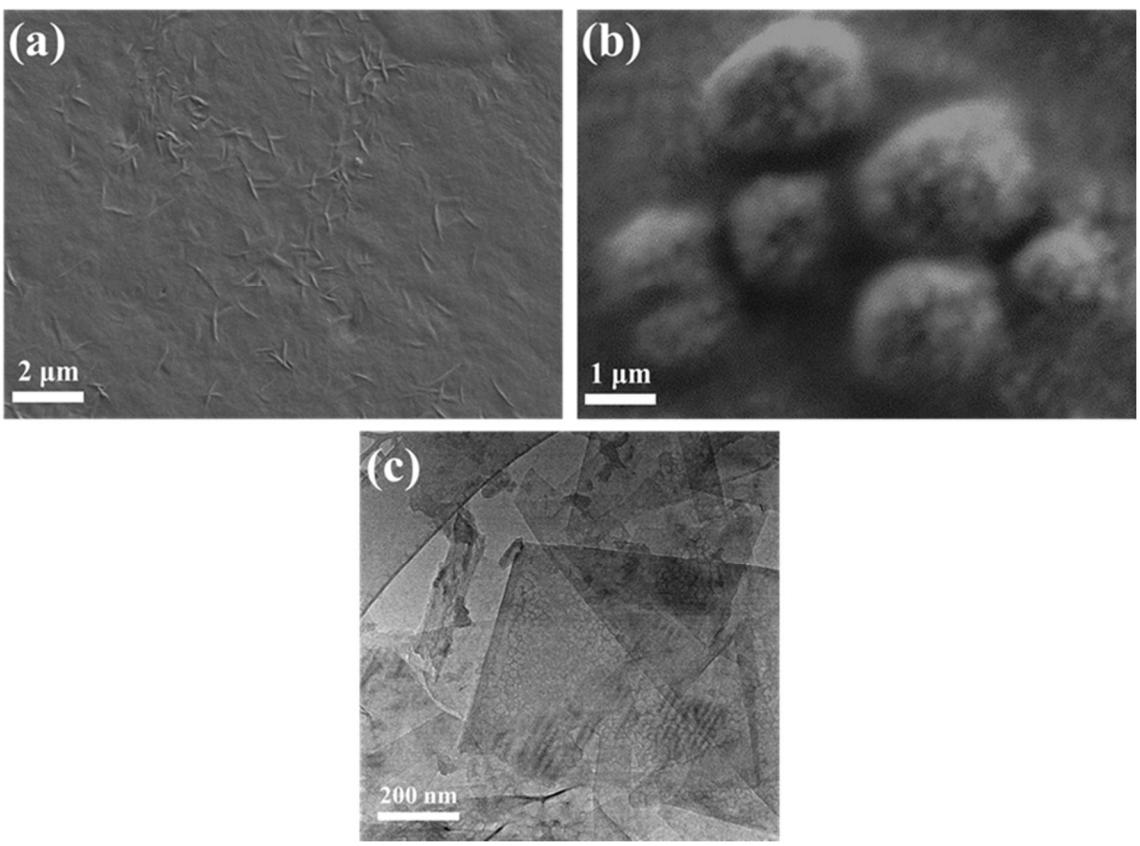

Figure 2.3.5. SEM images (a) pure PEG, (b) 5wt% PEG/PANI/rGO composite, and (c) TEM images of 5wt% PEG/PANI/rGO composite.

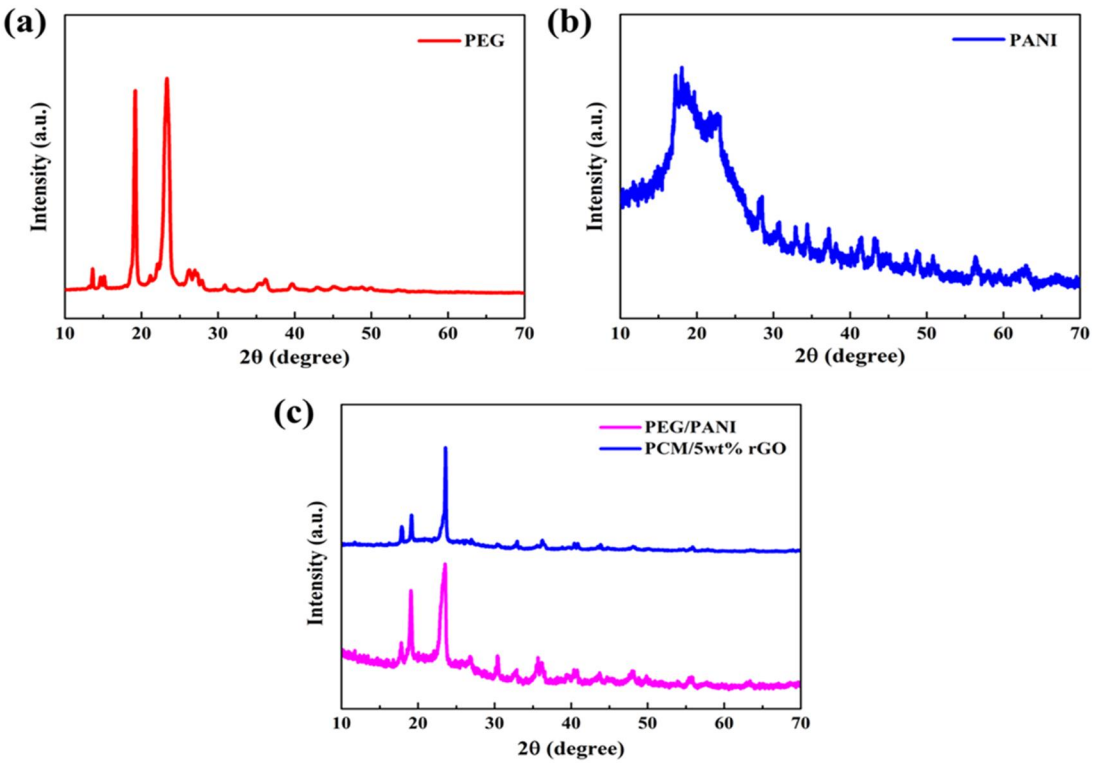

Figure 2.3.6. XRD peaks of (a) pure PEG, (b) PANI, and (c) 5wt% PEG/PANI/rGO composite.

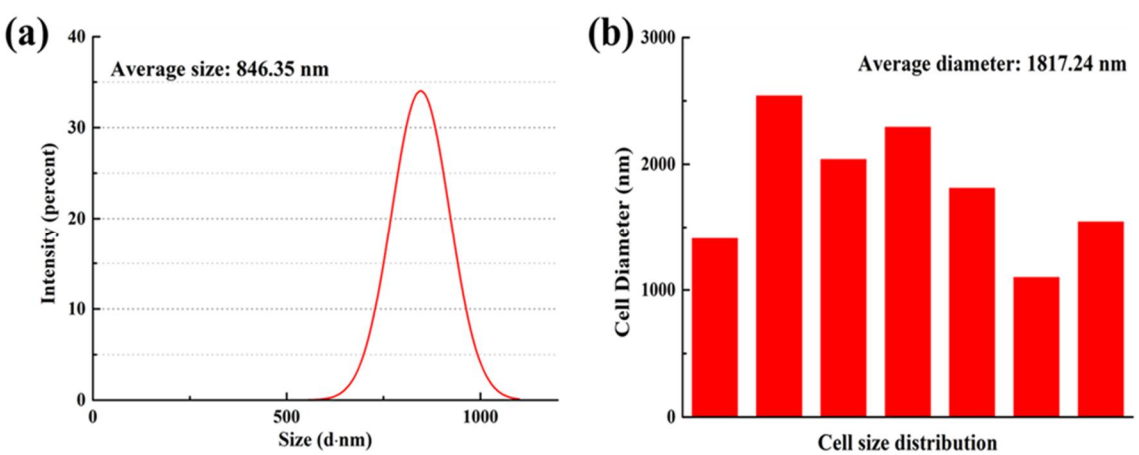

Figure 2.3.7. Results of (a) DLS measurement of the graphene powders and (b) cell size distribution of the microcapsules.

2.3.5.3. Thermal and electrical properties during phase transitions

The DSC result shows the phase transition temperatures and latent heat of PEG and PCM composites as shown in **Fig. 2.3.8**. Peaks for the melting and crystallization of the PCM are observed in the figure. Some of the typical parameters are listed in **Table 2.3.1** including onset/endset melting and crystallization, melting and crystallization peaks (T_{mp} and T_{cp}), and enthalpy of heating and cooling (ΔH_m and ΔH_c). Phase transition of the pure PEG occurs from 59.07 °C and 68.91 °C where the melting temperature is about 66.55 °C and the latent heat is calculated as 179.44 Jg^{-1}. During cooling, the crystallization temperature is 43.07 °C and the crystallization is completed around at 34.26 °C. The crystallization peak during cooling is 37.66 °C and the enthalpy of cooling is 153.75 Jg^{-1}. The PEG/PANI composite exhibits slightly shifted phase transition peaks in both heating and cooling cycles and lower latent heat than that of pure PEG due to the presence of PANI in the microcapsules. The melting and crystallization properties of 5wt% PEG/PANI/rGO composite clearly provide similar results to those of the PEG/PANI sample. Furthermore, the latent heat (ΔH) of the PCM composite is about 105.53 Jg^{-1}. In this case, PEG in the core can absorb or release high thermal energy with volume change during phase transition.

To determine optimum amount of the graphene powder, electrical properties of the PCM composites containing graphene powders from 1wt% to 10wt% are measured with respect to temperature variation as shown in **Fig. 2.3.9**. The electrical resistivity of all the samples decreased rapidly around at 50 to 70 °C upon heating, which is also observed over the solid-liquid phase transition in the working material. The PCM composite without graphene powders shows small variation due to the encapsulated micro-structure (**Fig. 2.3.9a**). Upon heating, the magnitude of the electrical resistivity for different weight fraction of the rGO is decreased by a factor of 444, 800, 1237, 959, and 922 for 1, 3, 5, 7, and 10wt% PEG/PANI/rGO composites respectively. Upon cooling, the magnitude of the electrical resistivity for each sample is increased by a factor of 601, 763, 1508, 983, and

996. The 5wt% graphene embedded PCM composite has better electrical reproducibility than any other samples and selected as an advanced electrical sensing material for thermal transformations.

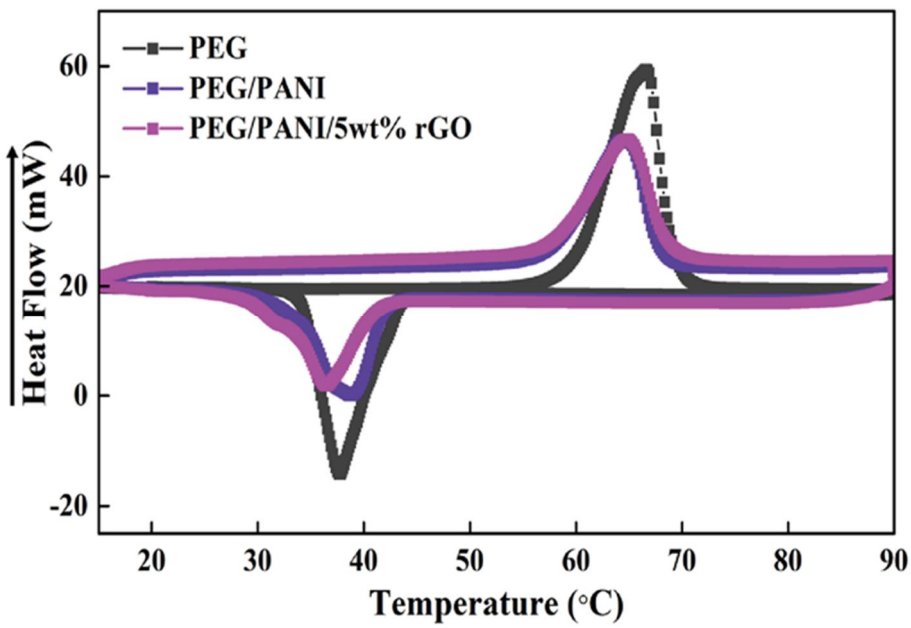

Figure 2.3.8. DSC peaks of pure PEG, PEG/PANI, and 5wt% PEG/PANI/rGO composite.

Table 2.3.1. DSC results of PEG, PEG/PANI, and 5wt% PEG/PANI/rGO composite.

Samples	T_{mo}(°C)	T_{me}(°C)	T_{mp}(°C)	ΔH_m(J/g)	T_{co}(°C)	T_{ce}(°C)	T_{cp}(°C)	ΔH_c(J/g)
PEG	59.07	66.55	68.91	179.44	43.07	34.26	37.66	153.75
PEG/PANI	58.46	68.32	64.77	118.01	41.38	33.94	38.78	109.77
PEG/PANI/rGO(5wt)	57.93	67.64	64.27	115.97	42.07	32.72	36.37	105.53

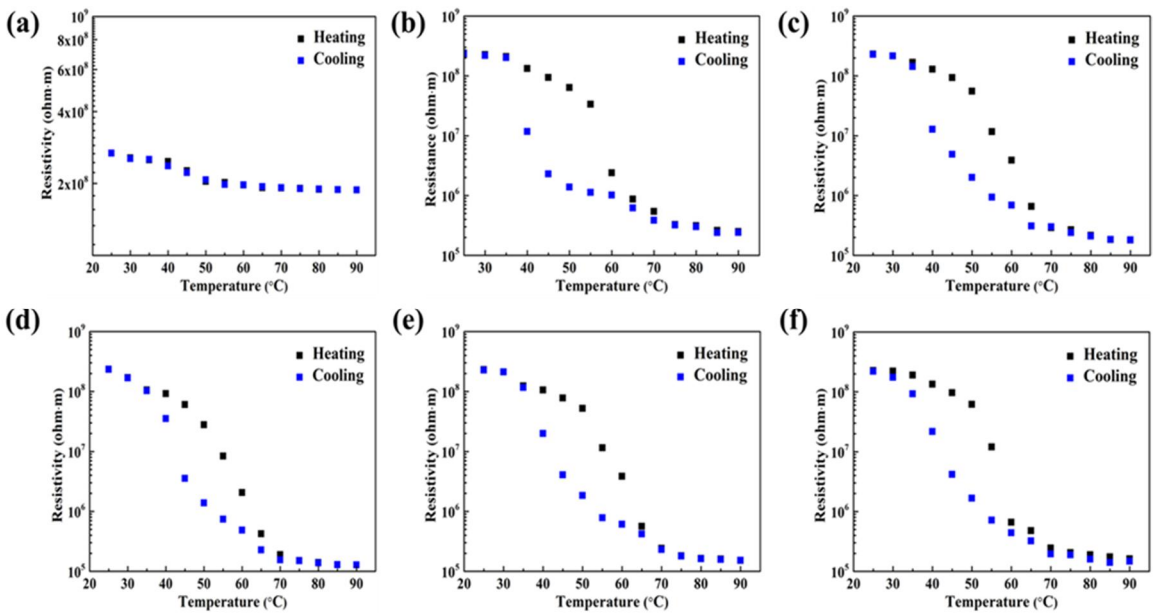

Figure 2.3.9. Electrical resistivity of the (a) PEG/PANI composite, (b) 1wt% PEG/PANI/rGO, (c) 3wt% PEG/PANI/rGO, (d) 5wt% PEG/PANI/rGO, (e) 7wt% PEG/PANI/rGO, and (f) 10wt% PEG/PANI/rGO composites.

2.3.5.4. Modeling of electrical properties

Numerical simulation is performed to predict the volume expansion ratio and electrical resistivity with respect to the temperature variation, and the numerical results of volume change and electrical resistivity are presented in **Fig. 2.3.10**. The microcapsule is initially subject to variation of the external temperature from 25 °C to 90 °C and the volume change is calculated during the heating process. It is clearly shown that the volume expansion ratio is increased dramatically when the temperature is varied from 50 °C and becomes 1.33 at 70 °C as shown in **Fig. 2.3.10a**. Deformation of the core shell structure is mainly caused by the volume expansion of the PCM in the core during the phase transition as indicated by the DSC measurement. When the composite is cooled from 90 °C to the room temperature as shown in **Fig. 2.3.10b**, the volume expansion ratio is decreased slowly until below 45 °C and the rate of shrinkage is distinct during the crystallization process. According to the volume expansion upon heating and cooling stages, the main factor influencing the electrical resistivity is phase transition of PEG in the microcapsule. Therefore, comparison of the simulation and experimental results is shown in **Fig. 2.3.10c**. The optimum amount of the graphene powder is 5wt% because 5wt% PEG/PANI/rGO composite exhibits good agreement between experimental and simulation results. It is proven by the numerical simulation that the electrical resistivity is decreased rapidly during phase transformation upon melting. It is expected that the flexible electrical properties are useful for the thermal sensing and photodetector applications.

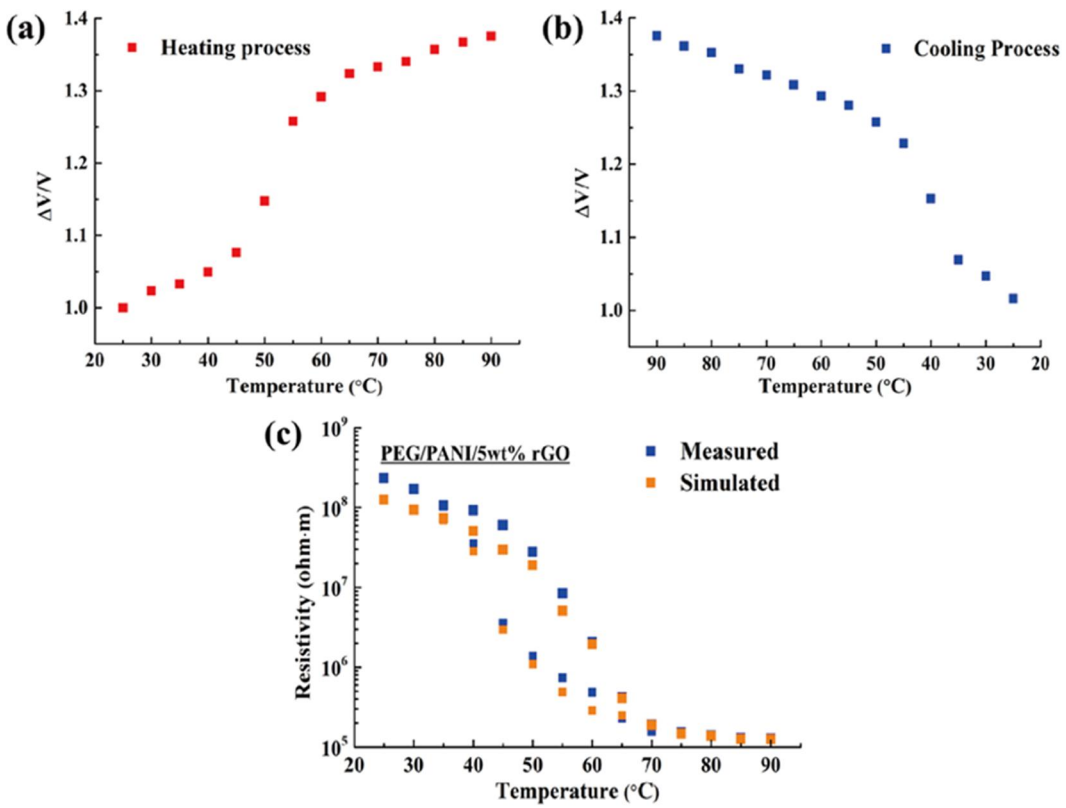

Figure 2.3.10. Volume expansion of the 5wt% PEG/PANI/rGO composite upon (a) heating and (b) cooling, and (c) predicted numerical simulation of the electrical resistivity with measured results.

2.3.6. Conclusions

An electrically flexible PCM composite is fabricated in this study and solid state of the PCM composite is sustained upon both heating and cooling. The graphene powders are well dispersed on the surface of PCM microcapsules and high electrical conductivity is obtained by promoting the electron movement. In addition, the synthesized polyaniline can maintain the solid state of PEG without any leakage and the PCM absorb and release the thermal energy efficiently without deformation of the microcapsules. The graphene embedded PCM composite shows the large change of electrical resistivity during phase transition and is form stable with volume expansion and shrinkage according to temperature variation. The 5wt% graphene incorporated PCM composite (5wt% PEG/PANI/rGO) demonstrates the best increase in the magnitude of electrical resistivity by 1237 and 1508 times upon heating/cooling cycles, respectively. The volume change ratio is modelled numerically by a finite element method. The numerical prediction of the volume expansion ratio is close to the experimental result during the phase transition. This study demonstrates that the electrical property of the PCM composite can be modified by absorbing or releasing thermal energy and the PCM composite can contribute to the thermal sensing applications such as heating circuit and photodetector chips.

2.4. Carbon nanotubes/PCM for microcapsules

2.4.1. Introduction

Nanocomposites with tunable electrical conductivity are widely used in various applications such as thermal switching, optical sensing, and electronic transformations [116-118]. Compared with inorganic and metal materials, organic materials have several advantages such as large surface area for electronics, physical reversibility, and low cost. In general, polymer nanocomposites are prepared by mixing a polymer matrix with plenty of nano-fillers to attain targeted material properties, e.g., electrical conductivity [119]. The electrical properties of the polymeric nanocomposites sharply decreases with respect to temperature especially across the melting temperatures of polymers [120]. When the polymer is fully melted, the electrical conductivity often dramatically changes. The main problem of this nanocomposite is the disorder of fillers in the matrix, which deteriorates the electrical conductivity during the phase transitions [121].

Phase change materials (PCMs) are generally selected as working materials due to their high heat of fusion under the phase transition, excellent thermal stability, and high thermal density [122, 123]. There are a lot of reports to investigate nanoparticles embedded PCM composites, which exhibit better electrical conductivities than pure PCMs. However, the leakage of PCMs is one of the most serious issues during the phase transition process, which leads to the limitation in their applications. For this reason, the supporting materials are required to retain the intrinsic shape over the melting point. In general, high density polyethylene (HDPE), melamine resin, and poly-methyl methacrylate (PMMA) are utilized as the supporting materials to keep the solid state during the melting period [124-126]. The materials encapsulate PCM to prevent the

leakage and to construct form stable PCM composite. Even though form stable phase change materials (FSPCMs) possess stable internal structures, the change of their volume hardly occurs during the whole melting and cooling processes due to the high rigidity of the shell materials. On the other hand, since polyaniline (PANI) is stable and flexible, it is considered as a proper supporting material [127].

Carbon nanoparticles, especially carbon nanotubes (CNTs) show great thermal and electrical conductivities [128]. Compared with graphene or carbon black, CNT has a large aspect ratio which allows electrons to easily transmit to other CNTs [129]. In recent years, many researches have been done to increase the electrical conductivity of CNT composites. The CNT embedded polymer composites manifest significant increase in the electrical properties even at a low CNT content. In this sense, CNT can act as an excellent filler in the PCM composites to tune the electrical conductivity of the composites according to the temperature variation.

In this study, polyethylene glycol (PEG) is utilized as a working material during the phase transition, and FSPCM composite is manufactured by encapsulating PANI. Multi-walled carbon nanotubes (MWCNTs) are dispersed between the PEG/PANI microcapsules. The electrical behavior of the CNTs embedded PEG/PANI composites are analyzed during heating and cooling cycles.

2.4.2. Preparation of PCM encapsulated composite

The aniline monomer is dispersed in the DI water, and the polyethylene glycol (PEG) is placed on a hot plate at 90 °C. The ammonium peroxydisulfate (APS) and the aniline emulsion are poured into the melted PEG stirring rigorously. After 6 hours, the PEG/PANI microcapsule is generated by evaporating the DI water. The MWCNTs are dispersed on the surface of the microcapsules at different mass fractions, and ultrasonication is applied for 30 min for dispersion. The final PEG/PANI/CNT composite is produced by evaporating the DI water and drying in a vacuum oven. The CNT embedded PCM composites with different weight fractions of CNT are labeled 1wt%, 3wt%, 5wt%, 7wt%, and 10wt% PEG/PANI/CNT.

2.4.3. Numerical analysis

The thermal expansion coefficient of the PCM composites is predicted by utilizing a finite element method (FEM) software, COMSOL Multiphysics. According to the internal structure of the microcapsule, the PEG and PANI are designated as a core material and a shell material, respectively. For the simulation, melting/cooling temperatures, latent heat (ΔH), young's modulus, and heat capacity are considered as input parameters. The spherical PCM composite is initially under 25 °C, and its temperature gradually increased to 90 °C in order to evaluate the volume expansion during the heating cycle. For the cooling cycle, the temperature decreased from 90 °C to 25 °C. The total number of finite elements in the numerical simulation is 17,384, and the number of boundary and edge elements are 17,384 and 8,304, respectively.

The governing equation for modeling the volume expansion of the unit cell is correlated with the structural mechanics as below:

$$\rho \frac{\partial^2 \mu}{\partial t^2} = \nabla \cdot S + Fv \tag{1}$$

where S is the Piola-Kirchhoff stress, which is expressed as $S = S_{ad} + C{:}\,\epsilon_{el}$. Here, ϵ_{el} is the linear elastic strain, which is given by

$$\epsilon_{el} = \epsilon - \epsilon_{inel} \tag{2}$$

$$\epsilon_{inel} = \epsilon_0 + \epsilon_{th} \tag{3}$$

The volume change from the phase transition causes the shape deformation and generate the internal stress due to thermal expansion. The relation between the thermal strain and temperature is described as below:

$$\epsilon_{th} = dL\,(T, T_{ref}) \tag{4}$$

where dL is the thermal strain, which is proportional to temperature and generally calculated by Young's modulus of the PCM composite. To evaluate the thermal strain during the heating and crystalline cycles, the solid-solid heat transfer equation is employed. The heat flow is directly related to the phase transition. The governing equation of heat transfer is

$$\rho C_p \frac{\partial T}{\partial t} + \rho C_p u \cdot \nabla T + \nabla \cdot \boldsymbol{q} = Q \quad (5)$$

where ρ is the density of the PCMs, and C_p is the heat capacity. The $\boldsymbol{q}$ represents the heat transfer rate expressed as $\boldsymbol{q} = -k\nabla T$. The heat capacity varies from the state of phase changes during heating and cooling as below:

$$C_p = \frac{1}{\rho}\left(\theta \rho_{phase1} C_{p\cdot phase1} + (1-\theta)\rho_{phase2} C_{p\cdot phase2}\right) + L\frac{\partial \alpha_m}{\partial T} \quad (6)$$

where α_m is the mass coefficient, and θ is the fill factor of phase 1 to phase 2. The heat flux under the natural convection is a function of heat transfer coefficient h and the temperature difference as below:

$$\boldsymbol{q_0} = h \cdot (T_{ext} - T) \quad (7)$$

The volume expansion ratio, ΔV/V can be calculated from the thermal strain during the phase transition process. The volumetric expansion ratio is related to the temperature difference as follows:

$$\frac{\Delta V}{V} = exp\left[\alpha_v\left(T_f - T_i\right)\right] - 1 \quad (8)$$

For the fillers embedded composite, the electrical resistivity is typically described as below

$$\rho' = \rho_0[(p_V - p_C)/(1-p_C)]^{-t} \quad (9)$$

The electrical resistivity of the composite ρ' is determined with the filler resistivity ρ_0, the filler volume fraction p_V, the percolation threshold p_C, and the critical exponent t. The filler volume fraction and the mass fraction p_m are related as

$$p_v = \frac{\rho_r}{\rho_f\left(\frac{1}{p_m} - 1\right) + \rho_r} \quad (10)$$

Here, the resin density ρ_r, the filler density ρ_f, and the filler mass fraction p_m changes according to the filler volume fraction in the PCM composite. The percolation threshold indicates the minimal filler content of the PCM composite to construct the

direct filler contact. The electrical resistivity is even correlated to thermal expansion coefficient as the following equation:

$$\rho(\mathrm{T}) = \rho'[1 + \alpha_V(T - T_0)] \quad (11)$$

2.4.4. Results and discussion

2.4.4.1. Morphologies of CNT embedded PCM composite

The internal structure of phase change material (PCM) is transmitted from solid to liquid state on the melting process as shown in **Fig. 2.4.1**. It is indicated the volume change of pure PCM during phase transition is accompanied by the leakage problem. To fabricate the form stable PCM without any leakage over the melting temperature, the supporting material is utilized as a shell structure to encapsulate the pure PCM. Hence, the encapsulated PCM exhibits spherical shape and sustain the intrinsic solid state during melting and cooling. While remains the heating cycle, the volume expansion is emerged due to the solid-liquid transition in the core working material. Thus, the PCM microcapsules could change their initial volume state on the temperature variation and use for the thermal sensing applications. Compared with graphene and other carbon fillers, the carbon nanotube (CNT) is well dispersed into the surface of microcapsules and significantly increased the electrical conductivities with high aspect ratio.

The CNT embedded spherical structures of PCM composite displays a higher electrical conductivity than graphene/PCM composite at the same filler contents. In other words, the CNT is selected as an advanced filler in the encapsulated PCMs to increase the electrical properties. To characterize the form stability at the different temperature, the pure PCM, PEG/PANI, and CNT embedded PEG/PANI composite are placed on the hot plate and captured by utilizing a digital camera as presented in **Fig. 2.4.2**. The pure PEG becomes partially melted when the temperature increases from 25 °C to 50 °C while the PEG/PANI and 5wt% PEG/PANI/CNT composites maintain the solid state. The temperature is reached to the 90 °C, the pure PEG is totally melted into the liquid state

and the PEG/PANI encapsulated PCM composites sustain the initial solid state without any leakage. The camera images indicate that the PANI wrapped PCM composites are able to prevent the leakage during the solid-liquid phase transition and even over the melting temperature. The SEM images are examined the surface morphology of the pure PEG, and the CNT embedded PCM as shown in **Fig. 2.4.3a**, and **2.4.3b**. In spite of some wrinkles on the surface of pure PEG, the sample has the flat surface in **Fig. 2.4.3a**. The PANI encapsulated PEG/PANI composite generates different structure from the pure PEG and a spherical encapsulated structure is emerged in **Fig. 2.4.3b**.

The SEM images indicate the pure PCM is encapsulated successfully by the PANI supporting material to produce spherical microcapsules and the PEG/PANI structures are occurring volume change during melting and cooling process. In order to obtain the CNT nano-rod on the surface of microcapsules, the TEM image is utilized to confirm the CNT structure as shown in **Fig. 2.4.3c**. It is implied that the CNT nano-rods are well dispersed and modified the arrangement with the volume change of these PCM microcapsules during the phase transitions. To evaluate the average size of CNT powder, the DLS result is presented in **Fig. 2.4.4a**. It is indicated that the CNT nano-particles are mainly close to the 198.17 nm and relatively more homogeneous than that of graphene powders. The calculated cell size distribution by image processing is given as **Fig. 2.4.4b**, and the average cell size of spherical structure is about 1992.22 nm. The XRD peak measurement can obtain the intrinsic structures in the PEG, and PANI as shown in **Fig. 2.4.4c**, and **2.4.4d**. The main structure of PANI is obtained at $2\theta = 19.9$ ° and the pure PEG typical peaks are appeared at $2\theta = 19.18$ ° and $2\theta = 23.33$ °. The PANI encapsulated PEG/PANI composite shows similar result with the pure PEG and it demonstrates the PEG maintains the pristine structure in the PANI wrapped microcapsules. After dispersing CNT into the PEG/PANI composite, the final PEG/PANI/CNT composite exhibits the main structures and thus the XRD peaks demonstrate that no chemical reaction occurs within the PEG, PANI, and CNT nano-rods.

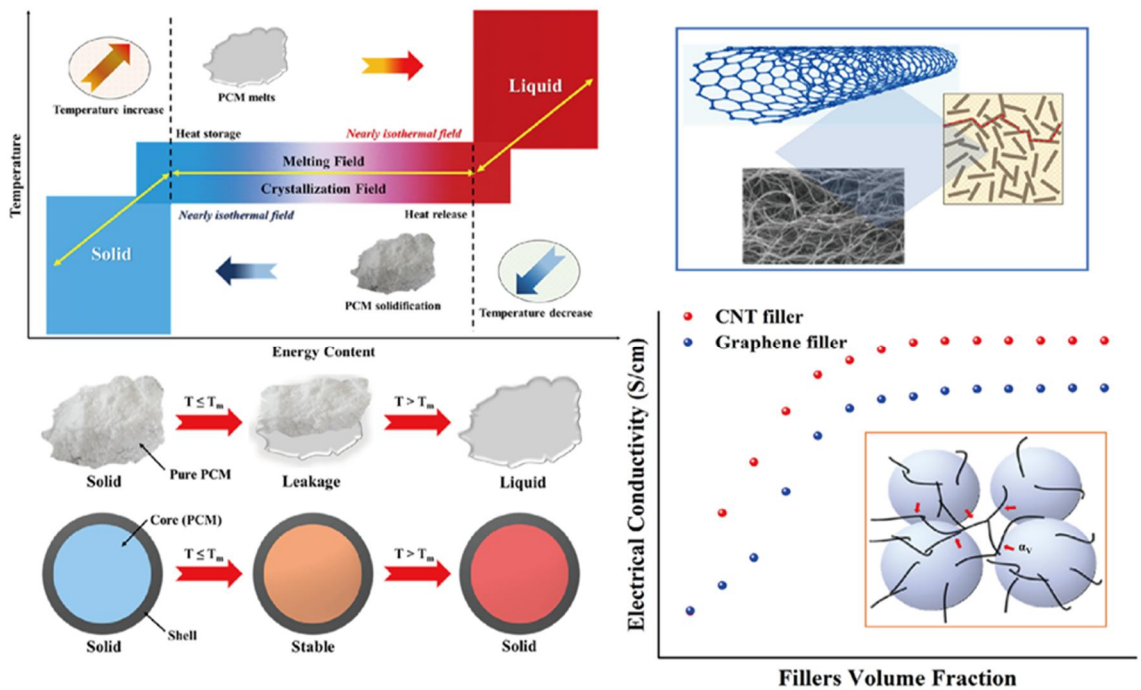

Figure 2.4.1. Schematic of phase transition diagram, form stable spherical microcapsule, volume change due to thermal expansion of the PCMs during phase transition, and electrical resistivity with CNT filler fractions.

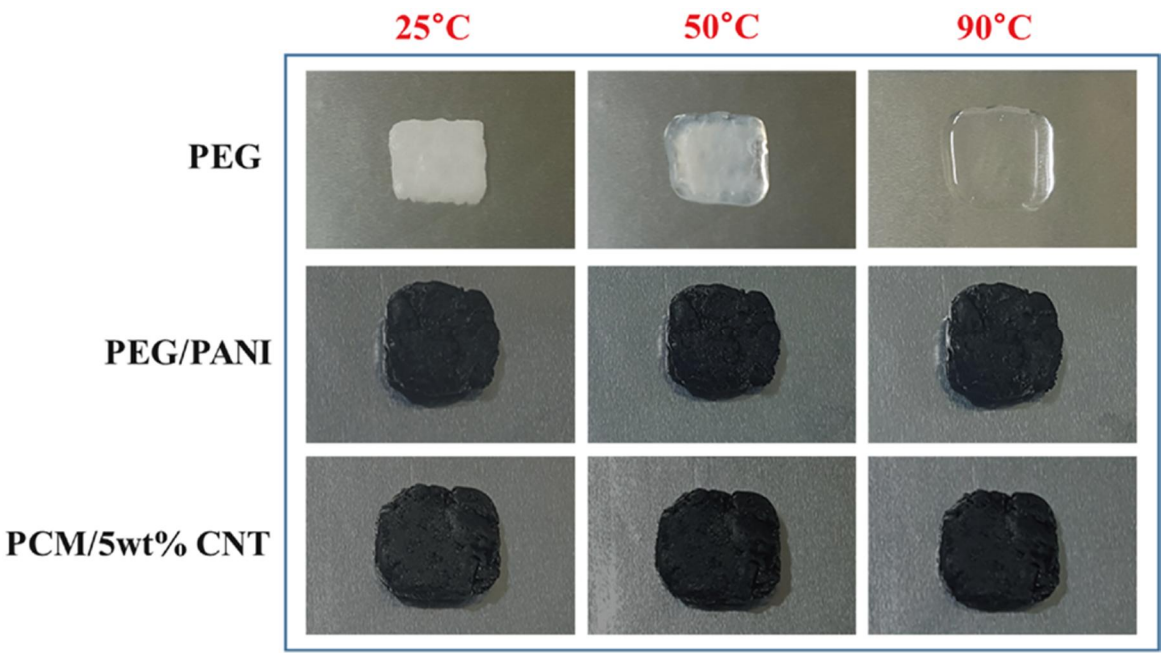

Figure 2.4.2. Form stable camera images of pure PEG, PEG/PANI, and 5wt% PEG/PANI/CNT composite with the different temperature.

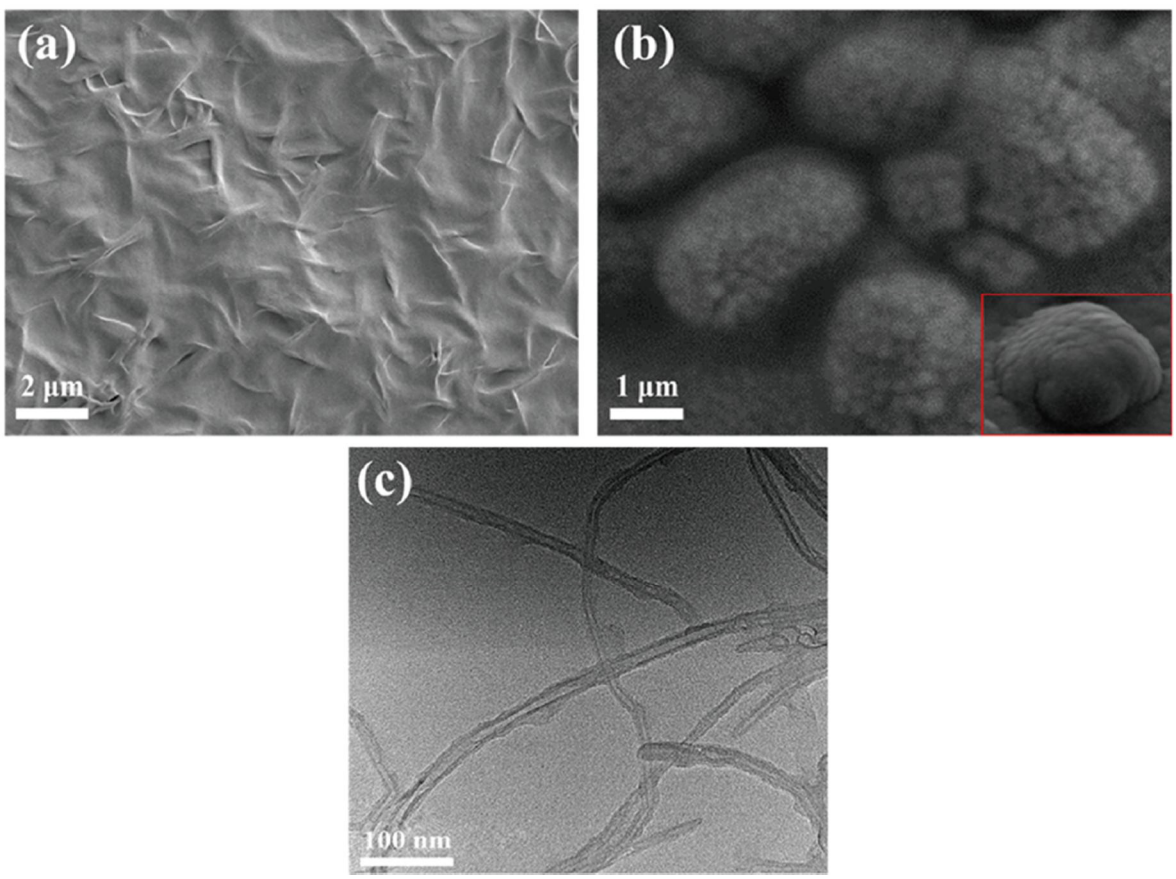

Figure 2.4.3. SEM images of (a) pure PEG, (b) 5wt% PEG/PANI/CNT composite, and (c) TEM image of 5wt% PEG/PANI/CNT composite.

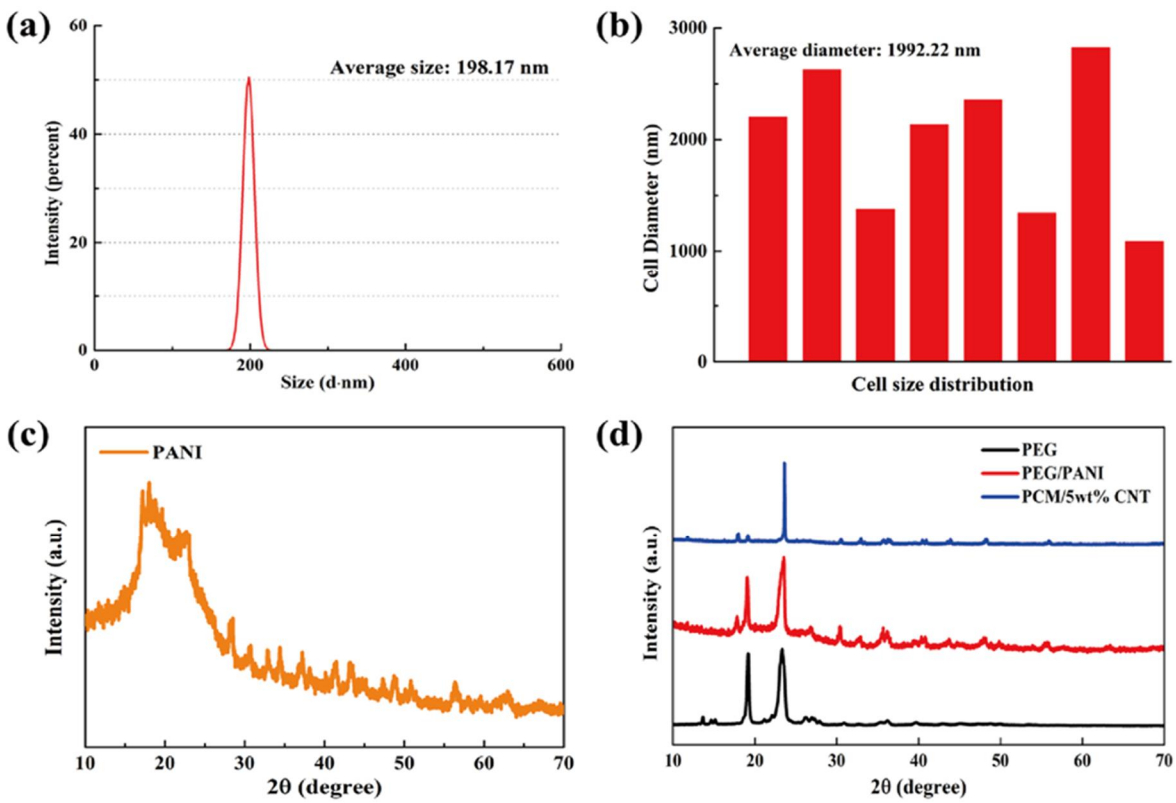

Figure 2.4.4. (a) DLS measurement of the CNT nano-rod, (b) cell size distribution of the spherical microcapsules, (c) XRD peaks of PANI, and (d) XRD peaks of pure PEG, PEG/PANI, and 5wt% PEG/PANI/CNT composite.

2.4.4.2. DSC results and electrical properties in the PCM composites

The thermal morphologies of PEG, and PANI encapsulated PEG/PANI composites are obtained by the DSC measurement and the results are presented in **Fig. 2.4.5**. The melting and cooling peaks of PEG/PANI composites with different CNT mass ratios are totally illustrated in the DSC figures and **Table 2.4.1** shows some of the typical parameters during heating and cooling cycle. The spherical structure of PEG/PANI composite exhibits similar onset/offset temperature with a slightly shifted peak in both melting and crystallization process. The enthalpy of PEG/PANI turns partially decreased due to the replacement of supporting material in the microcapsules. However, the spherical form stable PCM still exhibits the high latent heat (ΔH) over 100J/g in both heating and cooling cycles. When the CNT nano-rod is totally dispersed into the PEG/PANI composite, the DSC peaks are nearly similar and just slightly shifted as increase the CNT contents in the final PEG/PANI/CNT composite. The latent heat (ΔH) under the CNT embedded PCM composites are close to the PEG/PANI sample and all of the PEG/PANI/CNT composites could store or release high thermal energy with volume expansion during the phase transition process.

To find out the optimum amount of the CNT nano-rod, electrical resistivity of the PEG/PANI composites containing CNTs from 1wt% to 10wt% are measured with the change of temperature from 25 °C to 90 °C as shown in **Fig. 2.4.6**. The electrical resistivity of all the samples are slightly changed within 50 °C and decreased dramatically at about 50 to 70 °C under the melting cycle (**Fig. 2.4.6a**), which demonstrates the solid-liquid phase transitions and even coincided with the DSC results. The PANI encapsulated PCM without any fillers merely decreased slightly during heating and cooling process.

The magnitude of the electrical resistivity for different CNT mass ratios is decreased rapidly by a factor of 717, 835, 1249, 773, and 704 for 1, 3, 5, 7, and 10wt% PEG/PANI/CNT composites respectively. After removing the heat source, the electrical resistivity of each sample is reversely increased by a factor of 711, 824, 1230, 866, and 781 time. According to the Fig. 6a, the 5wt% CNT embedded PCM composite exhibits the best electrical reproducibility than other samples and even revealed a larger magnitude factor than that of 5wt% graphene embedded PEG/PANI composite as shown in **Fig. 2.4.6b**. Therefore, the 5wt% CNT embedded PCM composite is selected as a brand new thermal sensing material during the phase transition process.

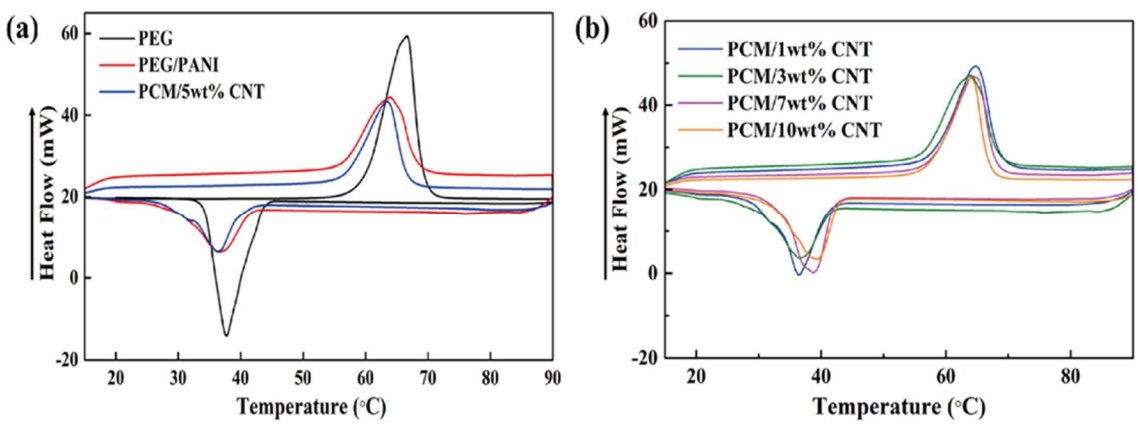

Figure 2.4.5. DSC peaks of (a) pure PEG, PEG/PANI, and 5wt% PEG/PANI/CNT composite; and (b) PEG/PANI composite with 1wt%, 3wt%, 7wt%, and 10wt% CNT weight fractions.

Table 2.4.1. DSC results of PEG, PEG/PANI, and CNT embedded PEG/PANI composites.

Samples	T_o(°C)		T_e(°C)		T_p(°C)		ΔH(J/g)	
	Heating cycle	Cooling cycle	Heating cycle	Cooling cycle	Heating cycle	Cooling cycle	Heating cycle	Cooling cycle
PEG	60.16	43.11	69.34	32.71	67.04	38.85	181.46	161.38
PEG/PANI	56.89	41.57	67.91	31.09	63.84	36.38	114.66	109.65
PEG/PANI/1wt% CNT	56.74	41.61	67.41	31.17	63.72	36.40	113.53	108.87
PEG/PANI/3wt% CNT	56.39	41.72	66.74	31.26	63.45	36.47	111.46	106.73
PEG/PANI/5wt% CNT	56.34	41.86	66.54	31.44	63.38	36.58	110.96	105.89
PEG/PANI/7wt% CNT	56.12	42.01	66.41	31.65	63.36	38.19	108.01	104.25
PEG/PANI/10wt% CNT	56.09	42.13	66.38	31.67	63.14	38.98	105.79	102.64

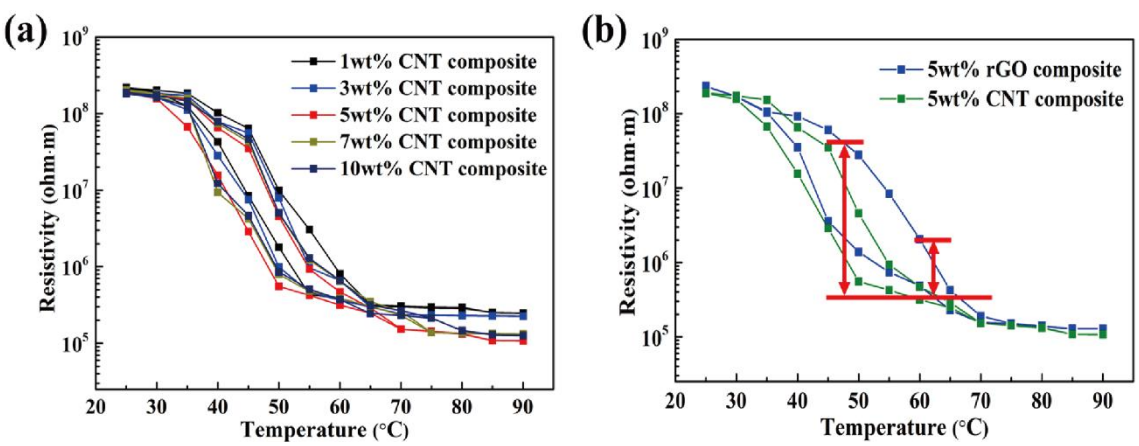

Figure 2.4.6. Electrical resistivity of the (a) PEG/PANI/CNT composites, and (b) comparing with the 5wt% graphene embedded PEG/PANI composite.

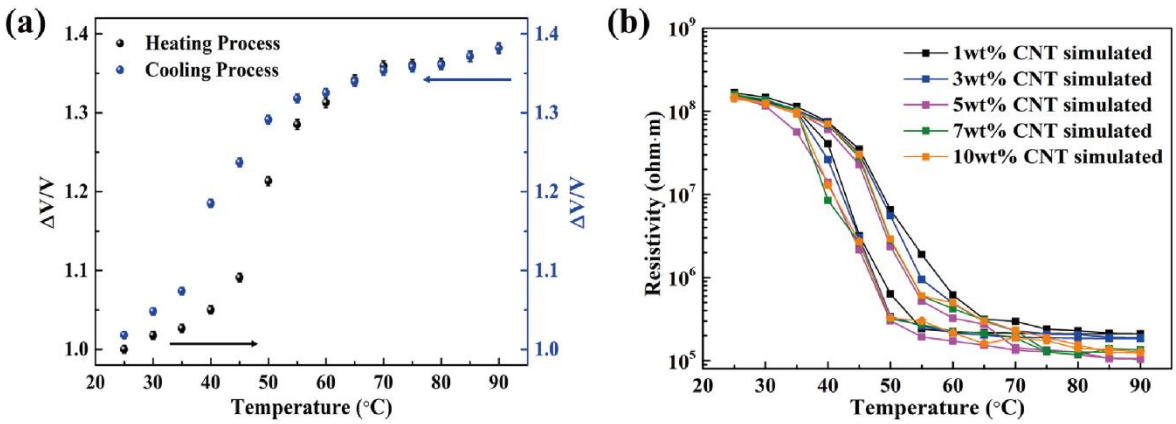

Figure 2.4.7. The results of (a) PEG/PANI volume expansion ratios during heating and cooling process, and (b) numerical simulation of electrical resistivity with different CNT weight fractions.

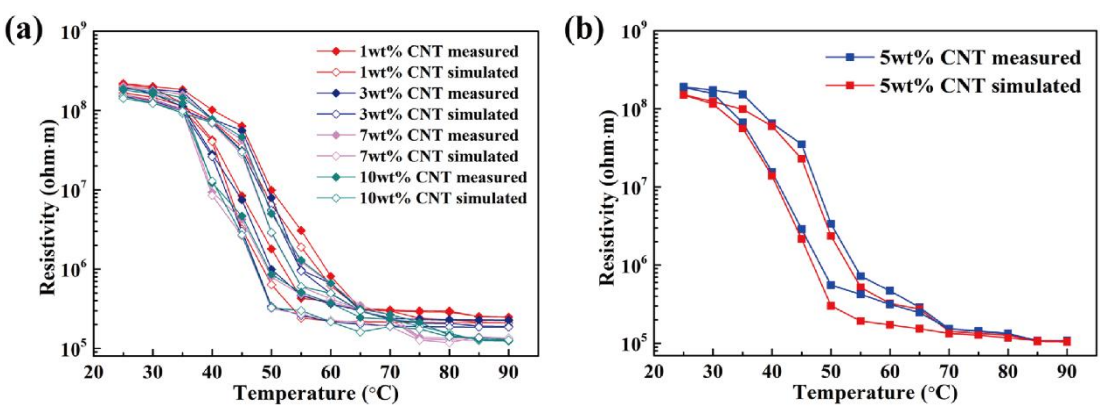

Figure 2.4.8. Compared with the experimental results of (a) 1wt%, 3wt%, 7wt%, and

10wt% CNT embedded PEG/PANI composites; and (b) 5wt% CNT embedded PEG/PANI composite.

2.4.5. Conclusions

An electrically sensible form stable PCM composite is manufactured in this study and keeps the intrinsic shape without any leakage on the heating and cooling process. The polyaniline (PANI) is performed as an excellent supporting material to wrap the pure PEG and CNT nano-rods are dispersed sufficiently on the surface of PCM microcapsules and contribute to the electrical conductivity in the PCM composite. The spherical PCM microcapsules can absorb and release high thermal energy with volume change of the microcapsules. The CNT embedded PCM composite exhibits the large variation of electrical resistivity during phase transitions. The 5wt% CNT weight fraction PEG/PANI composite is illustrated the best modification in the magnitude of electrical resistivity by 1249 and 1230 times under melting and cooling cycles, respectively. The volume expansion ratio is well calculated by a finite element method (FEM) and the numerical prediction is corresponding to the experimental result under the temperature variation. This study further indicates that the CNT embedded PCM composite has better electrical properties than that of some other carbon fillers and the form stable microcapsules are able to absorb or release thermal energy which contributes to the flexible electrical

modification and utilized for thermal probes or light controller applications.

2.5. Summary

In this chapter, the microencapsulated form stable phase change materials (PCMs) are manufactured and sustain their initial solid state during the phase transition process. The polyaniline (PANI) is selected as a shell material to encapsulate the pure PCMs and prevent the leakage problem upon melting. The PCM microcapsules exhibit a shape stabilized with volume expansion due to the melting of internal structures. The thermal expansion lead to the volume change can affect the electrical resistivity at the temperature variation and the graphene powder embedded PCM composites shows a tunable thermal flexibility and rapidly change their electrical conductivity under the phase transition process. In addition, the carbon nanotube (CNT) is utilized as a great filler to increase the electrical conductivity and the microcapsules can control the filler arrangement in both heating and cooling process. The microencapsulation system is considered as a thermal sensor, and photodetector in the practical applications.

Chapter III.

PCMs for energy harvesting

3.1. Overview

In this chapter, the two different phase change materials (PCMs) are utilized as a thermal energy storage matrix. The PN TEG is adopted in this energy harvesting system and generate the thermoelectric energy harvesting on the melting and cooling process.

In Section 3.2, the main contents of PCMs are described and has a brief introduction in Section 3.2.1. The theoretical background is then proved in the later Section 3.2.2, generally explained the research background of energy harvesting system. The combination of PCMs show the importance of utilizing two different PCMs and the further application in Section 3.2.3, and the final Section 3.2.4 Section would make a conclusion of PCMs for thermoelectric energy harvesting.

The single PN TEG for energy harvesting system is described in Section 3.3. The main goal of work is introduced in the Section 3.3.1, and the device combination with PCM composites are given in the Section 3.3.2. The numerical simulation is using a finite element method (FEM) from COMSOL Multiphysics program. The model is selected via heat transfer in solid at the time dependent as shown in Section 3.3.3. The supporting material is graphene aerogel and infiltrated the melted PCMs to fabricate the form stable PCM composites in Section 3.3.4. The results and discussion is illustrated in the Section 3.3.5. The conclusion is well obtained the induced current on the melting and cooling process as described in Section 3.3.6.

Consider the excessive thermal energy when the temperature difference is reversed such that the multiple energy harvesting system is utilized and shown in Section 3.4. The opposite placement of two PCMs are normally generated the electrical current in the circuit via phase transition process. In Section 3.4.1 has an introduction of the research background, and energy harvesting system is directly described in Section 3.4.2. The numerical simulation is completed and shown in Section 3.4.3. The preparation of PCM composites are fully illustrated and the method of this work has represented in Section 3.4.4. Both melting and cooling process are able to obtain the harvested current due to the temperature difference. The results and discussion is illustrated in Section 3.4.5, and conclusion is well completed in Section 3.4.6.

The thermal conductivity is directly affecting the external thermal transmission and increased the rate of the phase transition process as given in Section 3.5. The GNP filler is acted as a thermal transformer in the PCM composites and increased more weight fraction of GNP could achieve a new preparation of PCMs energy harvesting. The concept is shown in Section 3.5.1, and the design of energy harvesting system is described in Section 3.5.2. The numerical simulation is briefly illustrated in Section 3.5.3. The Preparation of PCM composites are described in Section3.5.4, and Section 3.5.5 shows the final results and discussion.

Based on the GNP embedded PCM composites which have increased the thermal conductivity to increase the thermoelectric energy conversion efficiency. In Section 3.6 the optimization components of PCM composites are carried out and the maximum output current is obtained under the melting and cooling process. The introduction is

represented in Section 3.6.1, and the optimization system of thermoelectric energy harvesting is well suggested in Section 3.6.2. The numerical analysis in Section 3.6.3 is approached and the preparation of PCM composites is mentioned in Section 3.6.4. The results and discussion could specially represented the optimum components as shown in 3.6.5, and concluded this study in Section 3.6.6.

Finally, the PCMs researches from single PN TEG combination to the optimization components are briefly described in Section 3.7. The strategy of each advantage or novelty in this Section is summarized sufficiently and the optimization of PCM components is the most appropriate combination in the current research and further applied to the modified supporting materials and increased the thermoelectric energy harvesting efficiency.

3.2. Review of PCMs

3.2.1. Introduction

Latent heat thermal energy storage (LHTES) is one of the most efficient ways of applying the sunlight or heat energy [130]. Unlike the sensible heat storage method, the latent heat thermal energy storage (LHTES) provides much higher storage density, with a smaller temperature difference between storing and releasing heat. This paper reviews previous work on latent heat thermal energy storage (LHTES) and provides an insight to recent efforts to develop new types of phase change materials (PCMs) for utilizing in thermal energy storage [3, 131]. Three aspects have been the focus of this researches like PCMs, form stable PCM composites, and applications. There are large numbers of phase change materials that melt and solidify at a wide range of temperatures, making them attractive in a number of applications. PEG and 1-TD are cheap and have moderate thermal energy storage density but low thermal conductivity and, hence, require large surface area. Hydrated salts have larger energy storage density and higher thermal

conductivity but experience super-cooling and phase segregation, and their application require the use of some nucleating and thickening agents. The main advantages of PCM composites are providing large heat transfer area, reduction of the PCMs reactivity towards the outside environment and controlling the changes in volume of the storage materials as phase change occurs. The different applications in which the phase change method of heat storage can be applied are also reviewed in this chapter. The problems associated with the application of PCMs with regards to the material and the methods used to contain them are also discussed.

Energy storage plays important roles in conserving available energy and improving its utilization, since many energy sources are intermittent in nature. Short term storage of only a few hours is essential in most applications, however, long term storage of a few months may be required in some applications. Solar energy is available only during the day, and hence, its application requires an efficient thermal energy storage so that the excess heat collected during sunshine hours may be stored for later use during the night. Similar problems arise in heat recovery systems where the waste heat availability and utilization periods are different, requiring some thermal energy storage. Also, electrical energy consumption varies significantly during the day and night, especially in extremely cold and hot climate countries where the major part of the variation is due to domestic space heating and air conditioning. Such variation leads to an off peak period, usually after midnight until early morning. Accordingly, power stations have to be designed for capacities sufficient to meet the peak load. Otherwise, very efficient power distribution would be required. Better power generation management can be achieved if some of the peak load could be shifted to the off peak load period, which can be achieved by thermal storage of heat or coolness. Hence, the successful application of load shifting and solar energy depends to a large extent on the method of energy storage used.

The most commonly used method of thermal energy storage in all the above mentioned applications is the sensible heat method. In solar heating systems, water is till used for heat storage in liquid based systems, while a rock bed is used for air based systems. The design of sensible heat storage units is well described in textbooks. In the application of load leveling, heat is usually stored in a refractory bricks storage heater, known as a night storage heater. These units are capable of providing space heating during the day from the

stored heat during the night, however, they are heavy and bulky in size. The latent heat method of storage has attracted a large number of applications, as will be discussed in this chapter. This method of heat energy storage provides much higher energy storage density with a smaller temperature swing when compared with the sensible heat storage method. However, practical difficulties usually arise in applying the latent heat method due to the low thermal conductivity, density change, and physical stability of properties under extended cycling and sometimes phase segregation and subcooling of the phase change materials. The latent heat refers to the latent heat of melting, as other phase changes, such as evaporation, are not practical due to the large volume change associated with it. The form stable PCMs are effectively utilized in various thermal energy storage applications.

3.2.2. Theoretical background

The request for new technologies to avert the growing concern about environmental problems, the hot issue of energy shortage and the high cost of energy and new power plants has been a scientific concern over the last three decades. Central to the problem is the need to store excess energy that would otherwise be wasted and also to bridge the gap between energy generation and consumption. Latent heat thermal energy storage (LHTES) is particularly attractive technique because it provides a high energy storage density. When compared to a conventional sensible heat energy storage systems, latent heat thermal energy storage (LHTES) system requires a smaller weight and volume of material for a given amount of energy. In addition, latent heat thermal energy storage (LHTES) has a high capacity to store the heat of fusion at a constant or nearly isothermal temperature which corresponds to the phase transition temperature of the phase change material (PCM). The study of phase change materials is pioneered by Telkes and Raymond in the 1940s but did not receive much attention until the energy crisis of late 1970s and early 1980s where it is extensively researched for use in different applications especially for solar heating systems. Less attention is further given to phase change material (PCM) energy storage research after the energy crisis until it emerged again recently. Since the late 1970s a number of studies have been conducted to assess the overall thermal behaviors of latent heat thermal storage systems (LHTES). Studies of phase change systems have investigated design fundamentals, system and process optimization, transient behavior, and field performance. The research and development has been broad based and productive, concentrating on both the resolution of specific phase change materials and problems and the study of the characteristics of new materials. The major disadvantage, as reported by many researchers has been the low thermal conductivities possessed by many PCMs, leading to low charging and discharging rates (especially for the organic based materials). The development of a latent heat thermal energy storage (LHTES) system therefore involves the understanding of heat transfers/exchanges in the PCMs when they undergo solid-to-liquid phase transition in the required operating temperature range, the design of the container for holding the PCM

and formulation of the phase change problem. This paper reviews the studies conducted on phase change materials for different applications and reported in the open literature.

Energy storage may be in the form of sensible heat in a liquid or solid state, as the heat of fusion (latent heat), or chemical energy or thermal energy products in a reversible chemical reaction. The classification of energy storage and the materials used are detailed in chemical energy storage has not as yet been used in practical applications and both technical and economical questions have not been answered for some of the possibilities. To summarize the most of the studies conducted on storage materials have concentrated on sensible and latent heat thermal energy storage (LHTES) systems. Kinds of researches conducted to indicate the phase change and sensible heat storages have shown that a significant reduction in storage volume can be achieved using PCM compared to sensible heat storage. The selection of an appropriate PCM for any application requires the PCM to have melting temperature within the practical range of application. Several applications have been proposed for PCMs studied. It can be seen that most of the research on phase change problems have been carried out within the temperature range 0-65 °C suitable for domestic heating and cooling.

Once the PCM has been selected mainly on the temperature range of application, the most important problem to consider is the 3D structure of the PCMs, and the thermal and physical parameters of the PCM structures are well required for a given amount of PCMs. Each of these problems has a direct influence on the heat transfer characteristics in the PCM and ultimately affects the melt time and the performance of the PCM storage unit. To ensure long-term thermal performance of any PCM system, the size and shape of the PCMs must correspond to the melting time of the PCM and the daily insolation at a given location. PCMs are typically placed in long thin heat pipes, cylindrical containers or rectangular containers. The results of previously published papers dealing with LHTES demonstrate that two geometries commonly employed as PCM containers are the rectangular and cylindrical containers. The most intensely analyzed LHTES unit is the shell and tube system, accounting for more than 70%. It indicates the most engineering systems employ cylindrical pipes and heat loss from the shell and tube system is adopted to fabricate the form stable PCM composites. Thus, the supporting material based PCMs are sustaining the intrinsic shapes in the whole melting and crystallization process.

3.2.3. Combination of PCMs

Thermoelectric energy harvesting system is an effective power generator in converting thermoelectricity based on Seebeck effect. As an all-solid state energy conversion model, this energy harvesting system is highly significant in improving the utilization of solar energy with a clean and noiseless process. However, efficient photo-thermal conversion and temperature difference control are the key challenges in enhancing the thermoelectric energy conversion. Herein, constructing a novel thermoelectric system with temperature difference upon melting and cooling is necessary in PCM utilization. The PCM with high phase change performance could provide enough hot energy to maintain the hot-side temperature while the lower phase transition PCM is placed on the cold-side of PN TEG. Temperature gradient is controlled using the change of external temperature based on the phase change temperature control characteristics.

Energy is the basic resource in human survival and development, the Earth is the largest energy storage place of materials and providing for human existence. Fossil energy is currently the most widely used resource, but the crisis of energy depletion and serious environmental pollution have become major challenges. Therefore, solar energy can be an effective solution to the energy shortage and environmental pollution due to the universal, abundant, and clean. Transforming thermal energy to electric output power is important to utilize the solar energy. This process mainly includes thermal energy storage and applications. The thermoelectric generator (TEG) which is based on the Seebeck effect, utilizes the temperature difference to convert thermal energy to electric energy. The thermoelectric generation device involves an all-solid-state energy conversion without chemical reaction or fluid medium, resulting in the absence of noise, wear, and medium leakage during power generation. However, thermoelectric power generation depends on stable temperature difference to convert the output electrical energy. The energy density of the solar or heat radiation is vital though the low efficiency of solar energy, and fluctuated by the conditions of season, climate, latitude and time. The thermal energy is certainly limited and even a little difficult to use especially the solar energy as a continuous heat source in the thermoelectric applications.

Herein, the new thermoelectric energy harvesting system is constructed and the two different PCMs are placed on each hot side and cold side planes and change the temperatures from 25 °C to 80 °C to obtain the induced electrical energy and cooling to the initial state for measuring the harvested energy upon phase transitions. Based on the phase change temperature control characteristics, the hot-side and cold-side materials provided a relatively stable temperature difference for the thermoelectric device to realize thermal-to-electric energy conversion.

3.2.4. Conclusions

In this section, the thermoelectric generator (TEG) with two different PCMs supply the controllable output current on the heating and cooling process, the PEG composite is placed on the hot side of PN TEG and 1-tetradecanol (1-TD) is placed on the opposite cold side plane. In general, the PEG rises the temperature as the 1-TD is under the solid-liquid phase transition. The single energy harvesting system is a conventional device to obtain the thermoelectric energy conversion and the excess thermal energy utilization is available to the multiple system. The arriving rate of PCMs could promote the thermoelectric energy conversion and the GNP is utilized to increase the PCM thermal conductivities. The optimum components of PCMs are carried out by measuring the maximum peak area in both heating and cooling process. Thus, the smart thermal control in the environmental change is subsequently confirmed by the present research.

3.3. Single PN cell for thermoelectric energy harvesting

3.3.1. Introduction

Finding a new energy source is our prime mission because of upcoming energy depletion on the Earth. A renewable energy is certainly required to replace the fossil fuels and reduce the energy crisis. Development of a sustainable energy such as solar energy, wind energy, and heat recovery energy is one of the hot issues in both science and engineering fields. In particular, efficient energy harvesting has attracted a lot of attention in recent years and the thermoelectric energy conversion device which is able to convert the thermal energy to the electric energy has been widely used for energy harvesting [132, 133]. Energy storage plays a considerable part in absorbing heat energy for thermoelectric energy conversion. Thermal energy storage (TES), one of the most popular systems for recycling energy, generally employs a phase change material (PCM) as a working material due to its high latent heat, appropriate phase transition temperature range, and high thermal stability [8, 134]. The latent heat thermal energy storage (LHTES) is a good example of PCMs applications and the energy storage density can be improved by combining these PCMs with thermoelectric devices [8, 135].

The PCMs can absorb or release a great deal of thermal energy isothermally during the heating and cooling process [136]. Since PCMs have the advantage of high latent heat, they have been applied to the energy field systems including solar cell utilization [137], smart textiles [138], energy storage building materials [139], and wasted heat energy utilization [140]. From the category of phase change materials (PCMs), the solid-liquid PCMs are generally studied in the energy storage system due to the high latent heat under the solid-liquid phase transitions [141, 142]. Since solid-liquid PCMs, however, have a leakage problem during the melting and cooling process, the field applications are restricted [143]. To manufacture the form stable PCMs, some supporting materials are required to improve the dimensional stability of PCMs. In recent decades, various supporting materials such as urea-formaldehyde (UF) [144], polyurethane (PU) [50], polyethylene (PE) [51], and polyaniline (PANI) have been used to retain PCMs with a core-shell composite structure [52]. Since a large portion of the working material has

been replaced with the supporting shell material, the overall latent heat of the composite is reduced. As a result, the conventional PCM composites have smaller energy storing capacity than the pure PCMs during the phase transition [53, 54].

In order to increase the weight fraction of pure PCMs in the final composites, utilizing 3D porous materials as a supporting material has been reported [145]. Compared with conventional supporting materials, the 3D porous materials have larger pore volume than shell materials to be filled up by the pure PCMs [146]. One of the carbon aerogels, graphene aerogel has been investigated as a supporting material to prevent the leakage of PCMs due to its large surface area and complicated internal structure [147]. Compared with other supporting materials, the graphene aerogel has a number of advantages, such as good mechanical properties and thermal stability [148]. The PCM composites stabilized by employing the graphene aerogel can store large thermal energy and then convert the thermal energy to electric current [149]. It is important that the PCMs have high thermal conductivity for the energy conversion efficiency. The thermal conductivity of the supporting materials is controlled by modifying their internal structure including the pore size and porosity [150].

Thermoelectric energy harvesting system which is composed of the shape-stabilized PCMs and semiconductors has shown a great potential in various applications [64, 65]. For the energy harvesting system, N and P type semiconductors are required to connect the PCMs for construction of an electrical circuit [66, 67]. The N and P type semiconductors including thermo-couples utilize two different effects for energy harvesting; Seebeck effect and Peltier effect [68]. The Seebeck effect induces electrons to move from hot side to cold side of the energy harvesting device by absorbing the heat energy and the Peltier effect results in a temperature difference between two side planes by using the supplied electric power. Recently, Jiang et al, [68] prepared an energy harvesting system to generate the electric current by placing PCMs on the hot side and a heat sink (e.g., ice water) on the cold side of N and P type semiconductor. However, the electric current is obtained only during the cooling stage after removing the heat source, i.e., when releasing the stored energy from the PCM. On the basis of former research, modified the energy harvesting system with two different form stable PCMs placed on the sides of N and P type semiconductor to achieve the thermoelectric energy harvesting

during the phase transition process. The environmental temperature is only adjusted to examine the harvested energy and efficiency.

In the present study, we designed and fabricated a reusable energy harvesting device by combining two phase change materials (i.e., PEG and 1-TD) with N and P type semiconductor. Since PEG and 1-TD had different phase transition temperature, a temperature difference between two sides of the semiconductor is generated on both heating and cooling process. In order to prevent the leakage of PCMs, graphene nano-platelet (GNP) embedded graphene aerogel is used as a supporting material. Electric current is measured and an LED lamp is lit by using the output electric energy. In addition, the thermoelectric energy of the device is simulated numerically to provide a meaningful understanding of the energy harvesting system.

3.3.2. Energy harvesting system

The PCM composites are fabricated by using the vacuum-infiltration method, which allowed the molten PCM to fill pores of the graphene aerogel. Before the infiltration, PEG and 1-TD are placed on each of petri dish and then put into the vacuum oven which adjusted the temperature at 80 °C to make the liquid state. After vacuuming for about 30 minutes to remove moisture, the graphene aerogels are immersed in the PEG and 1-TD melts and kept for 6 hours in the vacuum state. The PEG and 1-TD composites are successfully fabricated by the solidification method and selected to construct the energy harvesting system. The schematic of energy harvesting mechanism is shown in **Fig. 3.3.1**. The stabilized PCM composites containing the working materials, PEG and 1-TD are placed on each side of the N and P type semiconductor respectively, inducing the electron movement due to temperature difference. As temperature increases, the 1-TD composite first experiences the melting transition while the temperature of PEG composite kept increasing due to its higher melting temperature (T_m) than that of 1-TD. Therefore, the temperature difference between the two sides of the N and P type semiconductor is developed. Electrons in the N type semiconductor are excited from valence band to conduction band and move to the hot side of this semiconductor. Subsequently, the electrons move to the P type semiconductor, thus inducing the electron-to-hole movement

in the closed circuit.

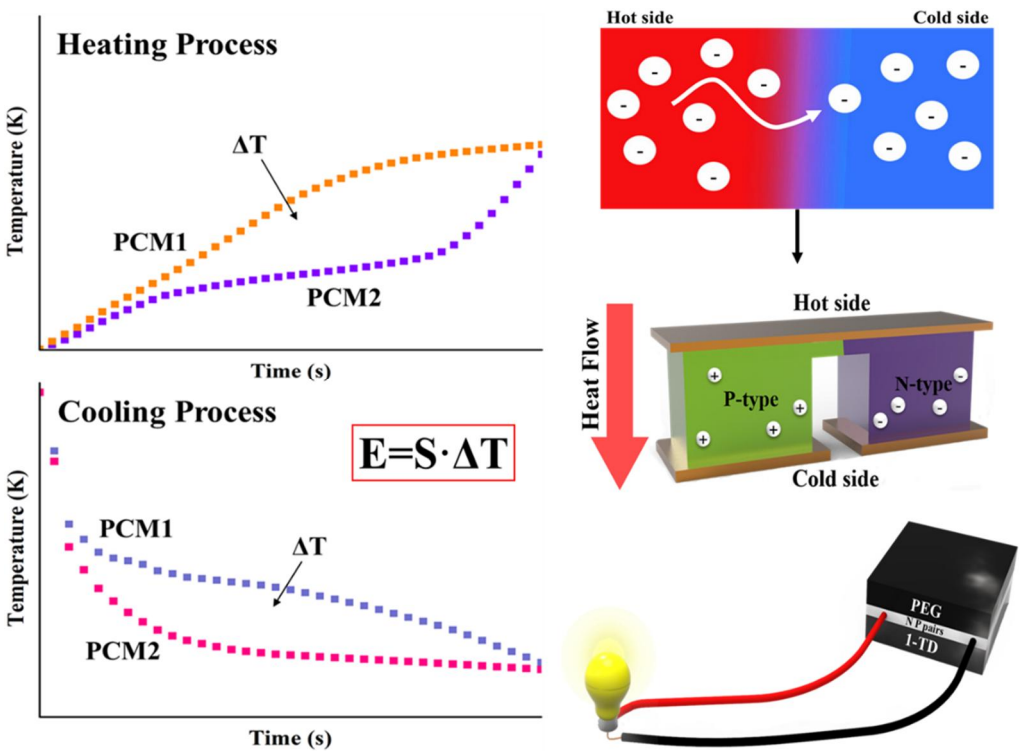

Figure 3.3.1. Schematic illustration of the energy harvesting system proposed in this study. The system is composed of the PCMs and the N P type semiconductor. The PCM composites are placed on the hot side and the cold side, and the LED lamp is turned on by the electric energy harvesting with the temperature difference between the two sides.

3.3.3. Numerical analysis

In order to predict the temperature difference between the two PCM composites, the temperature gradient during the heating and cooling process is calculated numerically. The Seebeck effect during the phase transition is demonstrated by employing a finite element method (FEM) software, COMSOL Multiphysics. The FEM mesh is constructed based on the geometry of the experiment and the system is composed of PEG composite, copper, N and P type semiconductor, and 1-TD composite. Density, thermal conductivity, heat capacity, latent heat (ΔH), and melting temperature (T_m) of PEG and 1-TD are obtained from the literature and employed for the simulation. The PEG composite is placed on the hot side of the device, and copper is selected to connect the N and P type semiconductor and the PCMs. Bi_2Te_3 are used as the N and P type semiconductor. It is assumed that the Seebeck coefficient is a function of temperature [151]. The input parameters are determined by measuring thermal conductivities of PCM composites and from DSC results. The dimension of PEG and 1-TD composites is the same for both the experiment and the calculation. It is assumed that the harvesting system is exposed to the air and the external temperature is increased from 25 °C to 80 °C for the heating process, which is coincident with the environmental conditions. In contrast, the cooling process proceeded under the natural environment and the temperature of harvesting system is decreased rapidly at the beginning time. The initial temperature of the cooling process is 80 °C and became close to the room temperature at the end. Furthermore, the heat transfer coefficient is vital for calculation of the convective heat flux in both heating and cooling processes and this transfer coefficient is defined for the natural convection of the air. The total number of finite elements is 415,596 as domain elements, 44,064 as boundary elements, and as 2,398 edge elements.

For simulation of the heat transfer within phase change materials, the following energy equation is used.

$$\rho C_p \frac{\partial \mathbf{T}}{\partial t} + \rho C_p \mathbf{u} \cdot \nabla \mathbf{T} + \nabla \cdot \mathbf{q} = Q \quad (1)$$

where ρ is the mass density, C_p is the heat capacity, and $\mathbf{q}$ is the heat transfer rate.

$$\mathbf{q} = -k\nabla T \tag{2}$$

where k is the thermal conductivity and T is the temperature of materials.

The density of phase change materials is expressed as $\rho = \theta\rho_{phase1} + (1-\theta)\rho_{phase2}$ considering the ratio of phase 1 to phase 2. Here, the θ is used as a fill-factor ranging from 0 to 1. Similarly, the parameters (C_p, k, and α_m) are calculated as functions of the fill-factor θ.

$$C_p = \frac{1}{\rho}\left(\theta\rho_{phase1}C_{p.phase1} + (1-\theta)\rho_{phase2}C_{p.phase2}\right) + L\frac{\partial\alpha_m}{\partial T} \tag{3}$$

$$k = \theta k_{phase1} + (1-\theta)k_{phase2} \tag{4}$$

$$\alpha_m = \frac{1}{2}\frac{(1-\theta)\rho_{phase2} - \theta\rho_{phase1}}{\theta\rho_{phase1} + (1-\theta)\rho_{phase2}} \tag{5}$$

where the mass coefficient α_m indicates the change of the mass density. For the calculation, the external natural convection boundary condition is assumed as below.

$$-n \cdot \mathbf{q} = \mathbf{q_0} \tag{6}$$

where **n** is the normal vector, and $\mathbf{q_0}$ is the convection heat flux. Since the heat flux is given by the following equation since it is proportional to the temperature difference and heat transfer coefficient (h_{air}).

$$\mathbf{q_0} = h_{air} \cdot (\mathbf{T_{ext}} - \mathbf{T}) \tag{7}$$

Temperature gradients of the two PCM composites (PEG and 1-TD) are obtained from the numerical calculation for the heating and cooling processes. The efficiency of this harvesting system is a percentage of thermal energy utilization and defined as the ratio of converted energy and total latent heat conservation energy. The equation is $\eta = \frac{W}{Q}$ and the total heat energy Q is correlated to the latent heat ΔH of PCM composites. The efficiency of this harvesting system is calculated by the numerical simulation which just considered the conversion heat energy (W) and total heat energy (Q); (The output Seebeck coefficient efficiency is neglected). Finally, the Seebeck coefficient S is given by $\sqrt{\frac{k}{\sigma T}}$, where σ is the electrical conductivity of the N and P type semiconductor. The

electric current is a function of the Seebeck coefficient S, the temperature difference ($\Delta \mathbf{T}$), and the resistance of the N and P type semiconductor (R) is shown as below.

$$\mathrm{I} = \frac{\mathrm{S}\Delta \mathrm{T}}{R} \tag{8}$$

3.3.4. Preparation of PCM composites

3.3.4.1. Preparation of GNP embedded graphene aerogel

Graphene oxide (GO) is synthesized by using modified Hummers' method. Firstly, 3.0 g of graphite is added to 12ml sulfuric acid (H_2SO_4) for pre-oxidation. The pre-oxidized graphite is stirred with 15 g $KMnO_4$ in an oil bath at 35 °C for 2 hours. Then, a small amount of H_2O_2 is poured into a deionized (DI) water diluted mixture to remove an excess of $KMnO_4$. After washing with 10 % HCl solution, the dilution with DI water is repeated to neutralize the graphite oxide solution and graphene oxide powder is obtained via freeze-drying. GNP embedded graphene oxide aerogel is fabricated by using the freeze-drying method. The graphene oxide (GO) powder and GNP particles are dispersed in DI water under ultra-sonic excitation with a 2:1 mass ratio. The suspension is poured into a mold with a size of 4x4x0.5 cm3 and freeze-dried for 2 days. After that, the hydrazine vapor reduction method is employed to prepare the reduced graphene oxide/GNP aerogel. Firstly, the 3D porous graphene oxide (GO) aerogel is placed on the petri dish and hydrazine is added to the dish. The hydrazine solution is transferred to the small vial bottle and then the temperature is maintained at 120 °C. The hydrazine is evaporated to obtain the reduced graphene oxide (GO) aerogel successfully. After 72 hours, the sealed system is removed and the color of aerogel became totally black. As the result, the reduced graphene oxide (rGO) aerogel is generated by the hydrazine vapor method.

3.3.4.2. Preparation of PCM based energy harvesting system

The PCM composites are fabricated by using the vacuum-infiltration method, which allowed the molten PCM to fill pores of the graphene aerogel. Before the infiltration, PEG and 1-TD are placed on each of petri dish and then put into the vacuum oven which adjusted the temperature at 80 °C to make the liquid state. After vacuuming for about 30 minutes to remove moisture, the graphene aerogels are immersed in the PEG and 1-TD melts and kept for 6 hours in the vacuum state. The PEG and 1-TD composites are successfully fabricated by the solidification method and selected to construct the energy harvesting system. The schematic of energy harvesting mechanism is shown in Fig. 1. The stabilized PCM composites containing the working materials, PEG and 1-TD are placed on each side of the N and P type semiconductor respectively, inducing the electron movement due to temperature difference. As temperature increases, the 1-TD composite first experiences the melting transition while the temperature of PEG composite kept increasing due to its higher melting temperature (T_m) than that of 1-TD. Therefore, the temperature difference between the two sides of the N and P type semiconductor is developed. Electrons in the N type semiconductor are excited from valence band to conduction band and move to the hot side of this semiconductor. Subsequently, the electrons move to the P type semiconductor, thus inducing the electron-to-hole movement in the closed circuit.

3.3.5. Results and discussion

3.3.5.1. Confirmation of reduced graphene oxide (rGO)

Once graphene oxide is reduced, its color changes from brown to black as shown in **Fig. 3.3.2**, and the characteristics of the reduced graphene oxide (rGO) aerogel is listed in **Table 3.3.1**. The graphene aerogel has a large specific surface area and high porosity which can fill up nearly 99% contents of pure PCMs. The contact angle indicates the hydrophilicity of the reduced graphene oxide (rGO) and graphene oxide (GO) (**Fig. 3.3.3**). The reduced graphene oxide (rGO) shows a 108.075 value which has higher hydrophobicity than the graphene oxide (63.029). It implies enhanced capacity for pure PCMs to infiltrate into the graphene aerogel [152]. To identify the reduction of graphene oxide (GO), the FT-IR and XPS results are shown in **Fig. 3.3.4** and **Fig. 3.3.5**, respectively. The characteristic peaks of graphene oxide (GO) corresponding to the oxygen functional groups such as the stretching vibration peak of O-H at the vicinity of 3,400cm^{-1}, C=O stretching vibration peaks around 1,700cm^{-1}, and the C-O stretching peak around 1,100cm^{-1} disappear after the reduction of GO. Furthermore, the change of binding peaks in **Fig. 3.3.5**, i.e., the binding energy of C=C peaks are rapidly decreased, and the intensity of graphene is slightly reduced compared with that of graphene oxide (GO) [153]. The functional groups binding energies become narrow and these results indicate that the graphene oxide is reduced successfully by the hydrazine vapor method [154].

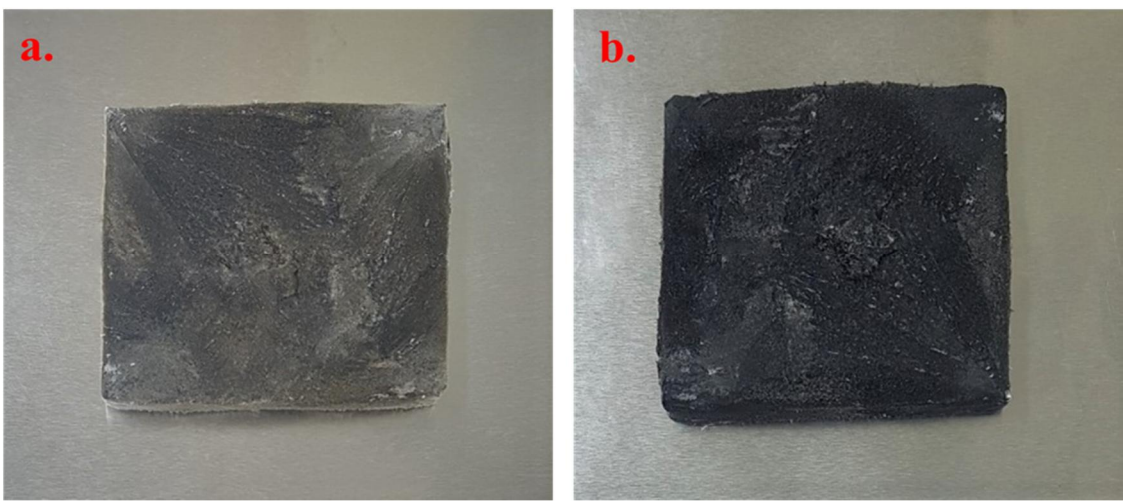

Figure 3.3.2. (a) Graphene oxide (GO) 3D structure aerogel, and (b) reduced graphene oxide (rGO) aerogel.

Table 3.3.1. The characterization of reduced graphene oxide (rGO) aerogel.

Samples	Graphene Aerogel
Specific surface area	373.95 (m^2/g)
Average mass	0.0667 (g)
Total pore volume	0.51 (cm^3/g)
Porosity	98.99 (%)
Graphene aspect ratio	1260.99

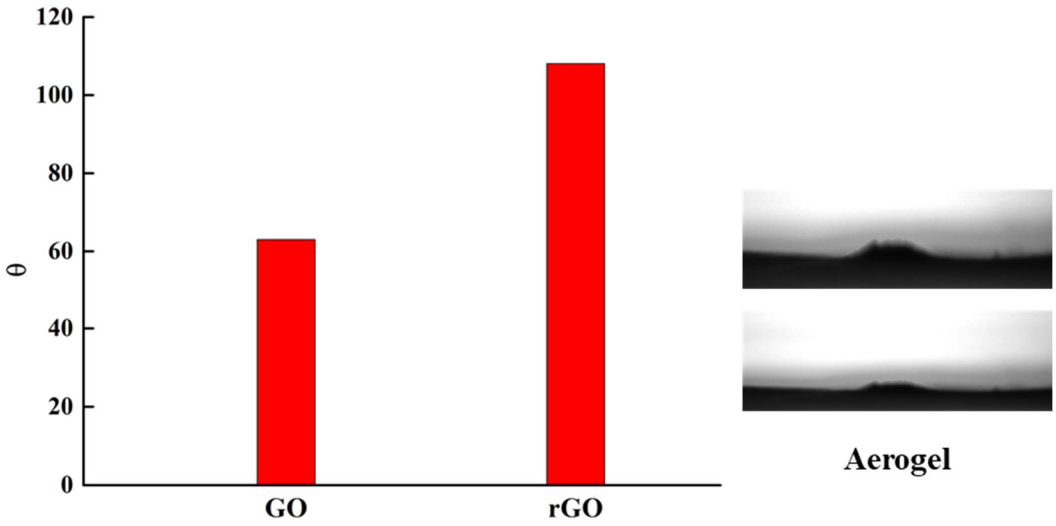

Figure 3.3.3. The contact angles of each graphene oxide (GO) and reduced graphene oxide (rGO).

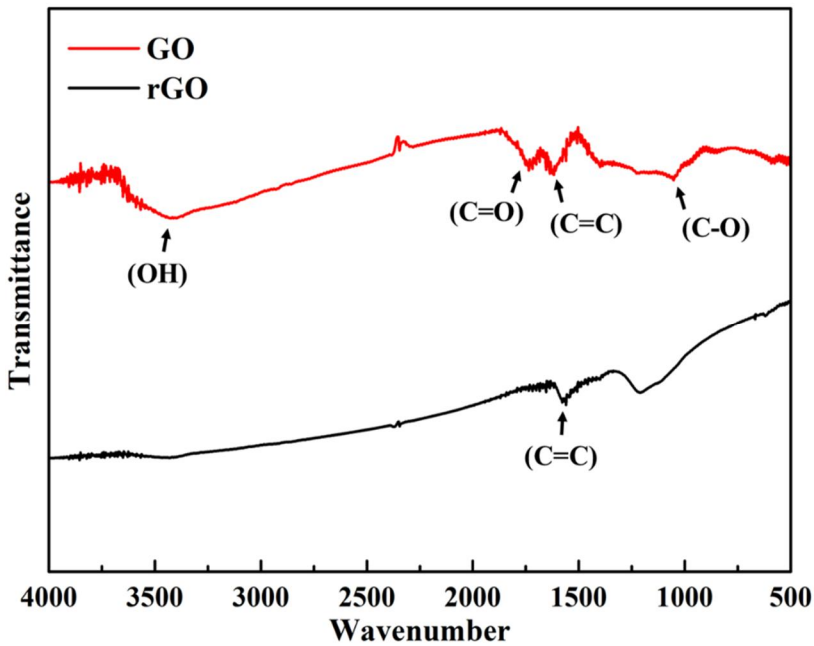

Figure 3.3.4. FTIR patterns of graphene oxide (GO) and reduced graphene oxide (rGO).

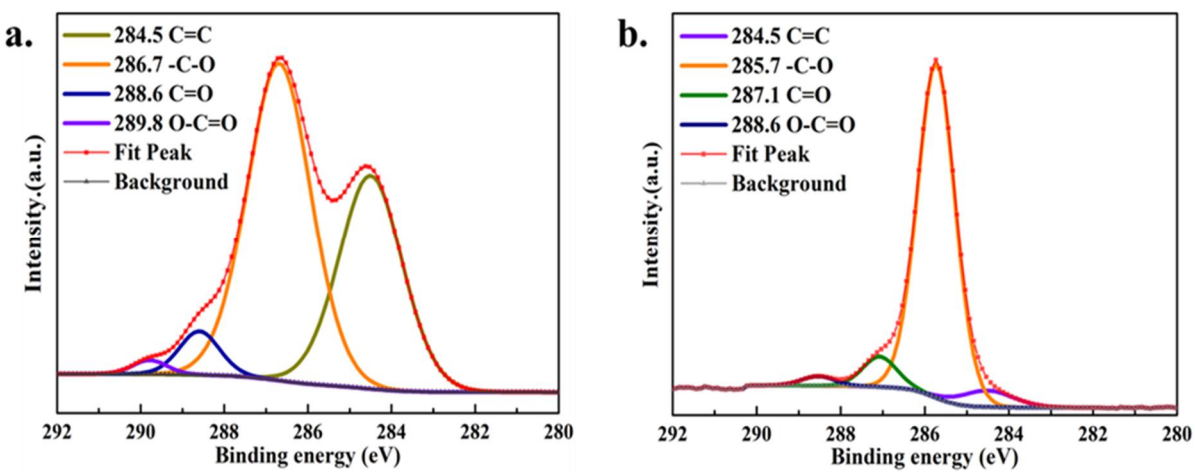

Figure 3.3.5. XPS spectra of (a) Graphene oxide (GO) and (b) reduced graphene oxide (rGO).

3.3.5.2. Experimental method

Fig. 3.3.6a shows the optimum sample thickness of PCM composites. The 0.5 cm is the optimum thickness to absorb and release the thermal energy and to obtain the high latent heat for maintaining the isothermal temperature field during the phase transition process. It demonstrates the limited thermal conductivity leads to the lower thermal-to-electrical conversion when the thickness is over than 0.5 cm. Hence, utilizing the 0.5 cm PCM composites in the energy harvesting system to obtain the induced current. The weight percentages between pure PEG and 1-TD in the PCM composites are shown in Fig. S5b. The working materials are both possessed 98.61% and 98.78% respectively due to the high porosity among the graphene aerogels. The shape stability of the PCM composites are characterized by a leakage test as shown in **Fig. 3.3.7.** The samples are placed on a hot plate and then heated from 25 °C to 80 °C. Thereafter, their thermo-behavior is captured using a digital camera. All samples maintained solid state in the initial stage of heating without any leakage. When the temperature of the hot plate is reached to 50 °C that is above the melting temperature of the 1-TD, the pure 1-TD is fully melted while the PEG maintained its initial shape [155]. On the other hand, the 1-TD composite still maintains the solid state at the same temperature [156]. When the temperature is increased up to 80 °C, the PEG melted, but the PCM composites retain their initial shape without any leakage [157]. This reveals that the porous graphene aerogel could play a role in enhancing the shape stability of PCMs during phase transition.

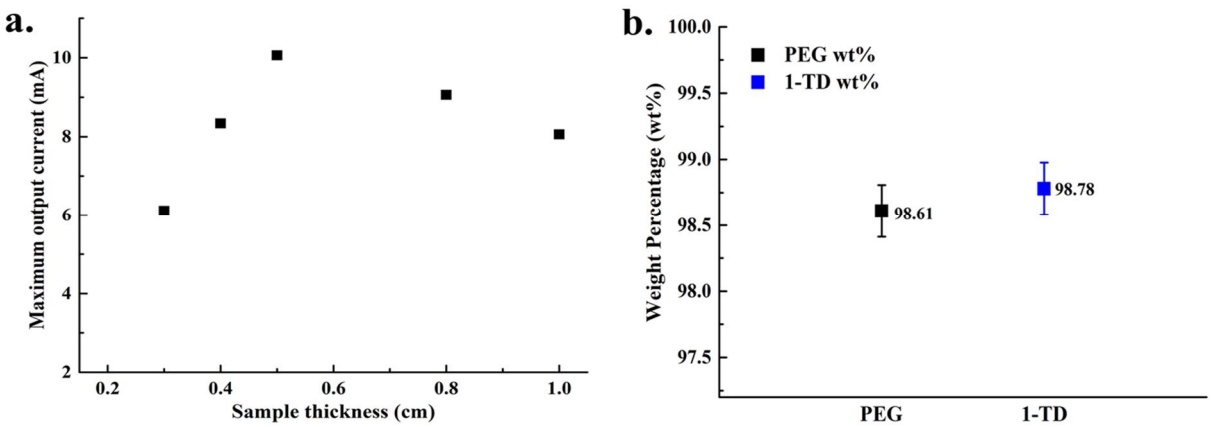

Figure 3.3.6. (a) The correlation diagram between the maximum output current and sample thickness, and (b) the weight percentage of each PEG and 1-TD in the PCM composites.

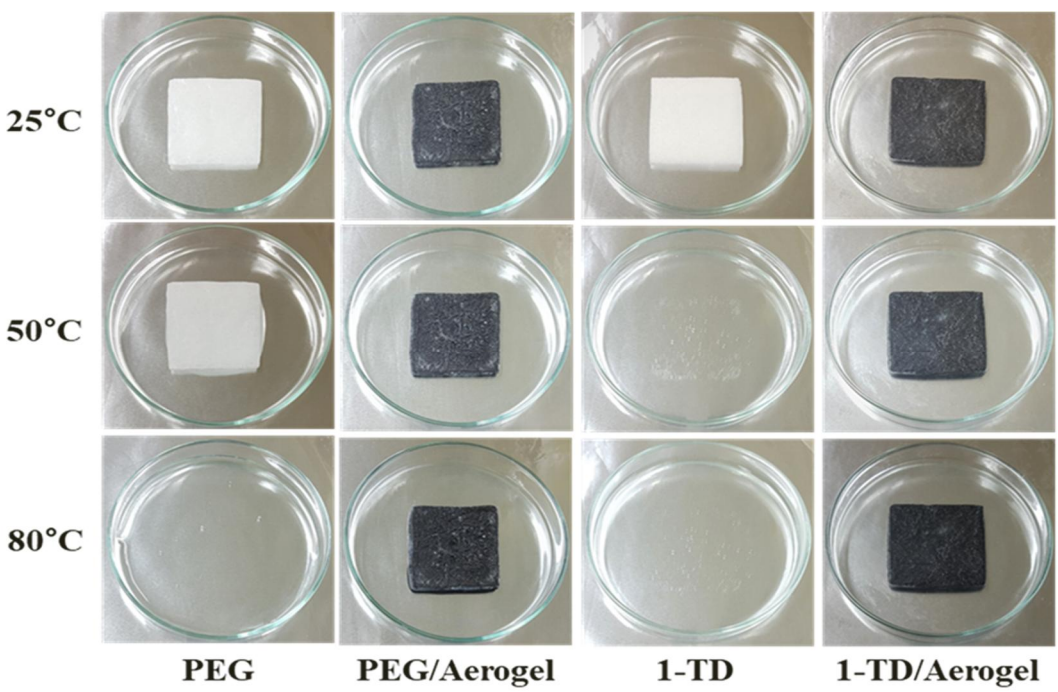

Figure 3.3.7. Photographs of PEG, PEG/Aerogel composite, 1-TD, and 1-TD/Aerogel composite at different temperatures.

3.3.5.3. Morphology of PCM composite

The SEM images of the GNP embedded graphene aerogel, pure PCMs, and PCM composites are shown in **Fig. 3.3.8**. The GNP embedded graphene aerogel shows the porous wrinkled structure (**Fig. 3.3.8a**), which is a typical microstructure of graphene aerogel [158]. **Fig. 3.3.8b** and **3.3.8c** demonstrate that the PCM composite has a fractured surface similar to that of the pure PEG. This indicates that the molten PEG infiltrated into the pore of the aerogel completely. That is, the pure PEG is placed in the internal space of the graphene aerogel. Therefore, the PCMs filling the GNP embedded graphene aerogel could hold their intrinsic properties without considerable loss. As shown in **Fig. 3.3.8d** and **3.3.8e**, there is a morphological difference between the pure 1-TD and the 1-TD composite due to the existence of the GNP embedded graphene aerogel. The XRD results are presented in **Fig. 3.3.9**. The diffraction peaks of the PEG are observed at $2\theta = 19.11°$ and $2\theta = 23.22°$, and those of the PEG composite appeared at $2\theta = 19.09°$ and $2\theta = 23.24°$. The 1-TD had at $2\theta = 21.34°$ and $2\theta = 24.16°$. These insignificant changes of the diffraction peaks adduce a strong evidence of the chemical inertness between the pure PCM and the GNP embedded graphene aerogels.

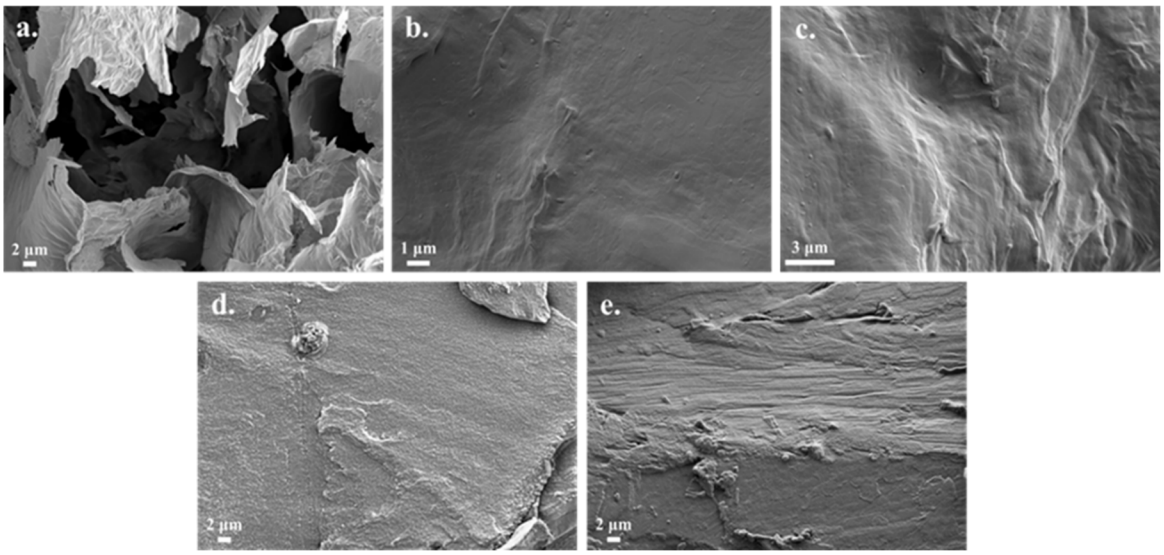

Figure 3.3.8. SEM images of (a) graphene/GNP aerogel, (b) pure PEG, (c) PEG/Aerogel composite, (d) pure 1-TD, and (e) 1-TD/Aerogel composite.

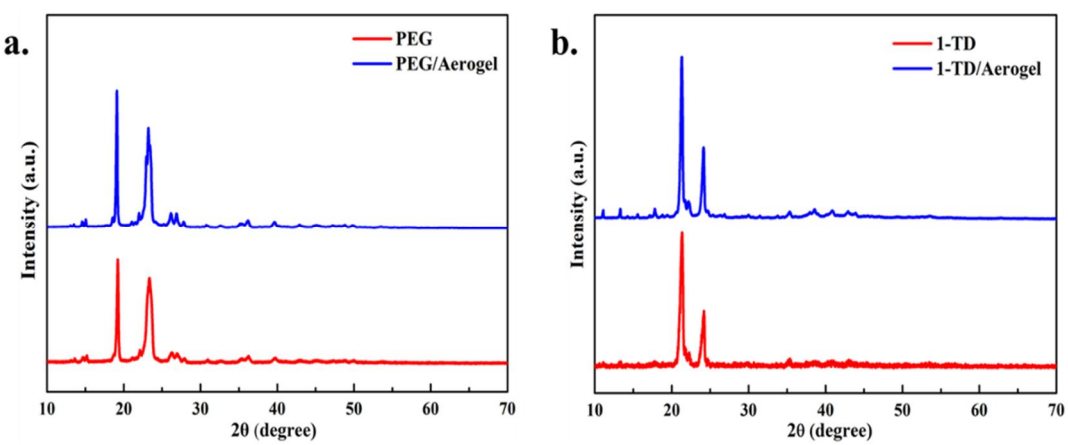

Figure 3.3.9. XRD peaks of (a) pure PEG, and PEG composite; (b) pure 1-TD, and 1-TD composite PCMs.

3.3.5.4. Thermal properties of PCM composite

The phase transition temperatures and latent heat of the PCMs are measured using DSC. **Fig. 3.3.10** shows the melting and cooling curves of the pure PEG, pure 1-TD, and PCM composites. From the DSC experiment, sharp peaks are observed at the solid-liquid phase transition of the PCMs. The onset melting and crystallization temperature (T_{mo} and T_{co}), end melting and crystallization temperature (T_{me} and T_{ce}), melting and crystallization peaks (T_{mp} and T_{cp}), and enthalpy of each process (ΔH_m and ΔH_c) are listed in **Table 3.3.2** and Table 2. In **Fig. 3.3.10a** and **Table 3.3.3**, phase transition of the pure PEG is observed between 50.94 °C and 68.60 °C with a melting temperature of 65.72 °C and a latent heat of 181.77 J/g. For the cooling process, the crystallization temperature ranged from 42.37 °C to 34.71 °C with a cooling temperature of 39.04 °C and a cooling enthalpy of 160.02 J/g. The PEG composite showed little variation of T_{mo}, T_{me}, T_{co}, and T_{ce} compared with the pure PEG, and the melting and crystallization peaks of the PEG composite are slightly shifted to higher temperature than those of the pure PEG [159]. The latent heat of the PEG composite decreased due to the reduced volume fraction of PEG in the composite. The onset melting temperature (T_{mo}) of the pure 1-TD is observed at 36.95 °C and slightly shifted to 36.40 °C when the 1-TD infiltrated into the aerogel. Similar to the onset melting peak, the end melting peak of the 1-TD composite is shifted to lower temperature than that of the pure 1-TD. It is found that the heating and cooling enthalpies of the 1-TD composites slightly decreased when introducing the supporting material. However, the latent heat of the PCM composites is very similar to that of the pure PCMs. In this regard, the PCM composites had sufficiently large latent heat to replace pure PCMs in the energy harvesting devices. The glass transition temperature (T_g) of PEG and 1-TD composites is presented in **Fig. 3.3.11**. The value of each PCM composite is -26.30 °C, and -20.24 °C that lower than phase transition temperature. It showed these PCM composites are under solid-liquid phase transformation on the melting and crystallization process. The thermal conductivity of PCM composites is important to obtain the thermoelectric energy conversion process and presented in **Fig. 3.3.12a**. The pure PEG just indicated 0.1764 W/mK and significantly increased to 0.4268 W/mK after

infiltrating into the graphene aerogel. The GNP embedded 3D porous graphene aerogel could positively raise the thermal transformation and contribute to the thermoelectric energy conversion efficiency. As well as the 1-TD, the thermal conductivity value of 1-TD composite is 0.3408 W/mK which showed approximately 4 times higher than that of pure 1-TD (0.0812 W/mK). Based on the thermal conductivities between the PEG, and 1-TD composites, the thermal diffusivity revealed the time of the thermal balance during the phase transitions and the result is presented in **Fig. 3.3.12b**. The graphene supporting material could promote the thermal transport rate of PEG and 1-TD from 0.1921 mm^2/s to 0.2918 mm^2/s; 0.1403 mm^2/s to 0.2369 mm^2/s, respectively. These thermal morphologies clearly illustrated the importance of graphene aerogel and input to the simulation program to calculate the numerical results.

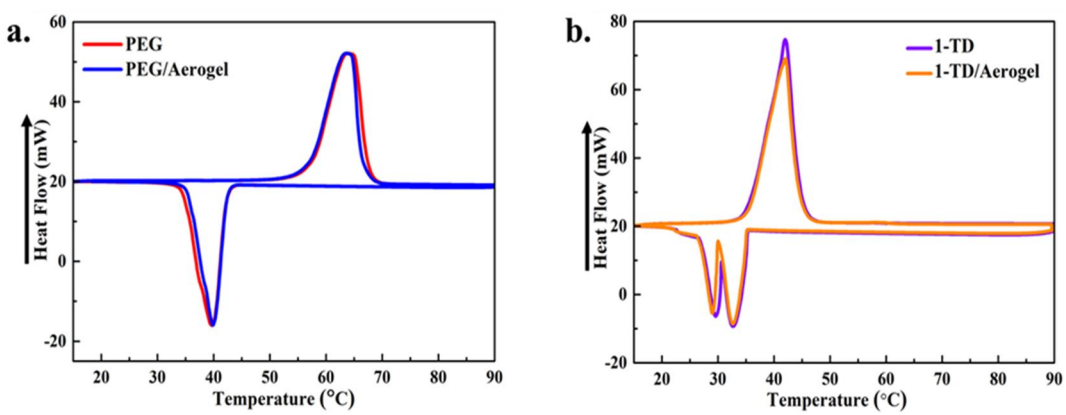

Figure 3.3.10. DSC curves of (a) PEG and PEG/Aerogel composite, and (b) 1-TD and 1-TD/Aerogel composite.

Table 3.3.2. DSC results of PEG and PEG/Aerogel composite.

Samples	T_{mo}(℃)	T_{me}(℃)	T_{mp}(℃)	ΔH_m(J/g)	T_{co}(℃)	T_{ce}(℃)	T_{cp}(℃)	ΔH_c(J/g)
PEG	50.94	68.60	65.72	181.77	42.37	34.71	39.04	160.02
PEG/Aerogel	50.01	68.38	65.55	181.24	43.85	36.98	39.25	159.76

Table 3.3.3. DSC results of 1-TDand 1-TD/Aerogel composite.

Samples	T_{mo}(℃)	T_{me}(℃)	T_{mp}(℃)	ΔH_m(J/g)	T_{co}(℃)	T_{ce}(℃)	T_{cp}(℃)	ΔH_c(J/g)
1-TD	36.95	45.01	42.47	223.78	35.29	20.24	30.95	216.42
1-TD/Aerogel	36.40	44.68	42.41	220.40	35.57	20.31	30.98	213.63

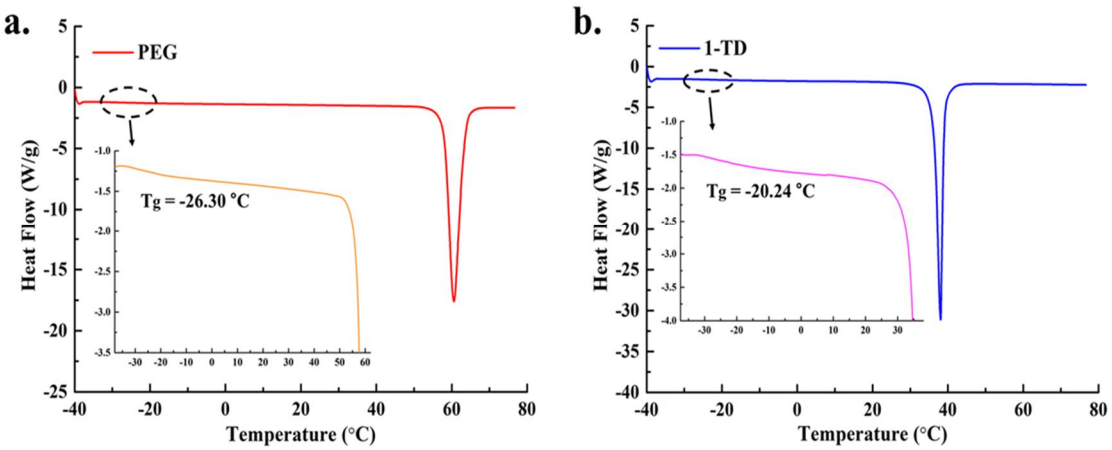

Figure 3.3.11. Tg transition results between the (a) PEG and (b) –TD composites.

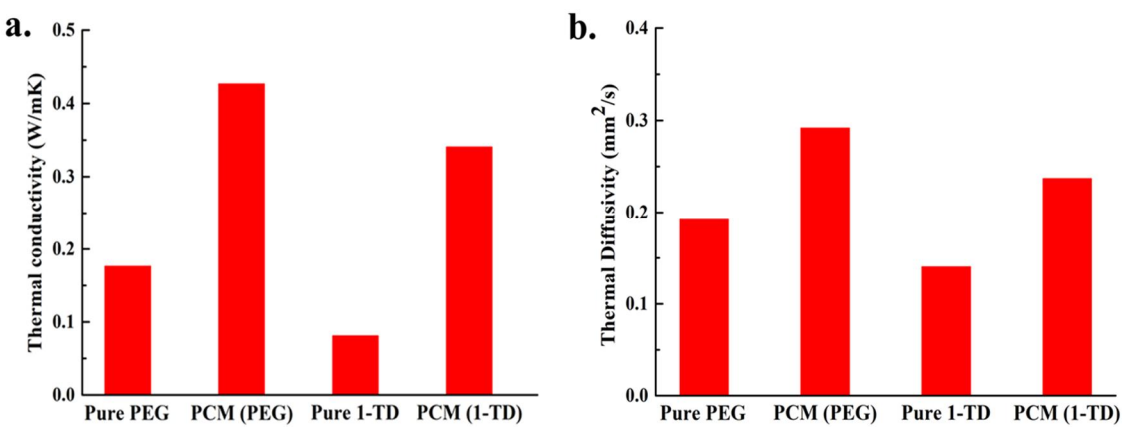

Figure 3.3.12. (a) Thermal conductivity among the pure PEG, PEG composite, pure 1-TD, and 1-TD composite. (b) The result of thermal diffusivity among these PCMs.

3.3.5.5. Current measurement of energy harvesting device

Fig. 3.3.13 showed the electric current measured from our energy harvesting device during increasing and decreasing environmental temperature. For the heating process, the energy harvesting device with the PEG, and 1-TD composites is placed in a heating chamber and heated the temperature is raised from 25 °C to 80 °C. **Fig. 3.3.13a** showed the peak of induced electric current during the heating process. When the temperature approached to the melting temperature of the PEG composite, the temperature of the 1-TD composite is not altered due to its relatively low melting temperature. Subsequently, the temperature difference between two sides of semiconductor is obviously produced and gave rise to the thermoelectric energy conversions. The heating result revealed that the maximum current is around 10 mA at 1,350 s, which corresponded to the moment at the biggest temperature difference during the heating process. The electric current is found to decrease until 1,900 s as no temperature difference in the harvesting system. After several hours, the device is taken out from the heating chamber and allowed the PCM composites to release the thermal energy on the external condition. In **Fig. 3.3.13b**, the electric current of the harvesting system is rapidly increased due to the high cooling speed. Reverse to the heating process, the PEG composite located in the crystallization field while the temperature of 1-TD is continuously decreased. It caused the temperature difference in the harvesting circuit and the current had a maximum value of 10 mA at 300 s and gradually decreased. The cooling process is terminated at around 850 s because of some stored energy is diffused into the air which reduced the thermoelectric energy conversion efficiency.

For the purpose of demonstrating usability of energy harvesting devices, a LED lamp is generally connected to the device and turned on using the harvesting energy. The power of the device is measured to evaluate the maximum power output. The power-current (P-I) characteristics during the heating and cooling processes are shown in **Fig. 3.3.13c**, and **3.3.13d**. The maximum power of these two process is approximately at 437 μW, and 433 μW which is not large enough to turn on the LED lamp. To improve the output power, a

voltage start-up converter (LTC 3108) is integrated into the energy harvesting device [160]. **Fig. 3.3.13e** showed that the LED lamp is lit when introducing the converter into the energy harvesting device. This result indicated that the electric energy of the harvesting system is large enough to be used for practical applications.

3.3.5.6. Numerical simulation of thermoelectric conversion

The energy characteristics of the PCM embedded energy system is numerically modeled to provide a profound understanding of underlying physics behind the system. During the heating process, the external temperature changed from 25 °C to 80 °C, as shown in **Fig. 3.3.14a**. The temperatures of the two composites rapidly increased in the initial stage. Since the melting temperature (T_m) of 1-TD is lower than that of the PEG, the 1-TD composite had the earlier phase transition than the PEG composite. As a result, the 1-TD composite stored a relatively large amount of heat in the initial heating stage. On the other hand, the temperature of the PEG composite continued to increase while the 1-TD composites underwent the phase transition. Consequently, the temperature difference between the composites increased and then declined. It turned out that the maximum temperature difference is near 17 °C at 1,500 s (**Fig. 3.3.14b**). The heating process is finished at about 2000s. It is found that the theoretically calculated current is in a good agreement with the experimental result as shown in Fig. 6c. In the cooling process, an initial temperature of 80 °C decreased to room temperature. The temperature profiles of the PCM composites with respect time are shown in **Fig. 3.3.15a**. Similar to the heating process, the maximum temperature difference is about 15 °C (**Fig. 3.3.15b**) at around 300s. The cooling process is completed at 900s in **Fig. 3.3.15c** and the maximum value of the calculated current is 10mA, which coincided with the experimental result. The calculation of thermoelectric energy conversion efficiency is presented in **Fig. 3.3.15d** and the heating and cooling efficiencies exhibited 52.81 %, and 30.29 %. It indicated the lower harvesting efficiency on the cooling process than that of heating period of time as a portion of stored energy is diffused to the external environment. The numerical calculation showed the energy harvesting system is controllable in a systematic manner and useful for practical applications.

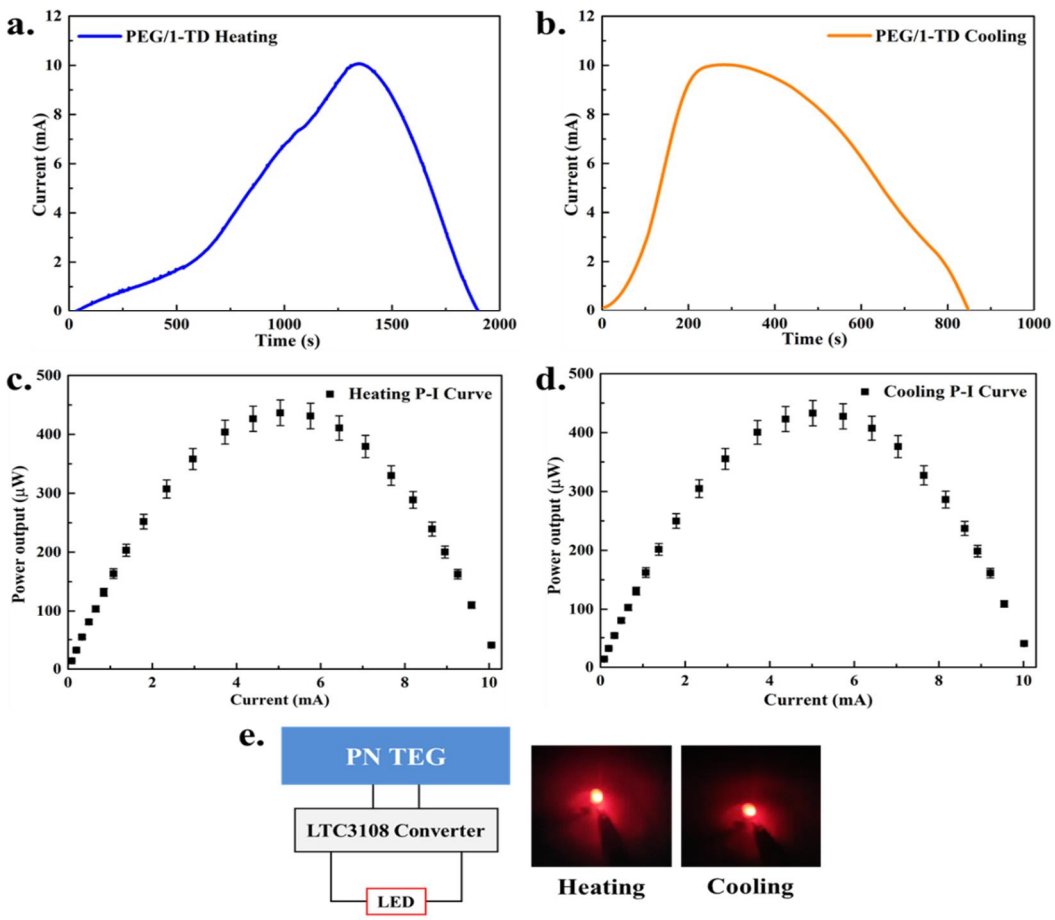

Figure 3.3.13. Experimental characterization of the energy harvesting system: (a) electric current during the heating process, (b) electric current during the cooling process, (c) power output during the heating process, (d) power output during the cooling process, and € image of the LED light turned on using the harvested electric energy.

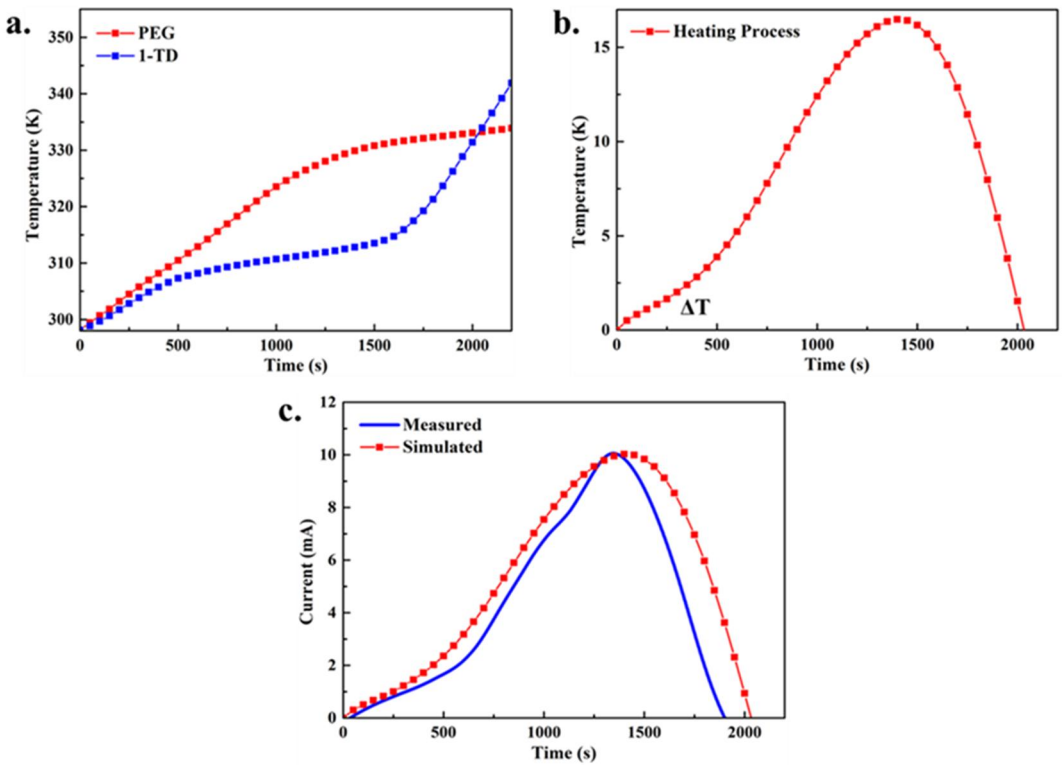

Figure 3.3.14. Numerical simulation of thermoelectric conversion during the heating process: (a) temperature profiles, (b) temperature difference and (c) comparison between predicted and measured electric currents.

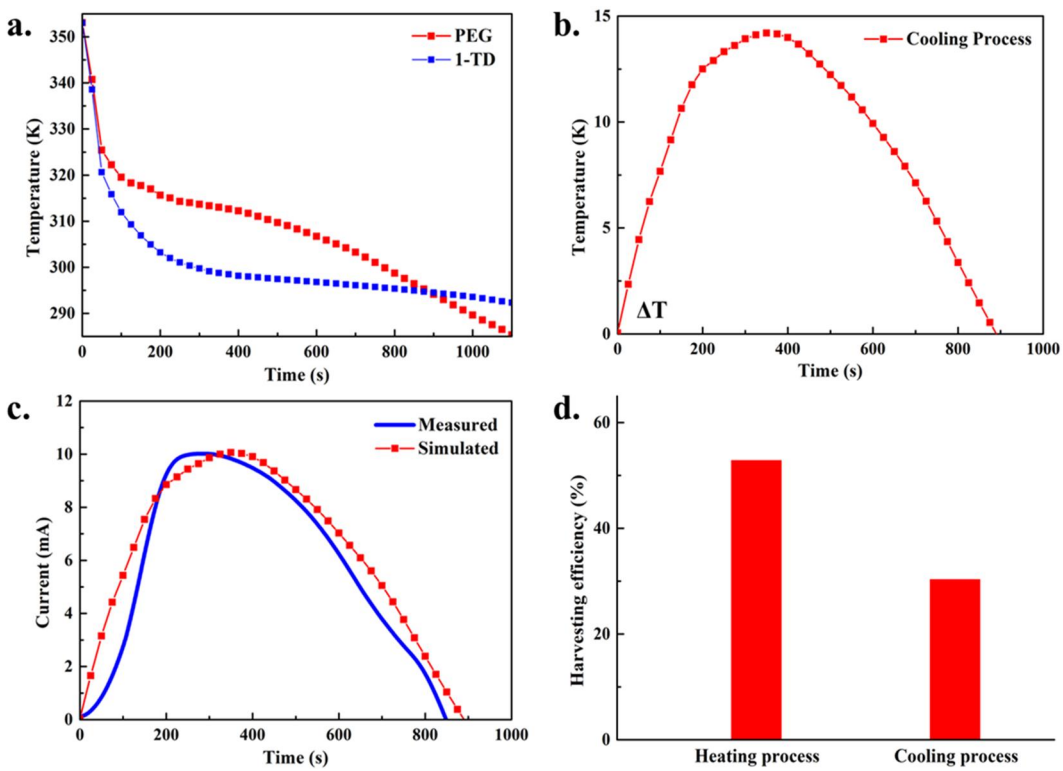

Figure 3.3.15. Numerical simulation of thermoelectric conversion during the cooling process: (a) temperature profiles, (b) temperature difference and (c) comparison between predicted and measured electric currents, (d) harvesting efficiency between heating and cooling process.

3.3.6. Conclusions

In the present work, we designed and prepared an energy harvesting system that consists of form stable PCM composites with N and P type semiconductor. The graphene oxide (GO) is successfully synthesized by modified Hummer's method and the GNP embedded graphene aerogel enhanced the shape stability without any loss of internal porous structure. The final PEG and 1-TD PCM composites had large latent heat, which yielded a considerable temperature difference between the opposite sides of the thermoelectric semiconductor. Furthermore, the phase transitions of the PCMs lasted for a sufficiently long period of time. Thermal conductivity of the PCM composite is increased significantly after infiltrating into the 3D porous graphene aerogels. The electric current harvested from the system is analyzed experimentally in an effort to demonstrate the availability of the energy harvesting system. The maximum harvesting current is 10 mA in both heating and cooling processes and the harvesting field is maintained at 1,900 s and 850 s. The obtained electric energy output is large enough to drive an electric element, i.e., a LED lamp. The temperature variation and the resulting electric current are modelled with respect to time using a finite element method (FEM). The numerical prediction is in good agreement with the experimental results and calculated thermoelectric conversion efficiency is 52.81 %, and 30.29 %, respectively. It is expected that this study will provide insight to thermoelectric energy conversion and contribute to design of energy harvesting devices for various applications such as wireless sensors and medical devices.

3.4. Multiple PN cells for energy harvesting syhstem

3.4.1. Introduction

These days, renewing energy is attracting a great deal of attention to handle energy consumption and depletion. It is critical to develop a new energy harvesting device using relatively simple, highly efficient, and easy-to-use technologies [161]. In this sense, the Seebeck effect based thermoelectric energy conversion allows us to increase the heat recyclable efficiency and reduce the energy loss in the actual productions [132, 162]. Thermal energy storage (TES) is one of the most common systems for absorbing and releasing a large amount of energy in the energy harvesting field.[149, 163] In general, TES employs phase change material (PCM) due to its strong points such as suitable phase transition temperature range, high latent heat, excellent thermal stability, and good energy storage efficiency [100, 164]. The latent heat thermal energy storage (LHTES) is one of the thermal applications that combine phase change materials (PCMs) with thermoelectric generator (TEG) to measure the electrical energy and evaluate the thermoelectric energy conversion efficiency [165, 166].

Although pure PCMs show some typical advantages, leakage is a general problem when temperature is over their melting point (T_m) and restricts its applications.[146] Therefore, a supporting material is needed to maintain the shape for absorbing or releasing thermal energy during the phase transition process [167, 168]. Thus far, some supporting materials such as diatomite[169], polyaniline (PANI)[52], and urea-formaldehyde (UF)[144] have been used to prevent leakage by using core-shell micro-structure method.[170] The mixture of phase change materials and supporting materials have smaller latent heat due to large replacement of the working materials[171]. As a result, the PCM composites possess lower energy storage function during the phase transition than that of pure PCMs [106, 172].

Carbon based materials, especially graphene aerogel is widely utilized as a supporting material for securing 3D porous internal structure and appropriate mechanical stabilities [173-175]. The porous structure can be constructed in the pure PCMs and prevent the leakage during the phase transition process [176-178]. Furthermore, since the graphene

aerogel has high porosity and can be infiltrated by a large amount of working PCM materials, it can minimize the decrease in the latent heat of PCM composites.[179] As a result, the graphene aerogel based PCM composite can provide large storing energy with high thermoelectric energy conversions[180]. In addition, thermal conductivity which is vital for the energy conversion efficiency is controlled by the internal structure of supporting materials such as porosity and pore size [181, 182].

To measure the energy harvesting peaks,[183] the thermoelectric generator (TEG) consisting of N and P type semiconductors is incorporated, and a closed circuit is built by using PCM composites [59, 184]. Due to the Seebeck effect, electrons are moved from hot side to cold side by absorbing the thermal energy[185], and the thermoelectric generator (TEG) is utilized as an electrical power supply under the temperature difference between two sides of device [186, 187]. Generally, two different PCMs are selected for the energy harvesting based on the Seebeck effect [188]. One PCM with a higher melting point (T_m) is placed on the hot side of the TEG cell, and the other is situated on the cold side [182, 189]. Normally, the PN junction is blocking the current movement on the reverse bias which results in the electric energy that is measured only when the temperature of the hot side is higher than that of the cold side [190, 191]. In other words, it is hard to detect the generated current when the temperature of the cold side exceeds that of the hot side of N and P type semiconductors. Thus, the system has acquired only part of thermoelectric energy during the heating and cooling processes. In order to harvest the entire amount of the thermoelectric energy generated during the processes, additional energy harvesting system needs to be introduced.

In the current study, we devised an advanced thermoelectric energy harvesting system with two different phase change materials (i.e., PEG and 1-TD), and N and P type thermoelectric generators (PN TEGs). By using the temperature difference between two PCM composites during heating and cooling processes, the enhanced energy harvesting is achieved. Graphene nano-platelet (GNP) is employed as a filler in the graphene aerogel to prevent the fracture and sustain the 3D porous internal structures [192]. After fabricating the graphene based form stable PCMs, the PEG and 1-TD are placed on the two sides of PN TEGs for inducing thermoelectric energy harvesting. The electric current is measured during the phase transition process with respect to the temperature difference between

two sides of semiconductors. An LED lamp is turned on by using the harvested electric energy. Besides, the thermoelectric energy conversion is numerically calculated to understand the energy harvesting mechanism.

3.4.2. Energy harvesting system

The fabricated PEG and 1-TD composites are placed on the two sides of N and P type thermoelectric generators (PN TEG). The temperature is increased from 25 °C to final temperature of 80 °C. **Fig. 3.4.1** shows the schematic illustration of the energy harvesting system. The electron movement is developed when the temperature of the hot side is higher than that of the cold side. The 1-TD composite undergoes the melting transition as temperature increases. However, the temperature of the PEG composite on the opposite side is still increasing because of its higher melting point (T_m) than that of the 1-TD composite. Hence, the temperature difference is created in both PN TEGs. Excited electrons from N type semiconductor are transported to the cold side due to the thermal energy as shown in **Fig. 3.4.2**. The electrons in the conduction band readily pass through the depletion layer to combine with the holes incorporated in the P type semiconductor (**Fig. 3.4.2a**). Thus, the electrons move into the closed circuit to generate the electrical current with barely low potential barrier as presented in **Fig. 3.4.2c**. When the temperature of hot side is lower than that of cold side, the electron movement becomes reversed (**Fig. 3.4.2b**). Therefore, the electron movement is restricted by the energy barrier of PN TEG (**Fig. 3.4.2d**), leading to the end of thermoelectric conversion of the 1st device in the system. When the phase transition of the 1-TD composite is completed, the PEG composite experiences the melting transition. Afterwards, the temperature difference begins to increase and then the temperature of the 1-TD composite exceeds that of the PEG composites. As a result, the second device in the system provokes the thermoelectric energy conversion to generate the electrical current instead of the first PN TEG. The PN TEG is composed of N and P type semiconductors with different doping concentrations. The internal structure is shown in **Fig. 3.4.3a**. The N type semiconductor is packed by extra electrons. Hence, the major carrier of the N type is the extra electrons doped in the semiconductor. In contrast, there are unsaturated Silicons in the P type semiconductor generating holes as shown in **Fig. 3.4.3b**. In this case, the major carrier is

the holes in the P type semiconductor. When a pair of N and P type semiconductors are employed, they suddenly develop a rectified function to pass through the electrons. It is demonstrated that the electrons at the forward bias are easily moved to generate the electrical current, while they are blocked at the reverse bias. The PN TEG can control the direction of electron movement. The harvested current is measured by using a potentiostat (**Fig. 3.4.4**). The energy harvesting system is placed in the chamber, and then temperature is increased to generate the thermoelectric energy conversion due to the Seebeck effect. When the temperature of the chamber is increased to 80 °C, the heating process is completed. After then, the harvesting system is removed from the chamber and then cooled in natural condition.

The PN TEG is generally composed of N and P type semiconductors that can rectify the direction of electron movement by the external conditions such as electric field, temperature gradient, and light source. The depletion layer of the PN TEGs is a special field with nearly zero energy barrier. Thus, the electrons excited by absorbing energy could easily cross the forward depletion layer and recombine with the holes in the P types. As a consequence, series of electron and holes are reduplicating the combination which can generate the electron movement in the closed circuit. However, when the excited electrons are transported reversely to the depletion layer, they should overcome the resistance of electric field to combine with the holes in the opposite side. In other words, the energy barrier is blocking the electron movement and the PN TEG works as an electrical resistance in the circuit. Therefore, the PN TEG produces the electrical current at the forward direction of N and P type semiconductor arrangements.

For N and P type semiconductors in the PN TEGs, the N type has large doping concentration of electrons such that some of the Silicons develop the group Ⅴ atoms. The electron doped in the N type semiconductor could easily move to the opposite side of semiconductor along with formation of N type inclusive junctions. Hence, the major carrier of N type is extra electrons doped in the semiconductor. The P type semiconductors are incorporating lots of missing electrons which remains in the holes of the internal structure. A portion of Silicons get group Ⅲ atoms and the major carrier of P type is the hole in the circuit. According to the rectification of PN junctions, the electric current at the forward bias is increased significantly while only few of leakage current is

generated at reverse bias. Although the energy barrier depends on the temperature due to the electron mobility at the high temperature, the saturation current peak is increased rarely to generate the electrical current. In a word, the PN TEG has a rectification property to produce a current merely at forward direction.

The experimental results are recorded in the PC by utilizing the potentiostat to observe peaks of the harvested electric current during the phase transition process. Initially, the energy harvesting system is placed into an environmental chamber and the temperature is adjusted from 25 °C to final 80 °C. When the 1-TD composite maintains the isothermal field, the system starts to generate the output electrical current as the temperature of PEG composite is incremented. After the 1-TD composite completes the phase transition and its temperature exceeds that of the PEG composite, the temperature difference is normally decreased and reversed. The PEG composite is exactly at the phase transition temperature and the temperature difference becomes increased due to the 1-TD composites. Thus, the two devices of harvesting system consist of PEG and 1-TD composites with opposite positions that can utilize the thermal energy sufficiently to generate the output electrical current.

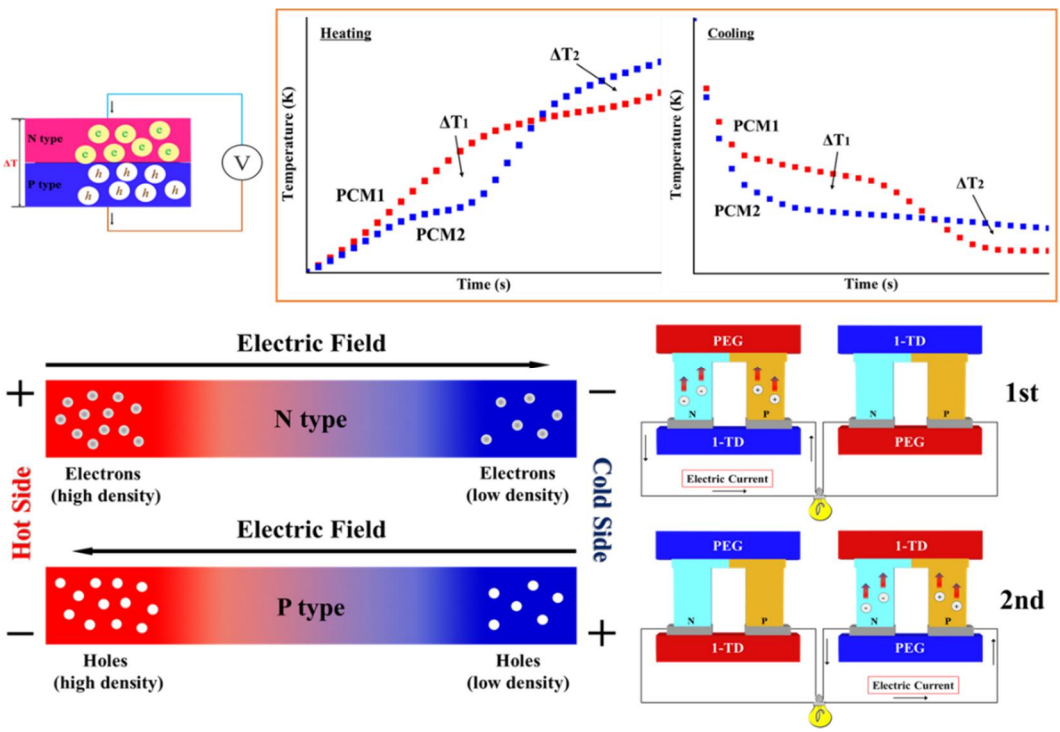

Figure 3.4.1. Schematic illustration of multiple energy harvesting system which is composed of PEG and 1-TD composites and PN TEGs.

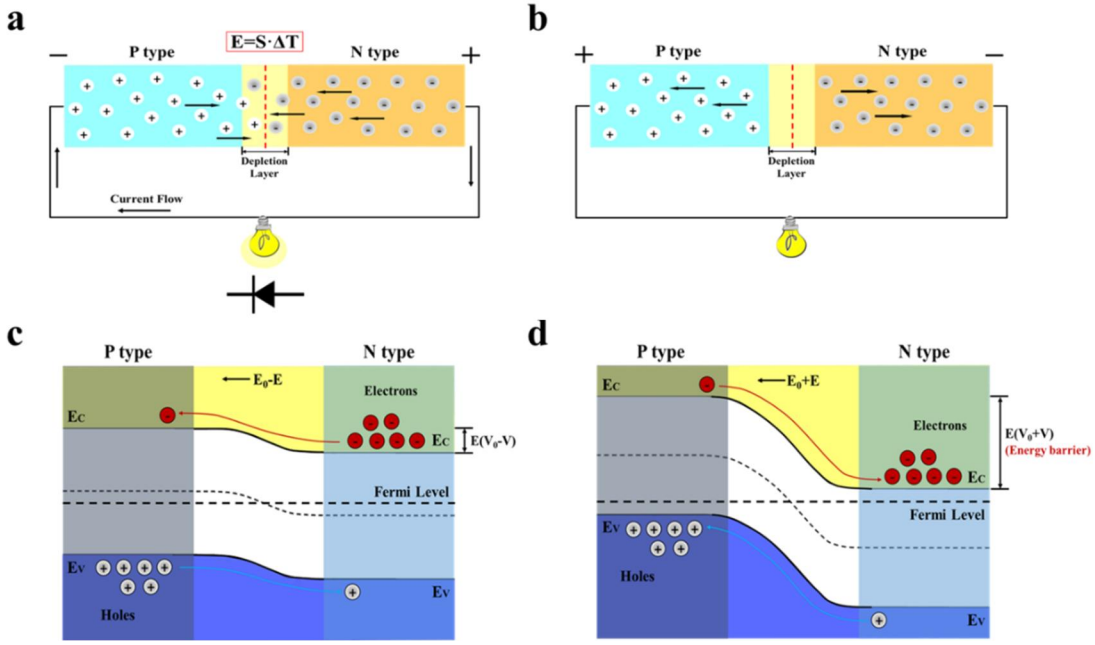

Figure 3.4.2. The schematic illustration of PN junction at (a) forward bias PN junction, (b) reverse bias PN junction, (c) forward bias energy bandgap, and (d) reverse bias energy bandgap.

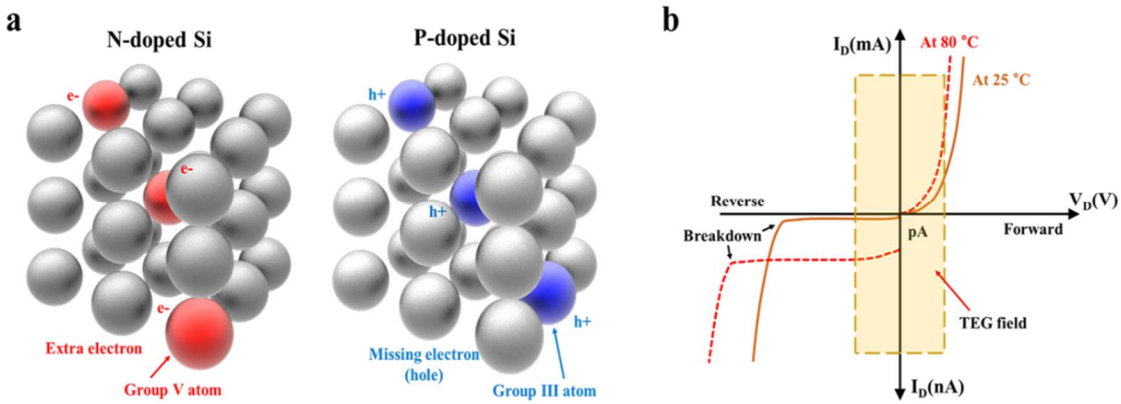

Figure 3.4.3. (a) schematic of N and P type semiconductor internal structures, and (b) I-V curve for a PN junction diode.

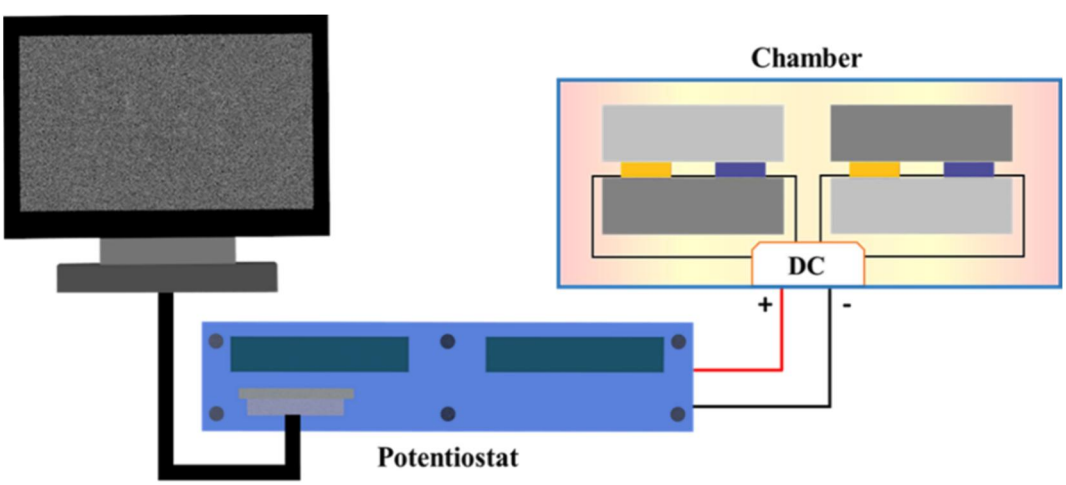

Figure 3.4.4. The apparatus setting by combination of the energy harvesting system.

3.4.3. Numerical analysis

To investigate the temperature difference during the phase transition process, COMSOL Multiphysics, a commercial software based on finite element method (FEM), is used. The temperature gradients in the PEG and 1-TD composites are calculated numerically, and the resulting Seebeck effect is demonstrated during the heating and cooling cycles. The device is comprised of copper, PEG composites, 1-TD composites, and N and P type semiconductors. For the N and P type semiconductors, Bi_2Te_3 and $Bi_{0.3}Sb_{1.7}Te_3$ are taken into account, respectively. The generated mesh contained 10,178 elements, and the Seebeck coefficient is considered to be a function of temperature gradient.

For the heat transfer within phase change modules, the governing equation is

$$\rho C_p \frac{\partial \mathbf{T}}{\partial t} + \rho C_p u \cdot \nabla \mathbf{T} + \nabla \cdot \mathbf{q} = Q \tag{1}$$

where ρ means the mass density, C_p is the heat capacity, and $\mathbf{q}$ is the heat transfer rate, which is defined as a function of thermal conductivity k and temperature gradient as follows:

$$\mathbf{q} = -k\nabla T \tag{2}$$

The density of phase change material (PCM) is expressed as

$$\rho = \theta\rho_{phase1} + (1-\theta)\rho_{phase2} \tag{3}$$

where θ is a fill-factor from 0 to 1. The material parameters used in the modeling are functions of the fill-factor θ as below.

$$C_p = \frac{1}{\rho}\left(\theta\rho_{phase1}C_{p.phase1} + (1-\theta)\rho_{phase2}C_{p.phase2}\right) + L\frac{\partial \alpha_m}{\partial T} \tag{4}$$

$$k = \theta k_{phase1} + (1-\theta)k_{phase2} \tag{5}$$

$$\alpha_m = \frac{1}{2}\frac{(1-\theta)\rho_{phase2} - \theta\rho_{phase1}}{\theta\rho_{phase1} + (1-\theta)\rho_{phase2}} \tag{6}$$

where α_m is the mass coefficient. The external natural convection is considered as the boundary condition.

$$-\mathrm{n} \cdot \mathbf{q} = \mathbf{q_0} \tag{7}$$

where n is the normal vector and $\mathbf{q_0}$ the heat flux by convection. The heat flux depends on the convection heat transfer coefficient ($\mathrm{h_{air}}$) and the temperature difference between the external air and surface.

$$\mathbf{q_0} = \mathrm{h_{air}} \cdot (\mathbf{T_{ext}} - \mathbf{T}) \tag{8}$$

For the Seebeck coefficient, S is expressed as the following:

$$\mathrm{S} = \sqrt{\frac{\mathrm{k}}{\sigma \mathrm{T}}} \tag{9}$$

where σ is the electrical conductivity of the N and P semiconductors. The current is proportional to the Seebeck coefficient S, temperature difference ($\Delta\mathbf{T}$), and resistance of the PN TEGs as follows:

$$\mathrm{I} = \frac{\mathrm{S}\Delta\mathbf{T}}{R} \tag{10}$$

The efficiency of thermoelectric energy conversion is defined as a ratio of the converted energy W to the total latent heat stored energy Q as given below.

$$\eta = \frac{W}{Q} \tag{11}$$

3.4.4. Preparation of PCM composites

Graphene oxide (GO) is synthesized to prepare the graphene aerogel. The modified Hummers' method is adopted in this study [193, 194]. The pre-oxidation is completed by mixing 3 g graphite (mesh size 45~75 μm) and 12 ml sulfuric acid (H_2SO_4). After then, 15g $KMnO_4$ is added into the pre-oxidized graphite and stirred at 350 rpm in an oil bath for three hours. Furthermore, the oxidized graphite emersion is diluted by 700 mL DI water and 20mL H_2O_2 is poured into the mixture, followed by washing with 10 % HCl solution. The filtered oxidized graphite is diluted with DI water to neutralize the graphene oxide (GO) solution by 10,000 rpm centrifugation treatment, and the graphene oxide (GO) powder is obtained by using freeze-dryer for 72 hours.

Graphene aerogel containing graphene nano-platelets (GNPs) is also fabricated by using freeze-drying process. The graphene oxide (GO) powder and graphene nano-platelets (GNPs) with a 2:1 mass ratio are dispersed into the DI water and ultra-sonication is applied for dispersion. After 30 min ultra-sonication treatment, the solution is poured into a 4cm*4cm*0.5cm mold and freeze-dried for 2 to 3 days. Thereafter, 3D porous GNP embedded graphene aerogel is fabricated using hydrazine vapor reduction method. The graphene oxide (GO) aerogels are placed on the sieves and hydrazine solution is poured into the small size of vial bottle, then the system is sealed to achieve the reduction of graphene oxide (GO). The temperature is increased to 120 °C and maintained for 72 hours. Finally, the color of aerogel became black after removing the sealed system, and the reduced graphene oxide (rGO) is successfully fabricated by the hydrazine vapors.

The PCM composites are produced using the vacuum-impregnation method. A large portion of the working materials are gradually infiltrated into the internal pores of graphene aerogel having highly porous structures. Firstly, the pure PEG and 1-TD are placed on the petri dish (diameter: 6cm) respectively, and stored in the vacuum oven at 80 °C. As the pure PEG and 1-TD are fully melted, the vacuum condition is maintained for about 30min to remove the moisture from the liquid PCMs. After that, the manufactured graphene aerogels are directly immersed into the liquid PEG and 1-TD for infiltrating in the internal space under the vacuum state. After solidification at the room temperature for 12 hours, the graphene aerogel filled PEG and 1-TD composites are fabricated completely.

3.4.5. Results and discussion

3.4.5.1. Morphologies of PCM composites

The reduced graphene oxide (rGO) is identified from the color change as shown in **Fig. 3.4.5.** The color of the graphene oxide (GO) is brown, and that of the reduced graphene oxide (rGO) after the hydrazine reduction changed to black (**Fig. 3.4.5a** and **3.4.5b**). To verify the micro-structural reduction of graphene aerogel, the FT-IR result is shown in **Fig. 3.4.5c**. The characteristic peaks of graphene oxide (GO) includes the peaks of carbon and

oxygen functional groups such as C-O stretching vibration peak at 1052 cm^{-1}, C=C peaks at 1617 cm^{-1}, C=O peaks at about the 1718 cm^{-1}, and the O-H stretching vibration peak at the 3397 cm^{-1} [195]. Furthermore, the reduced graphene oxide (rGO) has only the C=C peak at 1594 cm^{-1}, which is significantly different from the results of the graphene oxide (GO). This indicates that the graphene oxide (GO) is completely reduced by the hydrazine treatment. To observe the shape stability of the PCM composites, the images of thermal behavior are captured by using a digital camera. The PCM samples are placed on the hot plate, and then the temperature is increased from 25 °C to 80 °C as shown in **Fig. 3.4.6.** All the PCMs maintained the solid state without any leakage at room temperature. When the temperature is increased to 50 °C, the 1-TD is fully melted, but the PEG retained the solid state with a little leakage. When increasing the temperature up to 80 °C, the PEG is melted, but the PEG and 1-TD composites still remained as the solid state without any leakage. Thus, the 3D porous graphene aerogel could enhance the shape stability of PCMs during the phase transition process. **Fig 3.4.7** shows the SEM images of the internal structure for the graphene aerogel, pure PCM, and PCM composites. The porous structure of the graphene aerogel is shown in **Fig. 3.4.7a**. The porosity allowed the PCM matrix to infiltrate into the aerogel [152]. The pure PEG and PEG composite are found to have similar micro-structure, which implied successful infiltration of liquid PEG into the pore of the graphene aerogel (**Fig. 3.4.7b** and **3.4.7c**). Unlike the pure PEG, the PEG composite showed wrinkled surface structure due to the skeleton of graphene aerogel [150]. The GNP embedded graphene aerogel could retain intrinsic properties without significant weight loss. The morphologies of the pure 1-TD, and 1-TD composite are shown in **Fig. 3.4.7d** and **3.4.7e**. The structural characteristics are observed by using XRD as shown in **Fig. 3.4.8.** In this figure, the intrinsic peaks of PEG are found at 2θ = 19.12°, and 2θ = 23.24°, which are similar to those of the PEG composite, 2θ = 19.10 ° and 2θ = 23.25°, respectively. The peaks of the 1-TD appeared at 2θ = 21.32°, and 2θ = 24.14°. It is inferred from the typical peaks of PEG and 1-TD that the PCM composites retained the initial crystal structures. The XRD results indicated that the PCM composites had the same structural characteristics as that of pure PCM materials.

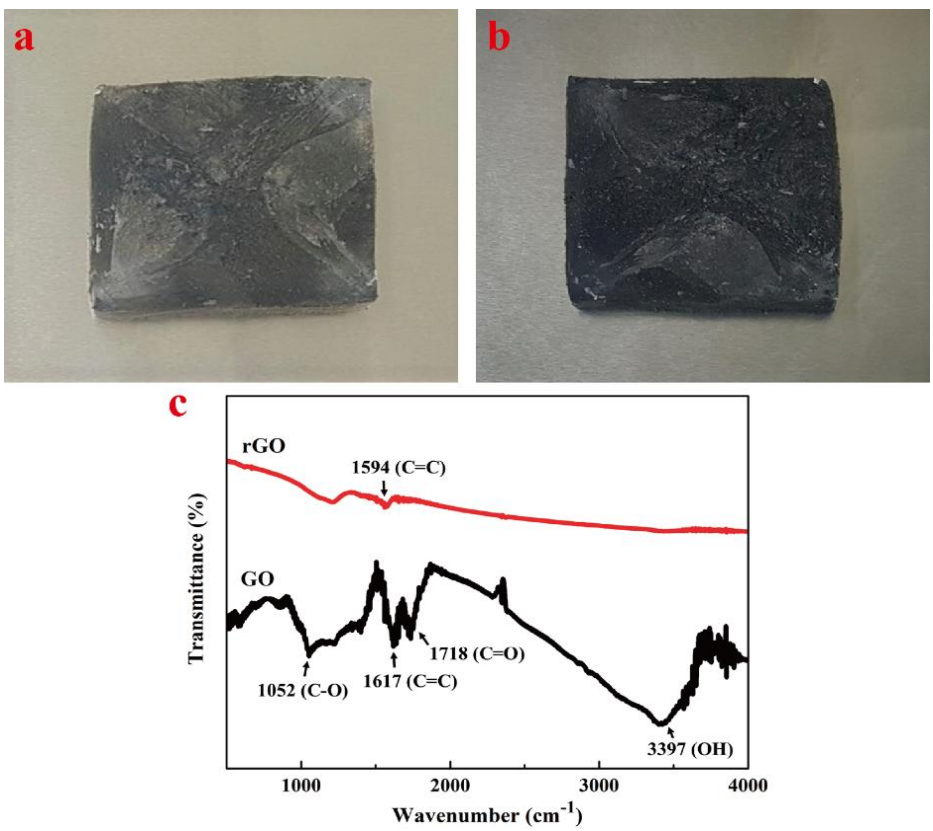

Figure 3.4.5. The 4cm*4cm size of (a) graphene oxide (GO) aerogel, (b) reduced graphene oxide (rGO) aerogel, and (c) FT-IR patterns of both graphene oxide (GO) and reduced graphene oxide (rGO).

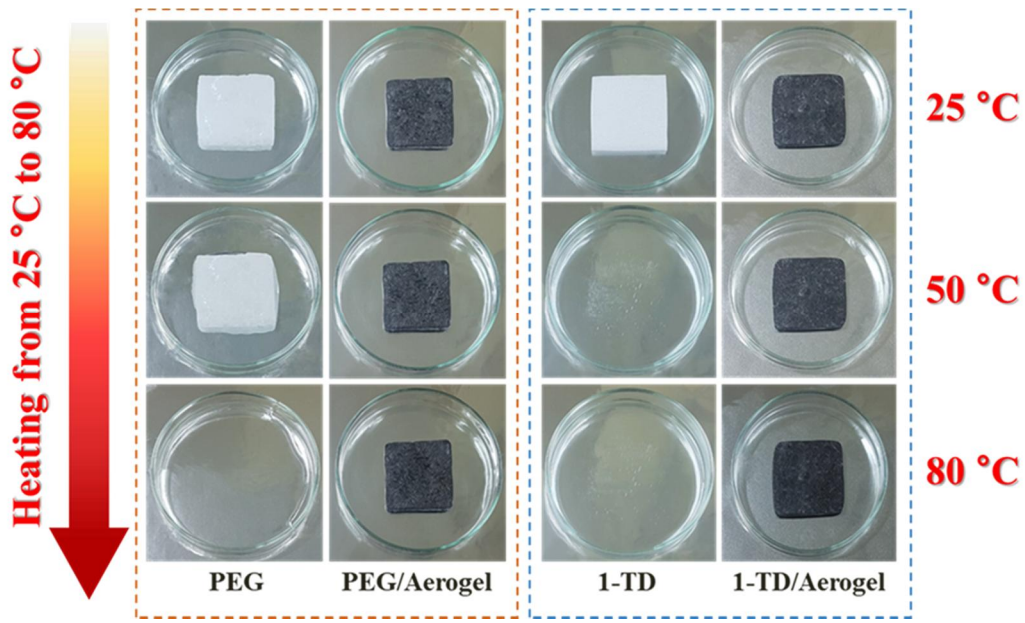

Figure 3.4.6. Form stable images of PEG, PEG composite, 1-TD, and 1-TD composite.

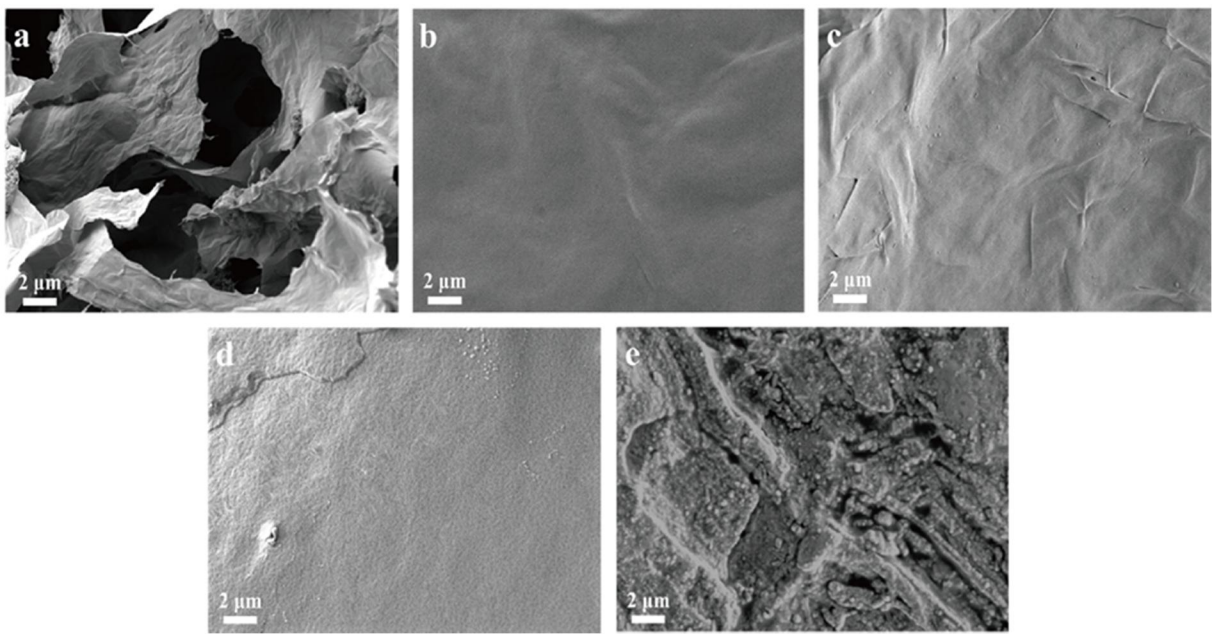

Figure 3.4.7. SEM images of (a) graphene/GNP aerogel, (b) pure PEG, (c) PEG/aerogel composite, (d) pure 1-TD, and (e) 1-TD/aerogel composite.

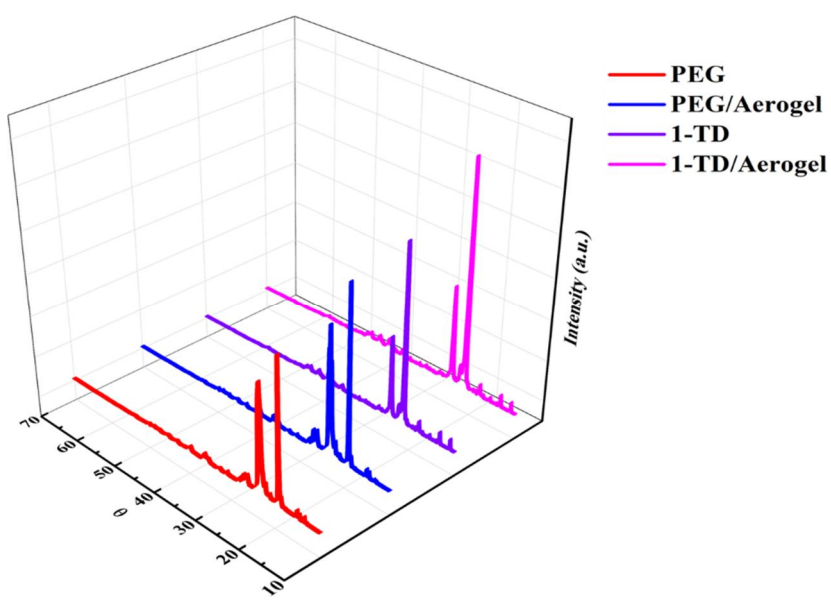

Figure 3.4.8. XRD patterns of PEG, PEG composite, 1-TD, and 1-TD composite.

3.4.5.2. Output current and DSC measurement

The induced currents are measured during heating and cooling processes as shown in **Fig. 3.4.9.** In this study, two kinds of energy harvesting devices are prepared. For the first device, the PEG composite is located on the hot side of the PN TEG, and the 1-TD composite is placed on the cold side since the PEG composite normally has higher melting temperature than the 1-TD composite. For the second device, the locations of PCM composites are switched in order to take advantage of the reversal of the temperature difference. The PN TEG combined with the PCM composites are placed in the heating chamber, and the temperature is increased from 25 °C to 80 °C. The obtained current during the heating process is shown in **Fig. 3.4.9a**. The 1-TD composite initially experienced the melting transition and the temperature of the PEG composite still increased continuously. At this moment, the temperature difference is generated in the first device of harvesting system, and the electric current induced by the thermoelectric conversion is measured. It is found from the heating process that the maximum value is around 8.62 mA at 1,270 s when the largest temperature difference is observed. The induced current is gradually decreased until 2,200 s. Once the temperature of the 1-TD composite became higher than that of the PEG composite, the second device of harvesting system began to work during the rest of heating process. The maximum value of the second current is around 6.14 mA at 3,250 s, and the current is gradually decreased until 5,000 s. The energy released during cooling process is measured by natural convection method. The peak current is generally increased with high cooling speed as presented in **Fig. 3.4.9b**. The maximum peak values of the first and the second harvesting system are 7.55 mA at 388 s and 5.53 mA at 1,290 s, respectively. The duration of the cooling process is shorter than that of the heating process due to stored thermal energy.

An LED bulb is connected to the PN TEG to demonstrate the practical possibility of the energy harvesting system. Maximum power of the harvesting system is measured for the heating and cooling processes. The output power results are shown in **Fig. 3.4.10.** The

first and second maximum values of the electric powers from the heating process are approximately 321 μW and 173 μW, respectively as shown in **Fig. 3.4.10a**. Furthermore, output power results from the cooling process are given in **Fig. 3.4.10b** and the maximum peak value is 246 μW, and 132 μW. Based on the power graph, the potential is not high enough to turn on the LED bulb. Thus, the LTC 3108 voltage converter is integrated to the device to amplify the output power (**Fig. 3.4.10c**). **Fig. 3.4.9c** shows that the LED is turned on in the 1st and 2nd processes. The intensity of the LED is decreased from the 1st peak to the 2nd peak due to the temperature difference [160, 196].

The latent heat and the phase transition temperature of the PCMs are measured by utilizing DSC measurement. The melting and cooling peaks of the pure PCM, and PCM composites are shown in **Fig. 3.4.11**. The phase transition temperatures and enthalpy of heating and cooling process ($\Delta H_m/\Delta H_c$) for the PEG and the 1-TD are listed in **Table 3.4.1** and **Table 3.4.2**, respectively. The phase transition temperature of the pure PEG changed from 50.54 °C to 68.53 °C with a melting point (T_m) of 65.70 °C, and the latent heat (ΔH_m) is 180.41 J/g. In the cooling process, the crystallization temperature changed from 43.77 °C to 33.21 °C with a crystallization point (T_c) of 38.03 °C, and a crystallization enthalpy (ΔH_c) of 164.67 J/g is obtained. A slight variation of the phase transition temperature and enthalpy is found for PCM composites when compared with those of the pure PEG, which indicated a little shifting of the pristine peaks. The enthalpy of the PEG composite decreased because of addition of the supporting materials. The phase transition temperature of the 1-TD composite varied from 36.78 °C to 44.49 °C. A little peak shifting is detected when the graphene aerogel is infiltrated. The heating and cooling enthalpies of the 1-TD composites decreased slightly due to the supporting material. In addition, the **Fig. 3.4.12** shows the thermal stability of PCM composites by measuring the DSC cycling, and the latent heat and melting/crystallization peaks after 100 cycles are listed in **Table 3.4.3**. It is indicated that the PEG and 1-TD composites maintain high thermal stability and reliability without any heat loss and even sustain their chemical structures (**Fig. 3.4.12c**, and **3.4.12d**) during the thermal cycling. Since the latent heat of the PCM composite is almost equal to that of the pure PCM, the PCM composite can absorb or release sufficiently large amount of thermal energy for the thermoelectric conversion system.

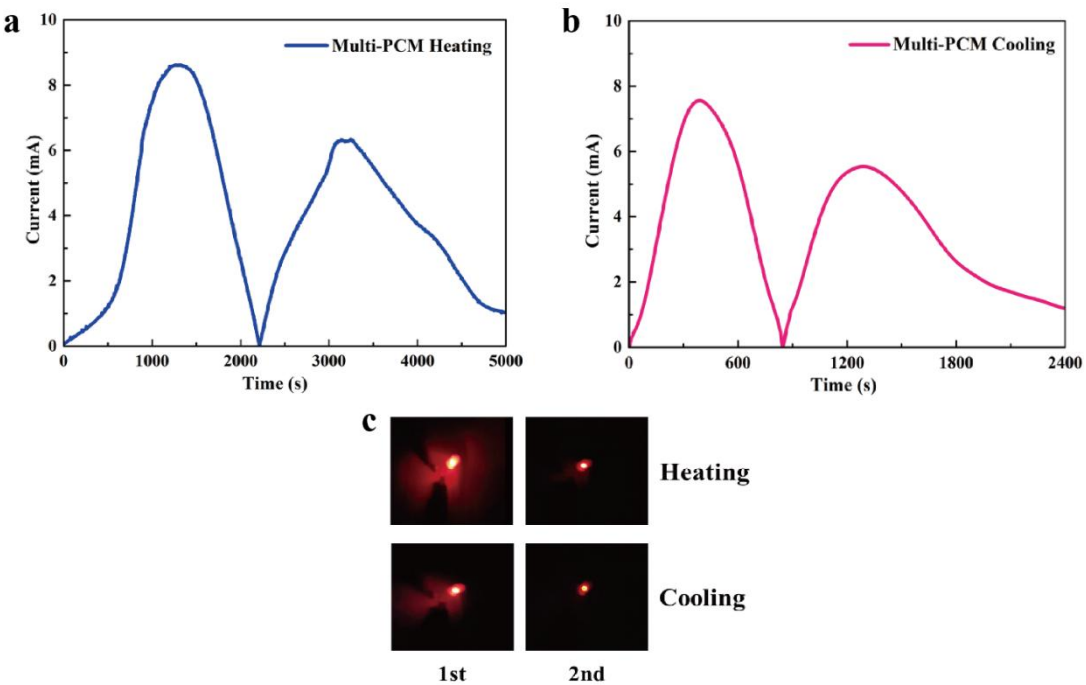

Figure 3.4.9. Experimental results of the multiple energy harvesting system: (a) electric current during the heating process, (b) electric current during the cooling process, (c) image of the LED bulb lit by using the harvested electric energy in the heating and cooling processes.

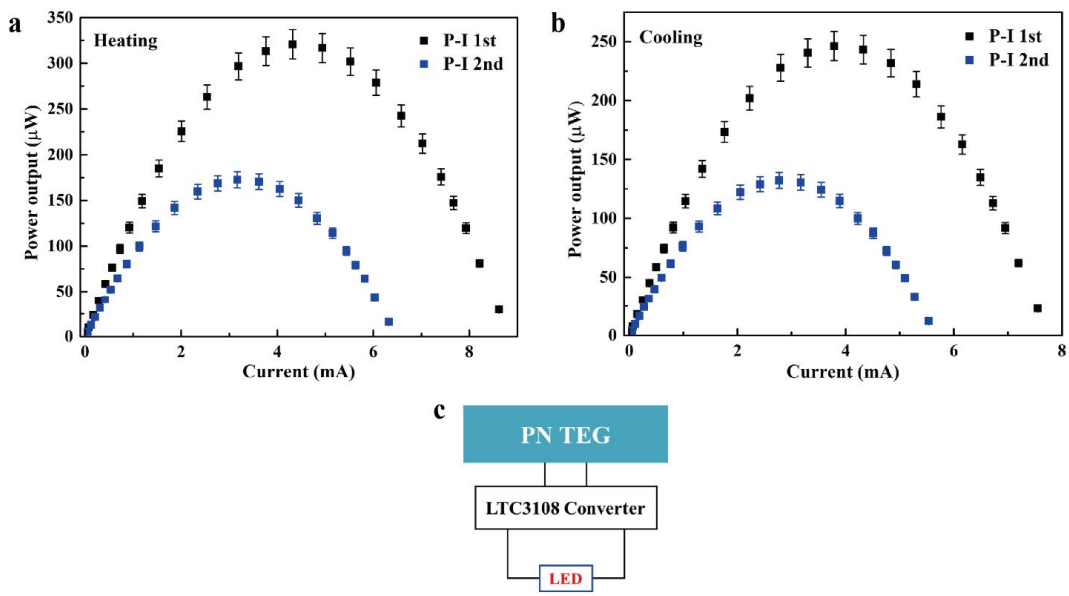

Figure 3.4.10. Total power output curves on (a) heating process, (b) cooling process, (c) The PN TEG and LED setup.

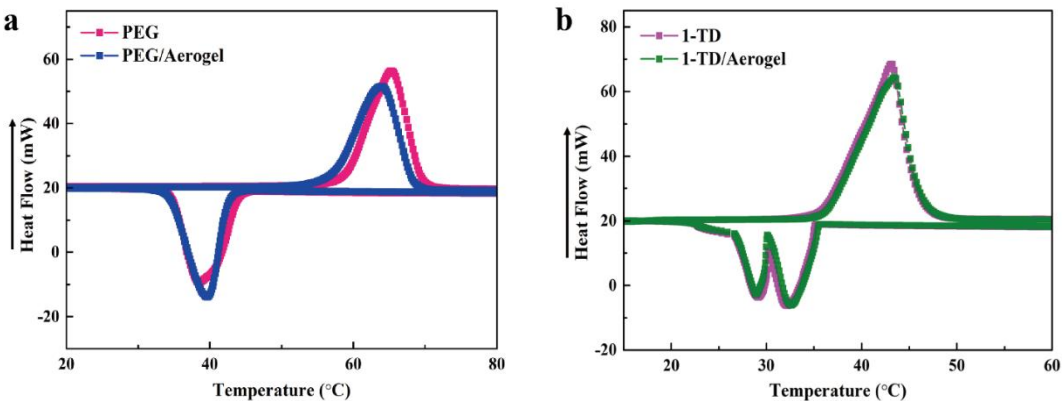

Figure 3.4.11. DSC data of (a) pure PEG and PEG composite and (b) pure 1-TD and 1-TD composite.

Table 3.4.1. DSC characteristics of pure PEG and PEG composite.

Samples	T_{mo}(°C)	T_{me}(°C)	T_{mp}(°C)	ΔH_m(J/g)	T_{co}(°C)	T_{ce}(°C)	T_{cp}(°C)	ΔH_c(J/g)
PEG	50.54	68.53	65.70	180.41	43.77	33.21	38.03	164.67
PEG/Aerogel	50.09	67.30	63.86	179.79	43.78	33.86	39.64	164.28

Table 3.4.2. DSC characteristics of pure 1-TD and 1-TD composite.

Samples	T_{mo}(°C)	T_{me}(°C)	T_{mp}(°C)	ΔH_m(J/g)	T_{co}(°C)	T_{ce}(°C)	T_{cp}(°C)	ΔH_c(J/g)
1-TD	36.78	44.49	41.90	223.25	35.30	20.61	30.02	211.41
1-TD/Aerogel	36.21	45.66	42.51	222.52	35.59	20.75	30.10	210.48

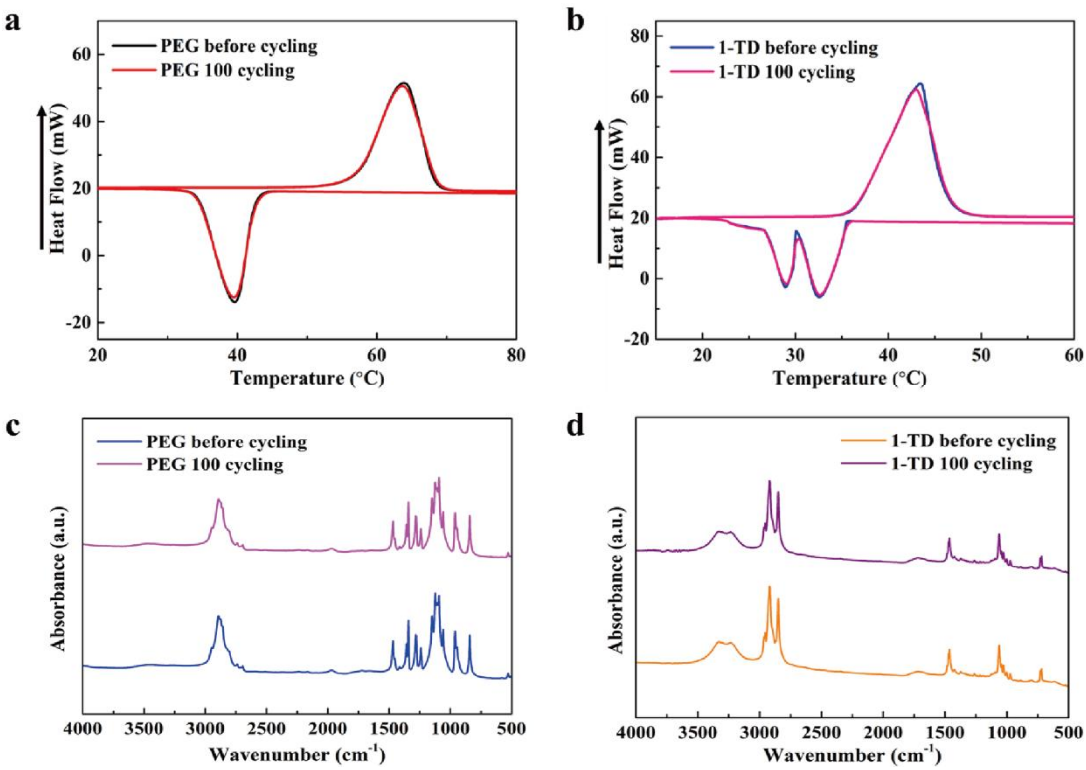

Figure 3.4.12. DSC cycling peaks of (a) PEG composite, (b) 1-TD composite, the FTIR in (c) PEG composites, and (d) 1-TD composites.

Table 3.4.3. DSC characteristics of PEG and 1-TD composites after 100 cycling.

Samples	T_{mp}(°C)	ΔH_m(J/g)	T_{cp}(°C)	ΔH_c(J/g)
PEG cycling	63.24	179.31	39.56	164.11
1-TD cycling	42.08	221.76	30.18	210.26

3.4.5.3. Numerical analysis of energy harvesting

Temperature distribution in the energy harvesting system is calculated from numerical simulation. For the heating process, the temperature is varied from 25 °C to 80 °C. The multiple peaks are shown in **Fig. 3.4.13a**. Since the 1-TD composite had phase transition earlier than the PEG composite, the temperature difference is initially increased over time. The 1-TD composites stayed in the phase transition state, while the temperature of the PEG composite is increased gradually. After that, the temperature difference is reduced, and even reversed. **Fig 3.4.13b** shows the cooling behavior of the composites, which is similar to the heating behavior. The temperature difference peaks of the heating process are 12 °C at 1,600 s and 8 °C at 3,400 s as shown in **Fig. 3.4.13c**. The temperature difference during cooling is demonstrated with respect to time in **Fig. 3.4.13d**. The temperature difference peaks are 11 °C at 400 s and 7 °C at 1,350 s during cooling. The temperature difference during both the heating and cooling processes can generate the electrical output current induced by the Seebeck effect. Comparison between the measured and the calculated peak values of the electric current is presented in **Fig. 3.4.14**. The numerically calculated current peaks coincided with the experimental results (**Fig. 3.4.14a**). The predicted peaks are obtained at 2,200 s with approximately same maximum value in the first harvesting process, and the temperature difference is reversed between 1-TD and PEG composites for expanded period of time. Similar to the heating process, the calculated simulation is in good agreement with the experimental results in **Fig. 3.4.14b**, and the calculated current peak is increased rapidly due to the high cooling speed. The first stage of energy harvesting is continued for 900 s and agreed well with the experimental results in the period of phase transition process. In addition, the thermoelectric energy conversion efficiency is shown in **Fig. 3.4.14c**. The calculated efficiency of heating and cooling processes is 56.55 % and 32.38 %, respectively. The efficiency of the cooling process is still lower than the energy efficiency for heating due

to the energy loss in air. The numerical simulation demonstrated that the energy harvesting devices could be applied to solar energy and heat recycling areas.

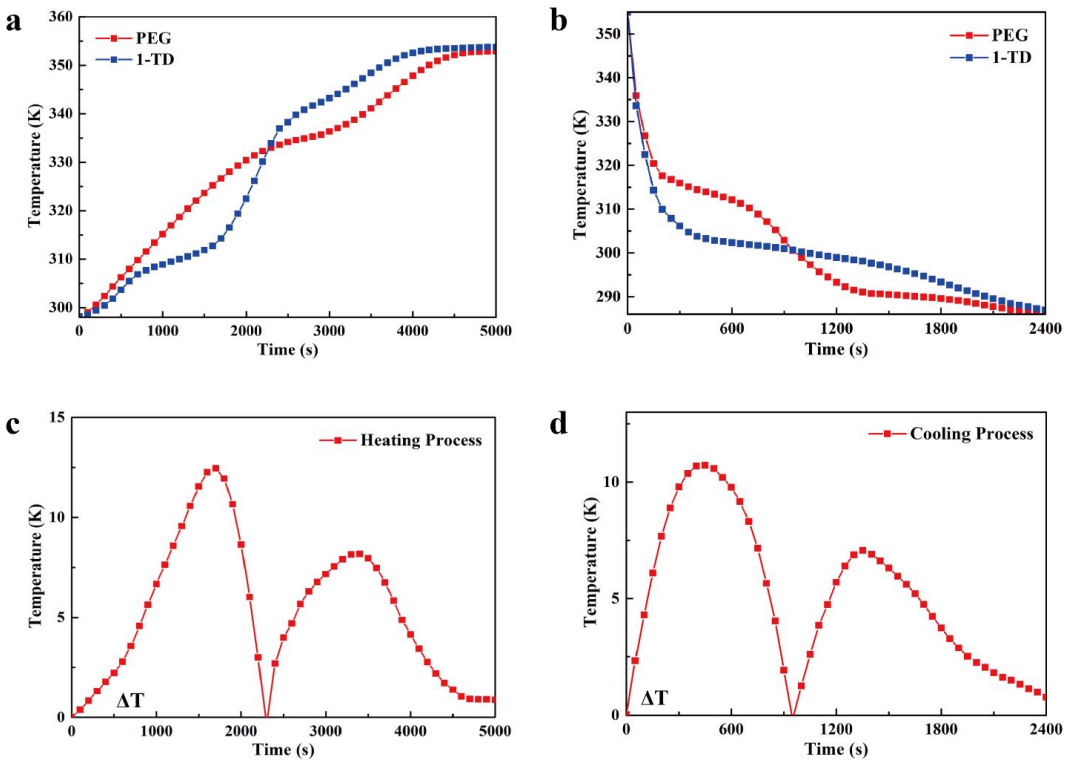

Figure 3.4.13. Simulation results of the multiple energy harvesting system (a) heating temperature profiles, (b) cooling temperature profiles, (c) temperature difference in the heating process, and (d) temperature difference in the cooling process.

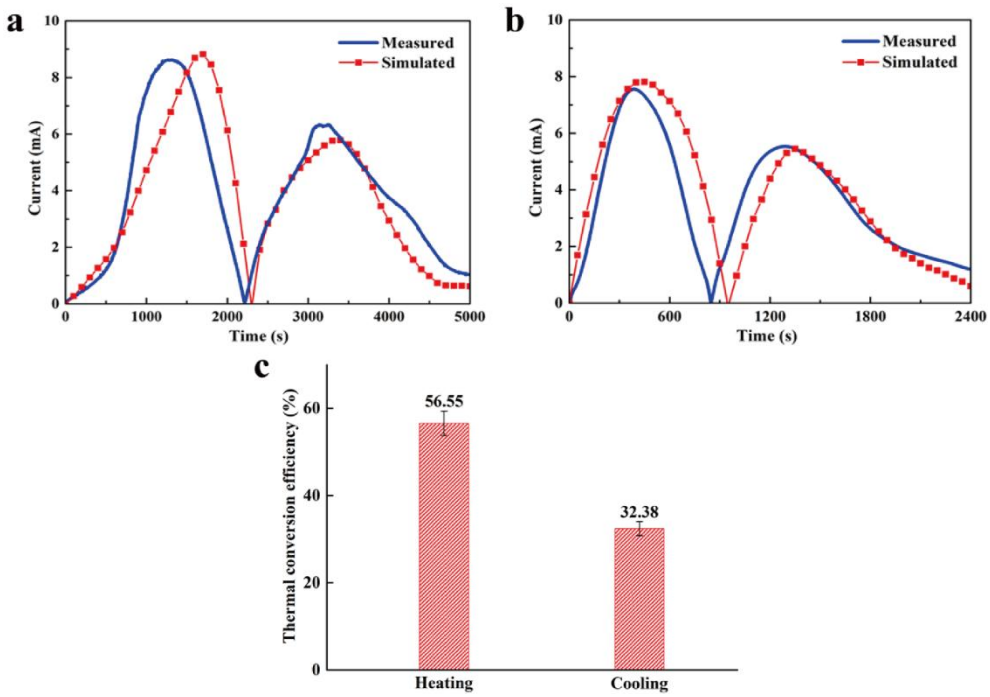

Figure 3.4.14. Comparison between experimental with simulation results: (a) heating electrical current peaks, (b) cooling electrical current peaks, and (c) thermoelectric energy conversion efficiency in the heating and cooling processes.

3.4.6. Conclusions

In this study, we exploited a multiple energy harvesting system that adopted the reversed temperature difference between phase change materials (PCMs). It consisted of the PEG and the 1-TD composites for generation of thermoelectric energy with PN TEGs. It is shown that the 3D porous graphene aerogel enhanced the shape stability and prevented leakage during the phase transition process. The PEG and 1-TD composites had nearly isothermal profiles owing to the large latent heat, and thereby generating a large temperature difference between the two sides of PN TEGs. By employing two different setups of energy harvesting system, additional current induced by the reversed temperature difference could be obtained during the heating and cooling processes. The maximum current peak is 8.62 mA at 1,270 s, 6.14 mA at 3,250 s during the whole heating period and 7.55 mA at 388 s, 5.53 mA at 1,290 s during the natural cooling process. Compared with the single energy harvesting system, the multiple energy harvesting system had relatively high energy efficiency and large amount of energy during the phase change of materials because of the temperature reversal. It is proved that the measured electric energy is large enough to operate an electric gadget, i.e., an LED bulb. The numerical simulation results are in coincident with the experimental results, and we anticipate that this study will contribute to advanced applications for renewable multiple energy harvesting based on the thermoelectric energy conversions.

3.5. GNP fillers affecting the rate of phase transitions

3.5.1. Introduction

With the passage of time, solar and heat energy is more and more attracted in the face of environmental pollution and energy crisis on the Earth. Hence, development of a renewable high efficient energy device is imperative in the human life and plenty of researches have been reported in recent years [180, 184, 186, 197, 198]. Among others, a thermoelectric energy conversion system has the most effective energy transformation and generally replaced to the fossil fuels [199]. Owing to the high latent heat, nearly isothermal in the phase transition field, excellent thermal liability, and abundant resources; the phase change materials (PCMs) are generally employed as working materials in the thermal energy storage (TES) system [124, 167, 168, 200, 201]. The thermoelectric energy harvesting system is consist of these phase change materials (PCMs) with N and P type thermoelectric generator (PN TEG) to obtain the electrical current and close to the application of energy harvesting.

Unlike the conventional thermal energy storage materials, the leakage is a large problem for phase change materials (PCMs) during the phase transition process that need some supporting materials to sustain the dimensional stabilities [202]. In general, the feasible manner is to manufacture the microencapsulated PCM composites from their pure intrinsic structures. Herein, some supporting materials are selected to encapsulate the pure phase change materials (PCMs) and prevent the leakage from melting states [146, 203]. The polyaniline (PANI) and urea-formaldehyde (UF) series are generally utilized as supporting encapsulation materials which can construct a core-shell like PCM composite and maintain their solid state during the phase transition process [105]. However, the core-shell like PCM composite causes a high reduction of latent heat under the melting and crystallization process when the supporting material is partially replaced the contents of phase change materials (PCMs) and ultimately restrict the high energy storage applications [204]. Therefore, a supporting material which can fill up most of working material with low content is commonly mentioned in the recent research.

As an advanced supporting material, the graphene aerogel with 3D porous internal

structure is appropriate to fabricate the form stable phase change materials (PCMs) and has been widely used as a new kind of supporting material which can stop leakage from melting process [205]. In spite of complicated internal structure, the graphene aerogel can absorb more contents of pure PCMs than that of conventional shell materials due to the large surface area and high porosity. Furthermore, the graphene aerogel has excellent mechanical property, thermal reliability, and chemical stability that the graphene aerogel based PCM composites are able to store a large amount of heat energy and subsequently apply to the thermoelectric energy conversions [147]. It is crucial for the PCM composites behave a high thermal conductivity to improve the energy conversion efficiency. Basically, embedding a filler such as graphene nano-platelet (GNP) and carbon nanotube (CNT) enhances both shape stability and thermal conductivity, and the contents of graphene nano-platelet (GNP) give rise to the enhancement of thermal conductivity[192]. Thus, the PCM composites with different contents of graphene nano-platelet (GNP) exhibit a series of thermal conductivity and effect on the thermoelectric energy conversion and storage [68].

For about the thermoelectric energy harvesting system, it has shown a great value by combining the PCM composites with PN TEGs [68]. From the PN TEG, connecting the PCM composites to construct the electric circuit are effectively contributed to the energy harvesting applications [206]. The spontaneous thermoelectric energy conversion is generated under the temperature difference between the two sides of PN TEG. The hot side which has higher temperature excites electron to move forward to the opposite side that appears the Seebeck effect in the circuit [207]. In other words, the different PCMs placed on each side of PN TEG are regarded as an electric power generator under the phase transition process. The temperature difference is exhibited due to the variation of isothermal field and the PN TEG energy harvester produces the electrical current in the circuit. When the cold side temperature is higher than that of hot sides, the electron movement is normally held up due to the energy barrier. To improve the thermoelectric energy conversion efficiency, multiple PN TEG energy harvesting system is constructed to collect the electrical current and measure the thermoelectric conversion efficiencies.

In this work, two phase change materials of polyethylene glycol (PEG) and 1-tetradecanol (1-TD) are combined with the PN TEGs to fabricate a sustainable energy

harvesting system and measure the electrical current on both of heating and cooling processes. The pure PCMs are infiltrated into the internal structure of graphene aerogel to compose form stable working materials and detect the arriving rates of harvesting field with the different GNP ratios. The optimum brightness time of LED lamp is subsequently observed during the phase transition process. In addition, utilizing a finite element method (FEM) to numerically simulate the thermoelectric energy conversion that provide an adjacent trend to the experimental result.

3.5.2. Energy harvesting system

The principle schematic of energy harvesting system is shown in **Fig. 3.5.1**. Based on the Seebeck effect, the PEG and 1-TD PCM composites with different contents of graphene nano-platelet (GNP) are placed on the PN TEGs. These connection could generate the electron movement from hot side to cold side under the temperature difference. As a heating process, the 1-TD composite experiences the melting transition field while the PEG composite maintains increasing its temperature due to the higher melting point than that of 1-TD composite. As development of the temperature difference, electrons in the N type semiconductor are excited to the hot side and subsequently moved to the P type of thermoelectric device. Hence, the system produces to the electrical current in the closed circuit. After the temperature of 1-TD composite is exceeded the opposite PEG composite, the second energy harvesting system starts to experience the energy conversion to continuously generate the electrical current. The PCM composites based PN TEG energy harvesting system is supposed to obtain the working time with different ratios of graphene nano-platelet (GNP). Increasing the embedded material is expected to increase the rate of arriving phase transition time and contribute to the efficiencies of thermoelectric energy conversions during the phase transition process.

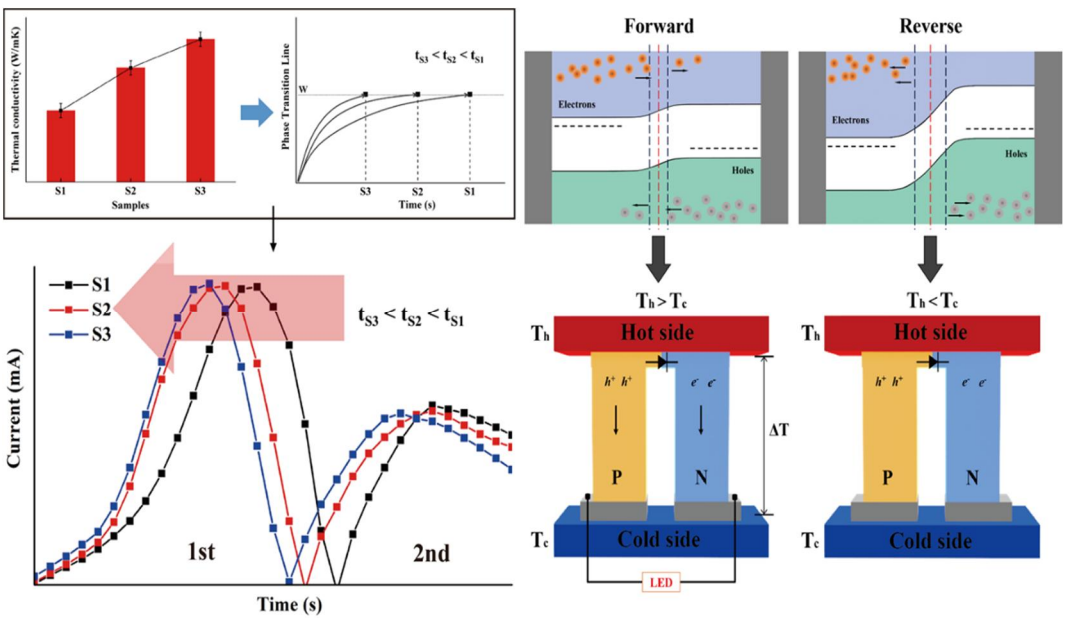

Figure 3.5.1. Schematic illustration in thermoelectric energy harvesting system. The system is composed of PCM composites with different thermal behaviors. The rapidly approach to the phase transition field under an increase of these thermal conductivities. The PCM composites are placed on the sides of each PN TEG and confirmed the electrical energy on the melting and cooling process.

3.5.3. Numerical analysis

Estimating the temperature gradient between the PEG and 1-TD composites, the heating and cooling temperature peaks are numerically calculated by using a finite element method (FEM), COMSOL Multiphysics commercial software. The geometry is consist of PEG composite, N and P type semiconductors, copper, and 1-TD composite in the 1st device of system as the opposite position of PCM composites in the 2nd device. The requirement parameters are density of each PCM composite, heat capacity, latent heat (ΔH), thermal conductivity with different embedding ratios, and phase transition temperature (T_m, T_c) of PCM composites. The copper is utilized to combine the N and P type semiconductor with PCM composites. For the N and P type semiconductors are designated Bi_2Te_3, $Bi_{0.3}Sb_{1.7}Te_3$, respectively and the Seebeck coefficient is considered to the temperature during the phase transition process. The elements of total mesh in this simulation is 10,178.

The governing equation within heat transfer is defined as:

$$\rho C_p \frac{\partial \mathbf{T}}{\partial t} + \rho C_p u \cdot \nabla \mathbf{T} + \nabla \cdot \mathbf{q} = Q \qquad \text{Eqn (1)}$$

where the parameter ρ is mass density and C_p is heat capacity. The heat transfer rate $\mathbf{q}$ is followed as a function of thermal conductivity k and temperature of employed materials:

$$\mathbf{q} = -k\nabla T \qquad \text{Eqn (2)}$$

The specific density equation within phase change material (PCM) is defined as:

$$\rho = \theta\rho_{phase1} + (1-\theta)\rho_{phase2} \qquad \text{Eqn (3)}$$

Involving the ratio of phase 1 to phase 2. Furthermore, the fill-factor θ is related to the parameters (C_p, k, and α_m) and calculated as below:

$$C_p = \frac{1}{\rho}\left(\theta\rho_{phase1}C_{p.phase1} + (1-\theta)\rho_{phase2}C_{p.phase2}\right) + L\frac{\partial \alpha_m}{\partial T} \qquad \text{Eqn (4)}$$

$$k = \theta k_{phase1} + (1-\theta)k_{phase2} \qquad \text{Eqn (5)}$$

$$\alpha_m = \frac{1}{2}\frac{(1-\theta)\rho_{phase2} - \theta\rho_{phase1}}{\theta\rho_{phase1} + (1-\theta)\rho_{phase2}} \quad \text{Eqn (6)}$$

In the former equations, α_m means the mass coefficient in which indicates the mass density during the phase transitions. The boundary condition is assumed under the external natural convections as followed:

$$-\mathrm{n} \cdot \mathbf{q} = \mathbf{q_0} \quad \text{Eqn (7),}$$

Initially the normal vector n, and the convection of heat flux $\mathbf{q_0}$ are mentioned. The heat transfer coefficient ($\mathrm{h_{air}}$) and external temperature are proportional to the heat flux. It means:

$$\mathbf{q_0} = \mathrm{h_{air}} \cdot (\mathbf{T_{ext}} - \mathbf{T}) \quad \text{Eqn (8)}$$

Integrating the temperature gradients under the heating and cooling process, the Seebeck coefficient S is utilized to calculate the electrical result and defined as:

$$\mathrm{S} = \sqrt{\frac{\mathrm{k}}{\sigma \mathrm{T}}} \quad \text{Eqn (9)}$$

From the equation, σ means the electrical conductivity of the N and P semiconductors, the nominal result of current is a function of the Seebeck coefficient S, temperature difference ($\Delta\mathbf{T}$), and the resistance of N and P type semiconductors (R) as below:

$$\mathrm{I} = \frac{\mathrm{S}\Delta\mathbf{T}}{R} \quad \text{Eqn (10)}$$

The thermoelectric energy conversion efficiency is determined to the ratio of converted energy W and the total stored energy Q as followed:

$$\eta = \frac{\mathrm{W}}{\mathrm{Q}} \quad \text{Eqn (11)}$$

3.5.4. Preparation of PCM composites

The first step is synthesized the graphene oxide (GO) by utilizing modified Hummers' method. 3.0 g graphite is mixed to sulfuric acid (H_2SO_4) for pre-oxidation. Then, added 15 g $KMnO_4$ into the pre-oxidized graphite with stirring for 2 hours under the oil bath (35 °C). After that, poured H_2O_2 into the diluted mixture to remove excess of $KMnO_4$, and washing with 10 % HCl solution to neutralize the graphene oxide solution and obtained the graphene oxide powder by freeze-drying method. For about graphene aerogel embedded graphene nano-platelet (GNP) is fabricated by a freeze-drying process. The graphene oxide (GO) powder and GNP particles are individually dispersed in distilled (DI) water under the ultra-sonication with 2:1, 1:1, and 1:2 mass ratios. Poured the suspension into a mold with the dimension of 4cm*4cm*0.5cm by freeze-drying method. Finally, prepared the 3D porous reduced graphene oxide/GNP aerogel by using a hydrazine vapor reduction method.

Fabricating the PCM composites are utilizing a vacuum-impregnation method. The pure PCMs are melted to infiltrate into the internal structure of supporting material. Before that, the PEG and 1-TD are placed into the vacuum oven at 80 °C and fully melted. The graphene aerogels are immersed in the liquid PCMs for over 6 hours in the vacuum state. After cooling to the room temperature for solidify the samples, the PEG and 1-TD composites are successfully fabricated and constructed the multiple energy harvesting system with PN TEGs. The PCM samples with different mass ratios between graphene oxide (GO) and graphene nano-platelet (GNP) are labelled 2:1 ratio PEG composite, 1:1 ratio PEG composite, and 1:2 ratio PEG composite respectively. For the other working material 1-TD is equally noted as 2:1 ratio 1-TD composite, 1:1 ratio 1-TD composite, and 1:2 ratio 1-TD composite. The synthesis of PCM composite is given by the **Fig. 3.5.2**. The graphene oxide (GO) powder and graphene nano-platelet (GNP) particles are dispersed well in the aqueous solution and fabricated the GO/GNP aerogel after the freeze-drying method as shown in **Fig. 3.5.3**.

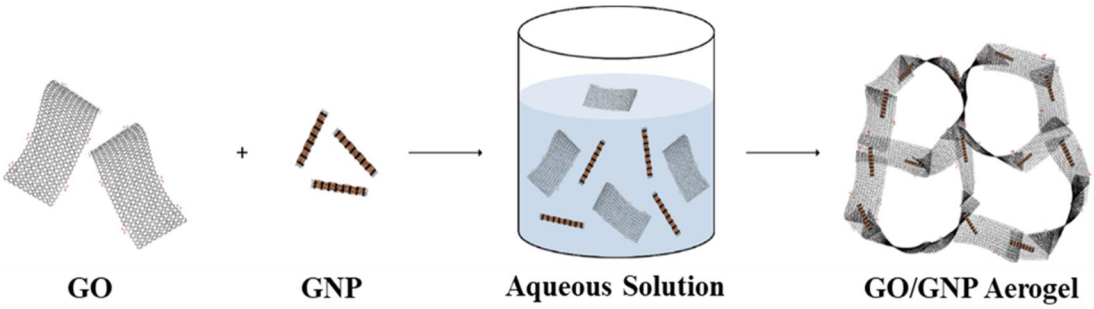

Figure 3.5.2. Schematic of GO/GNP aerogel fabricaton process.

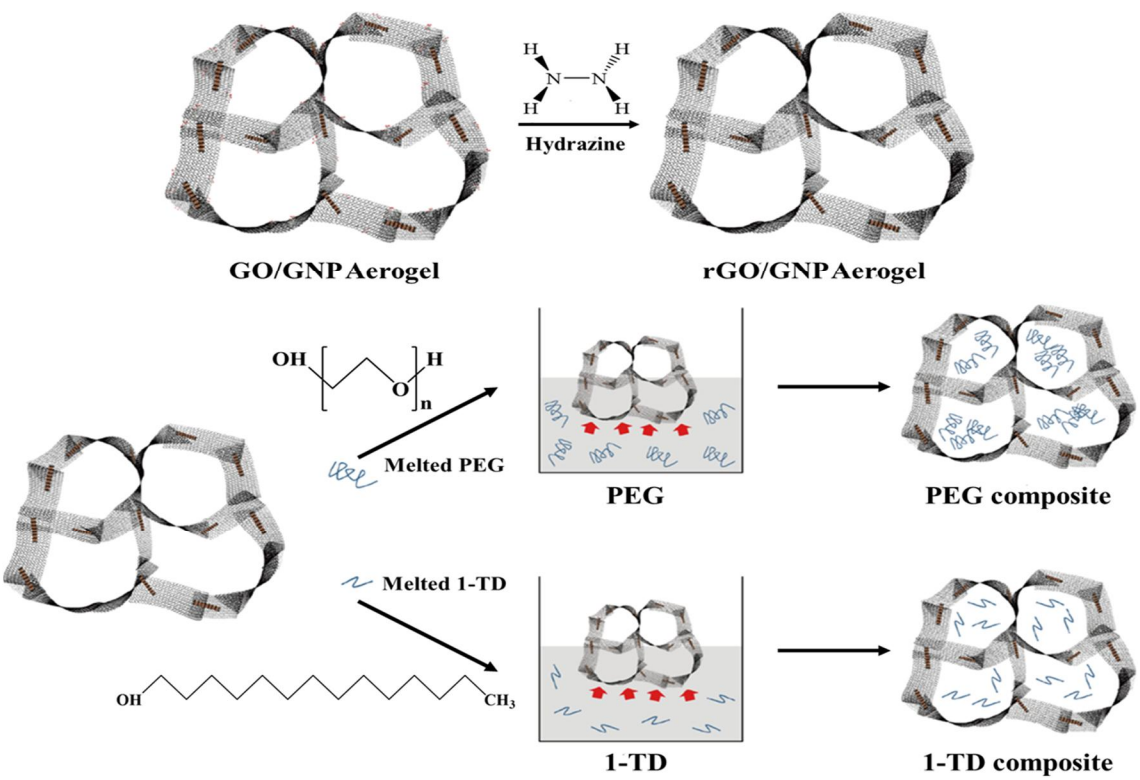

Figure 3.5.3. Fabrication of PCM composites. The GO/GNP aereogel is reduced well under the hydrazine vapor method. The rGO/GNP aerogel is gradually emerged into teh melted PEG and 1-TD to construct two different form stable PCM composites.

3.5.5. Results and discussion

3.5.5.1. Morphologies of graphene aerogel

To confirm the dispersion under the aqueous solution, the Zeta potential result is completely obtained and shown in **Fig. 3.5.4**, the dispersed ability is changed on the range of pH value. The absolute value over 30mV indicates that both of graphene oxide (GO) and graphene nano-platelet (GNP) are well easily dispersed in the DI water. The comparison at different mass ratios are implied in **Fig. 3.5.4b**, the solution pH is approached at 5.23 and the results of Zeta potentials are absolutely 48.7, 47.7, and 44.8 respectively. According to the Zeta potential, the embedded graphene nano-platelet (GNP) has an excellent dispersion ability under the GO solution which can construct a homogeneous graphene aerogels. The structural dimension of manufactured graphene oxide (GO) is confirmed by the TEM and AFM images as shown in **Fig. 3.5.5**. It is indicated that the graphene oxide (GO) has successfully produced from the result of TEM image and the average thickness is close to the 1.06 nm which is agree with the honeycomb lay structure of graphene powder. The graphene oxide (GO) average aspect ratio is 860.99 and effectively used for fabricating the graphene aerogel. To identify the reduced graphene oxide (rGO) with various graphene nano-platelet (GNP), **Fig. 3.5.6** shows the color changes during the graphene aerogels. In this figure, the brown colors are obviously disappeared and detected the black surface of each structure. In addition, the average surface area of graphene aerogels are obtained by the BET measurement as shown in **Fig. 3.5.7**, and the results are listed in **Table 3.5.1**. The peaks from 2:1 ratio to final 1:2 become slightly shift and well illustrate the internal pore size of each graphene aerogel is similar and infiltrate most of pure PCMs into the internal volume space. The pore diameter with average pore volume of each graphene aerogel is concentrated on the range of 0 ~ 10nm and obtained the 3D microporous network structures among these supporting materials. In order to demonstrate the reduced graphene oxide (rGO), the FT-IR results are entirely shown in **Fig. 3.5.8**. From the combination of graphene oxide (GO) and graphene nano-platelet (GNP) are illustrated in **Fig. 3.5.8a**, and obtained the typical peaks in each material. As embedding the different mass ratios of GNPs into the GO

solution, the peaks are slightly shifted within no changes in **Fig. 3.5.8b**. To determine the reduction peaks in **Fig. 3.5.8c**, the stretching vibration peak of O-H at 3401cm^{-1}, C=O peaks around 1720cm^{-1}, and the C-O stretching vibration peak at the 1054cm^{-1} are completely disappeared and only remained the C=C (1682cm^{-1}) peaks. Based on the FT-IR graph, the graphene oxide (GO) has successfully reduced by the hydrazine gas and no any chemical reaction with the embedding graphene nano-platelet (GNP). The **Fig. 3.5.9** shows the porosity of graphene aerogel with various ratios and the weight percent after infiltrating the PEG and 1-TD into the supporting materials. The porosity (**Fig. 3.5.9a**) is slightly decreased as increasing the contents of graphene nano-platelet (GNP) and the results data shows in **Table 3.5.2**. All graphene aerogels sustain high porosity in which can fill up plenty of working materials. For about the PCM composites, the PEG and 1-TD weight percentage among the different ratios are shown in **Fig. 3.5.9b**. The **Table 3.5.3** shows the weight percent in each sample and indicates a few decrease in the PCM composites. From these figures, the pure PCMs are fully occupied into the graphene aerogel and maintaining the pristine properties under the phase transition process.

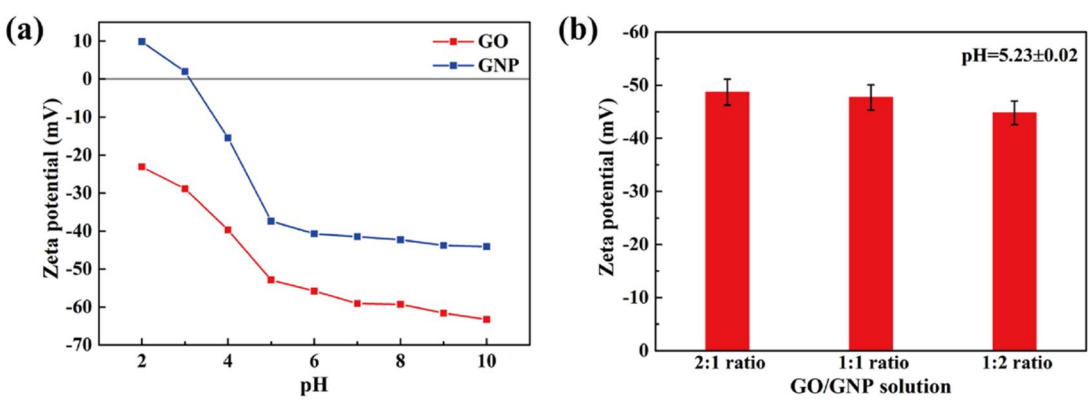

Figure 3.5.4. The Zeta potential value in (a) graphene oxide (GO) and graphene nano-platelet (GNP) under the range of pH value, and (b) solution Zeta potential with the different GNP ratio.

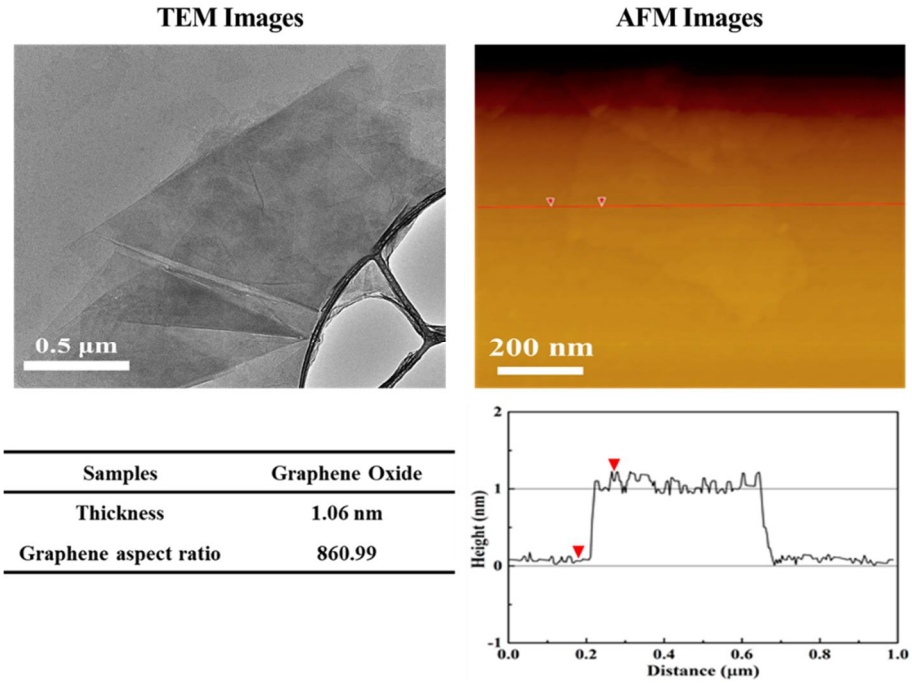

Samples	Graphene Oxide
Thickness	1.06 nm
Graphene aspect ratio	860.99

Figure 3.5.5. The TEM and AFM images of graphene oxide (GO).

3.5.5.2. Morphologies of PCM composites

To obtain the shape stability among the PCM composites under the different temperatures, the results of leakage test are shown in **Fig. 3.5.10**. The samples are initially placed on the hot plate at the room temperature (25 °C) and all samples kept the solid state without any leakage. When the temperature is heated to 50 °C, the 1-TD is melted to the liquid state while the PEG remained its solid structure with a little leakage. Among the PCM composites, they totally sustain the solid state without any leakage at the same temperature. When the temperature is increased to 80 °C, the PEG already melted completely as PCM composites well kept their solid structures. From the leakage test, the graphene aerogel can strengthen the shape stability of PCMs and prevent the leakage under the phase transition process.

The surface morphologies among the graphene aerogels and PCMs are obtained by the SEM images. As for GNP embedded graphene aerogels are shown in **Fig. 3.5.11**, they are porous internal structures and observed the graphene nano-platelet (GNP) at the graphene skeletons. It is found out more amount of GNPs in the higher mass ratios and immediately affect the thermal conductivities. Back to the SEM images of pure PCM and PCM composites, the **Fig. 3.5.12** shows the surface structure in various mass ratios. In **Fig. 3.5.12a**, the pure PEG had a nearly planet surface structure and slightly changed after infiltrated into the graphene aerogels. The morphologies of PEG composites are shown in **Fig. 3.5.12b**, **3.5.12c**, and **3.5.12d**. The surface of these composites are similar though added more amounts of embedding GNPs, just observed a little enhancement of fractured surface through the PEG composites. That means the pure PEG is fully infiltrated into the graphene aerogel and these PCM composites have their intrinsic physical morphologies under the phase transitions. In **Fig. 3.5.12e**, the pure 1-TD image is measured and comparing with the various mass ratios of 1-TD composites, the surface structures are slightly changed due to the different porosity and weight percent of working material. To obtain the crystallization among the PCMs, the XRD figures are implied in **Fig. 3.5.13**. The intrinsic peaks in pure PEG is detected at $2\theta = 19.09°$, and 2θ

= 23.22° (**Fig. 3.5.13a**); those peaks of PEG composites slightly shifted by the different GNP ratios. These results indicate the samples have similar internal structures without significant changes. The same as 1-TD samples, the pure 1-TD shows the peaks at 2θ = 21.32°, and 2θ = 24.16° and remained the working materials at the different embedded ratios in **Fig. 3.5.13b**. These results signify the existence of pure PCMs under the skeleton of graphene aerogel and hold a great crystallization in the final composite.

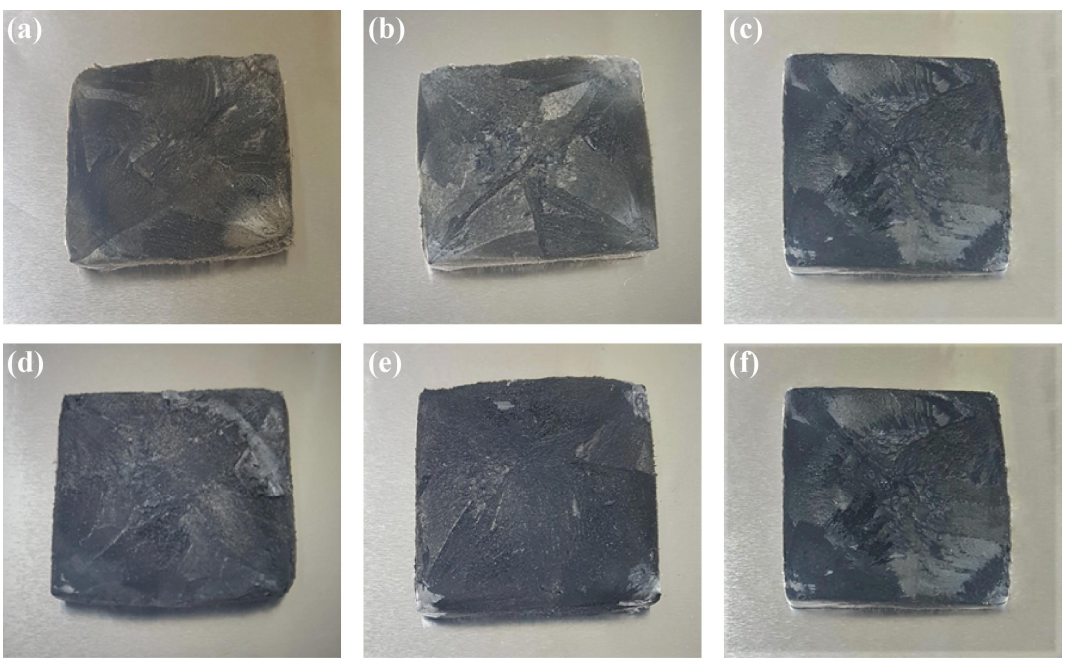

Figure 3.5.6. The camera images of graphene aerogel with different mass ratios. (a) 2:1 GO/GNP mass ratio, (b) 1:1 ratio, (c) 1:2 ratio. (d) reduced graphene oxide (rGO) with 2:1 GNP ratio, (e) 1:1 rGO/GNP ratio, (f) 1:2 rGO/GNP ratio.

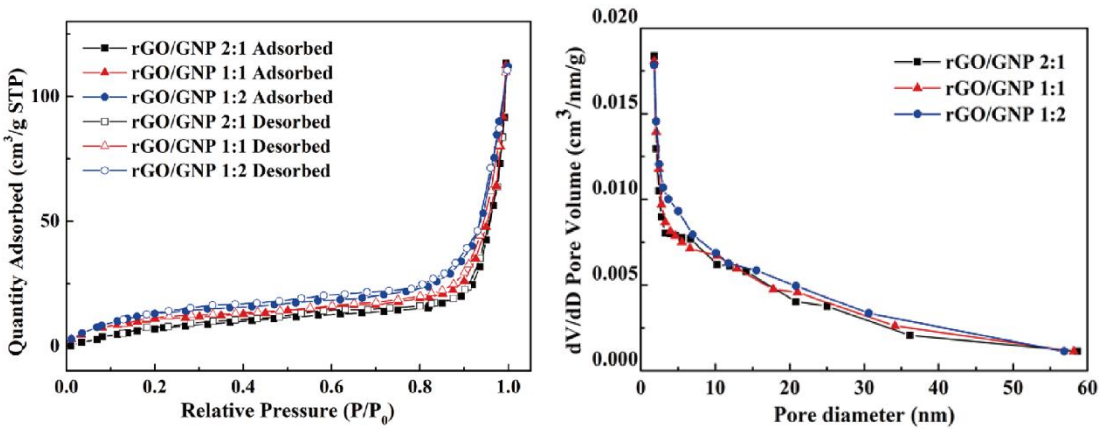

Figure 3.5.7. The BET peaks of graphene aerogels with Nitrogen adsorption/desorption and pore size distribution.

Table 3.5.1. BET results of graphene aerogels with different GNP mass ratios.

Samples	Graphene/GNP 2:1	Graphene/GNP 1:1	Graphene/GNP 1:2
Surface Area (m^2/g)	373.95	372.74	370.36

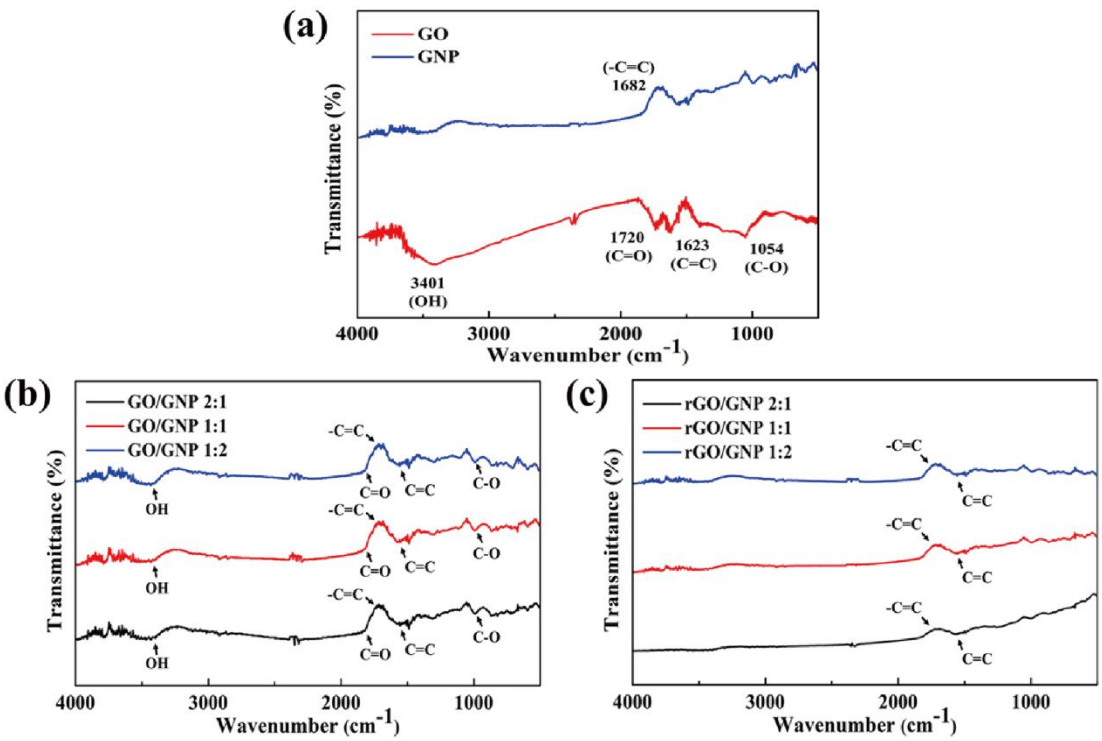

Figure 3.5.8. The FT-IR peaks at (a) graphene oxide (GO) and GNP, (b) graphene oxide with different ratios, and (c) rGO/GNP peaks.

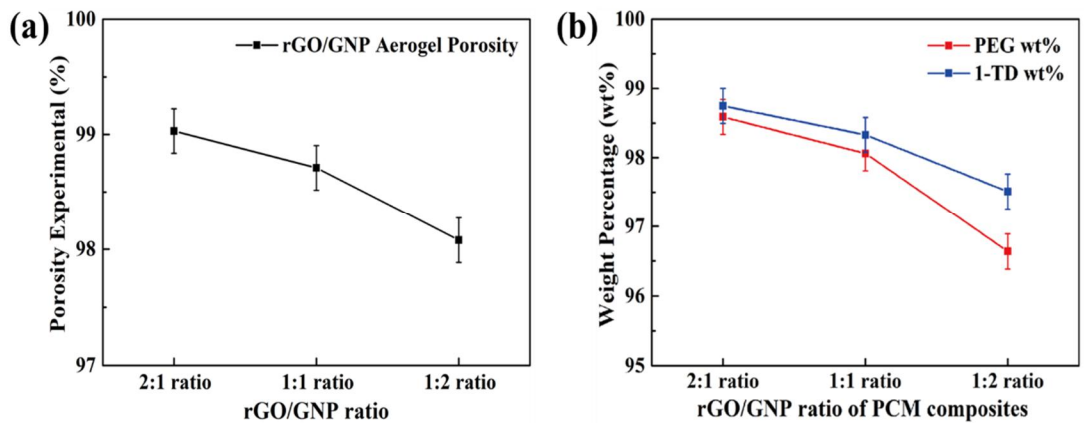

Figure 3.5.9. The characterization of (a) porosity in each graphene aerogel, and (b) weight percentage of PEG and 1-TD within the PCM composites, respectively.

Table 3.5.2. Graphene aerogel porosity results among the different mass ratios.

Samples	Graphene/GNP 2:1	Graphene/GNP 1:1	Graphene/GNP 1:2
Porosity (%)	99.03	98.71	98.08

Table 3.5.3. Weight percentage of each PEG, and 1-TD in the PCM composites.

Samples	2:1 ratio PCM composite	1:1 ratio PCM composite	1:2 ratio PCM composite
PEG wt%	98.59	98.06	96.64
1-TD wt%	98.75	98.33	97.51

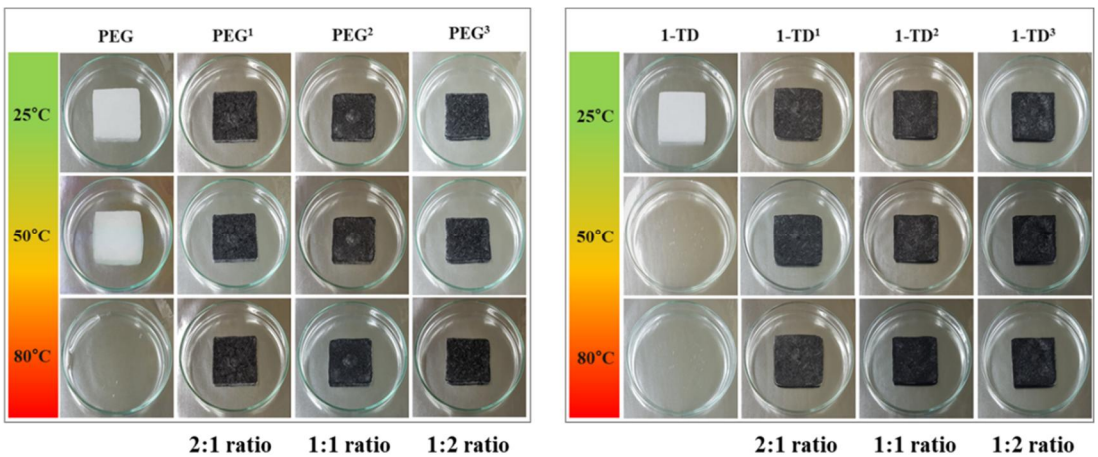

Figure 3.5.10. Form stable images among the PCM composites in (a) pure PEG, 2:1 ratio PEG, 1:1 ratio PEG, and 1:2 PEG; (b) pure 1-TD, 2:1 1-TD, 1:1 1-TD, and 1:2 1-TD.

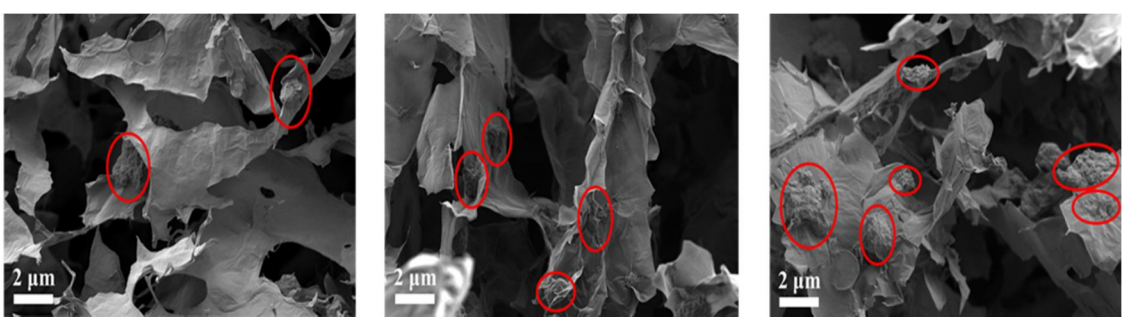

Figure 3.5.11. SEM images of embedded graphene nano-platelet (GNP) in (a) GO/GNP 2:1 ratio, (b) GO/GNP 1:1 ratio, and (c) GO/GNP 1:2 ratio.

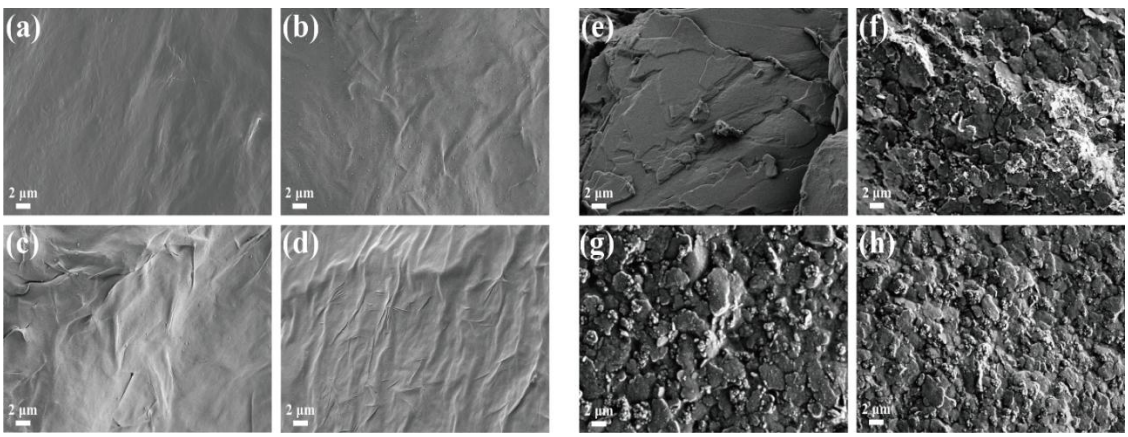

Figure 3.5.12. SEM images indicated (a) pure PEG, (b) 2:1 PEG, (c) 1:1 PEG, (d) 1:2 PEG, (e) pure 1-TD, (f) 2:1 1-TD, (g) 1:1 1-TD, and (h) 1:2 1-TD.

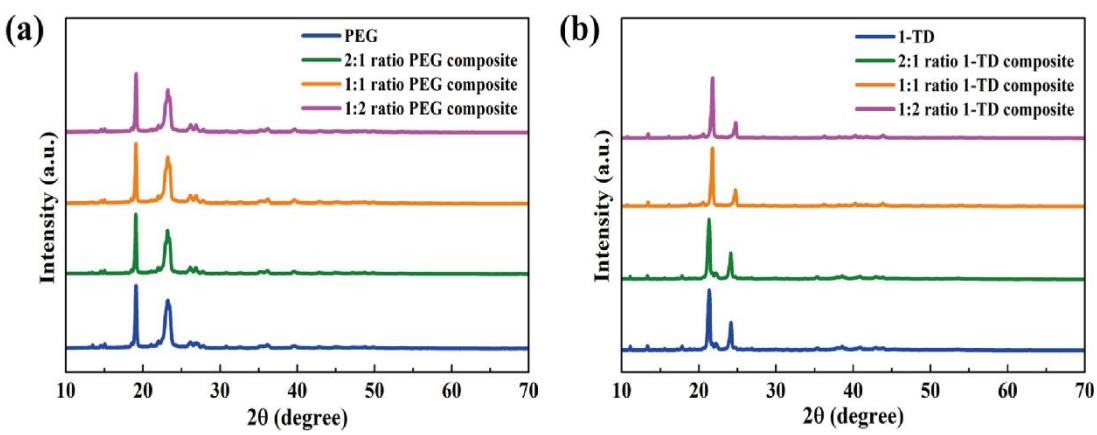

Figure 3.5.13. XRD peaks of (a) PEG series, and (b) 1-TD series.

3.5.5.3. Thermal properties of PCM composites

Before measuring the electrical current, the result of thermal conductivity on each PCM composite is shown in **Fig. 3.5.14**. From this figure, the pure PEG and 1-TD had low thermal conductivity at 0.175 W/mK and 0.08 W/mK, respectively. The thermal conductivity is gradually increased from 2:1 embedding mass ratio to 1:2 ratio in both PEG and 1-TD composite. The 2:1 ratio PEG composite shows 0.4233 W/mK, increased to 0.4929 W/mK as a ratio of 1:1 PEG composite; and exhibited higher 0.5828 W/mK values at the 1:2 ratio PEG composite (**Fig. 3.5.14a**). The **Fig. 3.5.14b** shows the series of different ratios of 1-TD composites and the results are indicated 0.3414 W/mK, 0.4135 W/mK, and 0.4974 W/mK respectively. Furthermore, the 1:2 ratio PCM composite had a similar thermal conductivity with the 1:3 ratio samples in this results. The **Fig. 3.5.14c** and **3.5.14d** shows the thermal diffusivity between PEG and 1-TD series. In **Fig. 3.5.14c**, the pure PEG has 0.2623 mm^2/s and gradually increased to 0.2897 mm^2/s, 0.3306 mm^2/s, and 0.3794 mm^2/s under the different GNP ratios. Similar to the 1-TD composite, the pure 1-TD initially shows 0.1404 mm^2/s and synergistically arises to 0.2373 mm^2/s, 0.2837 mm^2/s, and 0.3332 mm^2/s, respectively.

The **Fig. 3.5.14** demonstrates the graphene nano-platelet (GNP) played a role as a thermo-carrier and combine the fractures of internal porous structure. It is important to obtain an expected current peaks under the energy harvesting systems. The phase transition parameters are obtained by the DSC measurement and shown in **Fig. 3.5.15**. These figures indicated the melting and cooling peaks under the pure PCM and PCM composites at the solid-liquid phase transition process. The **Table 3.5.4**, and **Table 3.5.5** listed the onset melting and cooling temperature (T_{mo}/T_{co}), melting and cooling point (T_{mp}/T_{cp}), end melting and cooling temperature (T_{me}/T_{ce}), and melting and cooling enthalpy ($\Delta H_m/\Delta H_c$) among the different ratios. In **Fig. 3.5.15a**, the phase transition of the PEG is measured at 50.76 °C and 69.28 °C with a 66.61 °C melting point. The onset temperature of heating process is slightly shifted and a little faster than that of pure PEG. Under the cooling process, the cooling temperature is appeared from 41.57 °C to

32.75 °C with a cooling temperature of 36.45 °C as shown in **Fig. 3.5.15b**. There are similar to the heating process and increased the cooling transition temperature with the higher embedded GNP ratios. Consider the value of enthalpy, the pure PEG is 182.60 J/g on heating process and a little diminished under the PEG composites. This result is match with the weight percentage of pure PCMs due to the replacement of supporting materials. The 1-TD phase transition curves are shown in **Fig. 3.5.15c**, and equal to the result of PEG composites. The onset of 1-TD is 36.37 °C and ended at 44.06 °C with a melting point of 41.86 °C. When increased the GNP ratios, the curves are slightly shifted and changed on the embedding material. The cooling process is measured at 35.13 °C and ending of 29.78 °C, and the 1-TD composites shows higher shifted temperatures than that of pure 1-TD as given in **Fig. 3.5.15d**. The cooling enthalpy under the PEG and 1-TD samples, the results are consistent with heating process that the PCM composites have sufficient latent heat to utilize in the thermoelectric energy conversion applications.

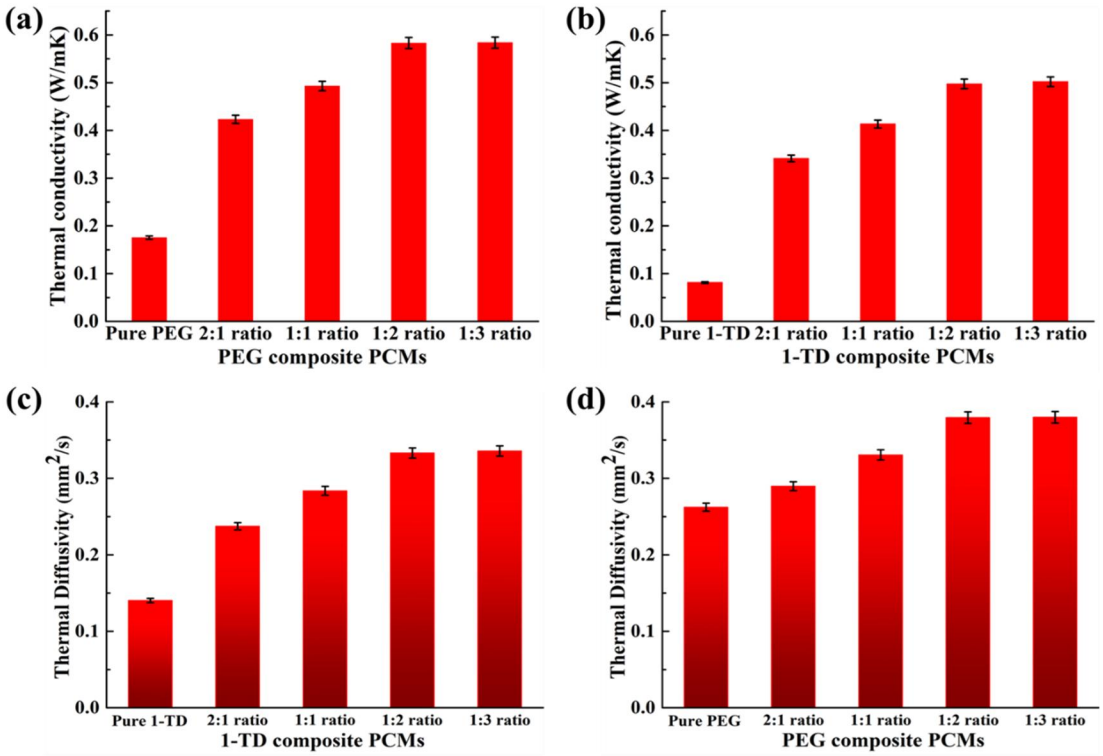

Figure 3.5.14. Thermal conductivity of (a) PEG series, (b) 1-TD series; the thermal diffusivity of (c) PEG series, and (d) 1-TD series.

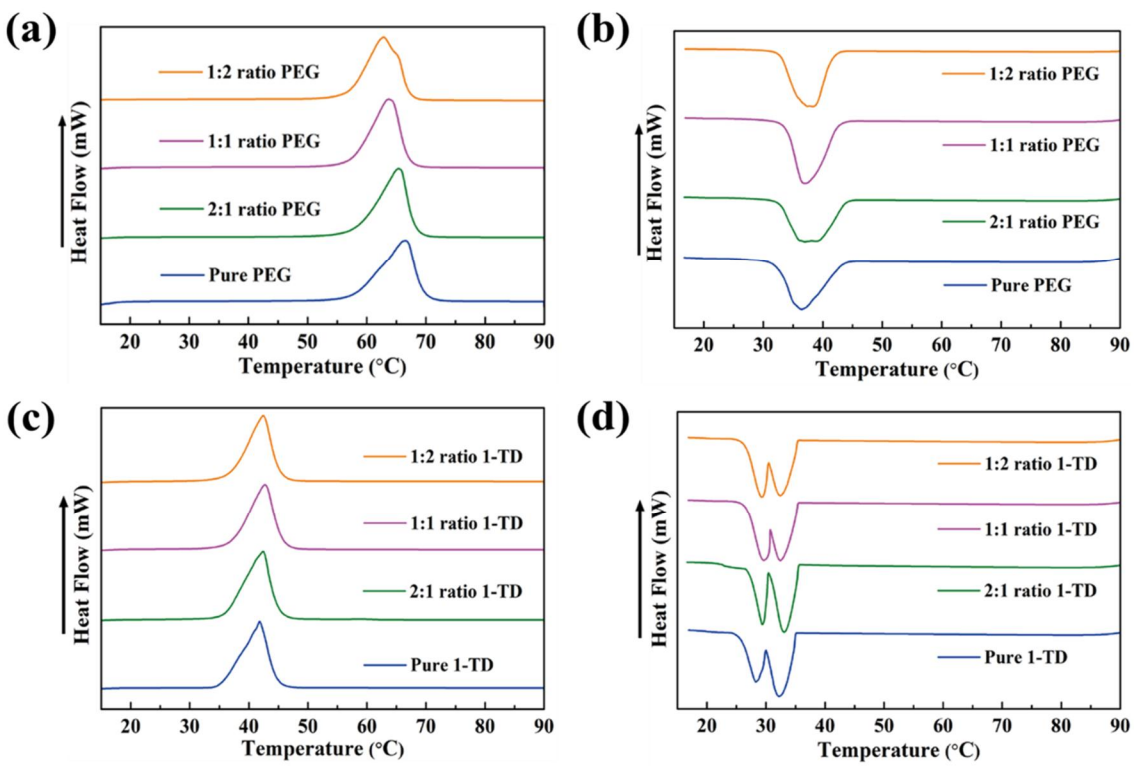

Figure 3.5.15. The DSC cureves with different ratios. (a) heating cycle of PEG series, (b) cooling cycle of PEGs, (c) heating process of 1-TDs, and (d) cooling cycle of 1-TDs.

Table 3.5.4. DSC results of pure PEG and PEG/Aerogel composites.

Samples	T_{mo}(°C)	T_{me}(°C)	T_{mp}(°C)	ΔH_m(J/g)	T_{co}(°C)	T_{ce}(°C)	T_{cp}(°C)	ΔH_c(J/g)
PEG	50.76	69.28	66.61	182.60	41.57	32.75	36.45	166.43
2:1 composite	50.30	67.96	65.38	179.79	42.57	32.87	36.93	164.61
1:1 composite	47.72	67.03	63.69	178.50	43.38	32.94	37.16	164.39
1:2 composite	46.97	66.88	62.83	177.83	43.95	33.97	38.32	163.87

Table 3.5.5. DSC results of pure 1-TD and 1-TD/Aerogel composites.

Samples	T_{mo}(°C)	T_{me}(°C)	T_{mp}(°C)	ΔH_m(J/g)	T_{co}(°C)	T_{ce}(°C)	T_{cp}(°C)	ΔH_c(J/g)
1-TD	36.37	44.06	41.86	225.75	35.13	19.82	29.78	215.72
2:1 composite	36.21	45.27	42.35	215.87	35.47	19.72	29.95	211.42
1:1 composite	35.86	44.87	42.77	214.08	35.51	19.76	30.17	210.81
1:2 composite	35.47	44.43	42.11	213.21	36.47	20.39	30.24	208.05

3.5.5.4. Current measurement in the energy harvesting system

The energy harvesting results during the phase transition process are shown in **Fig. 3.5.16**. For about the heating process, the energy harvesting system is placed in a heating chamber, and increased the temperature from 25 °C to 80 °C. **Fig. 3.5.16a** shows the electrical current with different ratios of PCM composites under the heating process. The temperature difference is existed and these peaks of current are further rapidly increased. The maximum peaks of 2:1 ratio PCM composite are 10.44 mA around 1,170 s and 6.40 mA around 2,570 s, respectively. As increased the contents of graphene nano-platelet (GNP), the two maximum peaks of 1:1 ratio PCM composite are close to 10.27 mA at 920 s and 6.19 mA at 2,230 s. The higher contents in 1:2 ratio PCM composite, the time of maximum curves are nearly exhibited 10.30mA at 780 s and 6.12mA at 2,098 s. Moreover, the 1st electrical current with 2:1 ratio PCM composite is generated until 1,709 s while 1,580 s and 1,367 s between 1:1 and 1:2 ratio PCM composites. The **Fig. 3.5.16b** shows the cooling curves with the PCM composites, the harvesting device is removed from the heating chamber and released the stored energy under a natural condition. The current of cooling results increased orderly due to the high cooling speed. The maximum cooling peaks of 2:1 ratio PCM composite is 9.95 mA in the 1st device of system at 288 s, and 6.01 mA in the 2nd device at 1,287 s. The higher 1:1 ratio PCM composite curve is 9.78 mA at 241 s, ended the 1st step at 701s, and shows 5.81 mA around 1,069 s. The last 1:2 ratio PCM composite is 9.95 mA at 204 s, began the 2nd step at 596 s, and maximum peak is 5.71 mA at 929 s. According to the current peaks, both of heating and cooling process indicates the faster rate for arriving the phase transition fields and thus the harvesting system is contribute to the efficiency of thermoelectric energy conversions.

To clarify the possibility of energy harvesting system, LED lamp is normally connected to the thermoelectric generator device and turned on with the harvested energy. The maximum output power is important to demonstrate the usability of former system and shown in **Fig. 3.5.17**. The power of heating process is indicated in **Fig. 3.5.17a** and **3.5.17b**; the maximum curves of 2:1 ratio PCM composite are 470.59 μW and 176.68 μW. The 1:1 ratio output power is 455.30 μW in the 1st step and 165.55 μW in the 2nd step.

The result of 1:2 ratio PCM composites shows 457.77 μW and 161.64 μW. The maximum output power on cooling process is shown in **Fig. 3.5.17c** and **3.5.17d**. The maximum peaks under 2:1 ratios are 427.78 μW in the 1st curve and 155.96 μW in the 2nd curve. As a higher contents 1:1 ratio PCM composites, the results shows 412.90 μW and 146.09 μW. In addition, the maximum output value for 1:2 ratios are observed in 427.22 μW and 140.57 μW. Following to the power graphs, the results commonly indicate the output powers are not enough to turn on the LED lamp. Hence, utilizing a low voltage start-up converter (LTC 3108) is necessary in the harvesting system to improve the output power [160]. **Fig. 3.5.16c**, and **3.5.16d** shows the turn on time of LED lamp during the heating and cooling process and the converter can amplify the output voltage to reach the range of opening values [196]. In addition, the measured maximum LED brightness for each PCM composite is almost equal to the experimental result. Thus, the energy harvesting system is able to provide the sufficient output voltage for the heat-to-electric applications.

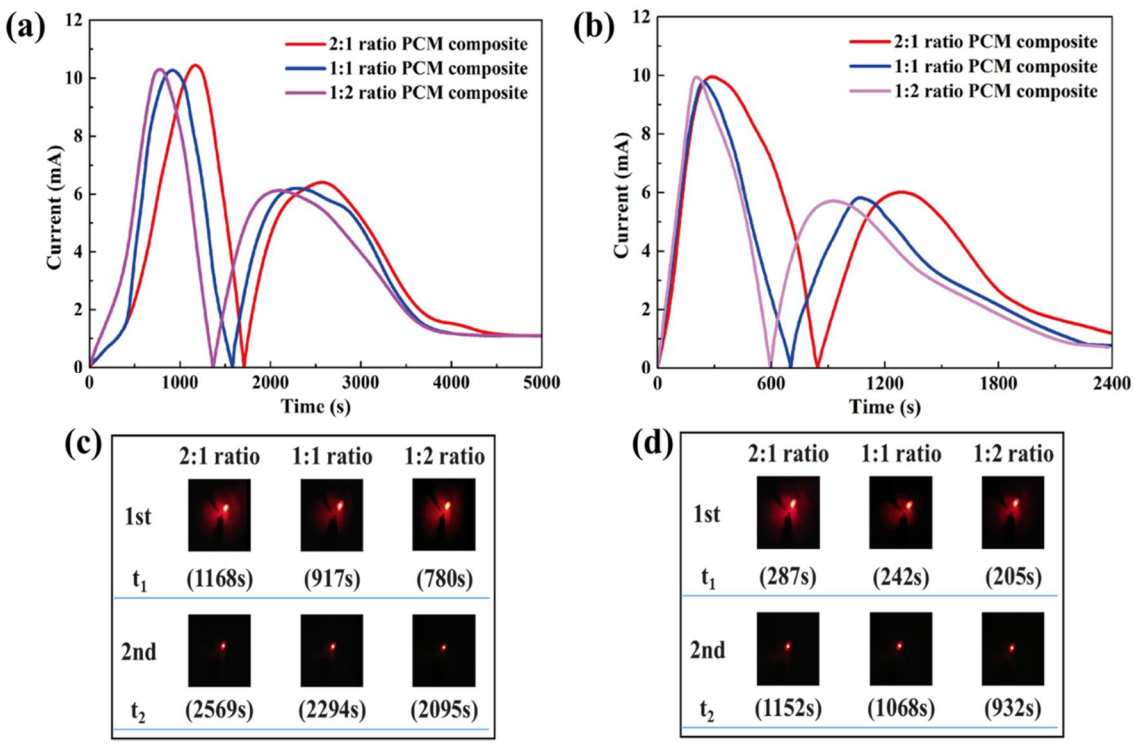

Figure 3.5.16. Experimental results of PCMs at (a) electrical current with different GNP ratios upon heating, (b) upon cooling process, (c) LED bulb images on the heating cycle, and (d) cooling cycle.

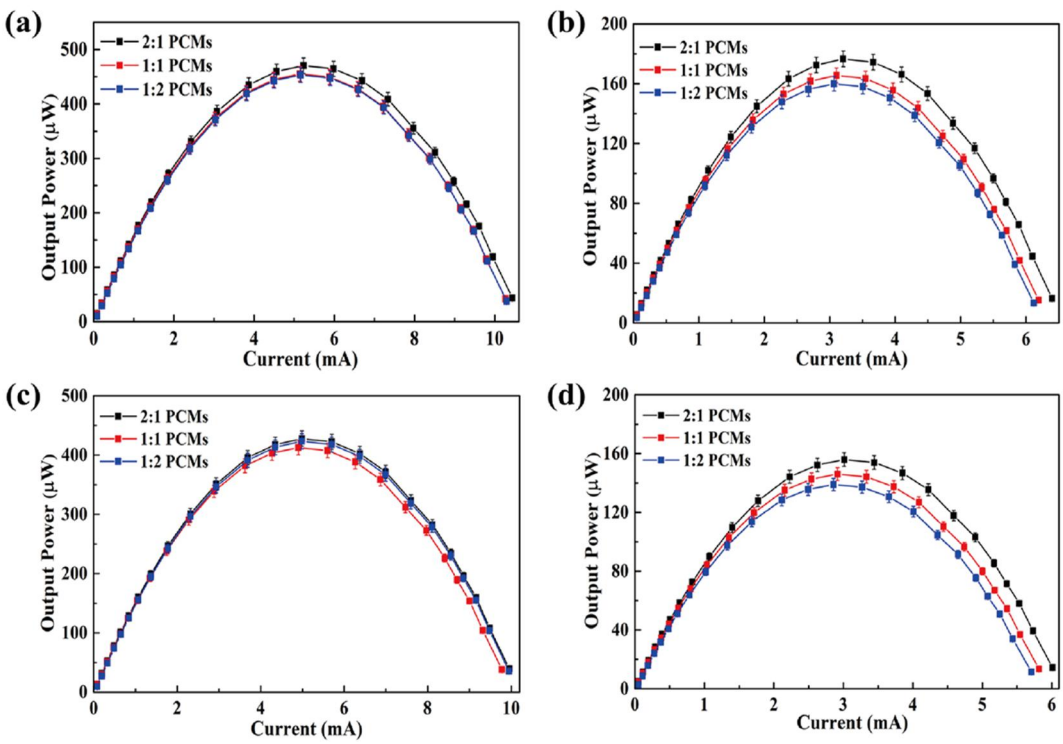

Figure 3.5.17. The output power graphs under (a) 1st heating cycle, (b) 2nd heating cycle, (c) 1st cooling cycle, and (d) 2nd cooling cycle.

3.5.5.5. Combination of numerical simulation

To understand more about the energy harvesting system, the modeled simulation is compared with the experimental result. The **Fig. 3.5.18** shows the temperature gradients and temperature difference on the heating process. The curves are increased rapidly with the high contents of embedding ratios, and the phase transition time of 1-TD and PEG composites are equally changed. For the maximum temperature difference among the PCM composites, it is 16 °C at 1,400 s in the 2:1 ratio PCMs (**Fig. 3.5.20a**), the 1st heating process is finished about 1,900 s in which theoretically approached to the experimental result in **Fig. 3.5.21a**. Besides the 2:1 ratios, the maximum temperature difference between the 1:1 and 1:2 ratio PCM composites are approximately closed to 16 °C within the distinct temperature gradients in **Fig. 3.5.20a**. The calculated current is finished at 1,700 s in the 1:1 ratio PCM composite and well agree with the measured curves as shown in **Fig. 3.5.21b**. For the 1:2 ratios, the 1st step is finished at 1,600 s and also matched with the experimental graph in **Fig. 3.5.21c**.

Consider the cooling process, the temperature is decreased from 80 °C to room temperature, and the **Fig. 3.5.19** shows the temperature profiles with the different ratios of PCM composites. It is similar to the heating process. The maximum temperature difference of 2:1 ratios are 12 °C in which the same value in other groups and the curves of temperature difference are slightly increased in **Fig. 3.5.20b**. The cooling process of 2:1 ratio PCM composite is firstly completed at 950 s with the 9.93 mA maximum current at 350 s, the calculated result has a well trend to compare the measured current in **Fig. 3.5.21d**. Therefore, the time of 1:1 ratio is finished at 850 s with 9.79 mA maximum current at about 300 s (**Fig.3.5.21e**), and the last 1:2 ratio PCM composite shows faster 750 s generating time and the maximum calculated current is 9.84 mA near the 250 s in **Fig 3.5.21f**. These numerical simulation results illustrate the possible composed of energy harvesting system and controlled the PN TEGs with the different PCM composites. To calculate the thermoelectric energy conversion efficiencies, **Fig. 3.5.22** shows the results of different GNP ratio PCM composites. It is demonstrated the efficiency of heating process possess higher than that of cooling process due to the heat loss under the natural

conditions. Some of stored energy is diffused to the air and shows the lower efficiency on the cooling process. The value of heating efficiencies are 54.76 % in the first 2:1 ratio PCM composite and slightly increased to 55.22 %, and 55.59 % for the 1:1 ratio and 1:2 ratio PCM composites in **Fig. 3.5.22a**. In spite of thermal diffusion on the cooling process, the efficiency is equally increased from 2:1 ratios to the final 1:2 ratio PCM composites as shown in **Fig. 3.5.22b**. The 1:2 ratio PCM composites system indicates the highest 33.33 % at the series of PCM combinations and the efficiency results are further demonstrate the GNP contents should influence the arriving rate of phase transitions and thermoelectric energy conversion process. Summarize with the simulation results, the different ratio PCM composites are useful for a high efficiency of thermoelectric energy conversion applications.

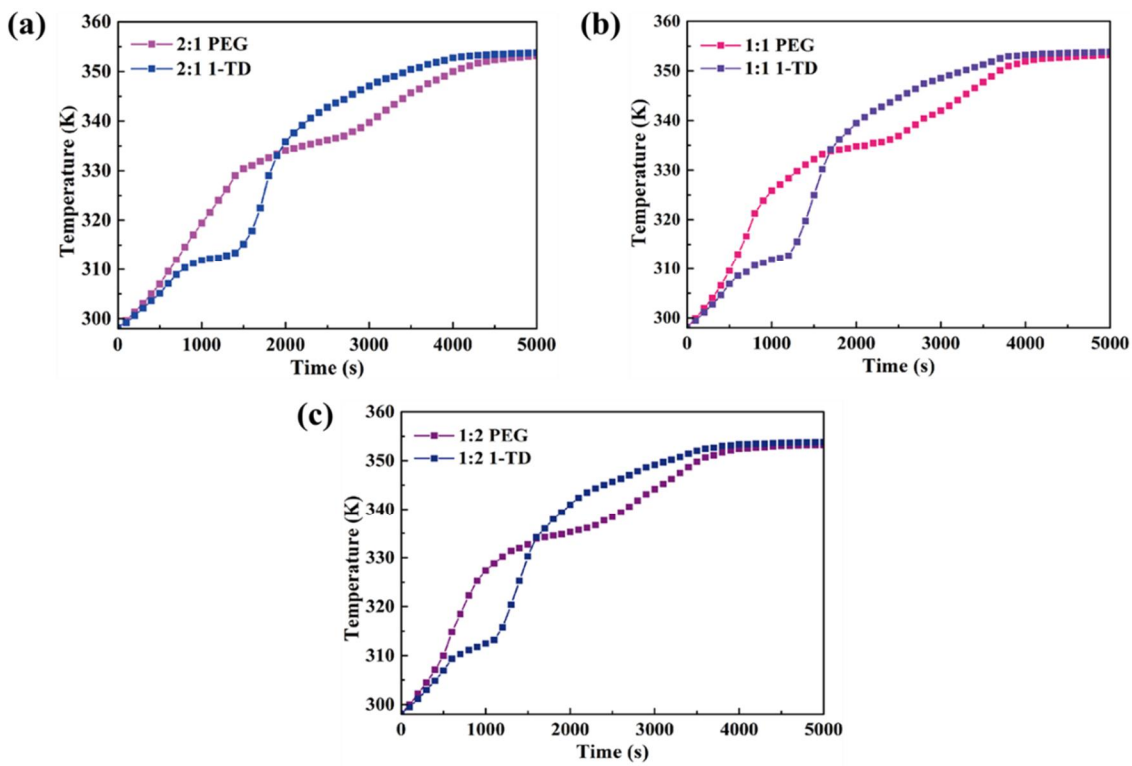

Figure 3.5.18. The temperature profiles during the heating cycle (a) 2:1 ratio PCMs, (b) 1:1 ratio PCMs, and (c) 1:2 ratio PCMs.

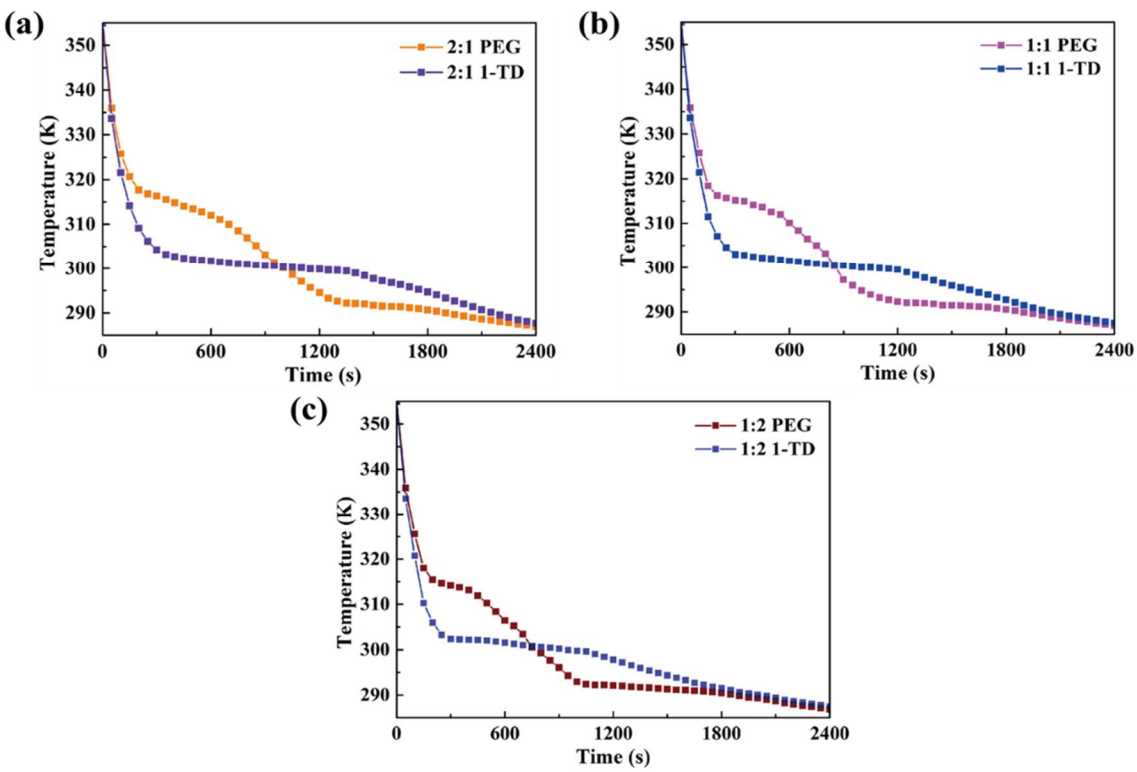

Figure 3.5.19. The temperature profiles upon cooling (a) 2:1 ratio PCMs, (b)1:1 ratio PCMs, and (c) 1:2 ratio PCMs.

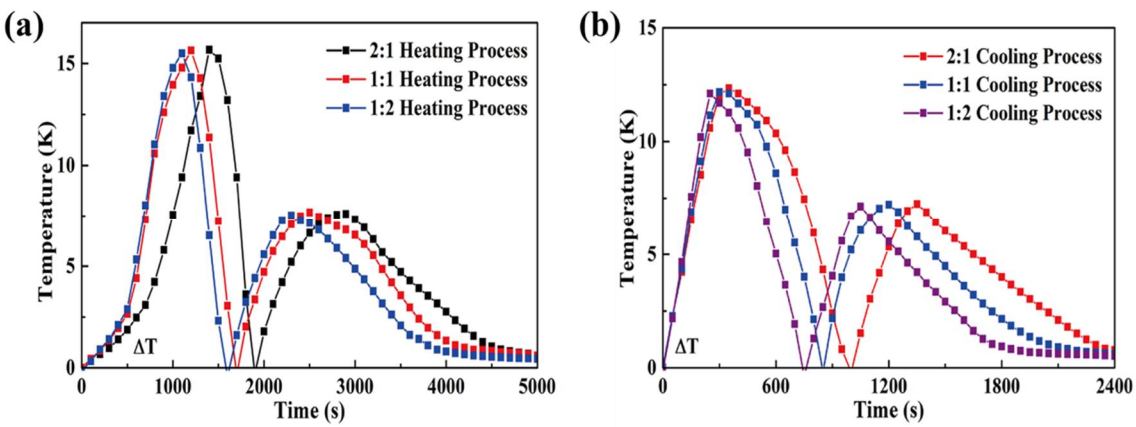

Figure 3.5.20. Temperature difference (a) heating process, and (b) cooling process.

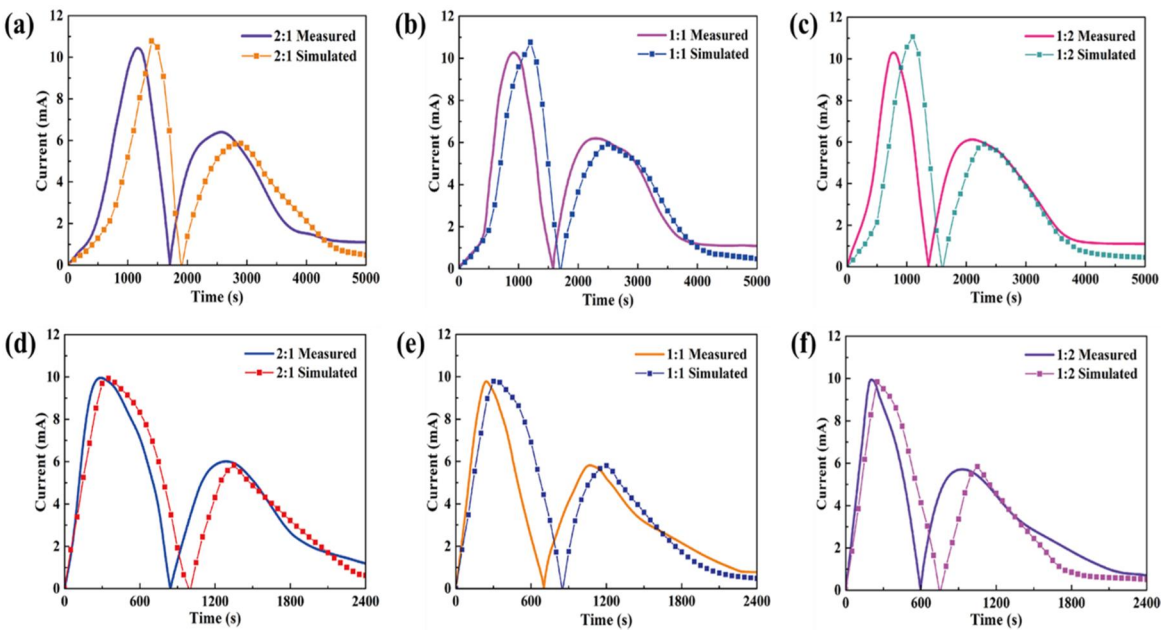

Figure 3.5.21. Comparison of experimental results with numerical calculation (a) 2:1 ratio heating, (b) 1:1 ratio heating, (c) 1:2 ratio heating, (d) 2:1 ratio cooling, (e) 1:1 ratio cooling, and (f) 1:2 ratio cooling.

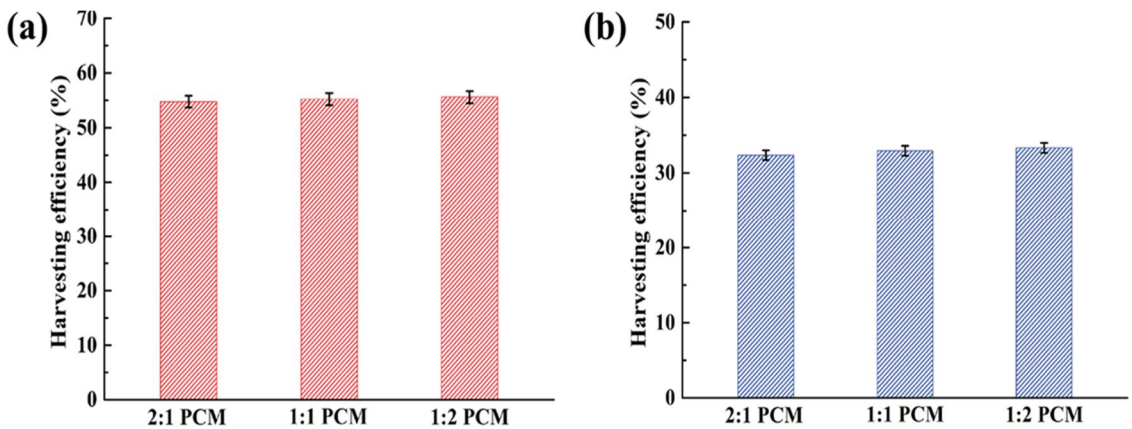

Figure 3.5.22. Thermoelectric energy conversion efficiencies on (a) heating cycle, and (b) cooling cycle.

3.5.6. Conclusions

In the present study, we designed an advanced energy harvesting system with different ratio PCM composites to observe an electrical energy harvesting. The embedding contents of GNP is demonstrated to increase the thermal conductivity and mechanical property. The PEG and 1-TD PCM composites can absorb or release a large amount of heat energy during the phase transition process and generating a considerable temperature difference under the energy harvesting system. Based on the temperature difference, the system is possibly occurring the thermoelectric energy conversion and the 1:2 ratio PCM composites showed the best result in the harvesting time. The collected energy is large enough to turn on the LED lamp in the circuit and promoted the working time in both heating and cooling states. The finite element method (FEM) is numerically calculated the temperature ranges under the time equations and the modelling had an excellent agreement with the experimental results. This study is primary verified the variation of thermoelectric energy conversion time and indicated the possibility of increasing the thermoelectric conversion efficiency of energy harvesting system. Thus, the novel energy harvesting devices are normally utilized in the thermal sensor, and smart textile applications.

3.6. Optimization of PCM composites with GNP ratios

3.6.1. Introduction

In recent years, renewable energy has been widely attracted to replace the fossil fuels because of energy crisis and severe pollution in human life. The solar and heat energy is the best clean energy to reduce the depletion of fossil fuels. It is important to develop a high efficient energy conversion device for utilizing the renewable energy that numerous researches have been reported in both science and engineering fields. Comparing with others, a thermoelectric energy harvesting device is easily transferred the heat energy to the electrical energy, and it has been widely used as a thermoelectric power generator to reduce the resource depletion [208]. Consider the phase change materials (PCMs) with high latent heat, great thermal stability, and nearly isothermal field under the phase transitions [42, 209, 210]. The PCMs are adequately employed as working materials to absorb and release a large amount of heat on the heating and cooling process [176]. Combination of the PCMs with N and P type semiconductor has opened a new route to improve the thermoelectric energy conversion efficiency and be applied to the latent heat thermal energy storage (LHTES) by employing the phase change materials (PCMs) [8, 42].

However, the leakage is a large problem around the phase change materials (PCMs) when the temperature is reached to the melting field in which demand some supporting materials for preventing the leakage problem during the phase transition process [150, 176]. Therefore, a series of supporting materials such as melamine-formaldehyde (MF) resin, phenolic resin, polystyrene (PS), polyurethane (PU), and polyaniline (PANI) are generally used as supporting shell materials to construct a core-shell composite structures [211]. Nevertheless, a large proportion of the working materials is replaced to these supporting materials in which cause a high decrease to the overall latent heat among the PCM composites [212]. Hence, these form stable PCMs have lower capacity for storing heat energy during the phase transition process than that of pure PCMs.

To prevent the leakage without significant loss under the melting and cooling process, graphene aerogel has been selected as a new supporting material due to the 3D porous

internal structure and large surface area [68, 148]. The graphene aerogel is able to absorb large contents of pure working materials than that of shell supporting materials though complicated internal skeletons [150]. Comparing with these shell materials, graphene aerogel has a great mechanical property, chemical stability, thermal reliability, and large porosity. Therefore, the PCM composites can incorporate most of working materials for storing heat energy and contribute to the thermoelectric energy conversion applications. The contents of embedded graphene nano-platelet (GNP) could improve the thermal conductivity and energy conversion efficiency, and the PCM composite can possess various thermal conductivity with the different mass ratio of graphene nano-platelet (GNP) [192]. To find out the optimum combination with two different phase change materials (i.e., PEG and 1-TD) is required for the thermal energy storage and electrical conversions.

The thermoelectric energy harvesting system is composed of N and P type semiconductor with form stable PCM composites [68]. The PCMs are placed on the each side of N and P type semiconductor to construct an electrical circuit. The automatic thermoelectric energy conversion is obtained under the temperature difference in the basis of Seebeck effect. The hot side has higher temperature than that of cold side which produces electron movement toward the hot side and subsequently appears the electrical current in the circuit. In other words, the different PCMs connected to the N and P type semiconductor are served as a power generator during the phase transition process [206]. It shows that output current in the harvesting system is proportional to the temperature difference, and increasing the temperature difference on the heating and cooling process is directly helpful to the induced current. As a result, PCM composites with high thermal conductivity and optimum phase transition temperature are vital to the thermoelectric energy conversions.

In the present work, we fabricated the form stable PEG and 1-TD composites and construct a self-sustainable energy harvesting system by combining with N and P type semiconductors. A temperature difference between the sides of device is obtained due to the different phase transition field between PEG and 1-TD composites. The graphene aerogel with different mass ratio of graphene nano-platelet (GNP) is utilized as a supporting material to infiltrate the pure PCMs into the porous internal structures. The various values of the temperature difference are evaluated by the different thermal

conductivity and phase transition temperatures. Therefore, the output electrical currents are depended on the combination of PEG and 1-TD composites with different contents of graphene nano-platelet (GNP). To obtain the optimum groups, the light intensity of output LED lamp is measured and the most appropriate combination between these PEG, and 1-TD composites is determined by the current peaks. Furthermore, the output electrical current is numerically calculated by utilizing a finite element method (FEM) and provided a simulative result on the energy harvesting system.

3.6.2. Energy harvesting system

Based on the Seebeck effect, the energy harvesting system is obtained the electron movement during the phase transition process. For about the heating process, the 1-TD composite is firstly reached to the melting transition field as the PEG composite increased the surface temperature due to the higher melting point than that of 1-TD composite. The electrons in the N type of semiconductor initially excited by absorbing the heat energy and moved to the hot side. Therefore, the plenty of electron movement from hot side to the cold side are gradually generated the electrical current in the circuit. When the PEG composite is under the phase transition process, the 1-TD surface temperature is increased and exceed the hot side. From this moment, 1-TD composite is regarding as hot side of harvesting system and the 1-TD placed on the hot side device started to generate the output induced current. Compared with the former research, adjusting the combination of PEG, and 1-TD composite with different graphene nano-platelet (GNP) contents could find out the most optimum field of current in both heating and cooling process. The harvesting system is connecting to the LED lamp and implied the output lightness by measuring the light intensities. According to the result of light intensity and current peak, the optimum groups composed of PEG, and 1-TD composites are obtained immediately. The output harvesting energy is collected to turn on the LED bulb and verify the optimum components of the energy harvesting system as shown in **Fig. 3.6.1**.

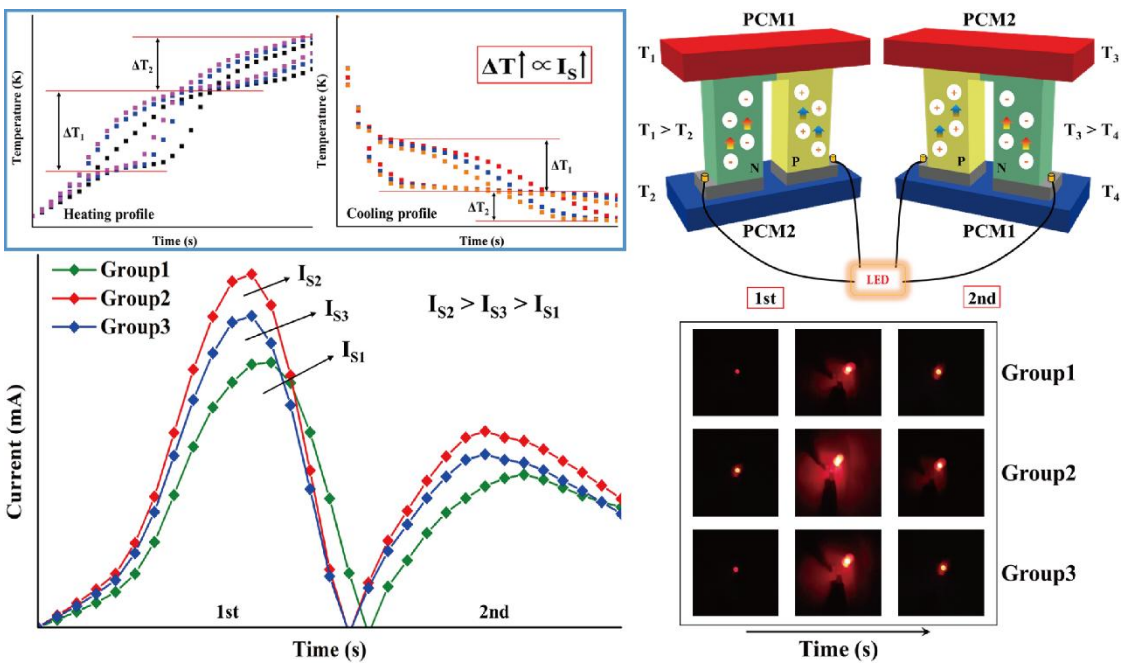

Figure 3.6.1. Schematic for optimum current peaks upon heating and cooling process. The output curernt is proportional to the temperature difference and selecting the optimum components of PCMs via thermoelectric energy harvesting.

3.6.3. Numerical analysis

For the sake of temperature difference between the two sides of device during the phase transitions, utilized a finite element method (FEM), COMSOL Multiphysics commercial software to calculate the output temperature profiles. The harvesting system is composed of two groups of N and P type semiconductors, PEG composite, coppers, and 1-TD composites. The PEG composite is connected to the hot side in the 1st device while the opposite positions in the 2nd device of system. The essential parameters are heat capacity, density of PEG, and 1-TD composites, latent heat (ΔH), thermal conductivity, temperature peaks (T_m, T_c) of each PCM composite. The copper is in the middle of N and P type semiconductor and two PCM composites. Based on the components of N and P type semiconductors, the device materials are designated Bi_2Te_3, and the Seebeck coefficient is proportional to the temperature during the melting and cooling process. The total mesh in this numerical simulation is 10178.

The model of heat transfer is defined as:

$$\rho C_p \frac{\partial \mathbf{T}}{\partial t} + \rho C_p u \cdot \nabla \mathbf{T} + \nabla \cdot \mathbf{q} = Q \qquad \text{Eqn (1)}$$

where ρ is mass density and C_p means heat capacity. The heat transfer rate $\mathbf{q}$ is descripted as a function of thermal conductivity k and $\mathbf{q} = -k\nabla T$ under the range of temperatures. The density of phase change materials (PCMs) is given by:

$$\rho = \theta\rho_{phase1} + (1-\theta)\rho_{phase2} \qquad \text{Eqn (2)}$$

Here, the fill-factor θ is depended on such parameters (C_p, k, and α_m) and expressed as:

$$C_p = \frac{1}{\rho}\left(\theta\rho_{phase1}C_{p.phase1} + (1-\theta)\rho_{phase2}C_{p.phase2}\right) + L\frac{\partial \alpha_m}{\partial T} \qquad \text{Eqn (3)}$$

$$k = \theta k_{phase1} + (1-\theta)k_{phase2} \qquad \text{Eqn (4)}$$

$$\alpha_m = \frac{1}{2}\frac{(1-\theta)\rho_{phase2} - \theta\rho_{phase1}}{\theta\rho_{phase1} + (1-\theta)\rho_{phase2}} \qquad \text{Eqn (5)}$$

where α_m is the mass coefficient under the mass density during the phase transitions and the boundary condition is defined under the external natural convections as below:

$$-\mathrm{n} \cdot \mathbf{q} = \mathbf{q_0} \quad \text{Eqn (6)}$$

Where n is the normal vector, and the convection of heat flux is $\mathbf{q_0}$ in the former equation. The convection heat flux is the function of heat transfer coefficient ($\mathrm{h_{air}}$) and the following equation is defined as:

$$\mathbf{q_0} = \mathrm{h_{air}} \cdot (\mathbf{T_{ext}} - \mathbf{T}) \quad \text{Eqn (7)}$$

The Seebeck coefficient S is utilized to estimate the value of output electrical current and given as:

$$\mathrm{S} = \sqrt{\frac{\mathrm{k}}{\sigma \mathrm{T}}} \quad \text{Eqn (8)}$$

Where, σ means the electrical conductivity of the device and the calculated current is a function of the Seebeck coefficient S, temperature difference under the phase transitions ($\Delta\mathbf{T}$), and resistance of semiconductors (R) as followed:

$$\mathrm{I} = \frac{\mathrm{S}\Delta\mathbf{T}}{R} \quad \text{Eqn (9)}$$

The converted energy W and total stored energy Q are the constants of calculating the thermoelectric energy harvesting efficiency and described as below:

$$\eta = \frac{W}{Q} \quad \text{Eqn (10)}$$

3.6.4. Preparation of PCM composites

3.6.4.1 Preparation of graphene aerogel supporting materials

To fabricate the graphene aerogel, the initial step is synthesized the graphene oxide (GO) by utilizing modified Hummers' method. Prepared 3.0 g graphite powder is put into the sulfuric acid (H_2SO_4) for pre-oxidation. Then, gradually added 15 g $KMnO_4$ into the pre-oxidation mixture and stirring for 2 hours under the 35 °C of oil bath. To remove the

excess of $KMnO_4$, poured H_2O_2 into the diluted system and washing with 10 % HCl solution to neutralize the oxidized graphite solution. After purification and obtained the graphene oxide powder by freeze-drying method. The embedded graphene nano-platelet (GNP) graphene aerogel is fabricated by the same freeze-drying method. The synthesized graphene oxide (GO) powder and GNP particles are completely dispersed in the distilled (DI) water with 1:1, and 1:2 mass ratios. After the ultra-sonication, the suspensions are poured into a mold with the dimension of 4cm*4cm*0.5cm and obtained the 3D porous structures by the freeze-drying method. Finally, utilized the hydrazine vapor method to prepare the reduced graphene oxide/GNP aerogels.

3.6.4.2 Fabrication of PEG and 1-TD PCM composites

In order to clarify the temperature difference with PEG, and 1-TD composites, a variety of embedding graphene nano-platelet (GNP) PCMs are modeled to estimate the temperature profiles within phase transitions. Consider the mass ratio between graphene oxide (GO) and graphene nano-platelet (GNP) is gradually increased from 2:1 to 1:2 in which increased the rate of progress on heating and cooling process. The output temperature gradients are shown in **Fig. 3.6.2**, the contents of graphene nano-platelet (GNP) could improve the thermal conductivity of PEG, and 1-TD composites so as to the temperature peaks had already shifted to attain the melting field in **Fig. 3.6.2a**. It obtained the numerical simulation is able to provide the output energy harvesting peaks correctly and the same result on the cooling process as shown in **Fig. 3.6.2b**. According to the heating and cooling temperature profiles, it emerged a series of groups by combination of each PEG and 1-TD composite. The overall temperature difference results within the heating and cooling process are shown in **Fig. 3.6.3**. The 1:2 ratio PEG composite initially had a large peak area by connecting to 2:1 ratio 1-TD composite. However, these combination groups appeared a lower peak area at the 2nd curves are hard to produce the energy harvesting. For about the 2:1 PEG composite with all series of 1-TD composite, the rate of melting and crystallization is lower than that of 1:1 and 1:2 PEG combinations. Thus, the selected optimum groups are listed 1:1 PEG with 1:2 1-TD, 1:2 PEG with 1:1 1-TD, and 1:2 PEG with 1:2 1-TD due to the great thermal conductivity and large peak area on the heating and cooling process as shown in Fig. 1c, and Fig. 1d. To further

realize the concept of present study, the schematic graph is clearly indicated the temperature difference is proportional to the output electrical current and found out the optimum harvesting field with PEG, and 1-TD composites.

Utilizing a general vacuum-impregnation method to fabricate the PEG and 1-TD composites. The pure PEG and 1-TD are placed on a hot plate at 90 °C and fully melted to the liquid states. After removing the moisture in the melted PCMs, the graphene aerogels are immersed in the liquid PCMs for 8 hours under the vacuum state. After cooling to the room temperature, the PEG and 1-TD composites are successfully fabricated. The PCM composites with different graphene nano-platelet (GNP) mass ratios are labelled 1:1 ratio PEG composite, 1:2 ratio PEG composite, 1:1 ratio 1-TD composite, and 1:2 ratio 1-TD composite. Based on the PEG and 1-TD composites, combined with N and P type semiconductor is shown as 1:1 PEG with 1:2 1-TD, 1:2 PEG with 1:1 1-TD, and 1:2 PEG with 1:2 1-TD composites.

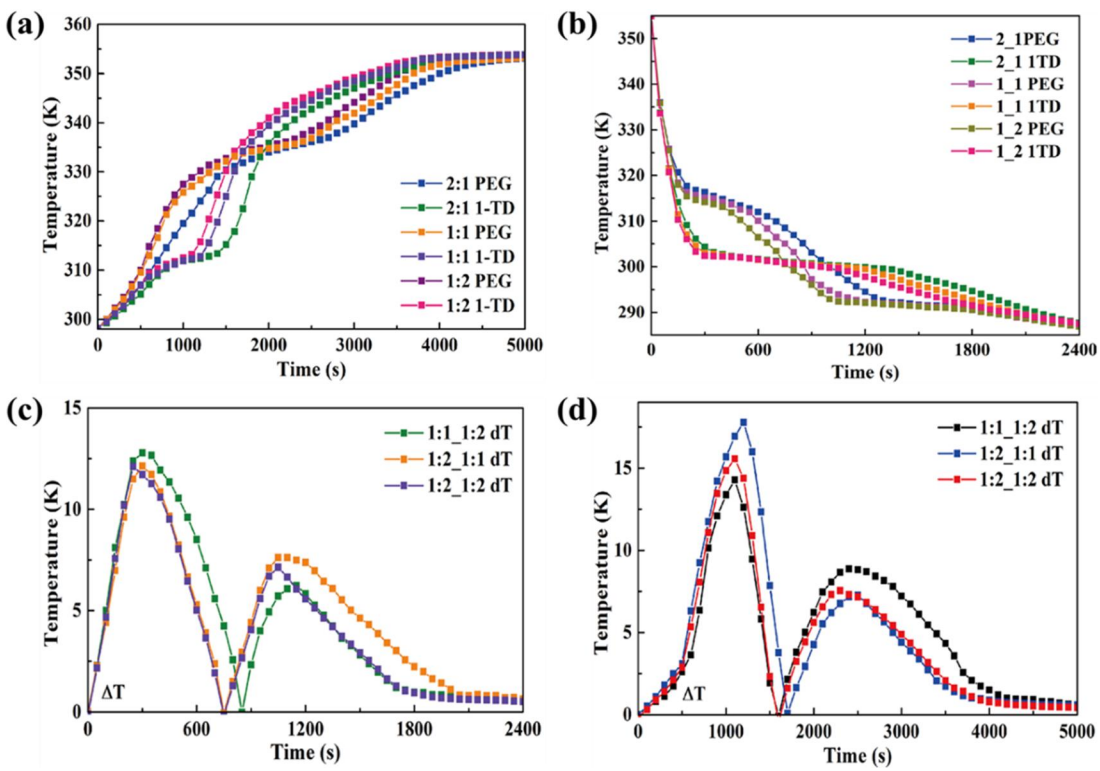

Figure 3.6.2. The temperature profiles with various components by the GNP ratios. (a)

Heating cycle, (b) cooling cycle, (c) the candidate of optimum components and temperature difference upon heating, and (d) temperature difference upon cooling.

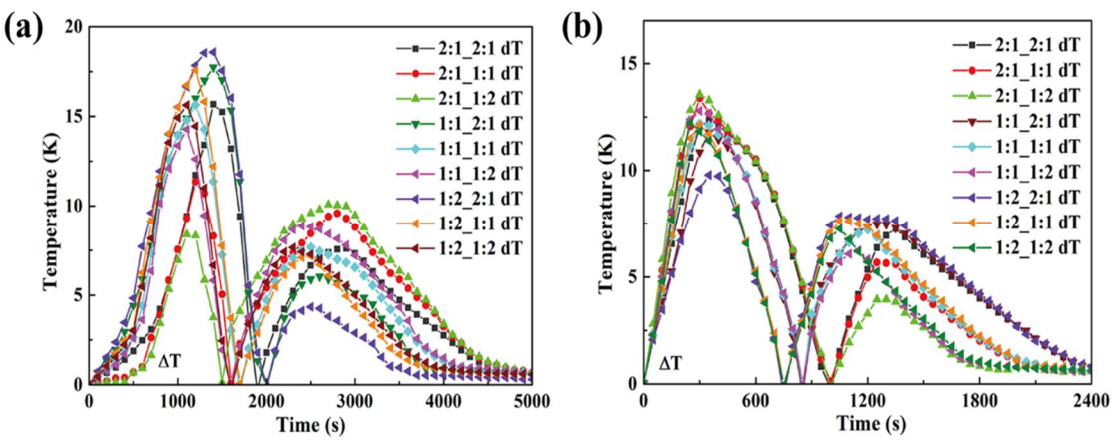

Figure 3.6.3. The temperature difference by each combination of PCMs. The temperature difference upon (a) heating process, and (b) cooling process.

3.6.5. Results and discussion

3.6.5.1 morphologies of PCMs

Before fabricating the PCM composites, the graphene oxide (GO) aerogel with GNP is observed in **Fig. 3.6.4**. It can be seen that the color of 1:1 ratio GO/GNP, and 1:2 ratio GO/GNP aerogel is bright and a little dark as increased the more GNP contents in **Fig. 3.6.4a**, and **Fig. 3.6.4b**. The color is changed to black with hydrazine vapor treatment as shown in **Fig. 3.6.4c**, and **Fig. 3.6.4d**. Demonstrating the reduction of graphene aerogels, the FT-IR peaks are measured and shown in **Fig. 3.6.5**. The GO/GNP aerogel peaks are observed in **Fig. 3.6.5a** and obtained the vibration peaks of some functional groups between the GO and GNP. After reducing the GO/GNPs, the stretching vibration peak of O-H at 3398cm^{-1}, C=O peaks at 1722cm^{-1}, and the C-O stretching vibration peak at the 1056cm^{-1} are totally disappeared and just remained the C=C (1593cm^{-1}, and 1682cm^{-1}) pristine peaks under the graphene and GNP. From the FT-IR graph, the graphene oxide (GO) has successfully reduced by the hydrazine vapor method and just showed the blend structures with the different contents of graphene nano-platelet (GNP).

The shape stability of PEG, and 1-TD composites are observed by a leakage test as shown in **Fig. 3.6.6**. The series of PCMs are placed on the hot plate and heated the temperature from 25 °C to 80 °C. Obviously, the thermal stability is confirmed by utilizing a digital camera. Both pure PEG and 1-TD maintained these solid state in the initial temperature without any leakage. When the temperature is heated to 50 °C, the PEG showed some loss of leakage while the 1-TD is totally melted to the liquid state. In the contrary, the PCM composites still sustained the solid structure at the same conditions. When the temperature is increased to 80 °C, the PEG is gradually melted to the liquid state, but the shape of PCM composites held their initial state without any leakage. It is indicated the 3D porous graphene aerogel can wrap the working materials to prevent the leakage during the phase transition process.

As a supporting material, the morphology of the GNP embedded graphene aerogel is observed in **Fig. 3.6.7**. The graphene skeleton is found to have a porous texture in which known a typical microstructure of graphene aerogel. In **Fig. 3.6.7a**, the embedded GNP is distributed to the graphene skeleton and served as a wrinkle connector and thermal carrier. Increasing the contents of GNP in the graphene aerogel, the surface structure had some more amounts of GNP particles as shown in **Fig. 3.6.7b**. The surface microstructures of PEG and 1-TD composites are shown in **Fig. 3.6.8**. It demonstrated the pure PEG had a flat structure by the **Fig. 3.6.8a**, and the PEG fully infiltrated into the graphene aerogel to make a fracture surface in **Fig. 3.6.8b**, and **Fig. 3.6.8c**. The surface of 1:2 ratio PEG composite had more fractures than that of 1:1 PEG composite due to the complicated internal structure. In **Fig. 3.6.8d**, the 1-TD surface image is similar to the PEG and after possessed the large volume of graphene aerogel, the 1-TD composites with 1:1 and 1:2 components exhibited lamellar structures as observed in **Fig. 3.6.8e**, and **Fig. 3.6.8f**. From the SEM images, there is a significant difference between the pure PCM and PCM composite as existing the GNP embedded graphene aerogel. The crystal structure of PCMs are completely obtained by using the XRD measurement as shown in **Fig. 3.6.9**. The PEG peak is found at 2θ = 19.11 °, and 2θ = 23.24 ° in **Fig. 3.6.9a**, the PEG composites had the same results and it means these samples just occurred the physical reactions on the infiltrating process. The typical peaks of 1-TD are appeared at 2θ = 21.30 °, and 2θ = 24.14 ° and no obvious changes among the 1-TD composites as shown in **Fig. 3.6.9b**. These curves can demonstrate the PEG and 1-TD composites have a great crystalline properties.

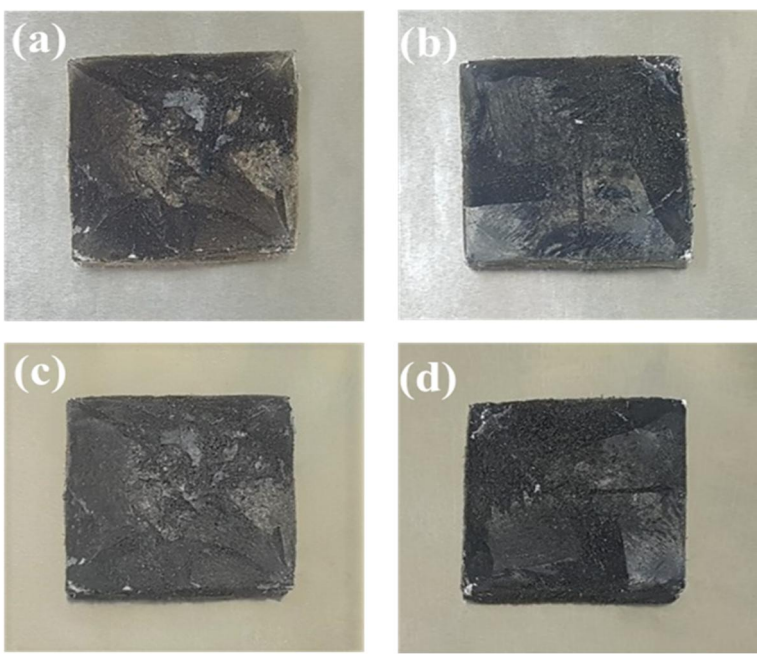

Figure 3.6.4. Graphene oxide (GO) aerogels with (a) 1:1 ratio, (b) 1:2 ratio; the reduced graphene oxide with (c) 1:1 ratio, and (d) 1:2 ratio.

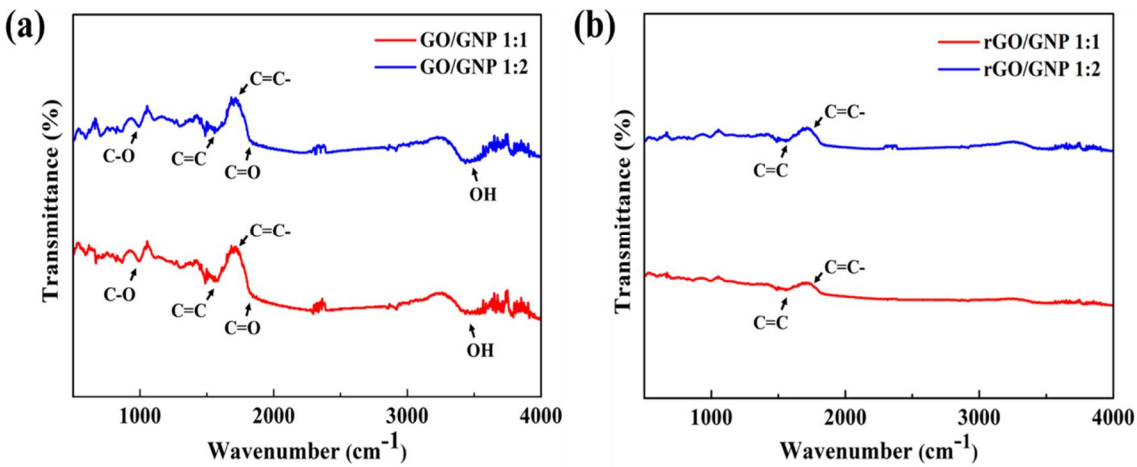

Figure 3.6.5. The FT-IR measurement of 1:1 ratio and 1:2 ratio aerogels. (a) GO/GNP aerogel, and (b) rGO/GNP aerogel.

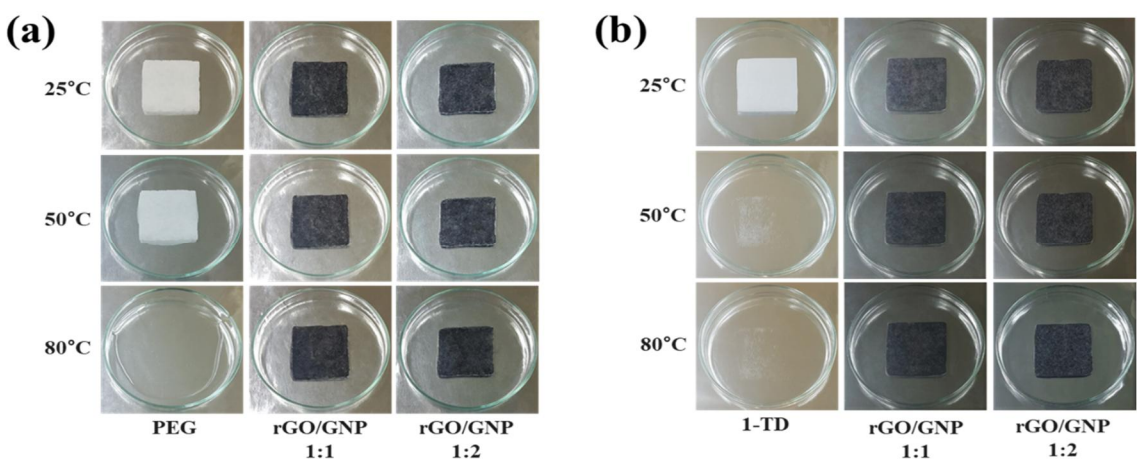

Figure 3.6.6. Form stable camera images of (a) PEG series, and (b) 1-TD series from

25 °C to 80 °C.

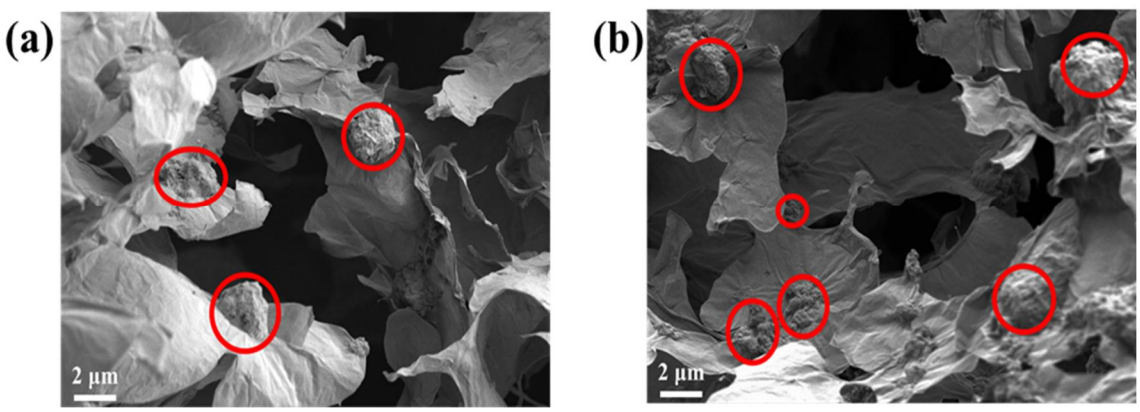

Figure 3.6.7. The graphene aerogel with different GNP weight fraction in (a) 1:1 graphene aerogel, and (b) 1:2 graphene aerogel.

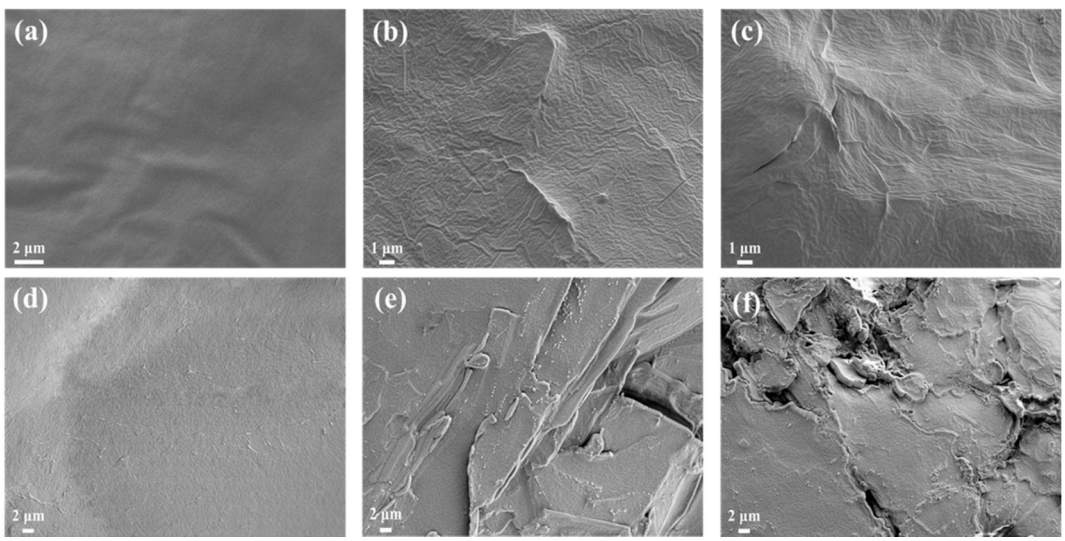

Figure 3.6.8. The SEM images of (a) pure PEG, (b) 1:1 ratio PEG, (c) 1:2 ratio PEG, (d) pure 1-TD, (e) 1:1 ratio 1-TD, and (f) 1:2 1-TD.

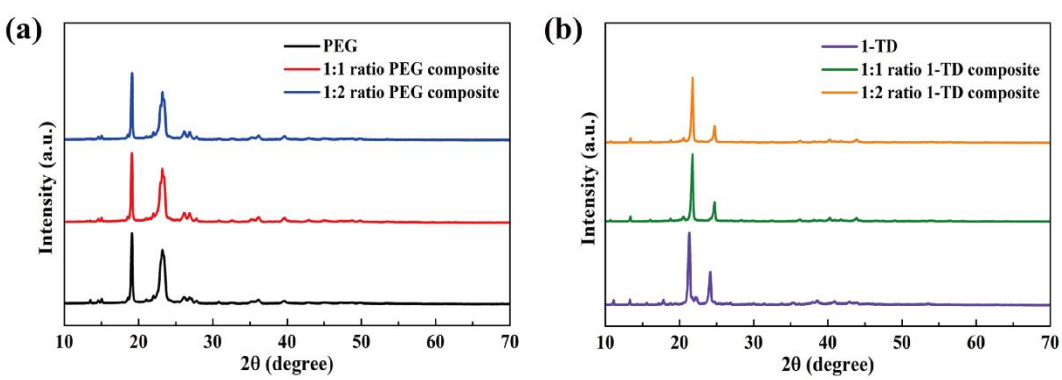

Figure 3.6.9. TheXRD peaks at (a) PEG series, and (b) 1-TD series.

3.6.5.2 DSC measurement of PCM composites

The **Fig. 3.6.10** showed the temperature of phase transitions and latent heat between PEG and 1-TD by utilizing the DSC measurement. The solid-liquid phase transitions are obtained by the sharp peaks on the melting and cooling process. The **Table 3.6.1**, and **Table 3.6.2** are listed the pure PCM, 1:1 ratio PCM composite, and 1:2 ratio PCM composite containing the onset melting and cooling temperature (T_{mo}/T_{co}), both melting and cooling point (T_{mp}/T_{cp}), endset melting and cooling temperature (T_{me}/T_{ce}), and enthalpy of heating and cooling ($\Delta H_m/\Delta H_c$). The onset phase transition temperature of the PEG is measured at 50.91 °C and completed at 70.15 °C to obtain the melting point at 67.22 °C as shown in **Fig. 3.6.10a**. The PEG composites had a little faster onset temperature than that of pure PEG due to the existence of supporting materials. For about the cooling process, the crystallization is started at 42.36 °C and ended at 32.70 °C to find out the cooling peak at 36.04 °C. Similar to the heating process, the PEG composite cooling peaks showed slightly shifted as incorporating the GNP embedded graphene aerogel. The latent heat of pure PEG is 181.71 J/g and 162.14J/g during the heating and cooling transitions. There are just a little diminish of latent heat in the PEG composites which indicated the PCMs could store a lot of heat energy. The **Fig. 3.6.10b** showed DSC curves of 1-TD and the result is similar to the PEG composites. The pure 1-TD is under a solid-liquid phase transitions at 35.54 °C and finished at 45.07 °C to estimate the melting point at 42.15 °C. The 1-TD composites showed a little decreased enthalpy from 223.89J/g to the 210.24J/g and the output results indicated the 1-TD composites maintained sufficient stored energy to utilize in the energy harvesting system applications.

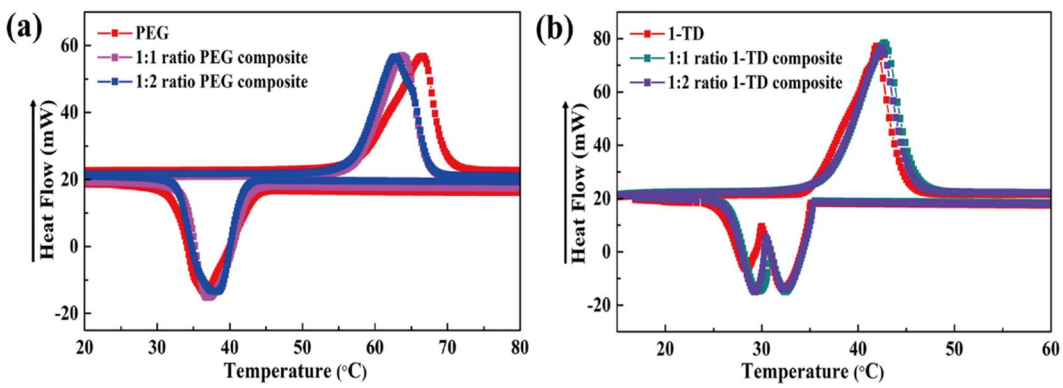

Figure 3.6.10. DSC peaks around the PCMs by (a) PEG series, and (b) 1-TD series.

Table 3.6.1. The DSC heating and cooling properties of PEG, and PEG composites.

Samples	T_{mo}(°C)	T_{me}(°C)	T_{mp}(°C)	ΔH_m(J/g)	T_{co}(°C)	T_{ce}(°C)	T_{cp}(°C)	ΔH_c(J/g)
PEG	50.91	70.15	67.22	181.71	42.36	32.70	36.04	162.14
1:1 composite	49.09	67.54	63.94	179.72	43.46	33.21	36.47	161.29
1:2 composite	47.93	67.94	63.42	178.67	44.09	33.67	36.95	160.65

Table 3.6.2. The DSC heating and cooling properties of 1-TD, and 1-TD composites.

Samples	T_{mo}(℃)	T_{me}(℃)	T_{mp}(℃)	ΔH_m(J/g)	T_{co}(℃)	T_{ce}(℃)	T_{cp}(℃)	ΔH_c(J/g)
1-TD	35.54	45.07	42.15	223.89	35.52	20.04	30.28	217.07
1:1 composite	35.26	45.89	43.19	211.60	35.87	20.24	30.83	211.82
1:2 composite	35.18	45.37	42.40	210.24	36.16	20.32	31.04	209.52

3.6.5.3 Optimum electrical measurement in the energy harvesting system

The selected PEG and 1-TD composites are placed on the sides of N and P type semiconductor and the output electrical current under heating and cooling process are observed in **Fig. 3.6.11**. The range of temperature defined from 25 °C to 80 °C and the electrical current with three different combination groups on the melting transition is showed in **Fig. 3.6.11a**. The 1:2 PEG and 1:1 1-TD composites exhibited the best current output peak in the 1st phase transition field and maintained a long field of energy harvesting while the rest 2 groups had lower output current in the range of melting conditions. The maximum current of 1:1 PEG and 1:2 1-TD PCM composite are 9.36mA around 840 s, and 6.92 mA at 2,344 s, respectively. Because of the higher temperature difference, the output maximum current by 1:2 PEG and 1:1 1-TD group showed 11.81 mA at 918 s and 2nd transition is 6.11 mA with 2,275 s. For the large contents of both 1:2 PEG and 1-TD combination groups appeared 10.30 mA at 780 s, and 6.12 mA at the 2,098 s in the melting process. For the cooling current peaks with the same combination groups are shown in **Fig. 3.6.11b**. The harvesting system is under the natural conditions to arrive at the room temperature. The cooling rate is increased rapidly due to the natural crystallizations. The maximum cooling peaks of 1:1 PEG and 1:2 1-TD group is 10.59 mA at 236 s, and 5.18 mA near the 1,100 s. The 1:2 PEG and 1:1 1-TD combination composites had the maximum output current of 9.71 mA at 283 s, and 6.63 mA at 994 s. The last combination group 1:2 ratio PCM composites showed the 9.95 mA at 205 s, 5.71 mA at about 930 s. According to the heating and cooling results, the 1:2 PEG and 1:1 1-TD PCM composites could generate the largest output current during the phase transition

process.

The combination with LED lamp is generally identified the output harvesting energy on the melting and cooling process. Before observing the LED lightness, it is necessary to demonstrate the maximum power and the peaks are shown in **Fig. 3.6.12**. During the heating time, the maximum value of 1:1 PEG and 1:2 1-TD is 378.27 μW at the 1st phase transition and 206.90 μW in the later process. As for the 1:2 PEG and 1:1 1-TD group had the largest output value of 602.25 μW at the first transition field and implied 161.23 μW at the 2nd curve. The 1:2 PCM composites showed the 457.77 μW and 161.64 μW in **Fig. 3.6.12a**. The result of cooling peaks indicated the 1:2 PEG and 1:1 1-TD had the optimum value of 484.62 μW and 115.65 μW as shown in **Fig. 3.6.12b**. The comparison between the 1:1 PEG, 1:2 1-TD group and 1:2 PCMs is found at 405.08 μW, and 189.73 μW; 427.22 μW, and 140.65 μW. Based on the former output maximum power result, the harvesting system had insufficient power to turn on the LED lamp. Thus, connected to a low voltage start-up converter (LTC 3108) between the harvesting system and LED lamp as shown in **Fig. 3.6.12c** [160, 196]. To investigate the harvesting time under the phase transitions, the LED arrangement results are observed in **Fig. 3.6.11c**, and **Fig. 3.6.11d**. The onset and maximum time of LED on the heating and cooling process are listed in **Table 3.6.3** and **Table 3.6.4**. The onset time is depended on the temperature rate that 1:2 PEG and 1:1 1-TD could turn on the LED lamp at 380 s under melting transitions. In addition, the maximum time of LED lightness is coincided to the experimental current among the PCM composites. The cooling process showed the similar result that the 1:2 PEG and 1:1 1-TD combination system appeared the larger harvesting field than that of other group. From the **Fig. 3.6.11**, the harvesting system connected the converter had an adequate output power to turn on the LED lamp and combination 1:2 PEG with 1:1 1-TD showed the optimum thermoelectric energy conversion on the phase transition process.

For the purpose of confirming the energy harvesting abilities, the output light intensity of LED lamp is obtained by following to the LED lightness in **Fig. 3.6.13**. Consider the heating process, the 1:2 PEG and 1:1 1-TD behaved the highest value of light intensity near the 1.2 $\mu molm^{-2}s^{-1}$. The average light intensity among the three combination groups showed the output energy usability in the harvesting field and the value is 0.188 $\mu molm^{-2}s^{-1}$ under the 1:1 PEG with 1:2 1-TD group as observed in **Fig. 3.6.13a**. The 1:2 PEG and

1:1 1-TD group showed the largest average output in **Fig. 3.6.13b** while the result is 0.190 μmolm^{-2}s^{-1} in the combination of 1:2 PCM composites (**Fig. 3.6.13c**). Unlike the heating process, the cooling results showed that the 1:1 PEG and 1:2 1-TD group had a similar average output intensity with the 1:2 PEG and 1:1 1-TD group in **Fig. 3.6.13d**, and **Fig. 3.6.13e**. The high GNP embedded 1:2 PCMs indicated the 0.185 μmolm-2s^{-1} of average value as shown in **Fig. 3.6.13f**. According to the experimental current peaks and light intensity results, the optimum selection group is 1:2 PEG and 1:1 1-TD combinations.

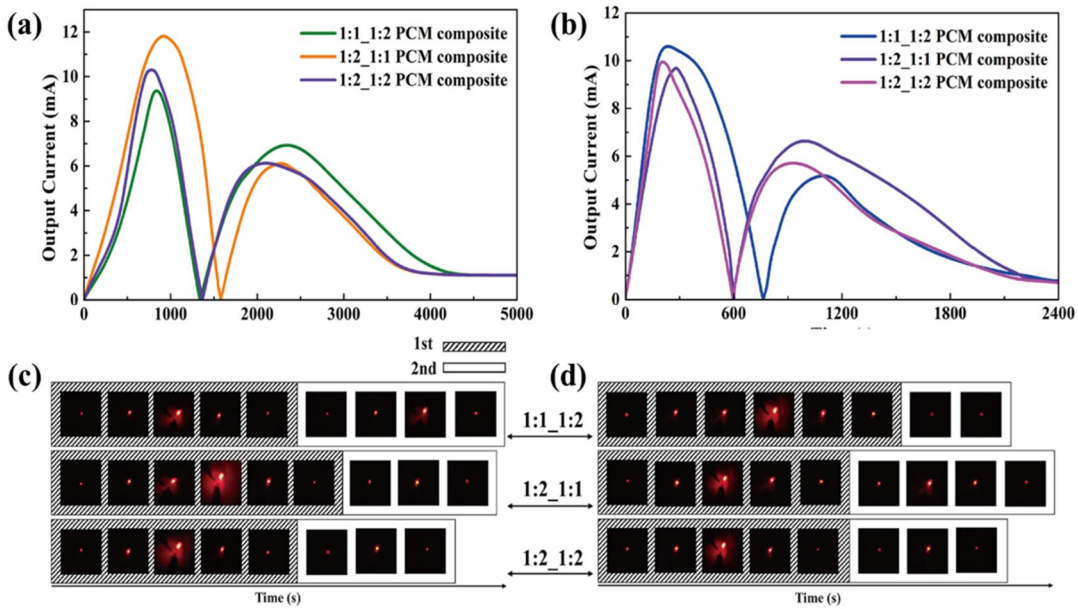

Figure 3.6.11. (a) current peaks upon heating, (b) current peaks upon cooling, (c) The LED bulb truned on process upon heaitng, and (d) LED images upon cooling.

Table 3.6.3. The LED start-up time, maximum lightness, and endset time for heating process.

Time (s)	Onset (1st)	t_1 (max)	Endset (1st)	Onset (2nd)	t_2 (max)	Endset (2nd)	Total
(PEG)1:1_(1-TD)1:2	544	838	1121	1778	2343	2968	1767
(PEG)1:2_(1-TD)1:1	380	919	1422	1958	2274	2647	1731
(PEG)1:2_(1-TD)1:2	472	779	1149	1746	2097	2691	1622

Table 3.6.4. The LED strat-up time, maximum lightness, and endset time for cooling process.

Time (s)	Onset (1st)	t_1 (max)	Endset (1st)	Onset (2nd)	t_2 (max)	Endset (2nd)	Total
(PEG)1:1_(1-TD)1:2	84	235	627	1048	1099	1141	636
(PEG)1:2_(1-TD)1:1	109	282	503	767	995	1404	1031
(PEG)1:2_(1-TD)1:2	98	206	466	790	928	1108	686

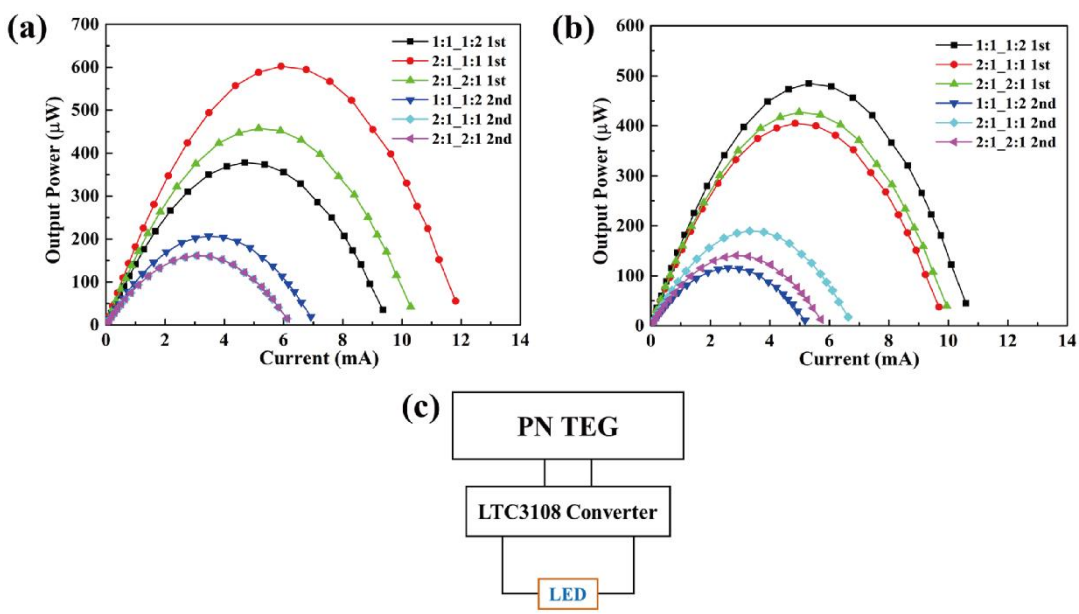

Figure 3.6.12. The power output during (a) heating cycle, and (b) cooling cycle. The transformer (LTC 3108) of (c) combine with LED bulb.

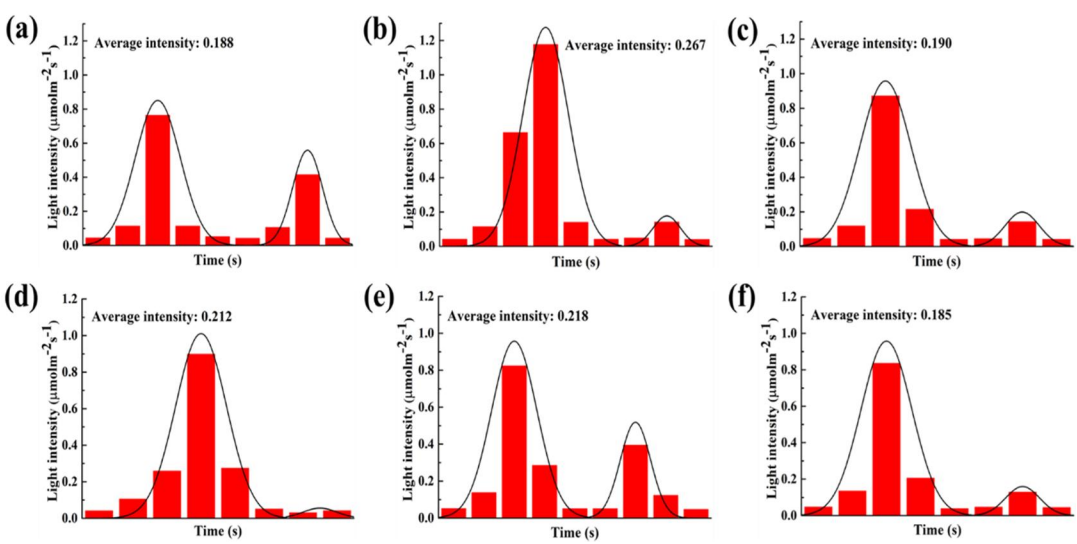

Figure 3.6.13. The light intensity results with (a) 1:1 PEG and 1:2 1-TD component, (b) 1:2 PEG and 1:1 1-TD component, (c) 1:2 PEG and 1:2 1-TD. The cooling of (d) 1:1 PEG and 1:2 1-TD, (e) 1:2 PEG and 1:1 1-TD, and (f) 1:2 PEG and 1:2 1-TD.

3.6.5.4 Numerical analysis and thermal stability of optimum PCMs

In order to calculate the optimum PCMs during the heating and cooling process, the numerical simulation results with experimental currents are shown in **Fig. 3.6.14**. The range of temperature is from 25 °C to 80 °C on the melting transition and the result is indicated in **Fig. 3.6.14a**. The change of temperature is similar in the arising curves, and the maximum current is calculated 12.45 mA at 1,200 s in the 1st phase transition and near 5.8 mA at the 2,500 s in the 2nd position. The theoretical calculation is close to the experimental result which indicated the correct output peak during the melting process. For the cooling transition, the temperature is decreased from 80 °C to room temperature and the temperature profile is shown in **Fig. 3.6.14b**. The two maximum numerical peak is 9.75 mA at 300 s and about 6.20 mA at the 1,100 s. Similar to the heating process, it is generally matched with the experimental result and the numerical calculation indicates the 1:2 PEG and 1:1 1-TD group is selected to the optimization groups of the thermoelectric energy harvesting system. The **Fig. 3.6.14c** shows the calculation of thermoelectric energy harvesting efficiencies during the heating and cooling process are 62.26 %, 39.96 % respectively.

In order to obtain the maximum current from the selected PCM composites, peak ratios

are directly measured as shown in **Fig. 3.6.15**. There are easy to find that the 1:2 PEG and 1:1 1-TD group has the highest ratio of peak area in both heating and cooling process. The value of these ratios calculated upon heating and cooling are given as 1.16, and 1.22 (1:1 PEG and 1:2 1-TD group shows 1.05 upon heating; 1.10 upon cooling. The 1:2 PEG&1-TD group is a standard in this **Fig. 3.6.15** and shows 1.0 upon heating and cooling). Furthermore, obtaining the thermal stability of optimum PCMs, TGA results are shown in **Fig. 3.6.16** and derivative data is listed in **Table 3.6.5**, and **Table 3.6.6**. The 1:2 PEG showed significant weight loss at 380.15 °C which is lower than that of pure PEG due to the enhancement of thermal conductivity in **Fig. 3.6.16a**. The residual mass of 1:2 PEG is about 3 % and it indicated the existence of graphene and embedded GNP. The onset temperature of 1:1 1-TD is 170.66 °C and remained the supporting materials during the phase transition process. Hence, the combination of 1:2 PEG and 1:1 1-TD had a great thermal stability during the phase transitions which could be expected to utilize in the solar cell, and heat recovery applications.

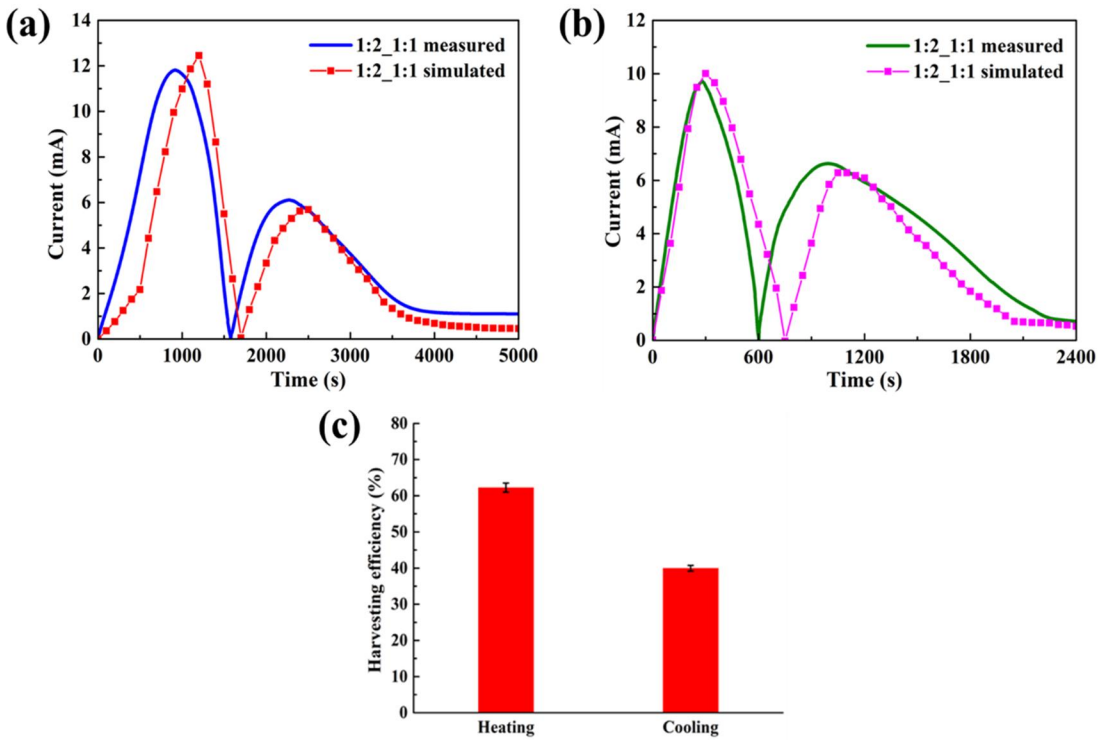

Figure 3.6.14. The experimental current with numerical calculation (a) upon heating process, (b) upon cooling process, and (c) thermoelectric energy harvesting efficiencies.

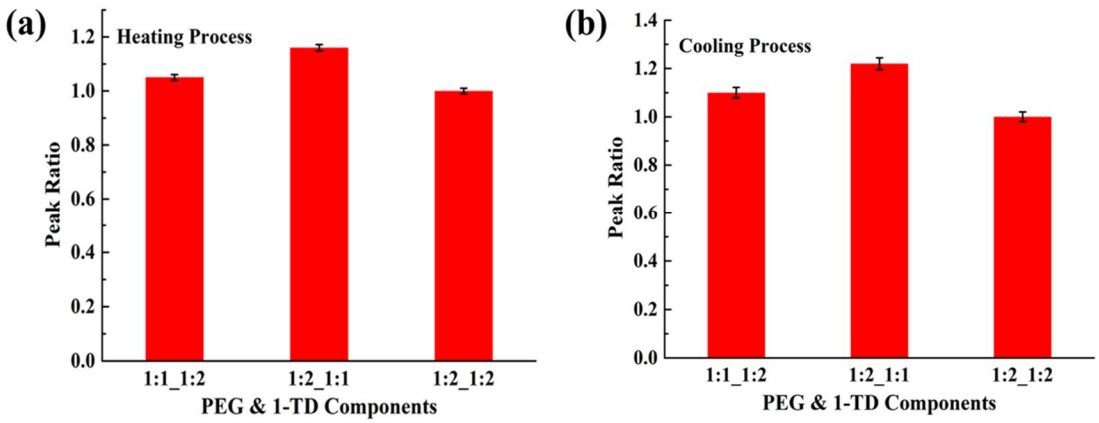

Figure 3.6.15. The ratio of current peaks upon (a) heating process, and (b) cooling process.

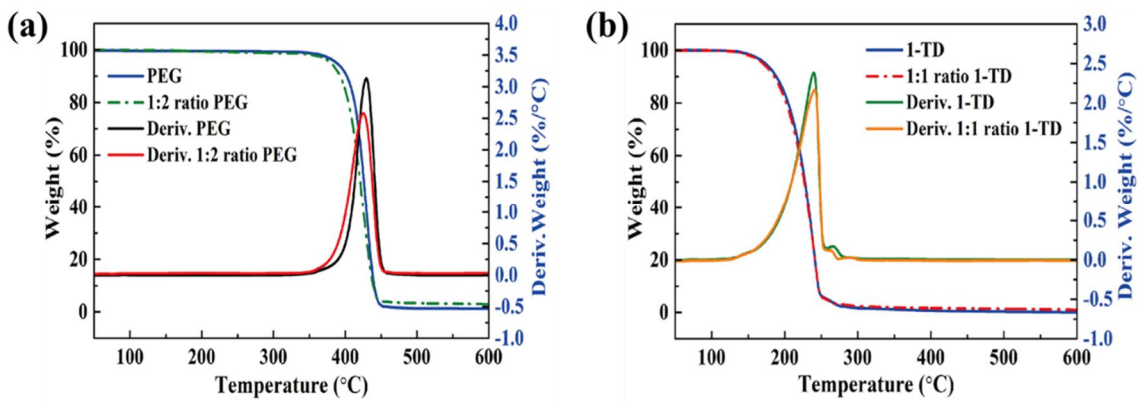

Figure 3.6.16. The TGA results of (a) PEG series, and (b) 1-TD series.

Table 3.6.5. TGA data of pure PEG, and 1:2 ratio PEG composite under N_2 atmosphere.

Samples	Onset (°C)	Peak (°C)	Endset (°C)	Residual mass (%)
PEG	388.15	429.27	444.40	1.52
1:2 PEG	380.16	425.13	442.84	3.03

Table 3.6.6. TGA data of pure 1-TD, and 1:1 ratio 1-TD composite under N_2 atmosphere.

Samples	Onset (°C)	Peak (°C)	Endset (°C)	Residual mass (%)
1-TD	173.61	239.70	264.74	0.12
1:1 1-TD	170.66	240.92	263.61	1.05

3.6.6. Conclusions

In the present study, we successfully obtained the optimum combination of PEG and 1-

TD composites with different GNP mass ratio. Modified the working materials in which is able to generate more electrical output current on the heating and cooling process. The PEG and 1-TD composites are stored and released large heat energy with no significant loss under the phase transitions to generate a renewable thermoelectric energy conversions. The electrical output current from the device of system is experimentally observed and found out the most appropriate fields of PCM composites. These output harvesting result is confirmed by the light intensity and selected the optimum 1:2 PEG and 1:1 1-TD group during the phase transition process. The variation of temperature profiles are numerically calculated the induced current using a finite element method (FEM). The simulation result is agreed with the experimental peaks and further demonstrated the optimum constitution of thermoelectric energy harvesting system and prospected to the heat sensor, bio-energy, and medical device applications.

3.7. Summary

The PCMs for thermoelectric energy harvesting system can generate the output electrical current upon heating and cooling process. The temperature difference within the phase transition field could lead to the induced current in the closed circuit due to the electron movement around the PN TEG. In Section 3.3, the single PN cell energy harvesting system is directly demonstrated the two different PCMs (PEG, and 1-TD) combined with the PN TEG can generate the electrical current. The developed harvesting system is composed of multiple phase change materials and sufficiently utilized the excess thermal energy in the 2nd step upon melting/cooling process in Section 3.4. The GNP ratios affecting the rate of thermoelectric energy harvesting system are effectively obtained in Section 3.5 and 1:2 GO/GNP manufactured graphene aerogel exhibits the highest heat transfer rate during the phase transition process. Consider the GNP weight fraction of PCM composite, the optimization group of energy harvesting system with PEG, and 1-TD are obtained by calculating the maximum output electrical energy and the group of 2:1 PEG with 1:1 1-TD composite produces the maximum output electrical energy in comparison of other PCM groups (Section 3.6). The optimization group of PCM composites are subsequently utilized in the modified supporting material application and even increased their thermoelectric energy conversion efficiency.

Chapter IV.

Modified PCMs for energy harvesting

4.1. Overview

Graphene aerogel is a type of widely utilized aerogel which is strong enough for latent heat thermal energy storage (LHTES) applications due to the large surface area, appropriate electrical conductivity and excellent chemical stability. Hence, three dimensional interconnected micro-pores offer many potential advantages such as low density, high porosity and mass transfer, and easy to access the container like material storage applications. These fantastic properties allow graphene aerogels to be intensively applied for thermoelectric energy harvesting applications. However, the manufactured graphene aerogels still suffer from their low mass fraction and high fragility [213]. Both relatively low mechanical property especially the brittleness of physically cross-linked graphene aerogels become a critical challenge for their new applications. Until now, some of modified attempts have been indicated to overcome these problems. In this perspective, the present research suggests the recent research development towards the advanced modified graphene aerogel based PCM composites according to the different kinds of approaches such as internal porosity, composition of graphene skeleton, and structure controls. The recently proposed supporting materials of graphene aerogel is improving the internal performance of capacities and mechanical durability of the pristine graphene aerogels for a new applications [214].

In addition, the volume shrinkage of the graphene aerogel causes the mass loss of the working material during the infiltration process. The capillary force which gives rise to the deformation of graphene aerogel and construct a rugged surface structure. Thus, the PDMS embedded graphene aerogel could resist the capillary force until the end of reaction and sufficiently infiltrate the pure PCM into the internal volume space. The thermal energy is correlated to the weight fraction of working materials which is

implicated in the governing equation of latent heat theory. More incorporated pure PCMs could absorb or release more thermal energy to transmit the output electrical energy and increase the thermoelectric energy conversion efficiency.

Porous graphene based aerogels hold great features for infiltration method due to their high porosities. However, weak connections between the graphene oxide nano-sheets cause poor connectivity and incompressibility around the graphene aerogels for their practical applications. Herein, the small organic molecule of cysteamine is selected as a covalent cross-linker to fabricate the graphene cross-linked aerogel (GCA) through a solvent vapor method. The mechanical property of GCA is significantly improved due to strong covalent cross-linking between the graphene oxide nano-sheets with the cysteamine as a linkage. The resultant GCA maintains the excellent structural stability at over melting temperature and even tolerate the external force. Therefore, the as-prepared aerogels with high porosity and mechanical property, structural stability and excellent recoverability have a great potential in recyclable and durable materials for infiltrating more working materials and increase the thermoelectric energy conversion efficiency.

4.2. Review of modified PCMs

4.2.1. Introduction

The form stable phase change materials (PCMs) composite is well fabricated by using vacuum infiltration method in previous work. It is indicated that the graphene aerogel can sustain the most of working materials to prevent the leakage problem upon melting process. The large porosity of graphene aerogel is one of the typical advantages as compared with the microcapsule of shell material. However, the existence of capillary force during the infiltration process appears the volume shrinkage of graphene aerogel and lead to some of the volume loss for infusing working material. The key point of thermoelectric energy harvesting efficiency is the mass of PCM composite and the shrinkage problem causes the decrease of energy harvesting efficiency during the phase transition process.

In order to overcome the volume shrinkage problem, two different method for manufacturing the modified supporting material is directly mentioned and these new kind of graphene aerogels are able to infiltrate more pure PCMs than that of pristine aerogels. The graphene aerogel with flexibility is a great solution for reducing the shrinkage problem where the PDMS dispersed into the graphene skeleton can resist the capillary force under the infiltration process. The second alternative for modified graphene aerogel is fabricating the cross-linked graphene aerogel which significantly improved the mechanical property to tolerate the volume shrinkage. In this cross-linking method, cysteamine acts as a cross-linker to connect the graphene oxide (GO) nano-sheets and construct a net-like internal structure. The chemical process to modify the initial graphene oxide (GO) aerogel can hold the external force over the melting temperature (T_p) without any weight loss and sufficiently fabricate the form stable PCM composite.

4.2.2. Theoretical background

The leakage problem is well worked out by using supporting materials such as microencapsulated shell materials, and 3D structural aerogels. Comparing with the shell materials, the 3D aerogels can wrap more working materials due to the high porosity [215]. The infiltrated PCM composites are almost hold their typical properties and relatively high thermoelectric energy harvesting efficiency in the combination of PN TEGs. However, the volume shrinkage as mentioned before exists the decrease of pure PCMs infiltrating into the internal pore structures. The weight of pure PCM is proportional to the output thermal energy and directly influence the thermoelectric energy conversion efficiency.

In recent years, the PDMS embedded supporting materials are began to utilize for manufacturing an advanced shape stabilized aerogels. Owing to the flexible property among the PDMS, the modified aerogels especially graphene aerogel become more stable and increase the weight of pure PCMs. The shrinkage is reduced significantly and the fabricated PCM composites possess the relatively flat surface structure and directly utilized for the thermoelectric energy harvesting system. However, the external force is a challenge to the PCM composites and enhancing the mechanical property becomes an important mission for manufacturing the form stable PCM composites. According to the weak durability at the high temperature, this study will provide the cross-linked graphene aerogel with cysteamine and highly improved the mechanical property of PCM composite. As a result, the cross-linked aerogel/PCM can maintain the intrinsic state without any weight loss or even leakage during the heating and cooling process.

4.2.3. Combination of PCMs

In the previous research, the combination of 1:2 PEG and 1:1 1-TD composites is demonstrated as an optimization group for the thermoelectric energy harvesting system. Based on the latent heat thermal energy storage (LHTES) applications, increase the output energy harvesting efficiency is important for the utilization of thermal energy storage (TES). The PDMS embedded graphene aerogel is emerged on the melted PCM for several hours, the volume shrinkage is directly reduced and the final weight of PCM composite should be increased. The contact angle measurement can obtain the hydrophobicity to confirm the infiltration ability and fabrication of the PCM composite. To further increase the mechanical property of these supporting materials, the cross-linked graphene aerogel is the most appropriate way to fabricate the shape stabilized porous structure. Before constructing the cross-linked aerogel/PCM composite, the cysteamine can develop the net-like internal structure by connecting the graphene oxide (GO) nano-sheets. Thus, the cross-linked graphene aerogel supported PCM composite shows a high mechanical property and even resist the external force under the melting and crystallization process.

4.2.4. Conclusions

The modified supporting materials for fabricating the PCM composites are able to increase the mechanical property and contribute to the thermoelectric energy harvesting efficiency. Consider the volume shrinkage during the vacuum infiltration process, preventing the volume loss is vital to generate a fully charged PCM composite. Except the leakage under the solid-liquid phase transition process, overcome the shrinkage makes a form stable with high efficiency of thermoelectric energy harvesting. The first method for fabricating the modified graphene aerogel is embedded PDMS to prevent the volume loss. The PDMS incorporated graphene aerogel has a flexible property to recovery the initial state and maintain 3D porous structure upon melting and cooling. Hence, more weight of working material causes the higher thermoelectric energy harvesting efficiency due to the increase of pure PCM. The second way for fabricating the modified PCM is constructing the cross-linked supporting material and increase the thermoelectric energy harvesting efficiency. It is demonstrated that the high mechanical property can hold the shape stability and directly prevent the volume shrinkage.

4.3. PDMS modified PCMs for energy harvesting

4.3.1. Introduction

Polymer nanocomposites, where including the supporting materials have been reported to increase the form stability, have been investigated to sustain the intrinsic state at the temperature variation [216, 217]. The supporting materials are utilized as a container with low mass fraction and make more applications related to the organic materials. The thermal energy storage (TES) is the popular project in the polymer research due to the high thermal density for absorbing the initial thermal energy to transmit the electrical or optical energy [218]. Therefore, the phase change materials (PCMs) which regarding as the optimum candidate for the thermal energy utilization with high heat of fusion, appropriate phase transition field, and high thermal stabilities [219]. Kinds of PCMs categories are mentioned in various studies and the organic PCMs possess the large portion of their thermal energy storage applications. The organic PCMs are able to generate the solid-to-liquid phase transition upon melting and recovery the initial shape after removing the heat source and store a great deal of thermal energy for energy harvesting [220]. In spite of the high thermal energy storage advantage, leakage problem is inevitable challenge around the PCMs which is restricted seriously in the normal utilizations [63, 221].

To address the leakage problem, the supporting materials are described as form stabilizer and combined with the pure PCMs. In the conventional researches, the spherical structure of PCM nanocomposites are produced by using microencapsulation method and the supporting materials can entangle to the pure PCMs [222]. Hence, the PCM microcapsules maintain the solid state without any leakage under the phase transition process. However, the spherical microcapsules still give rise to the high reduction of latent heat due to the replacement of supporting materials [223]. It is indicated that only the pure PCMs have ability for controlling the thermal energy and increase the weight fraction is the vital matter in the PCM composite. Except for solving the leakage problem,

incorporating the most of working material in the PCM composite becomes a primary task and selects a new supporting material with high porosity is desirable and improved the PCM weight fraction.

Based on the requirements of supporting materials, the aerogel like materials are generally utilized for the manufacture of form stable PCM composites due to the 3D high porous internal structure and have enough pore space to infiltrate the working materials. These PCM composites possess high weight fraction of working material and sustain the solid state during the melting and cooling process. In spite of high porosity of these aerogels, low thermal conductivity and brittle properties are limited the applications and recommend the carbon based aerogel especially graphene aerogel is more attracted than any other supporting material. For about the graphene aerogel, relatively high thermal conductivity and mechanical property is the main advantages and maintains the porous structure under the temperature variation [224]. Therefore, the graphene aerogel based PCM composites exhibit a high energy storage density and effectively apply to the thermoelectric energy harvesting [225]. Consider the thermal conductivity is important for the rate of thermoelectric conversion, embedding graphene nano-platelet (GNP) is one of the practical way in the previous work. As a result, the supporting material consists of graphene aerogel, PDMS, and graphene nano-platelet (GNP) performs high thermal energy capability without any weight loss upon melting and cooling process [72].

In this study, we introduce PDMS attached two different PCM composites such as polyethylene glycol (PEG) and 1-tetradecanol (1-TD) for developing the thermoelectric energy harvesting system. The PN TEGs are employed in the harvesting system which can generate the electron movement under the temperature difference due to the Seebeck effect. The PCM composites are placed on the PN TEGs and obtain the electrical current during phase transition process. In addition, higher weight fraction of working material could extend the harvesting time and increase the thermoelectric energy harvesting efficiency. To calculate the prediction of temperature variation upon heating and cooling cycles, the numerical modeling is examined by using a finite element method (FEM) and comparing with the experimental result.

4.3.2. Preparation of energy harvesting system

Based on the Seebeck effect, the PDMS embedded graphene aerogel is selected as a new supporting materials and constructed a modified PCM composite. According to the previous research, the energy harvesting system is composed of modified PCM composites with multiple PN cells. The PEG and 1-TD composites are placed to the edge of PN cells and obtaining the electrical current due to the temperature difference. As the temperature profiles are reversed and the harvesting system can generate the 2nd electrical current due to the Seebeck effect. The increase of working materials gives rise to the higher thermoelectric energy conversion efficiency. The output harvesting energy is ensure to turn on the LED bulb and the illustration of the PDMS modified energy harvesting system is shown in **Fig. 4.3.1**.

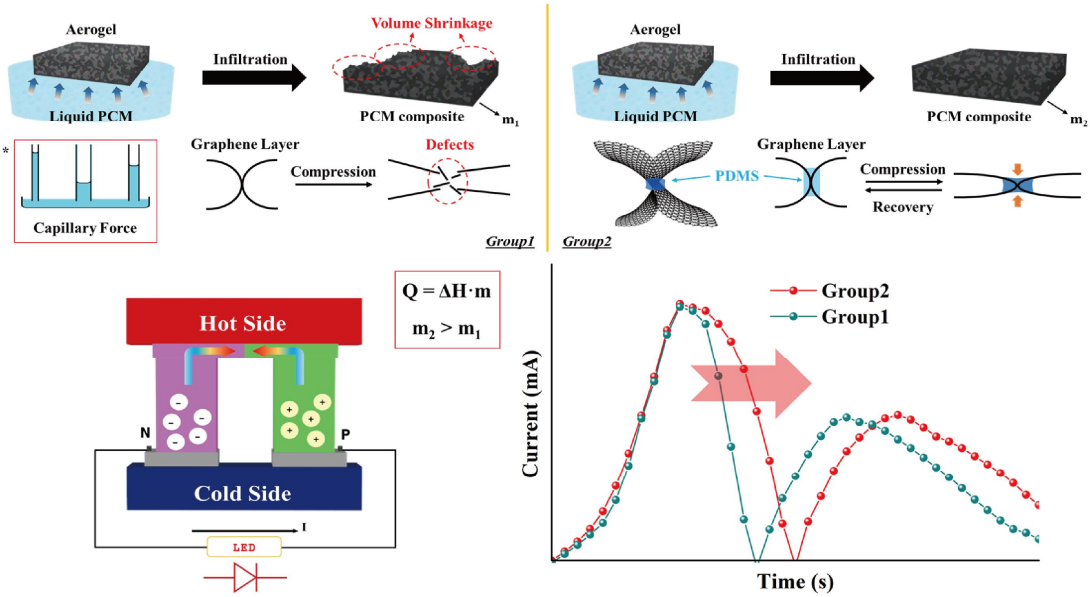

Figure 4.3.1. Schematic of PDMS embedded graphene aerogel and PCM composites for thermoelectric energy conversion.

4.3.3. Numerical analysis

The modeling for predicting temperature profiles is utilized a finite element method (FEM), COMSOL Multiphysics commercial software. The energy harvesting system is composed of two groups of PN TEGs, PEG composites, coppers, and 1-TD composites. The PEG composite is designated to the hot side of PN cells due to the higher melting temperature than that of 1-TD composite. The density of PEG, and 1-TD composites, latent heat (ΔH), thermal conductivity, heat capacity, melting temperature (T_m, T_c) of each PCM composite. The copper is combined the PN cells with two different PCM composites. Based on the features of PN TEGs, the doped materials are given as Bi_2Te_3, and $Bi_{0.3}Sb_{1.7}Te_3$; and the Seebeck coefficient is depended on the temperature variation during the melting and cooling process. The numerical simulation has the 10,178 total mesh.

The basic governing equation of heat transfer model is defined as:

$$\rho C_p \frac{\partial \mathbf{T}}{\partial t} + \rho C_p u \cdot \nabla \mathbf{T} + \nabla \cdot \mathbf{q} = Q \qquad \text{Eqn (1)}$$

where ρ is mass density and C_p means heat capacity. The heat transfer rate $\mathbf{q}$ is correlated to the thermal conductivity k and $\mathbf{q} = -k\nabla T$ which depends on the temperature variation. The density of phase change materials (PCMs) is described as:

$$\rho = \theta\rho_{phase1} + (1-\theta)\rho_{phase2} \qquad \text{Eqn (2)}$$

where, the fill-factor θ is related to some of these parameters ($C_p, k, \text{and } \alpha_m$) and given as:

$$C_p = \frac{1}{\rho}\left(\theta\rho_{phase1}C_{p.phase1} + (1-\theta)\rho_{phase2}C_{p.phase2}\right) + L\frac{\partial \alpha_m}{\partial T} \qquad \text{Eqn (3)}$$

$$k = \theta k_{phase1} + (1-\theta)k_{phase2} \qquad \text{Eqn (4)}$$

$$\alpha_m = \frac{1}{2}\frac{(1-\theta)\rho_{phase2} - \theta\rho_{phase1}}{\theta\rho_{phase1} + (1-\theta)\rho_{phase2}} \qquad \text{Eqn (5)}$$

where, α_m is the mass coefficient during the phase transitions process and the boundary condition is referred to the external natural convections as follow:

$$-\mathrm{n} \cdot \mathbf{q} = \mathbf{q_0} \qquad \text{Eqn (6),}$$

where n means the normal vector, and the convection of heat flux is $\mathbf{q_0}$. The heat transfer coefficient ($\mathrm{h_{air}}$) is one of the parameters in heat flux equation as below:

$$\mathbf{q_0} = \mathrm{h_{air}} \cdot (\mathbf{T_{ext}} - \mathbf{T}) \qquad \text{Eqn (7)}$$

The Seebeck coefficient S is the key of constant to calculate the value of output electrical current and given as:

$$\mathrm{S} = \sqrt{\frac{\mathrm{k}}{\sigma \mathrm{T}}} \qquad \text{Eqn (8)}$$

where, σ shows the electrical conductivity and the calculated current from modeling is a function of the Seebeck coefficient S, temperature difference ($\Delta\mathbf{T}$), and resistance of PN TEG (R) as followed:

$$\mathrm{I} = \frac{\mathrm{S}\Delta\mathbf{T}}{R} \qquad \text{Eqn (9)}$$

The efficiency of thermoelectric energy conversion is corresponding to the converted energy W and the total stored energy Q as below:

$$\eta = \frac{W}{Q} \qquad \text{Eqn (10)}$$

4.3.4. Preparation of PDMS embedded PCM composites

Before manufacturing the PDMS embedded graphene aerogels, the graphene oxide (GO) is synthesized by using the modified Hummers' method. The GO/GNP aerogel is obtained by the freeze-drying process which has mentioned in our previous work. After the hydrazine treatment, the color of graphene aerogel turns black and it indicates the reduced graphene/GNP aerogel is fabricated successfully. The graphene aerogel then placed on the vacuum oven at 80 °C and PDMS/Hexane solution is sprayed effectively into the graphene aerogel to impregnate the PDMS dispersed in the internal skeleton of

graphene aerogel. After 2 hours at 80 °C, the PDMS embedded graphene aerogel is removed and utilized as a supporting material. The fabrication of PCM composites are same to the previous research in which utilizing the vacuum-impregnation method to obtain the PDMS embedded PEG and 1-TD composites.

4.3.5. Results and discussion

4.3.5.1. Confirmation of PDMS embedded PCMs

The manufactured PEG, and 1-TD PCM composites are shown in **Fig. 4.3.2**, and the characteristics of the component is listed in **Table 4.3.1** and **Table 4.3.2**. It is indicated that the graphene aerogel has a high porosity with low weight fraction of PDMS. The surface of PEG and 1-TD composites are more flat than that of intrinsic PCMs which shows the PDMS can prevent the volume shrinkage under the infiltration process. In addition, the weight of PCM composites especially the PEG exhibits high increase and further implies the modified graphene aerogel can resist the capillary force to reduce the volume shrinkage. The shape recovery test can demonstrate the flexibility in the PDMS embedded graphene aerogel as given in **Fig. 4.3.3**, and listed in **Table 4.3.3**. The conventional graphene/GNP aerogel is failed to recover the initial shape while the PDMS/graphene aerogel can recover their 3D porous structure in the pressure of external force. **Fig.4.3.4** shows the shape recovery test by using the compressor at the 60 % strain and the PDMS embedded graphene aerogels are directly recovered to the initial state. It shows the PDMS has a joint property to connect the graphene nano-sheets for preventing the fragile of volume shrinkage.

The form stable test is confirmed by a digital camera and the temperature is increased from 25 °C to 80 °C as shown in **Fig. 4.3.5**. According to the camera images, both of pure PEG and 1-TD are fully melted to liquid state when the PCM composites keep their intrinsic shapes at the temperature variations. The PDMS embedded PCM composites are able to prevent the leakage problem during the melting process and subsequently utilize to the thermoelectric energy harvesting system. To identify the reduction of graphene oxide (GO), the FT-IR result can demonstrate the typical peaks as shown in **Fig. 4.3.6**. The functional groups of pure PDMS are concentrated on the 1000 cm^{-1} and $–CH_3$ group

near the 3000 cm^{-1}. In the modified graphene aerogels, the PDMS peaks are appeared in both 1:1 graphene and 1:2 graphene aerogels, and the intensity of graphene is slightly reduced compared with that of graphene oxide (GO) [153]. To investigate the PDMS in the supporting material, the decomposition under the high temperature is able to recognize the PDMS by the TGA measurement as shown in **Fig. 4.3.7**. In the TGA peaks, graphene aerogels are maintaining high thermal stability while the PDMS starts decomposed at over 400 °C. There are a few of gaps between graphene aerogel and PDMS/graphene aerogel and confirmed the PDMS is dispersed sufficiently into the internal skeleton. The TEM and EDS mapping images of modified graphene aerogels are shown in **Fig. 4.3.8** which can demonstrate the existence of PDMS. The graphene skeletons in both 1:1 and 1:2 graphene aerogels are obtained and found out the PDMS from the EDS mapping images. In addition, the weight fraction of PDMS in these two graphene aerogels are evaluated to 5wt% from the EDS analysis results. The surface morphologies of modified graphene aerogels and PCM composites are obtained by the SEM images as shown in **Fig. 4.3.9**. In **Fig. 4.3.9a** and **4.3.9b** exhibit the porous structure of PDMS embedded graphene aerogels and further indicates the modified graphene aerogels can infiltrate large portion of pure PCMs. The manufactured PCM composites are presented in **Fig. 4.3.9c** and **4.3.9d** and nearly similar with the pristine PCM composites. The confocal results can confirm the distribution of PDMS in the graphene aerogels and there are dispersed sufficiently in the graphene skeletons as shown in **Fig. 4.3.9e** and **4.3.9f**. The XRD peaks in **Fig. 4.3.10** shows the pure PDMS, and PCM composites in which indicates that no any sharp peaks are appeared between the PDMS and PCMs. It means no chemical reaction among the working materials and embedded fillers.

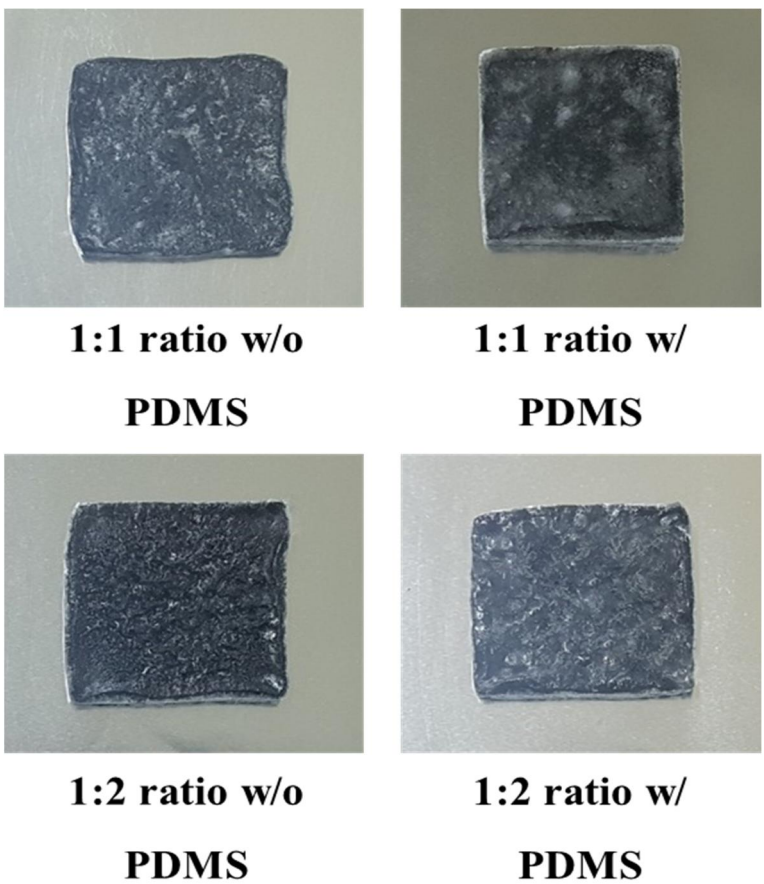

Figure 4.3.2. The camera images of PCM composites and PDMS embedded PCM composites.

Table 4.3.1. Characteristics of PDMS embedded graphene aerogels

Aerogel & PDMS	1:1 ratio	1:2 ratio
w/o PDMS	0.0968 g	0.1450 g
w/ PDMS	0.1016 g	0.1524 g
Porosity	98.73	98.10
PDMS weight	0.0048 g	0.0074 g

Table 4.3.2. Characteristics of PCM&PDMS composites

PCM & PDMS	1:1 ratio	1:2 ratio
w/o PDMS PCM	5.33436 g	6.8479 g
w/ PDMS PCM	6.2869 g	9.2586 g
PCM weight increase	0.9478 g	2.4033 g
ΔQ (ΔH·m) increase	208.90 J	435. 57 J
PDMS weight fraction	0.076 %	0.080 %
PCM weight fraction	98.38 %	98.35 %

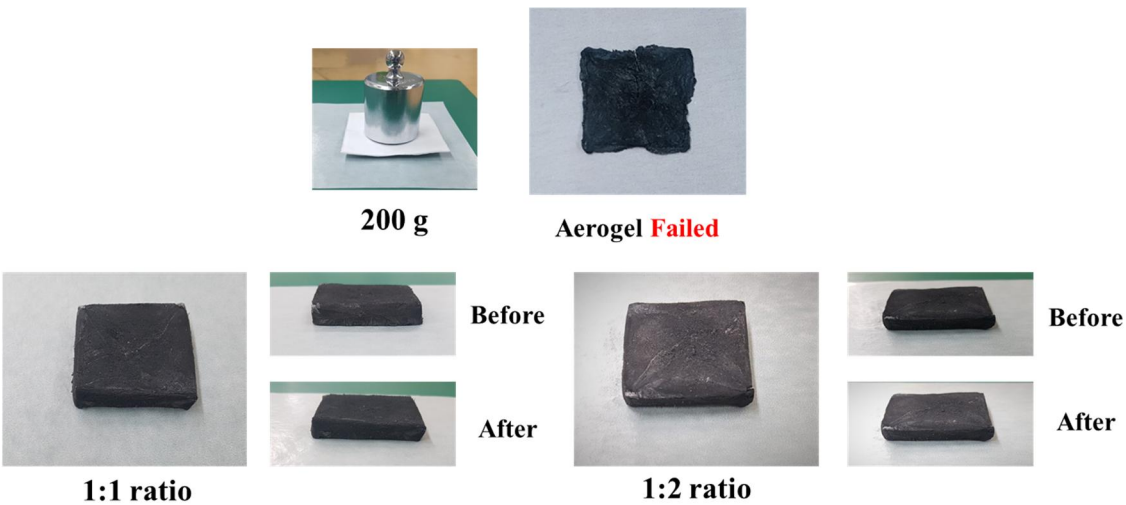

Figure 4.3.3. Shape recovery test in the PDMS embedded graphene aerogel.

Table 4.3.3. Recovery test of graphene aerogels

Aerogels	1:1 ratio	1:2 ratio
Before compression	0.5010 cm	0.5008 cm
After compression	0.4998 cm	0.4999 cm
Recovery time	1.16 s	1.04 s
Recovery %	99.76	99.82

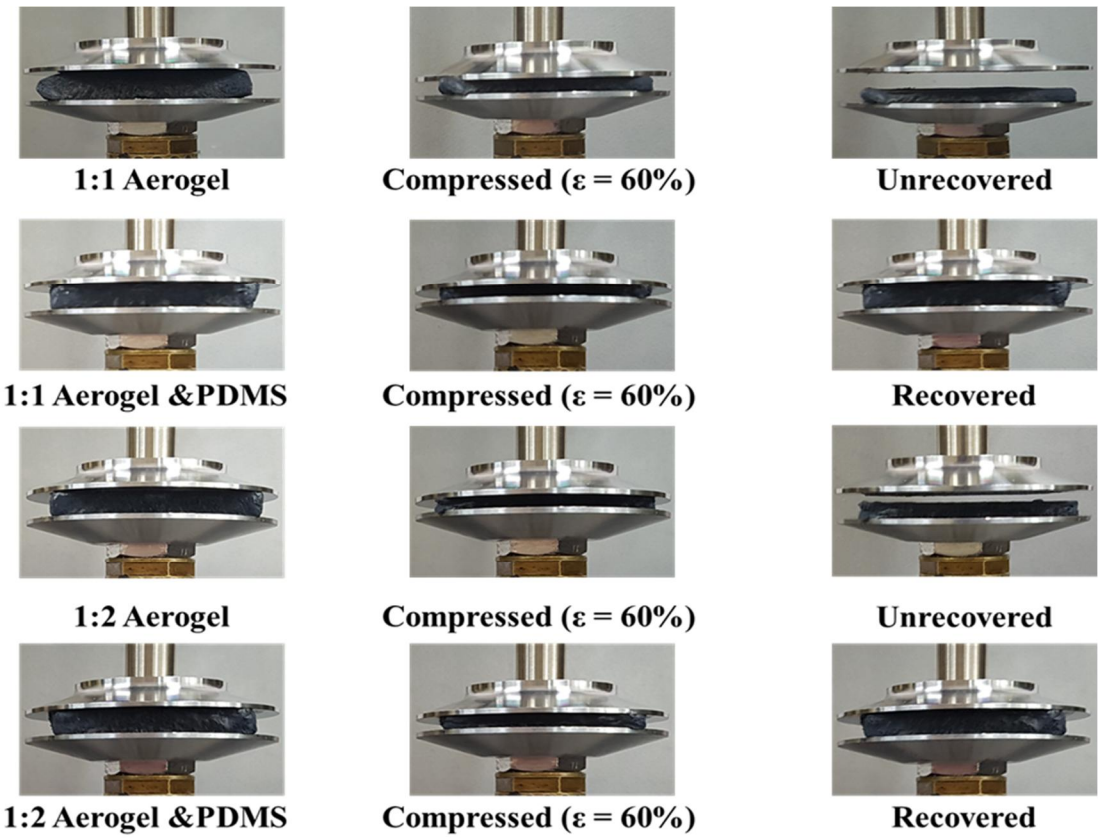

Figure 4.3.4. The shape recovery test of intrinsic graphene aerogels, and PDMS embedded graphene aerogels.

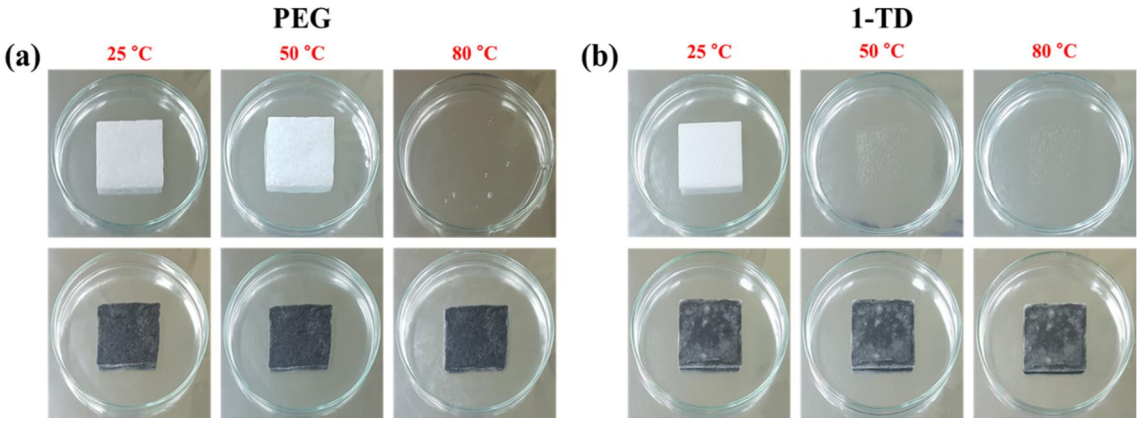

Figure 4.3.5. Form stable camera images of (a) pure PEG, and PEG&PDMS composite, and (b) pure 1-TD, and 1-TD&PDMS composite.

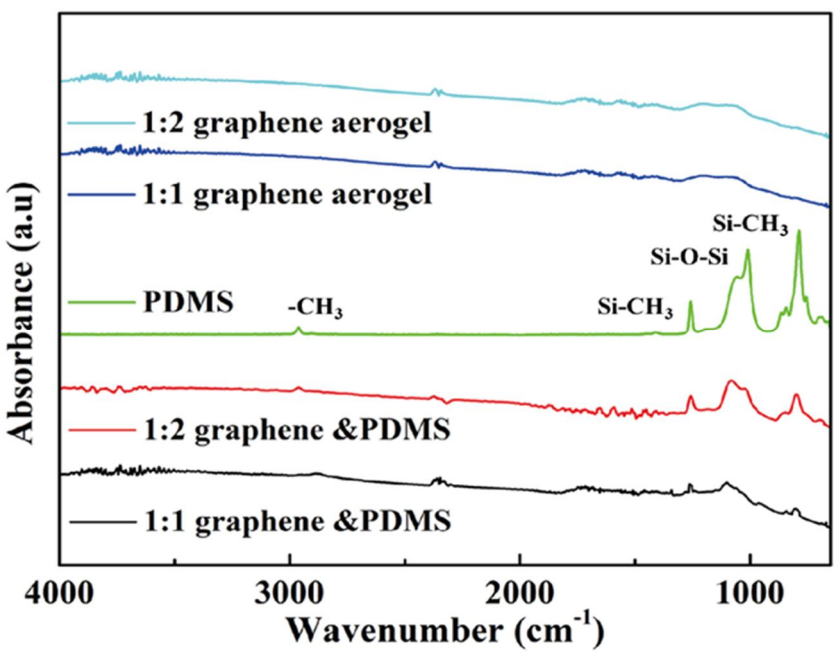

Figure 4.3.6. FTIR result of conventional graphene aerogels and PDMS embedded graphene aerogels.

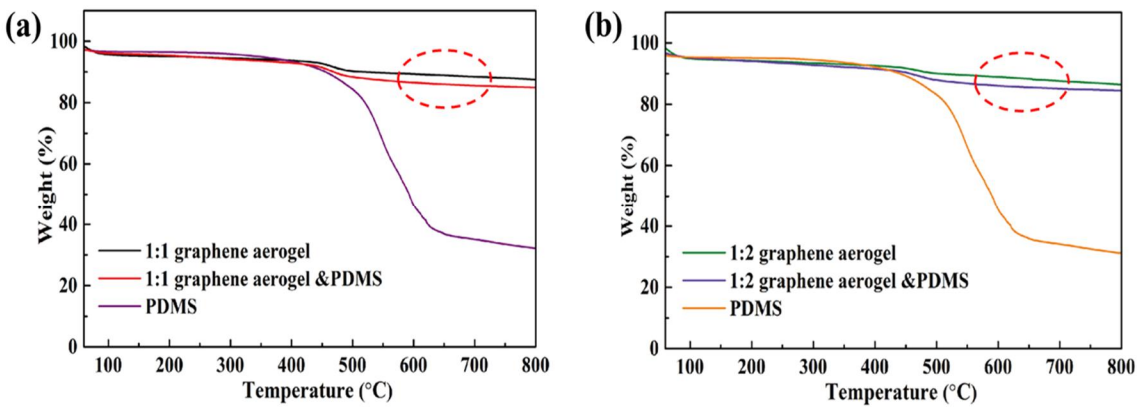

Figure 4.3.7. TGA measurement of 1:1 ratio graphene aerogels, and 1:2 ratio graphene aerogels.

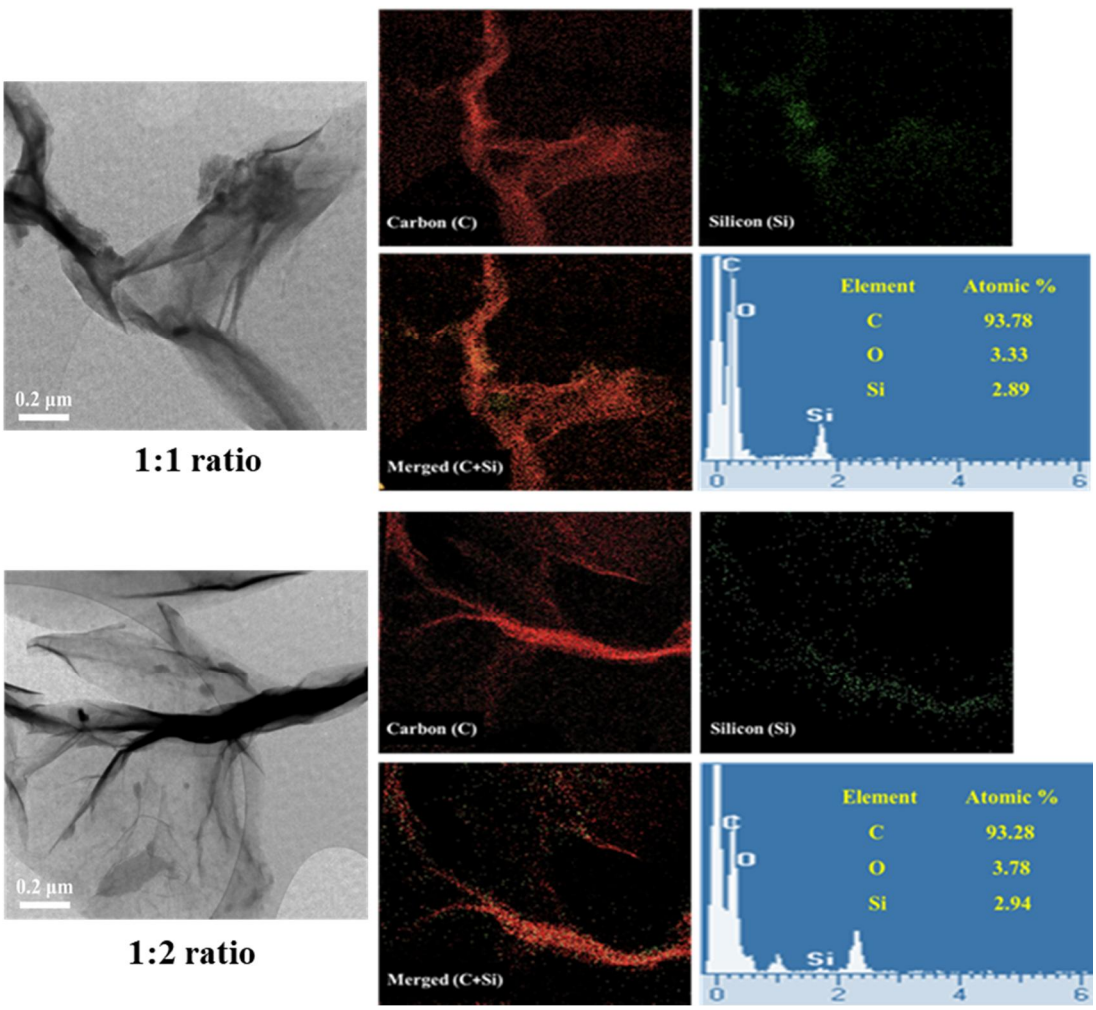

Figure 4.3.8. The TEM images of PDMS embedded graphene aerogels; EDS mapping for carbon (C), silicon (Si), and their merged images (C + Si); and EDS analysis of the modified graphene aerogels.

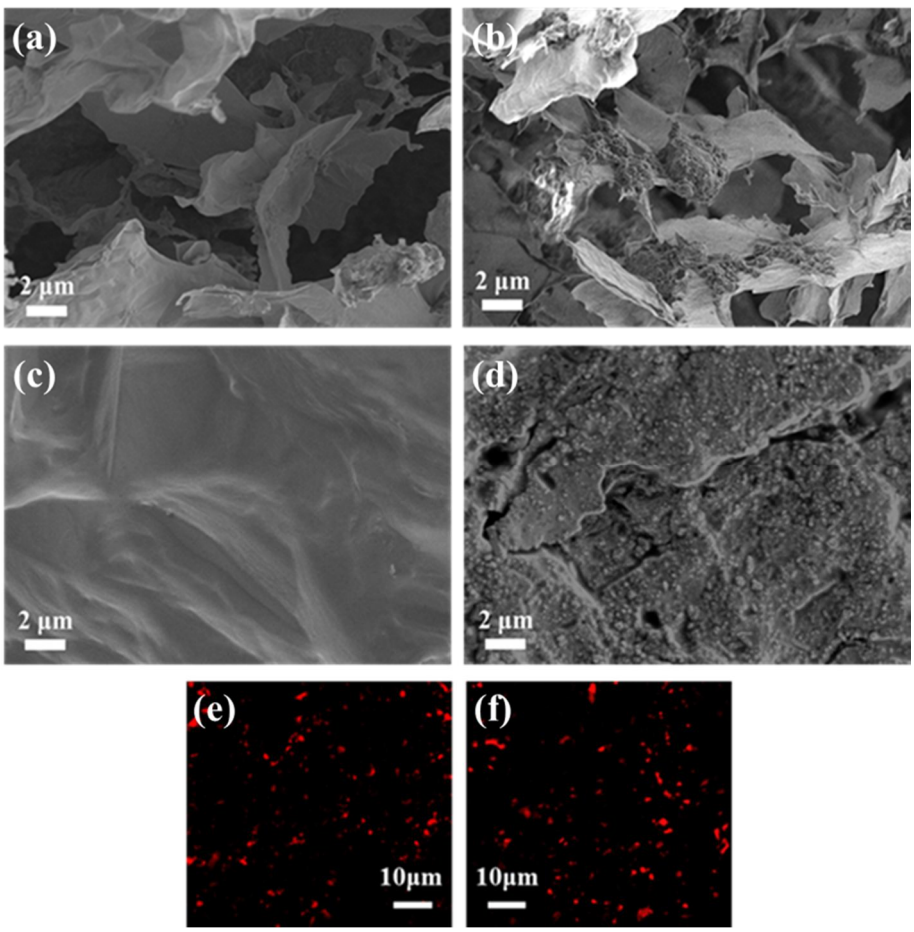

Figure 4.3.9. SEM images of modified (a) 1:1 graphene aerogel, (b) 1:2 graphene aerogel, (c) 1:2 PEG composite, and (d) 1:1 1-TD composite. The confocal images of modified (e) 1:1 graphene aerogel, and (f) 1:2 graphene aerogel.

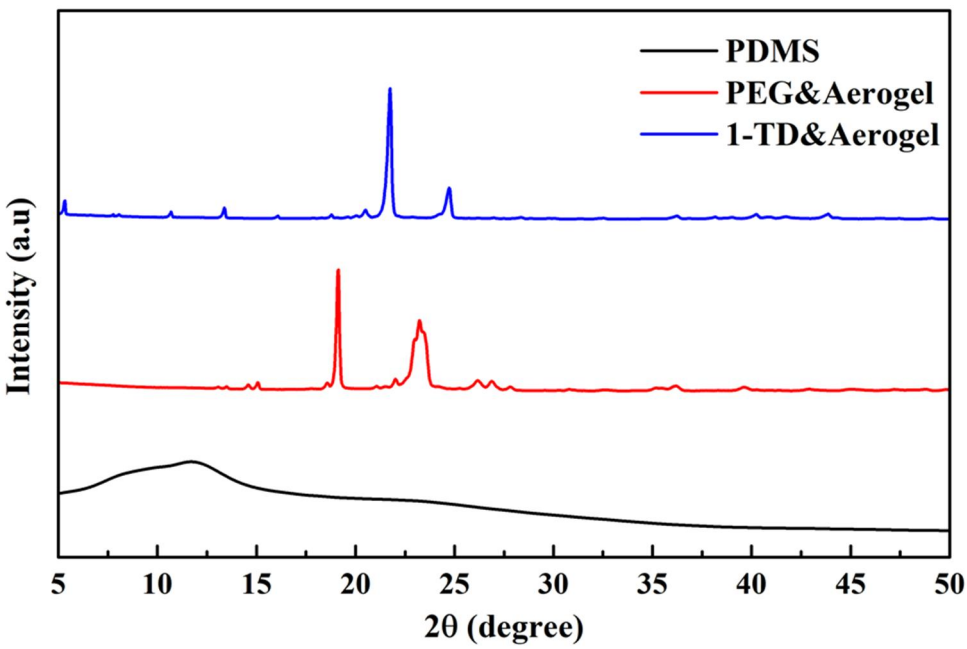

Figure 4.3.10. XRD peaks of pure PDMS, PEG composite, and 1-TD composite.

4.3.5.2. Thermal morphologies and electrical current measurement

The **Fig. 4.3.11** showed the thermal conductivity and the phase transition temperatures and latent heat upon melting and cooling by measuring the DSC test. In **Fig. 4.3.11a** shows the thermal conductivity between pristine PCM composites and PDMS embedded PCM composites. Both of PEG and 1-TD composites with PDMS calculate the 0.5818 W/mK, 0.4127 W/mK which exhibit similar thermal conductivity to the pristine PCMs. The heating and cooling sharp peaks of phase transitions are obtained and the value of the typical results are list in **Table 4.3.4**. There are clearly indicated that the results of PCM composites such as the onset melting and cooling temperature (T_{mo}/T_{co}), melting and cooling temperature (T_{mp}/T_{cp}), endset melting and cooling temperature (T_{me}/T_{ce}), and heating and cooling enthalpy ($\Delta H_m/\Delta H_c$). The onset phase transition temperature of the PEG composite is measured at 50.87 °C and finished at 68.29 °C and the melting temperature is 65.21 °C as shown in **Fig. 4.3.11b**. The latent heat of PEG composite is 179.11 J/g and 160.81J/g during the heating and cooling process. The **Fig. 4.3.11c** shows the peak of 1-TD composite and the phase transition field is from 35.08 °C to 45.92 °C and the melting temperature is obtained at 43.39 °C. The enthalpy of melting and cooling process are 214.82 J/g, 212.53 J/g respectively. The results of temperature and enthalpy indicate that the PDMS modified PCM composites are quite close to their pure PCM matrix and sufficiently utilize for the thermoelectric energy harvesting system.

Fig. 4.3.12 shows the DSC cycling and FT-IR results to obtain the thermal reliability and chemical stability and the characteristics of cycling results are listed in **Table 4.3.5**. According to the **Fig. 4.3.12a** and **4.3.12b**, the PCM composite cycling peaks are just a little shifted and it shows the PDMS embedded PCM composites show great thermal reliability upon melting and cooling process. It is well demonstrated that no chemical reaction occurred during the thermal cycling and the PCM composites exhibit wonderful chemical stability as given in **Fig. 4.3.12c**, and **4.3.12d**. The experimental current peaks of PDMS embedded PCM composites are illustrated in **Fig. 4.3.13** and compares with the pristine group of PCM composites. The peak area under the PCM composites become increased due to the additional working materials have infiltrated into the modified

graphene aerogels. The 1st peak upon heating is completed at 1,861 s and the maximum value of the 2nd step is appeared at 2,731 s. The maximum currents in the melting process exhibit 11.87 mA and 6.15 mA, respectively. For about the cooling process, the total harvesting field is more elongated than that of pristine PCMs and the maximum current values upon cooling show 9.70 mA and 6.60 mA, respectively. The present thermoelectric energy harvesting system needs LTC 3108 to turn on the LED lamp due to the low output power which has been mentioned in previous work. The PDMS embedded PCM composites are have a great chance to act as thermal transformer and directly utilized for the various thermoelectric energy harvesting system.

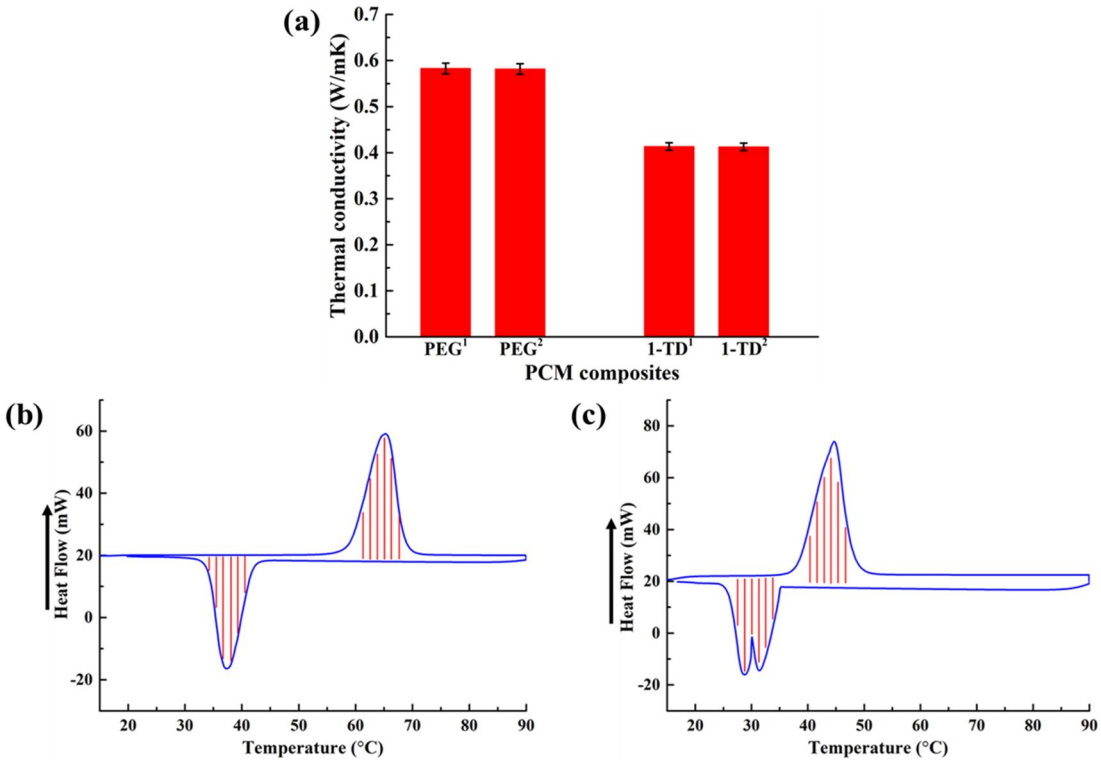

Figure 4.3.11. Thermal conductivity of pristine PCM composites (PEG^1, $1\text{-}TD^1$), and PDMS embedded PCM composites (PEG^2, $1\text{-}TD^2$). DSC curves of (b) PEG composite, and (c) 1-TD composite.

Table 4.3.4. Characteristics of PDMS embedded PEG, and 1-TD composite.

Samples	T_{mo}(°C)	T_{me}(°C)	T_{mp}(°C)	ΔH_m(J/g)	T_{co}(°C)	T_{ce}(°C)	T_{cp}(°C)	ΔH_c(J/g)
PEG&PDMS	50.87	68.29	65.21	179.11	43.37	34.20	38.22	160.81
1-TD&PDMS	35.08	45.92	43.39	214.82	37.14	20.26	30.62	212.53

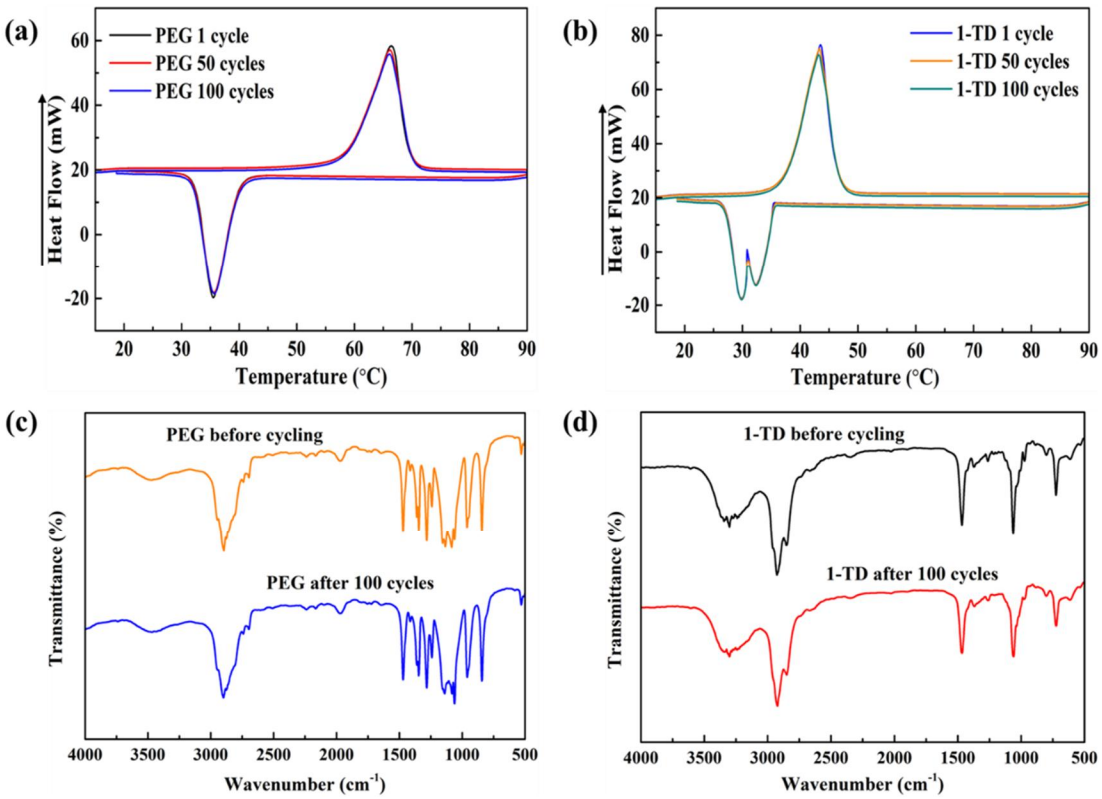

Figure 4.3.12. DSC cycling results of (a) PEG, and (b) 1-TD composite; FT-IR peaks after 100 cycling test for (c) PEG, and (d) 1-TD composite.

Table 4.3.5. Characteristics of PCM composites after 100 cycling test

Samples	T_{mp}(°C)	ΔH_m(J/g)	T_{cp}(°C)	ΔH_c(J/g)
PEG cycling	65.10	178.87	38.14	160.63
1-TD cycling	43.26	212.97	30.51	211.79

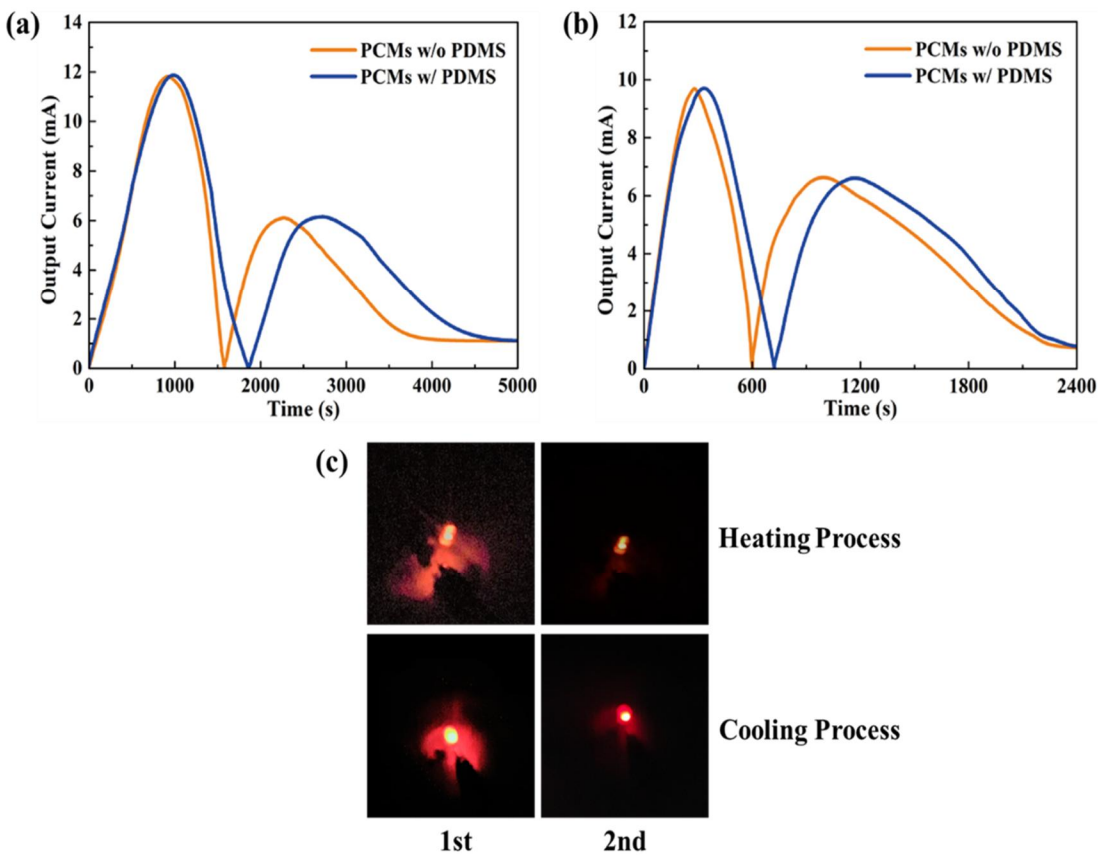

Figure 4.3.13. Electrical current of (a) heating process, (b) cooling process, and (c) LED images upon heating and cooling.

4.3.5.3. Simulation results and efficiency of energy harvesting system

The PDMS embedded PCM composites are composed of thermoelectric energy harvesting system and the numerical simulation provides the correct results to the thermal energy utilization during the melting and cooling process. The range of temperature variation is equal to the previous work and the temperature profiles upon phase transitions are shown in **Fig. 4.3.14a**, and **4.3.14b.** The 1-TD composite still has the faster solid-liquid phase transition process due to the lower melting temperature (T_m) than that of the PEG composite. The temperature difference between two PCM composites cause the electrical current and the current is gradually increased as the nearly isothermal field of 1-TD composite. On the other hand, the PEG temperature continues to increase while the 1-TD composite are under the phase transition process. When the temperature difference is reversed, the system begin to generate the 2nd output electrical energy as prepared by the isothermal field of PEG composite. The cooling temperature profiles are same as the heating process and produces electrical current. The maximum temperature differences on the heating process are close to 18 °C and 7 °C, respectively as shown in **Fig. 4.3.14c**. On the cooling process, the temperature of PCM composites is decreased rapidly due to the natural convection. Furthermore, the maximum temperature at the 1st and 2nd steps are appeared 12 °C and 8 °C in **Fig. 4.3.14d**.

The modeling calculation results in both heating and cooling cycles are presented in **Fig. 4.3.15**. In **Fig. 4.3.15a**, the numerical calculation is close to the experimental result during the heating process. The maximum current of modeling peak exhibits higher than that of experimental result, and it indicates the excess electrical current could be generated by the thermoelectric energy harvesting process. The cooling peaks are shown in **Fig. 4.3.15b** in which the simulation result is well agreement with the experimental peak. According to the comparison of two different current analysis, completed at 900s and the maximum value of the calculated current was 10mA, the results of thermoelectric energy harvesting system is correct to produce electrical current and widely used for thermal energy storage (TES) applications. The thermoelectric energy harvesting efficiency is shown in Fig. 4.3.15c and the heating and cooling efficiencies are 65.37 %, and 41.43 %. It provides the higher harvesting efficiency than that of pristine result. The

PDMS embedded graphene aerogel can reduce the volume shrinkage and increase the weight of pure PCM during the infiltration process. As a result, the modified graphene aerogel supported PCMs are conducive to the thermoelectric energy harvesting system and utilize for practical applications.

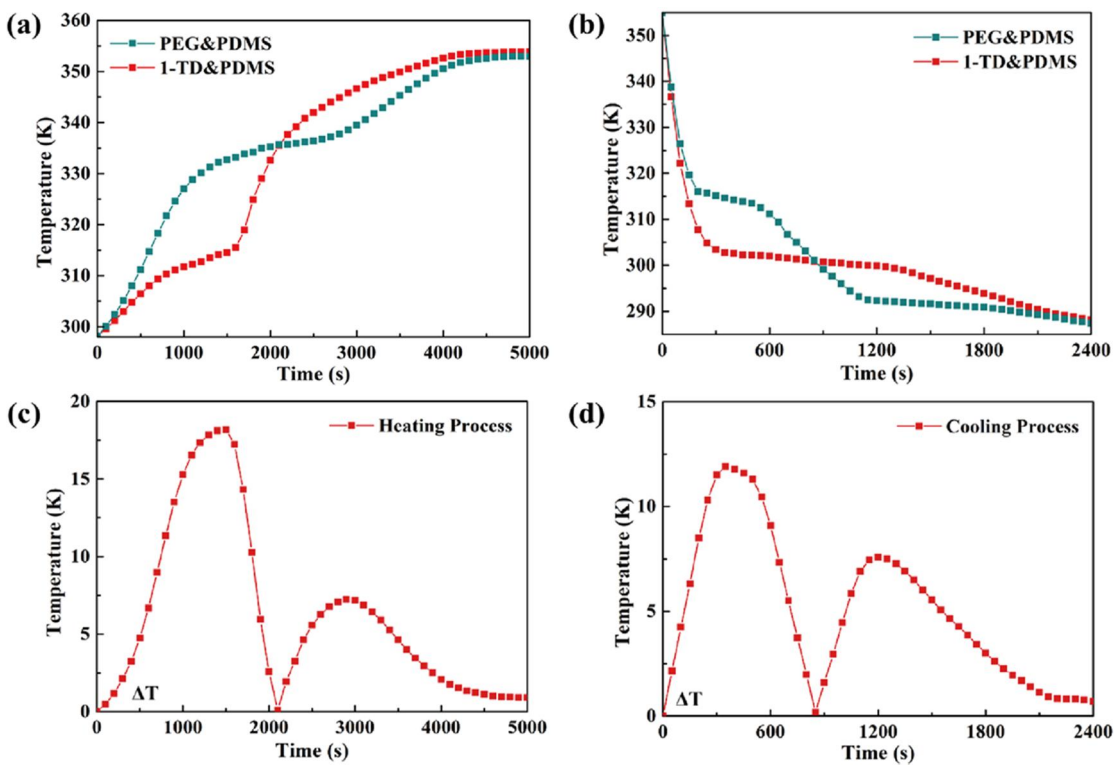

Figure 4.3.14. Temperature profiles under (a) heating process, and (b) cooling process. The temperature difference between (c) heating process, and (d) cooling process.

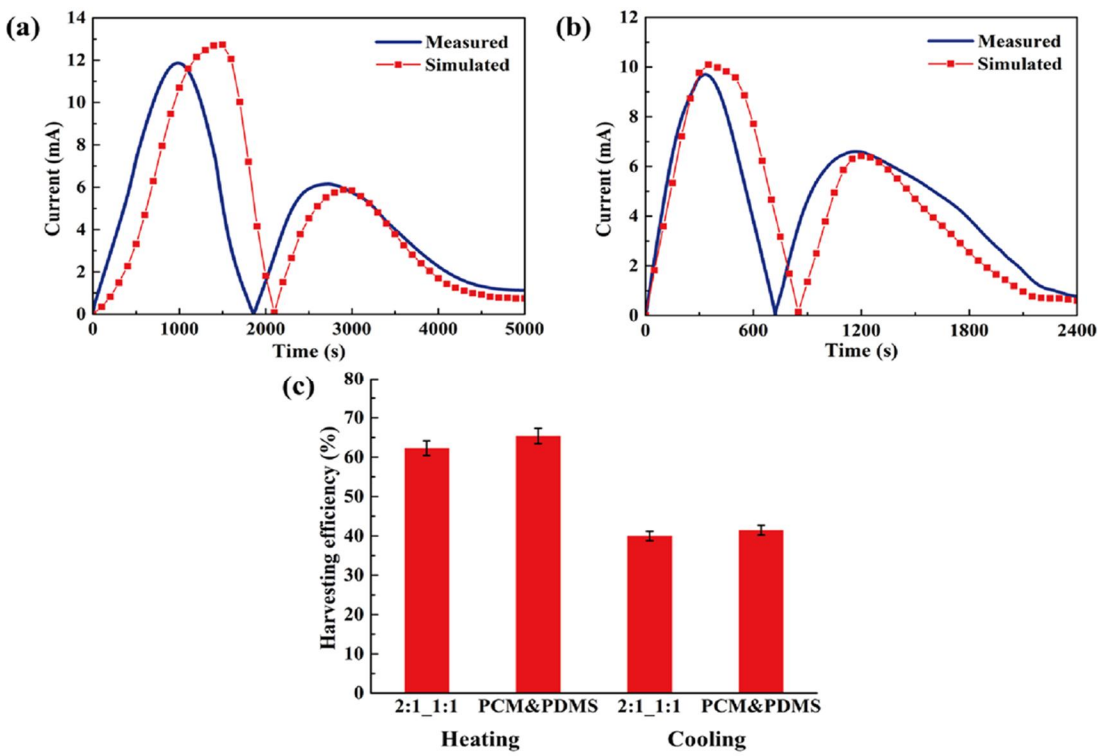

Figure 4.3.15. Compare simulation results with experimental peaks upon (a) heating process, and (b) cooling process. (c) The harvesting efficiency during the phase transitions.

4.3.6. Conclusions

In this section, we fabricated the modified graphene aerogel and utilized as a new supporting material. The PDMS embedded graphene/GNP aerogel exhibits a flexible properties and reduce the volume shrinkage during the infiltration process. As a result, the PDMS embedded PCM composites can incorporate more weight of working materials than that of pristine PCMs. It indicates that the stored energy is proportional to the mass of pure PCM and these advanced PCM composites are able to increase the thermoelectric energy harvesting efficiency during the melting and cooling process. The flexible skeleton based porous aerogels can effectively support the pure PEG, and 1-TD to prevent the leakage and keep their initial solid states under the phase transitions. In addition, the modified graphene aerogel can develop a new approach for PCMs thermal energy storage and thermoelectric energy harvesting applications.

4.4. Cross-linked aerogel/PCMs for energy harvesting

4.4.1. Introduction

It has been widely used in a variety of fields because of its remarkable, physical and chemical properties on the graphene research, such as high thermal conductivity, great mechanical strength and high theoretical surface morphologies [226]. The aerogel is a synthetic solid-state substance with extremely low density (which ranges from 0.0011 to ~0.5 gcm^{-3}), which consists of three dimensional (3D) internetworked porous structures by using freeze-drying method [227]. The three most common types of aerogel are derived from silica, metal oxides, and carbon aerogel. In particular, graphene aerogels are a kind of carbon-based aerogels synthesized by graphene or reduced graphene oxide (rGO) nano-sheets and regarded as promising porous carbon materials [228]. There have been considered as high volumetric materials for porous structures because of indicating the advantages of 3D microporous combination with the intrinsic properties of constitutive graphene skeletons [229]. The manufactured graphene aerogels with high porosity can offer fast thermal transport pathways, easy access to the phase transitions of working material, and low-resistant diffusion, while graphene sheets provide a large surface area, high carrier mobility, and chemical inertness.

Cysteamine is a small molecule and the edge of carbon chain has active thiol group, which makes it a great cross-linker to connect two or more GO sheets [230]. In many recent works have mentioned that the cysteamine is utilized as a functionalizing agent to generate some of the synthesized composites. However, few works have been reported that fabrication of modified graphene oxide (GO) aerogels with incorporation of cysteamine. Graphene/cysteamine aerogels (GCA) are synthesized using the cross-linked chemical process and the cysteamine in this reaction is acting as a covalent cross-linker under the high temperature solvent vapor method. The manufactured graphene/cysteamine aerogel (GCA) is constructed with various cross-linked chains and increase the mechanical properties and chemical inertness. As predicted, the graphene/ cysteamine aerogel (GCA) exhibits a high porosity to infiltrate working materials and also remain high surface area as comparing with some of the conventional carbon

aerogels. The modified graphene aerogels lead to the highly effective fabrication and cross-linked graphene aerogel is selected to utilize broader practical applications.

Consider the high latent heat thermal energy storage (LHTES), the phase change materials (PCMs) are appropriate for utilizing as working matrix to absorb or release a large amount of thermal energy. In addition, the thermoelectric energy harvesting is a hot issue of solving the energy crisis and sustainable development. The solar energy is a renewable energy and directly used in the thermal energy storage (TES) applications [231]. It indicates that the solar energy has never restriction in the Earth and more broad applications. However, the recent researches have reported merely on the solar intensity at atmosphere that the 100 mW/cm^2 intensity is selected as an irradiation of heat source. There are no any information about the sunlight intensity on the surface of working materials and the solar irradiation is hard to maintain the initial 100 mW/cm^2 intensity due to the energy loss around the environmental conditions. For utilizing the light energy effectively, the present study will measure the sunlight intensity at the surface of working materials and utilizing for thermal energy storage (TES) applications. The phase change materials (PCMs) are able to store the external heat source due to their high latent heat, good thermal stability and thermal reliability. However, the leakage problem is blocking the application of PCMs and selecting the carbon based aerogels as supporting materials to prevent the leakage during the phase transition process. As mentioned in previous research, the infiltration method can hold large weight fraction of pure PCMs in spite of the volume shrinkage which cause some weight loss of working materials. In order to reduce the volume shrinkage, modified supporting materials are reported in various researches without the manufacture of PCM composites. Hence, the cross-linked graphene aerogel is recommended as supporting material to fabricate the form stable PCM composites.

In this Section, synthesize a cross-linked graphene/cysteamine aerogel (GCA) is fabricated and the prepared graphene oxide (GO) is refluxed in nitric acid with high temperature to produce more carboxyl, hydroxyl, and carbonyl groups at the defect sites of graphene layers. After that these functional groups are oxidized effectively with potassium permanganate ($KMnO_4$) solution (in perchloric acid) to achieve additional carboxyl groups on the graphene surface. After removing the excess potassium

permanganate by adding the citric acid and purified to achieve the oxidized graphene oxide (GO). The oxidized GO/GNP aerogel is fabricated by freeze-drying method, and finally cross-linked by the cysteamine to obtain the graphene/cysteamine aerogel (GCA).

4.4.2. PCM composites for energy harvesting system

The PCM composites are fabricated by using the vacuum impregnation method as before, which infiltrates the molten PCM into the pore volume of graphene/cysteamine aerogel (GCA). Both of pristine PEG and 1-TD composites exhibit better sunlight absorption than that of pure PCMs due to the incorporation of graphene skeleton as shown in **Fig. 4.4.1**. Based on the UV-vis result, the cross-linked graphene aerogels can absorb the sunlight sufficiently and convert to the thermal energy upon light-on process. As mentioned in previous work, the pure PEG and 1-TD are placed on each of petri dish and put into the vacuum oven at 80 °C to prepare the liquid state. After vacuuming for about 30 minutes to remove moisture, the graphene/cysteamine aerogels (GCAs) are immersed in the liquid PCMs and kept for 8 hours under the vacuum state. The modified PEG and 1-TD composites are successfully fabricated and selected to construct the thermoelectric energy harvesting system. The schematic of energy harvesting mechanism is shown in **Fig. 4.4.2**. The stabilized PCM composites are combined with the PN TEGs to generate the electrical current upon melting and cooling process. The heat source in this work is using solar lamp which can provide the sunlight to the PCM composites. The system is prepared to measure the thermoelectric energy harvesting with a new method.

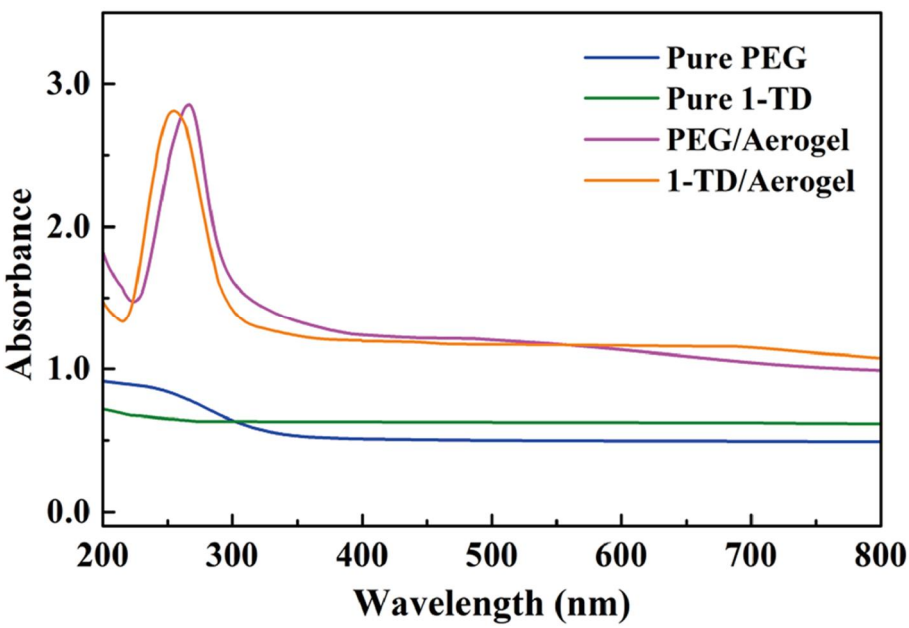

Figure 4.4.1. UV-vis measurement of pure PCM, and PCM composites.

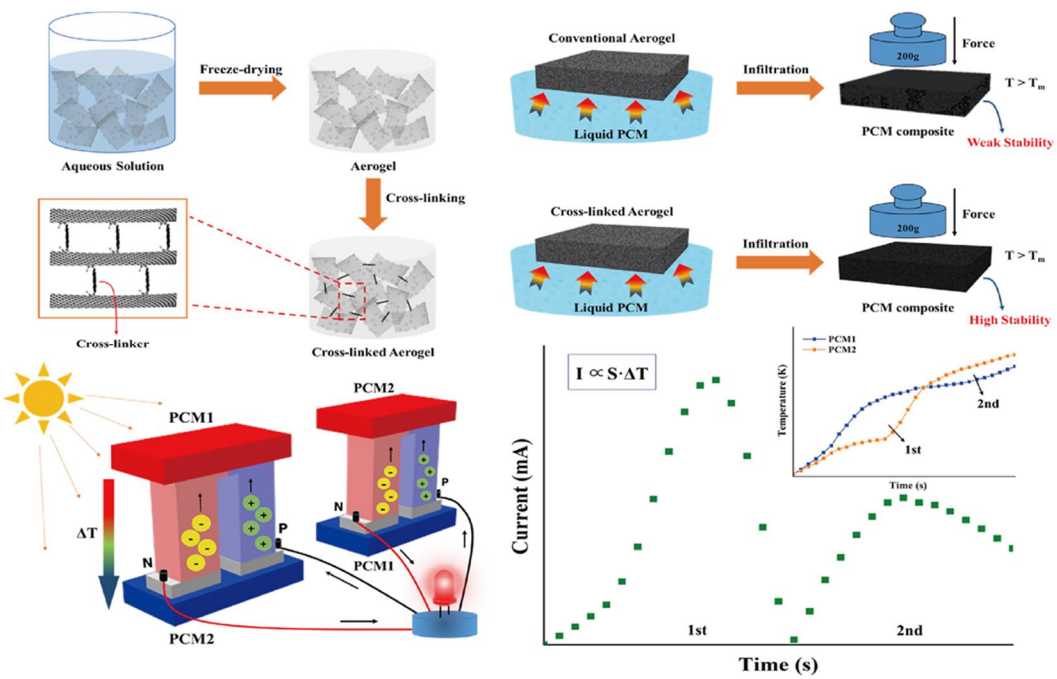

Figure 4.4.2. Schematic of cross-linked graphene aerogel and applied to the thermoelectric energy harvesting system.

4.4.3. Numerical analysis

The numerical simulation is utilizing the COMSOL Multiphysics, a commercial software based on finite element method (FEM) to calculate the temperature profiles. The resulting Seebeck effect is obtained as the existence of temperature difference upon melting and cooling. The energy harvesting system is composed of PCM composites, PN TEGs, and solar lamp. For the PN TEGs, Bi_2Te_3, $Bi_{0.3}Sb_{1.7}Te_3$ are inserted in each electrode. The total mesh has 10,178 elements, and the Seebeck coefficient is changed by the temperature variations.

For the heat transfer with phase change modules, the governing equation is shown as:

$$\rho C_p \frac{\partial \mathbf{T}}{\partial t} + \rho C_p u \cdot \nabla \mathbf{T} + \nabla \cdot \mathbf{q} = Q \tag{1}$$

where ρ is the mass density, C_p means the heat capacity, and the heat transfer rate $\mathbf{q}$, the heat transfer rate is corresponding to the thermal conductivity k and temperature gradient as below:

$$\mathbf{q} = -k\nabla T \tag{2}$$

The density of phase change material (PCM) is described as:

$$\rho = \theta\rho_{phase1} + (1-\theta)\rho_{phase2} \tag{3}$$

where θ is a fill-factor of mass fraction. The parameters in the numerical simulation are the functions of the fill-factor θ as below:

$$C_p = \frac{1}{\rho}\left(\theta\rho_{phase1}C_{p.phase1} + (1-\theta)\rho_{phase2}C_{p.phase2}\right) + L\frac{\partial \alpha_m}{\partial T} \tag{4}$$

$$k = \theta k_{phase1} + (1-\theta)k_{phase2} \tag{5}$$

$$\alpha_m = \frac{1}{2}\frac{(1-\theta)\rho_{phase2} - \theta\rho_{phase1}}{\theta\rho_{phase1} + (1-\theta)\rho_{phase2}} \tag{6}$$

where α_m means the mass coefficient. The external natural convection is defined as the boundary condition.

$$-n \cdot \mathbf{q} = \mathbf{q_0} \tag{7}$$

where n is the normal vector and $\mathbf{q_0}$ is the heat flux by the external convections. The

heat flux depends on the convection heat transfer coefficient (h_{air}) and the temperature difference as below:

$$\mathbf{q_0} = h_{air} \cdot (\mathbf{T_{ext}} - \mathbf{T}) \tag{8}$$

The external temperature is decided by the heat flow or solar irradiations. For the Seebeck coefficient, S is presented as:

$$S = \sqrt{\frac{k}{\sigma T}} \tag{9}$$

where σ is the electrical conductivity of the PN TEGs. The current is corresponding to the Seebeck coefficient S, temperature difference ($\Delta \mathbf{T}$), and resistance of the PN TEGs as below:

$$I = \frac{S\Delta \mathbf{T}}{R} \tag{10}$$

The efficiency of thermoelectric energy conversion was defined as a ratio of the converted energy W to the total latent heat stored energy Q as given below.

$$\eta = \frac{W}{Q} \tag{11}$$

4.4.4. Preparation of modified PCM composites

In order to fabricate the PCM composites, the cross-linked graphene aerogel is synthesized with the four steps as shown in **Fig. 4.4.3**. It is important for increasing the amount of functional groups on the graphene layer and the prepared 0.1 g graphene oxide (GO) is added to the 90 mL nitric acid at 130 °C for 6 hours with 275 rpm stirring in the step 1. After removing the excess nitric acid, the 0.3 g potassium permanganate ($KMnO_4$) is dispersed in 160 mL DI water and poured into the GO&HNO_3 suspension mixture with oil bath for 2.5 hours as given in step 2. The 90 mL perchloric acid ($HClO_4$) is need for improving the degree of oxidation and 4 g citric acid with 200 mL DI water is prepared to neutralize the oxidized solution. The oxidation of graphene oxide labeled GO&$KMnO_4$ is obtained by freeze-drying method and utilized for manufacturing the graphene aerogel.

The step 3 shows the preparation of GO&$KMnO_4$ aerogel with graphene nano-platelet (GNP) which could increase the thermal conductivity in the 3D structure. Finally, the cysteamine dispersed solution is utilized and the system is placed in the vacuum at 150 °C for 72 hours. The evaporated cysteamine can reach to the graphene oxide (GO) sheets and construct the cross-linked chemical chains in the internal skeletons. Hence, the graphene/cysteamine aerogel (GCA) is completed effectively by the chemical synthesis method. The PCM composites are produced by infiltrating pure PEG, and 1-TD into the modified graphene aerogels. The cross-linked graphene aerogel can effectively increase the mechanical property and even tolerate the external force at over the melting temperature.

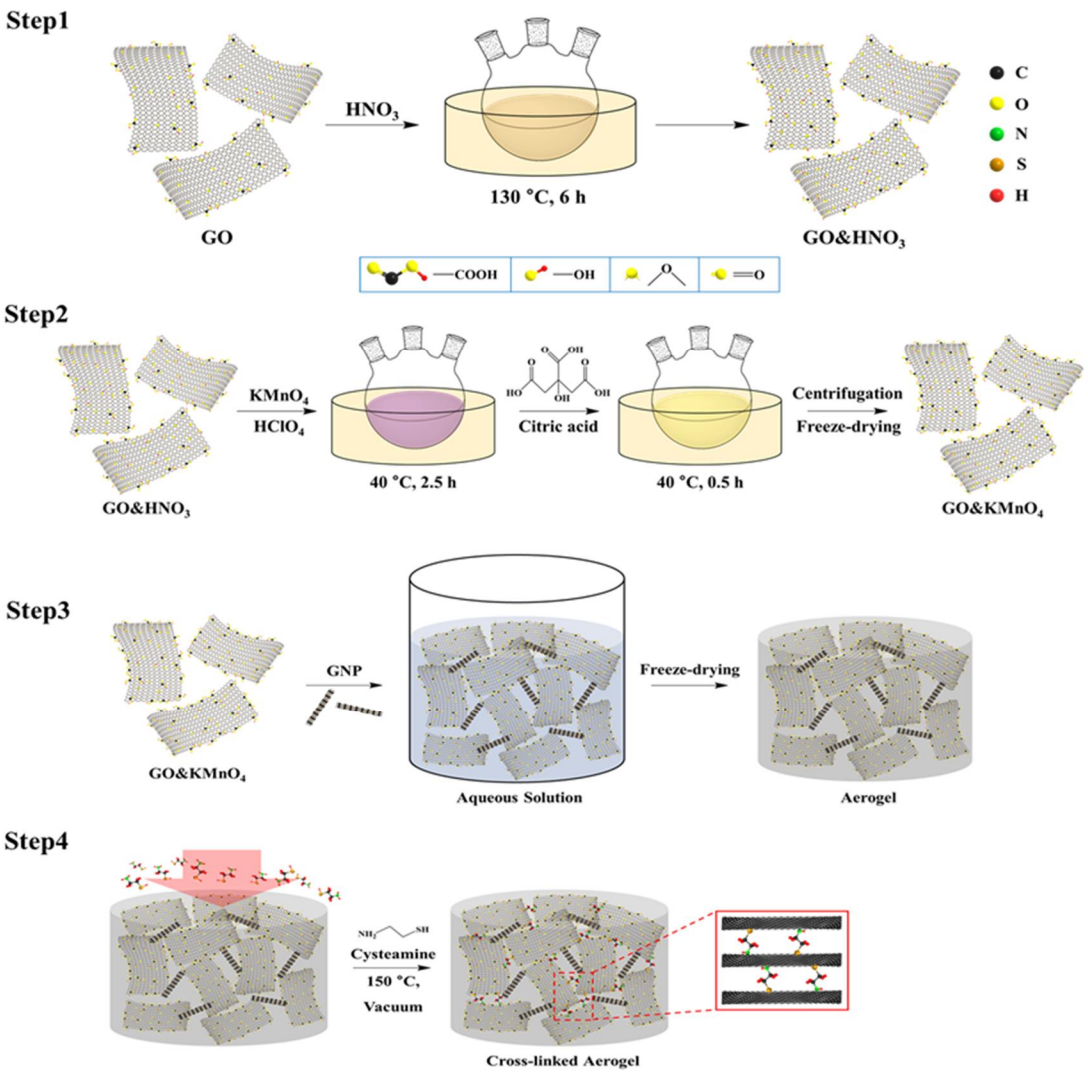

Figure 4.4.3. The route for fabricating the graphene/cysteamine aerogel (GCA).

4.4.5. Results and discussion

4.4.5.1. Morphologies of GCA

In order to confirm the dispersion ability between the oxidized graphene oxide (GO) and graphene nano-platelet (GNP), the Zeta potential is measured and given in **Fig. 4.4.4**. The oxidized graphene oxide (GO) exhibits more hydrophilic property than that of conventional graphene oxide (GO), and exhibits an excellent dispersion ability in the DI water. It demonstrates that the GO&$KMnO_4$ and GNP are well dispersed in the aqueous solution. The GO&$KMnO_4$ aerogels and the cross-linked graphene aerogels are shown in **Fig. 4.4.5**, and the cross-linked graphene/cysteamine aerogels (GCAs) turn to black color. The contact angle indicates the hydrophilicity of the GCA and shown in **Fig. 4.4.6**. The reduced graphene oxide (rGO) shows a 107.1 ° which has higher hydrophobicity than the graphene oxide (GO). The GCA is obtained 118.0 ° which is higher hydrophobic than the rGO sheet and it implies that the GCA has an enhanced capacity for infiltrating the pure into the pore volume [152]. To identify the reduction of graphene oxide (GO), the FT-IR and XPS results are shown in **Fig. 4.4.7** and **Fig. 4.4.8**, respectively. The characteristic peaks of graphene oxide (GO) corresponding to the oxygen functional groups such as the stretching vibration peak of O-H at the vicinity of 3,400cm^{-1}, C=O stretching vibration peaks around 1,700cm^{-1}, and the C-O stretching peak around 1,100cm^{-1} disappear after the reduction of GO. The two new peaks around the 750cm^{-1}, and 1,250cm^{-1} which shows the generation of C-S and C-N curves. In addition, the change of binding peaks in XPS indicate the C-C/C=C, C-O, C=O, and O-C=O four functional groups in the graphene oxide (GO) and the relative contents are listed in **Table 4.4.1**. The C-O, and C=O binding peaks are rapidly increased due to the oxidation of $KMnO_4$ as shown in **Fig. 4.4.8b**. The graphene/cysteamine aerogel (GCA) exhibits the decrease of C-O, and C=O binding energy instead of C-S/C-N peaks in **Fig. 4.4.8c**. According to the GO&$KMnO_4$ and GCA peaks, the typical functional groups in graphene oxide (GO) have been reduced by the cysteamine treatment and further indicate the generation of cross-linked structure in the

GCA. The construction of cross-lined chains are measured by the N1s, and S2p binding conditions to confirm the combination of graphene sheets. The **Fig. 4.4.8d**, and **4.4.8e** show the binding peaks between graphene oxide (GO) and cysteamine which can demonstrate the cross-linked chain is correctly connected to the graphene nano-sheets.

To further demonstrate the oxidation degree of graphene oxide (GO), the Raman peaks are mentioned in **Fig. 4.4.9**. The GO&HNO_3 exhibits higher intensity than that of pristine graphene oxide (GO) which shows the additional generation of functional groups on the graphene layer. The GO&$KMnO_4$ has the highest intensity in both D, and G peaks and rapidly decreased by the cysteamine treatment. The intensity ratio of I_D/I_G of GO is 0.90 and a little increased to 0.94 at the GO&HNO_3. Furthermore, the GO&$KMnO_4$ has 1.01 intensity ratio and GCA turns into the 1.08 at the end of reduction. The Raman peaks indicates the importance of nitric acid and provides more functional groups for oxidizing to the carboxyl structures. To indicate some of typical properties for the GCAs, the BET test and weight fraction of pure PCMs are shown in **Fig. 4.4.10**, and the results are listed in **Table 4.4.2**. The nitrogen gas absorption peaks become shifted due to the generation of cross-linked structure as given in **Fig. 4.4.10a**. The pore size distribution of each graphene aerogels concentrates on the range of 0 to 10 which indicates the microporous internal shapes towards the graphene aerogels in **Fig. 4.4.10b**. The surface area of 1:1 GCA, and 1:2 GCA is high enough and porosities of each structure is 98.37 % and 97.86 %, respectively. The weight fraction of pure PCMs are shown in **Fig. 4.4.10c**, have 97.95 %, and 98.16 % for their PCM composites. Owing to the volume shrinkage problem at the external force, the **Fig. 4.4.11** shows the shape recovery test and the results are mentioned in **Table 4.4.3**. Both of 1:1 GCA and 1:2 GCA are recovered to their initial shapes nearly 100 % and briefly demonstrate the GCA can effectively prevent the volume shrinkage. When the modified graphene aerogels are considered as new types of composite, the mechanical test of composite like structure is shown in **Fig. 4.4.12**. It is indicated that the GCA has the best mechanical properties than any other graphene aerogels and tolerate the external force even over the melting temperature.

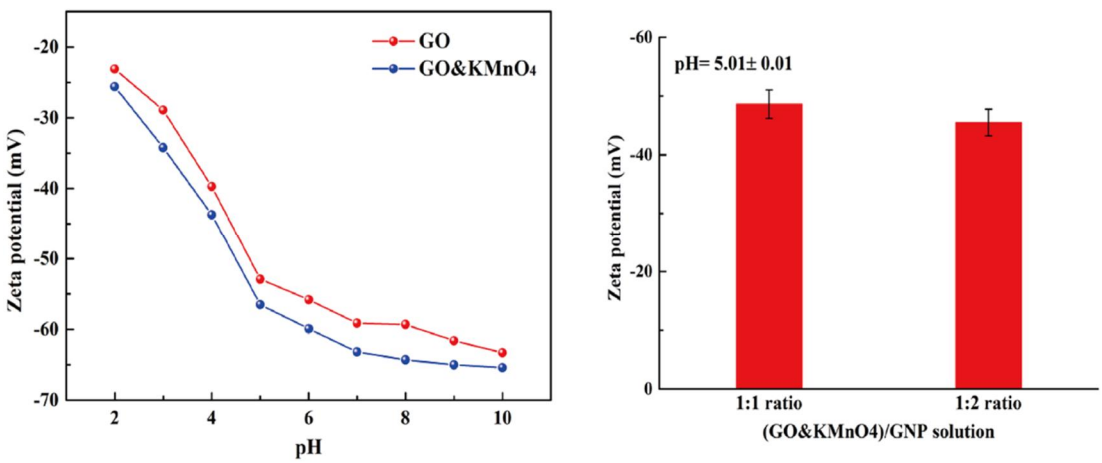

Figure 4.4.4. Zeta potential between graphene oxide and oxidized graphene oxide.

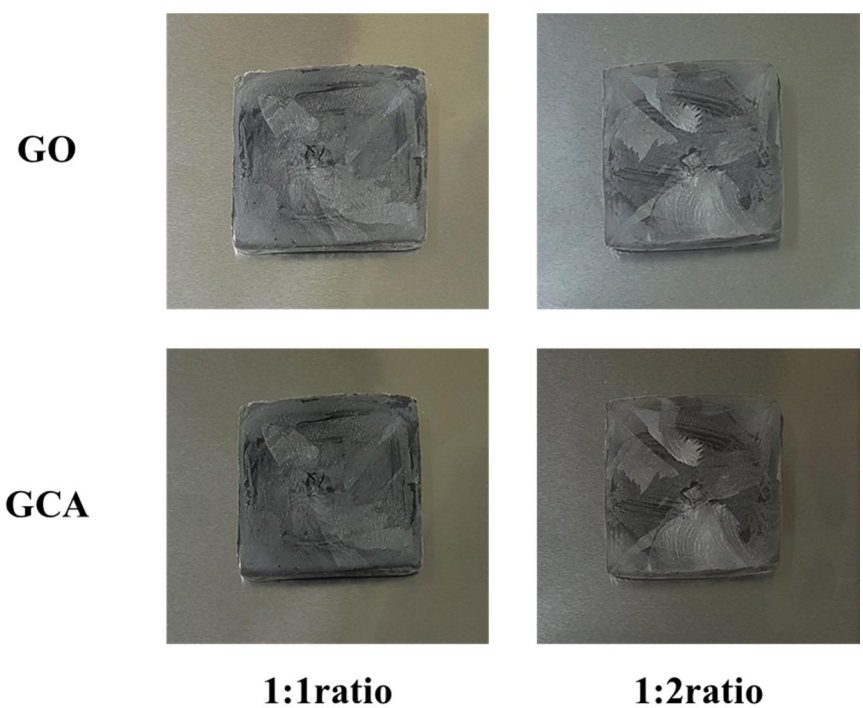

Figure 4.4.5. The camera images of GO&$KMnO_4$ aerogels, and graphene/cysteamine aerogels (GCAs).

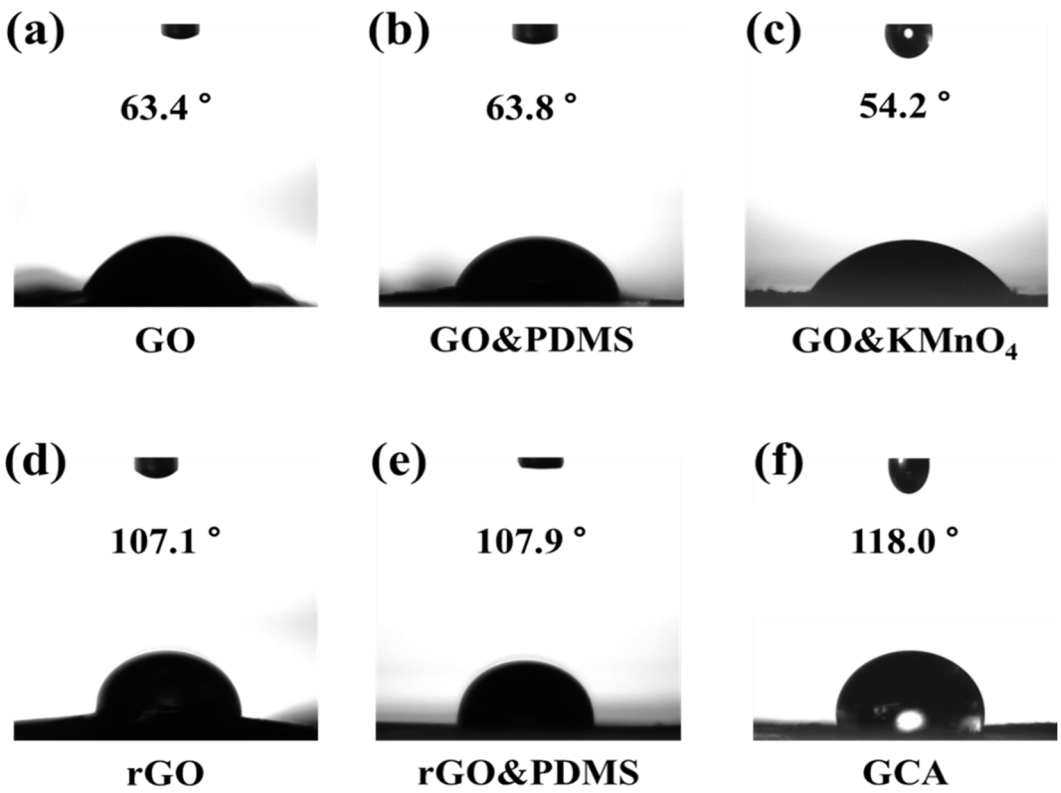

Figure 4.4.6. Contact angles of (a) GO, (b) GO/PDMS, (c) GO&$KMnO_4$, (d) rGO, (e) rGO/PDMS, and (f) GCA.

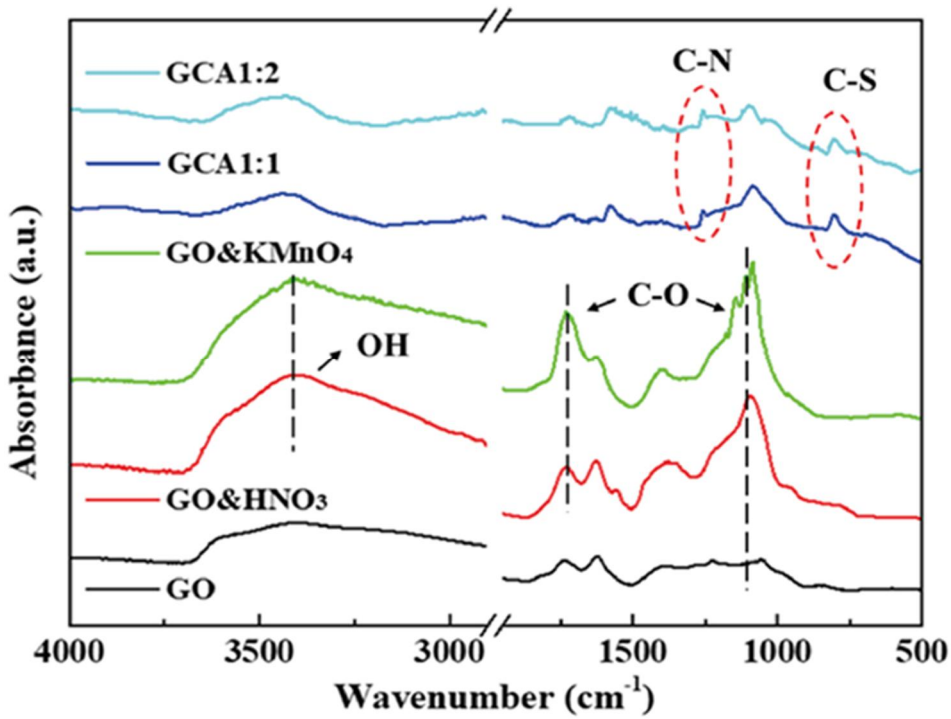

Figure 4.4.7. FT-IR results of GO, GO/HNO_3, GO&$KMnO_4$, GCA1:1, and GCA1:2.

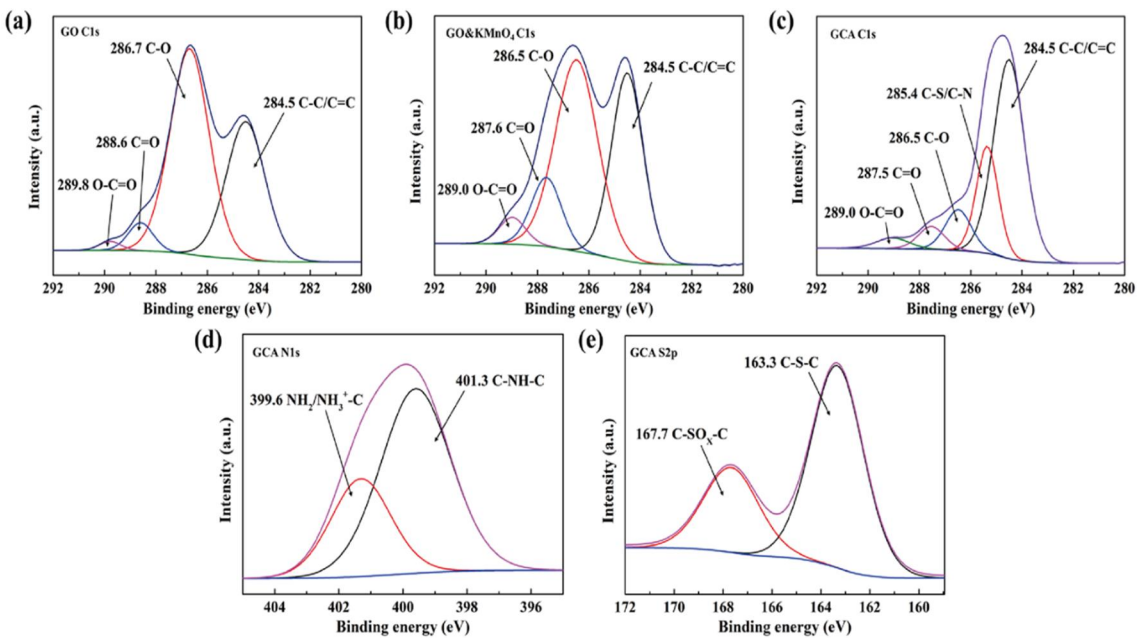

Figure 4.4.8. XPS C 1s for (a) graphene oxide (GO), (b) oxidized graphene oxide, and (c) GCA. (d) Deconvolution of XPS N 1s for GCA, and (e) S 2s for GCA.

Table 4.4.1. Relative contents of GO, GO&$KMnO_4$, and GCA.

Relative content (%)	C-C/C=C	C-S/C-N	C-O	C=O	O-C=O
GO	37.68	0	56.09	4.89	1.35
GO&$KMnO_4$	35.44	0	48.11	12.27	4.18
GCA	58.29	22.43	10.24	5.71	3.32

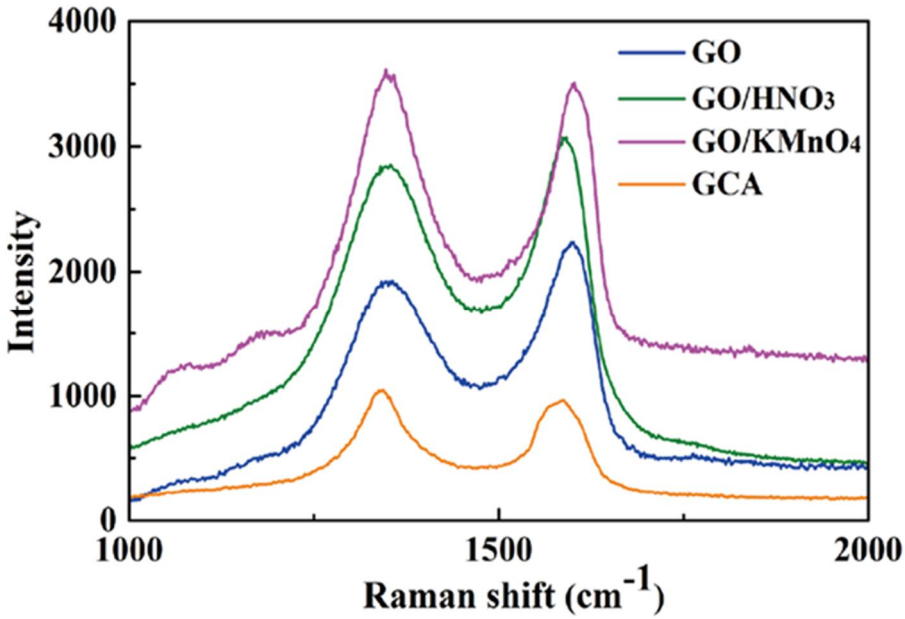

Figure 4.4.9. The Raman peaks of GO, GO&HNO_3, GO&$KMnO_4$, and GCA.

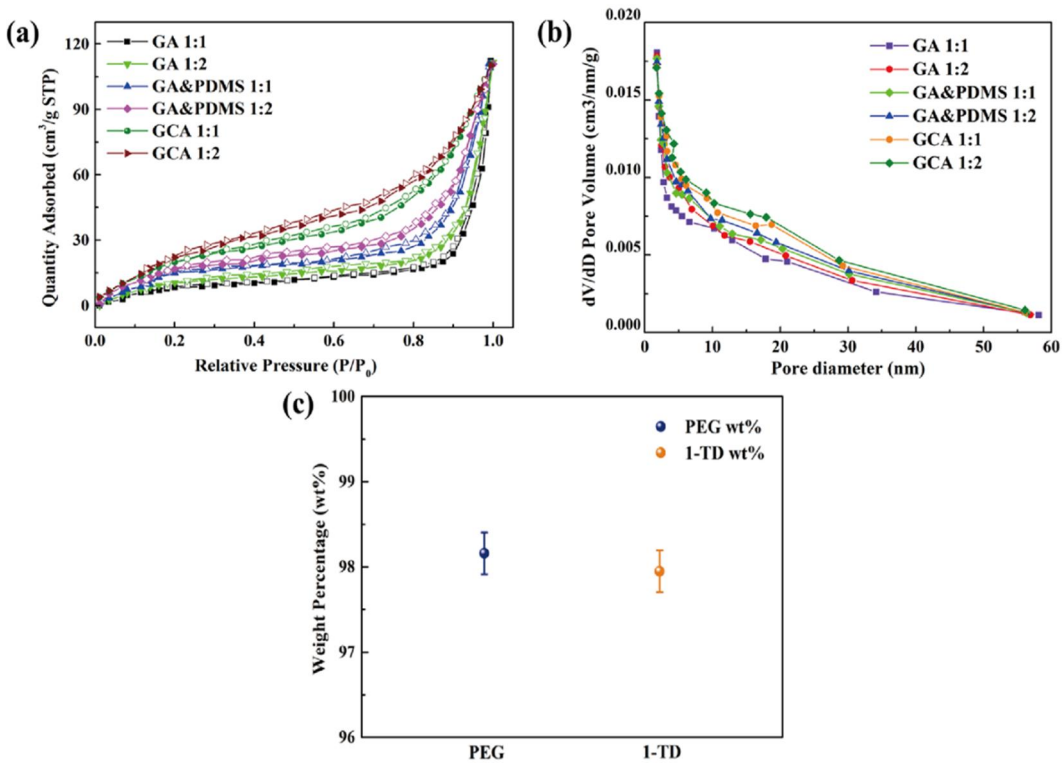

Figure 4.4.10. BET measurement of graphene aerogels (a) Nitrogen adsorption/desorption peaks, and (b) pore size distribution. (c) Weight fraction of pure PEG, and 1-TD in the PCM composites.

Table 4.4.2. The characteristics of graphene aerogels and PCM composites.

Samples	Weight (g)	Surface Area (m^2/g)	Porosity (%)	PCM Weight (g)	Pure PCM %
GCA1:1	0.1308	371.45	98.37	6.3883	97.95
GCA1:2	0.1714	369.53	97.86	9.2994	98.16

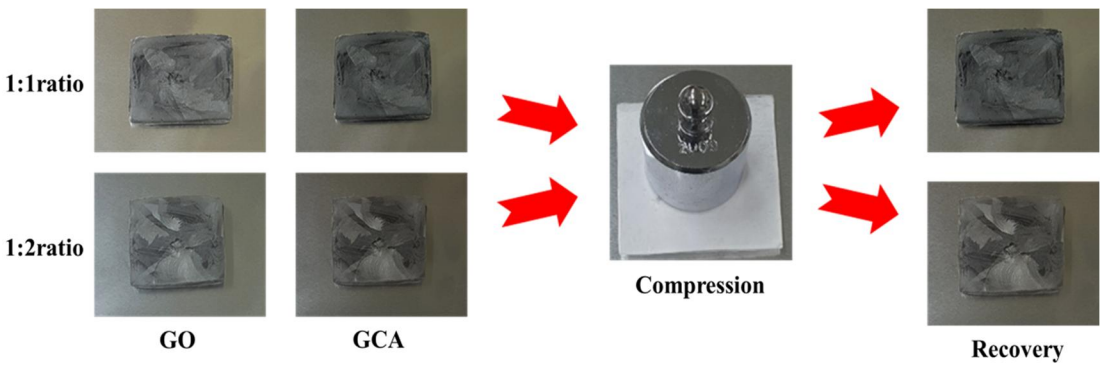

Figure 4.4.11. Shape recovery test of graphene/cysteamine aerogel (GCA).

Table 4.4.3. The characteristics of GCA recovery test.

Samples	Before compression	After compression	Recovery time	Recovery %
GCA1:1	0.5004 cm	0.4991 cm	0.52 s	99.75
GCA1:2	0.5010 cm	0.5000 cm	0.48 s	99.80

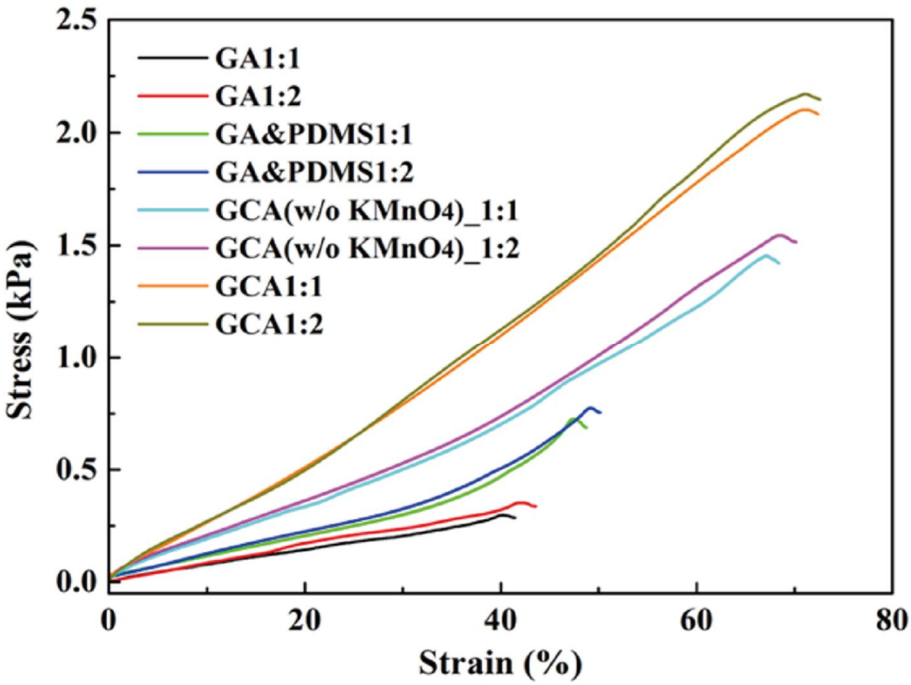

Figure 4.4.12. The mechanical property test of graphene aerogels.

4.4.5.2. Shape stability of PCM composites

The shape stability of PEG, and 1-TD composites are observed by a leakage test as shown in **Fig. 4.4.13**. The PCMs are placed on the hot plate and increased the temperature from 25 °C to 80 °C. From the camera images, all of the graphene aerogel supported PCMs sustains the solid state under the temperature variation. Hence, the PCM/GCA composites are form stable during the phase transitions without any leakage. The **Fig. 4.4.14** shows the mechanical test under the external force at 80 °C. The force is 2N and the pristine PCM composites and PDMS embedded PCM composites appear the leakage due to the weakness of their mechanical properties. On the other hand, the GCA supported PEG, and 1-TD composites exhibit high tolerance without any volume leakage and the GCA has better thermal and mechanical stabilities than PDMS modified PCMs. It is well demonstrated that the GCA supported PCM composites can maintain the intrinsic solid state at the change of external conditions. In addition, the DMA measurement is directly obtained the mechanical properties at the change of temperature as shown in **Fig. 4.4.15**. The storage modulus of PEG composites are rapidly decreased at about 60 ~65 °C which occurring the solid-liquid phase transition in the pure PEG. However, the PEG/GCA composite has less shrinkage than any other PEG composites because of the high mechanical property. The 1-TD has a low melting temperature and easy to change the solid state on the melting process. Similar to the PEG composites, GCA supported 1-TD composite still exhibits the best mechanical property and these PCM composites have a new approach for the thermal energy storage (TES) applications.

The surface images of GCAs, and PCM composites are shown in **Fig. 4.4.16**. There are net-like wrinkles around the internal skeletons and briefly indicates the combination of cross-linked molecular chains in **Fig. 4.4.16a**, and **4.4.16b**. The GCAs still keep their high internal porosities which can infiltrate working materials to fabricate the form stable PCM composites. In **Fig. 4.4.16c**, the PEG is sufficiently filled up into the GCA and observed the both flat surface and textured skeletons. The 1-TD composite is obtained by

infiltration method as presented in **Fig. 4.4.16d**. To investigate the crystalline structures of PCM composites, the XRD peaks are illustrated in **Fig. 4.4.17**. The typical sharp peaks are obviously appeared at the PEG, and 1-TD composites and subsequently demonstrate that there are no chemical reactions between PCMs with GCAs.

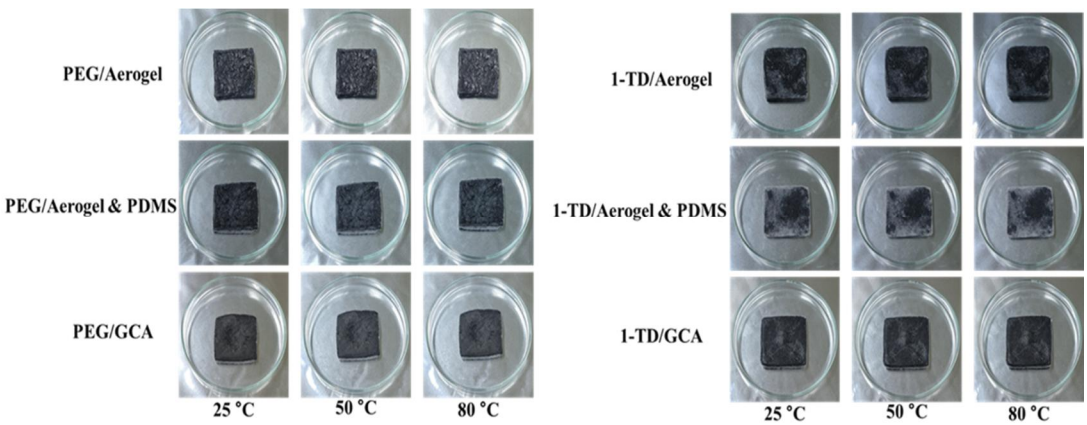

Figure 4.4.13. The form stable camera images of PEG, and 1-TD composite.

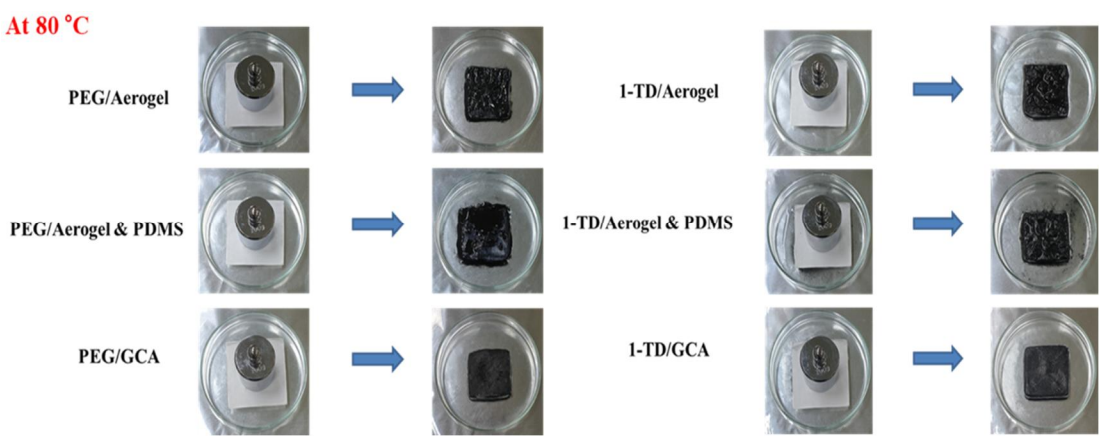

Figure 4.4.14. Form stable test under the external force at 80 °C.

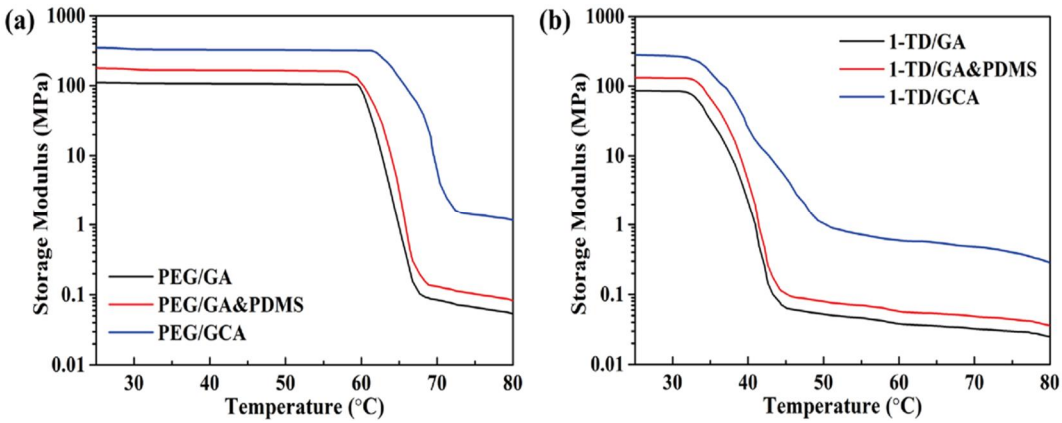

Figure 4.4.15. DMA compression test of (a) PEG composites, and (b) 1-TD composites.

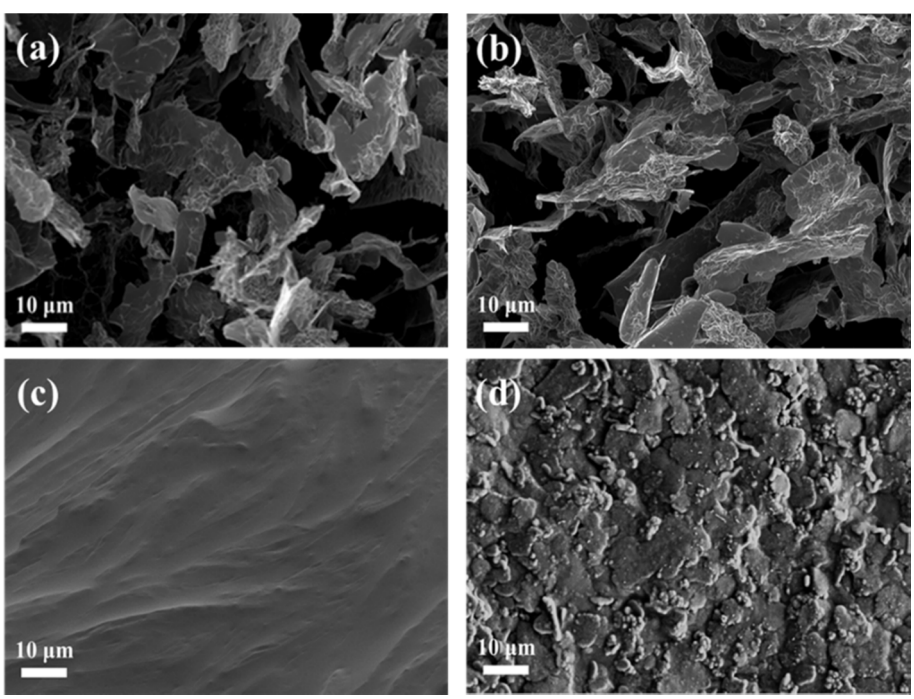

Figure 4.4.16. The SEM images of (a) GCA1:1, (b) GCA1:2, (c) PEG/GCA composite, and (d) 1-TD/GCA composite.

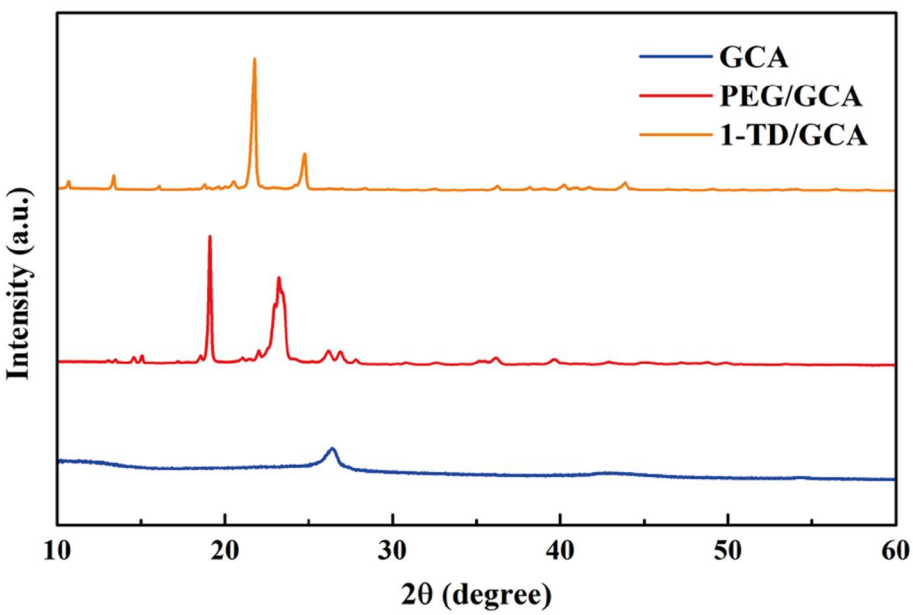

Figure 4.4.17. The XRD peaks of GCA, PEG/GCA, and 1-TD/GCA.

4.4.5.3. DSC measurement and light source morphologies

For confirming the thermal conductivities of PCM composites with graphene nano-platelet (GNP), the **Fig. 4.4.18a** shows the results of PCMs at two different structures. As the PCM composites without GNP merely exhibit the 0.3376 W/mK and 0.2621 W/mK, respectively, while the GNP embedded PCMs are significantly increased to 0.5798 W/mK, and 0.4069 W/mK. Thus, the GNP fillers are affecting the rate of heat transmission and even phase transitions. In **Fig. 4.4.18b**, and **4.4.18c** show the DSC measurement of PEG/GCA, and 1-TD/GCA composites and the characteristics of temperature and thermal enthalpy are listed in **Table 4.4.4**. The onset of melting temperature is began at 50.26 °C, and terminated at 68.30 °C around the PEG composite. The melting temperature (T_m) is obtained at 64.84 °C, and the latent heat (ΔH) is 178.90 J/g. The 1-TD composite starts to occur the phase transition at 35.17 °C, and complete at 45.96 °C. The latent heat (ΔH) is measured as 213.72 J/g. For the case of cooling process, the PEG composite are crystallized at 43.69 °C, and ended at 34.24 °C. The cooling enthalpy is 159.22 J/g and nearly close to the value of pure PEG. In addition, the 1-TD composite has the 36.76 °C onset of cooling temperature and fully completed at 20.06 °C. The cooling enthalpy is 212.41 J/g and still remain the high stored energy. According to the DSC results, both of PEG, and 1-TD composites are utilized to construct the thermoelectric energy harvesting system due to their high thermal energy storage. Furthermore, the thermal stability is important for the PCMs and the **Fig. 4.4.19** shows the DSC thermal cycling and FT-IR results. After 100 cycling test, both of PEG, and 1-TD composites exhibit the similar peaks and keep the intrinsic high thermal enthalpies. The FT-IR peaks obtain the chemical structures after the thermal cycling and there are no new peaks appeared at the PCM composites. It demonstrates the PCM composites have a great thermal stability during the heating and cooling process.

The temperature profiles under the solar irradiation are mentioned in **Fig. 4.4.20**.

Light-On process represents the melting of PEG composites by the heat source and **Fig.4.4.20a** shows the temperature gradients with different sunlight intensities at the surface of device. Easy to find that the maximum temperature of pure PEG is observed at 60 °C due to the low sunlight absorption. However, the temperature of PEG composite is rapidly increased over 80 °C at the solar irradiation especially under the 20 mW/cm^2. After removing the heat source, the temperature peaks are decreased under the natural conditions with similar platforms due to the phase transitions. The temperature gradients of 1-TD composite are similar to the PEGs which appears the increase under the solar irradiation as shown in **Fig. 4.4.20b**. The pure 1-TD has lower sunlight absorption than that of PEG and hard to convert the effective thermal energy storage (TES) on the melting and cooling process. The output electrical current upon Light-On/off process is obtained and shown in **Fig. 4.4.21**. The solar intensity of 10 mW/cm^2 cause the relatively low increase of electrical current and exhibits the small 2nd peak area in **Fig. 4.4.21a**. In addition, the 20 mW/cm^2 intensity lead to rapidly change of temperature gradient and performs a low peak area at the 1st step. As a result, the Light-On harvesting peak under the 15 mW/cm^2 shows the optimum output current. Though the cooling peaks of electrical current are similar under the Light-Off process as presented in **Fig. 4.4.21b**. Based on the Light-On/Off results, the ratios of peak area around the three different light intensities are shown in **Fig. 4.4.21c**. It is estimated that the 15 mW/cm^2 has the largest 1.32 value which is higher than that of 20 mW/cm^2 (Peak ratio: 1.15), and 10 mW/cm^2. The power peaks and LED images are illustrated in **Fig. 4.4.22**, and the maximum power upon Light-On shows 511.58 μW, and 159.03 μW while the cooling process appears the 409.18 μW, and 184.59 μW. The output power of energy harvesting is hard to turn on the LED lamp and combine with the amplifier (LTC 3108) to observe the luminous LED lamp as shown in **Fig. 4.4.22c**. As a result, the thermoelectric energy harvesting system with modified PCM composites can directly generate the electric energy under the existence of solar irradiation and convert solar-to-thermal energy to the output electrical current.

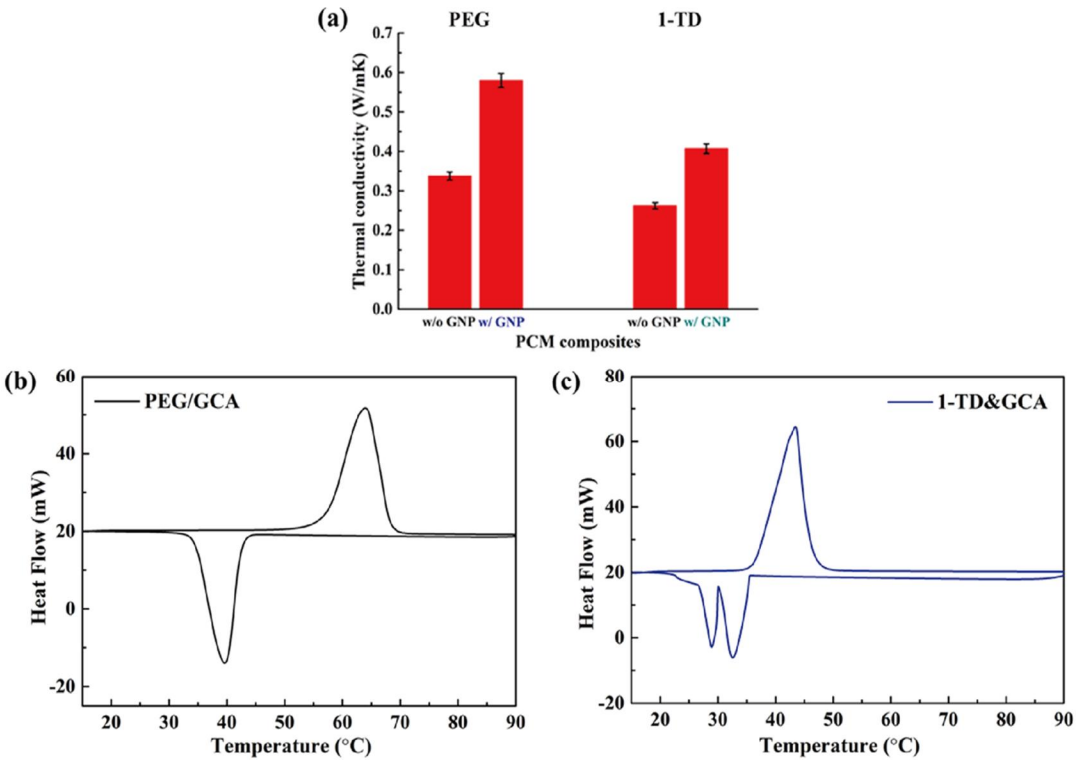

Figure 4.4.18. (a) The thermal conductivity of PCM composites; DSC curves of (a) PEG/GCA composite, and (b) 1-TD/GCA composite.

Table 4.4.4 Characteristics of PEG, and 1-TD PCM composites.

Samples	T_o(°C)		T_e(°C)		T_p(°C)		ΔH(J/g)	
	Heating cycle	Cooling cycle	Heating cycle	Cooling cycle	Heating cycle	Cooling cycle	Heating cycle	Cooling cycle
PEG/GCA	50.26	43.69	68.30	34.24	64.84	39.01	178.90	159.22
1-TD/GCA	35.17	36.76	45.96	20.06	42.87	30.27	213.72	212.41

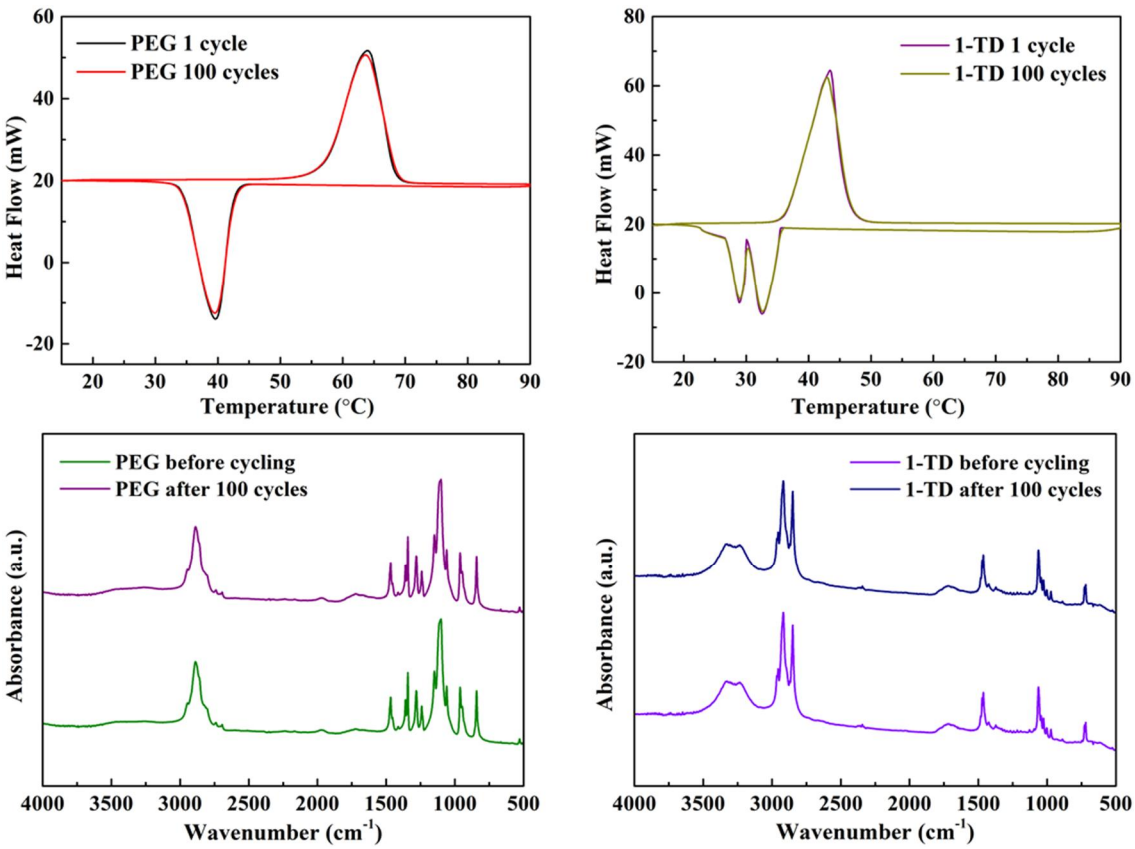

Figure 4.4.19. DSC cycling and FT-IR graph after 100 cycles.

Table 4.4.5. The characteristic of cycling results.

Samples	T_{mp}(°C)	ΔH_m(J/g)	T_{cp}(°C)	ΔH_c(J/g)
PEG cycling	64.17	178.41	38.75	158.80
1-TD cycling	42.06	213.11	30.02	212.18

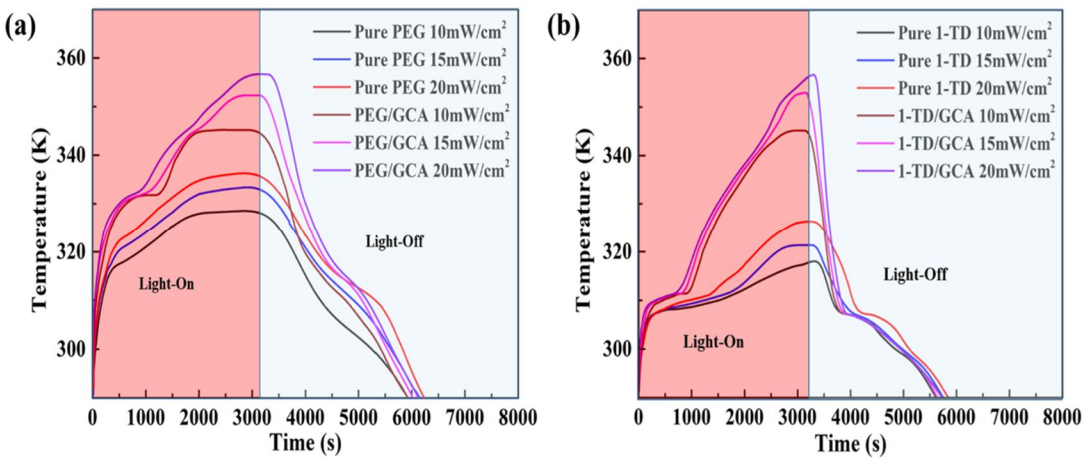

Figure 4.4.20. Temperature change of (a) pure PEG and PEG/GCA, and (b) pure 1-TD and 1-TD/GCA.

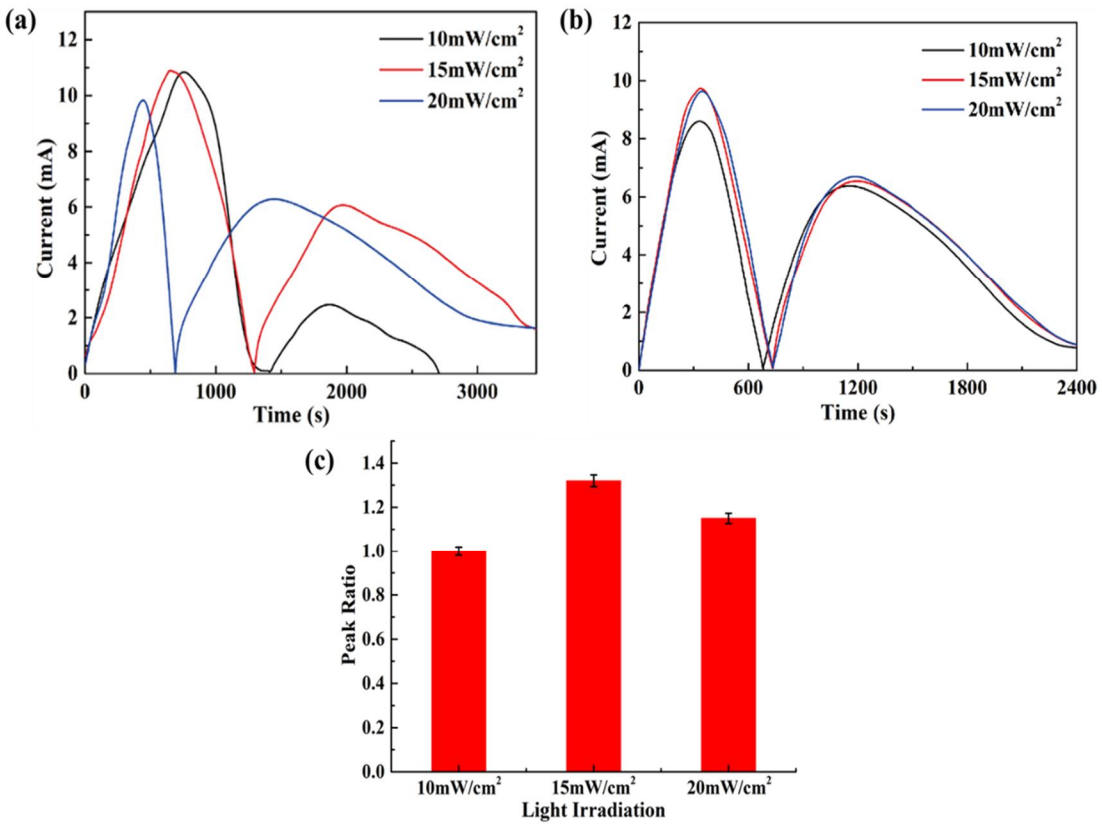

Figure 4.4.21. Electrical current at the different light intensities on (a) melting process, and (b) natural cooling process; the ratio of peak area under the different light intensities..

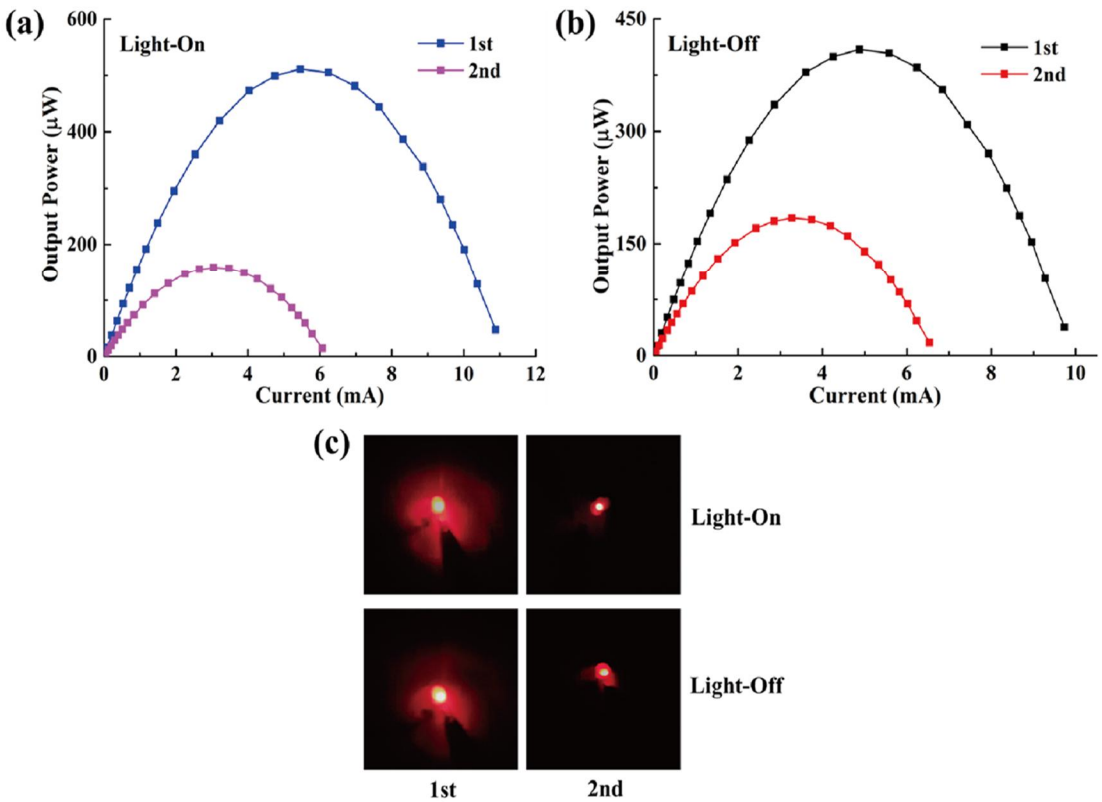

Figure 4.4.22. The power peaks of (a) Light-On process, and (b) Light-Off process. (c) LED images upon Light-On/Off.

4.4.5.4. Numerical simulation of thermoelectric energy harvesting

The temperature profiles under the Light-On/Off process are shown in **Fig. 4.4.23**. From the results of numerical simulation, the temperature peaks are developed at the different profiles as shown in **Fig. 4.4.23a**, and **4.4.23b**. Owing to the lower phase transition temperature as mentioned in DSC result, the 1-TD composite is directly stopped at the nearly isothermal field when the temperature of PEG is still increased upon Light-On process. The 2nd step is appeared that the PEG starts to access the solid-liquid phase transitions and the temperature of melted 1-TD are increased directly. The concept is adopted to the cooling process which the light source is already removed. The temperature is reversed between these two different PCM composites and subsequently obtain the multiple effects of thermoelectric energy harvesting. The maximum temperature difference under the Light-On process is close to the 17.1 °C and 7.2 °C, respectively. The Seebeck effect in the 1st step is maintained 1,400 s when the 2nd step is terminated at about 3,600 s due to the temperature difference between PEG and 1-TD composites upon solar irradiation as shown in **Fig. 4.4.23c**. The Light-Off result is a natural cooling and exhibits the maximum value of 12.5 °C and 7.6 °C, respectively. The temperature difference peaks can realize the Seebeck effect under the energy harvesting system and predict the current peaks on the melting and cooling process.

The experimental current peaks are well compared with the numerical calculation results as shown in **Fig. 4.4.24**. The modeling results are close to the experimental current peaks in both Light-On and natural cooling process. In **Fig. 4.4.24a**, the maximum currents are nearly 11 mA and 6 mA and in accordance with the experimental result. The cooling is terminated at 2,400 s under the natural condition and the maximum currents and peak areas are adjacent with little difference in **Fig. 4.4.24b**. Finally, the output harvesting efficiency is obtained upon Light-On/Off and the results are directly presented in **Fig. 4.4.24c**. The calculated harvesting efficiency is 67.92 % as existence of solar irradiation while the cooling efficiency is 41.72 % after removing the light source. The cooling efficiency is exactly lower than that of melting result due to the energy loss under the natural convection. From the Light-On/Off measurement, the thermoelectric energy

harvesting system is sufficiently utilized at the solar energy applications and further providing a new approach for solar cell, photo-thermal energy utilization, and aerospace power generators.

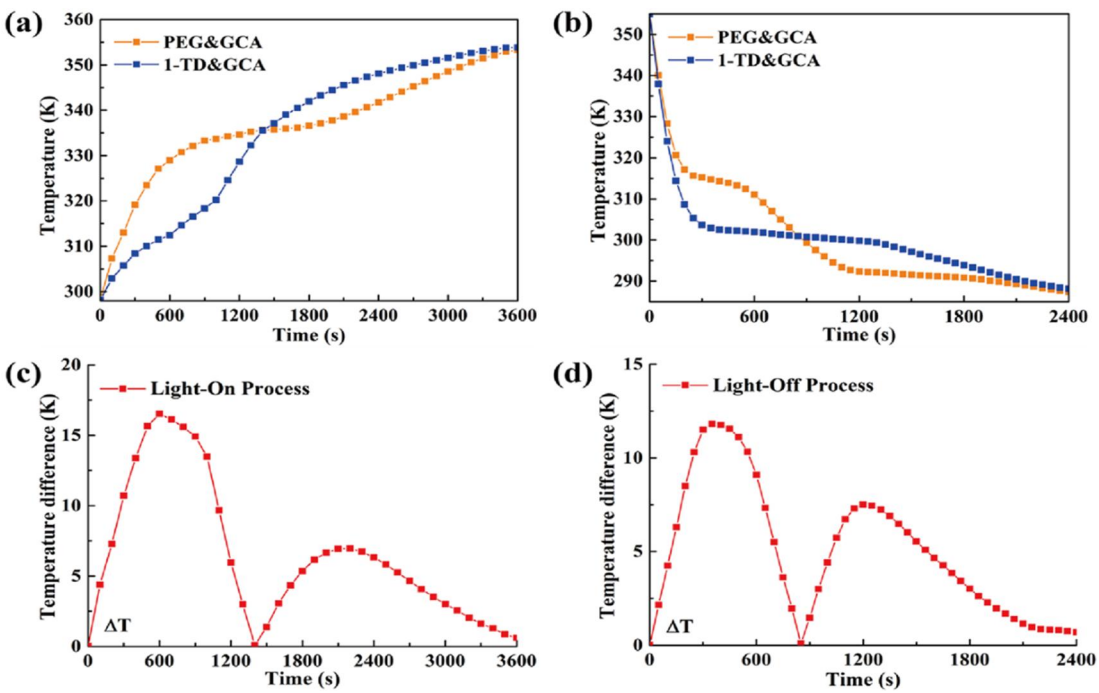

Figure 4.4.23. Temperature profiles of (a) Light-On process, and (b) Light-Off process. The temperature difference under (c) Light-On process, and (d) Light-Off process.

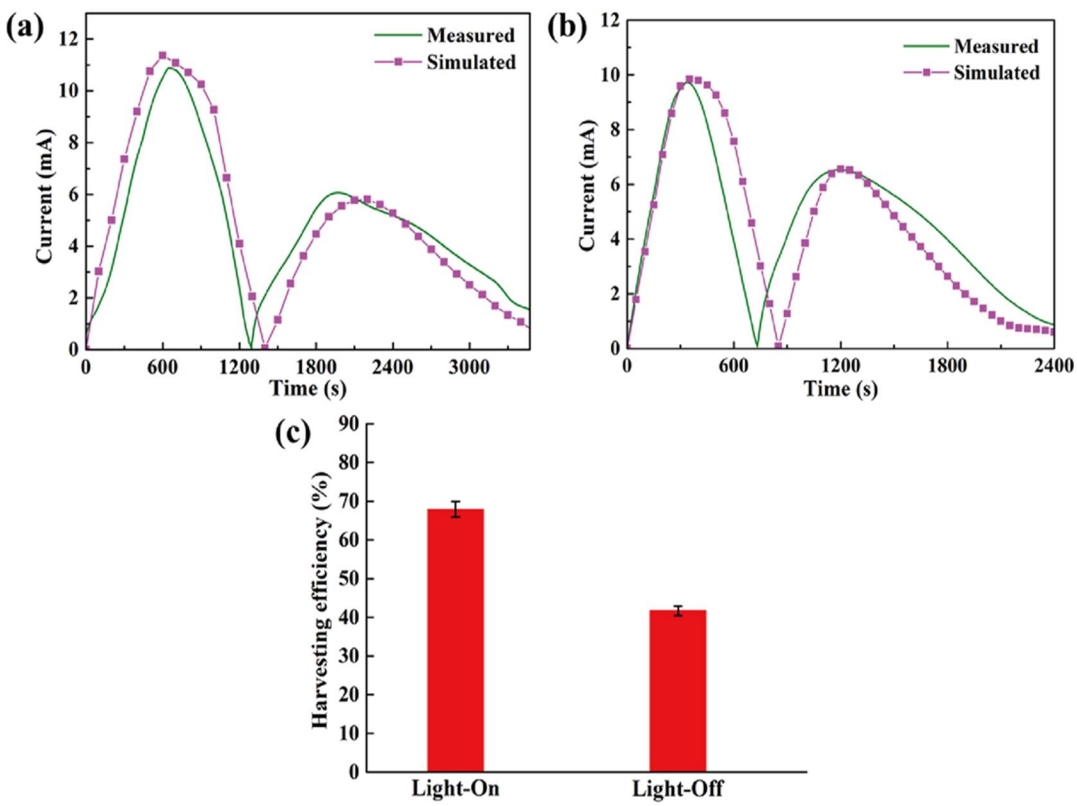

Figure 4.4.24. The combination of simulation results with experimental peaks under (a) Light-On process, and (b) Light-Off process. (c) The harvesting efficiency of Light-On/Off.

4.4.6. Conclusions

In this section, the cross-linked graphene/cysteamine aerogel (GCA) is successfully fabricated and exhibited high porous structure. The modified graphene aerogel has a large surface area and reduce the volume shrinkage under the infiltration process. Both of PEG/GCA and 1-TD/GCA composites can tolerate the external force without any structural damage over the melting temperature. The GCA supported PEG, and 1-TD composites shows a prominent mechanical properties without any leakage upon Light-On/Off process. The solar irradiation in this work has 10 mW/cm^2, 15 mW/cm^2, and 20 mW/cm^2 different intensities on the surface of working materials and further indicates the optimum condition of sunlight power. The electrical current are generated from the energy harvesting system and the 15 mW/cm^2 sunlight holds the maximum peak area and utilized as the optimization solar irradiation in the high latent heat thermal energy storage (LHTES) applications. Furthermore, the GCA supported PCM composites are sufficiently applied to the solar energy collecting system and have a potential applications in the light energy development and aerospace light-to-electric energy harvesting system.

4.5. Summary

The modified graphene aerogels supported phase change materials (PCMs) are successfully fabricated by two kinds of method. The volume shrinkage during the infiltration process is a new challenge to the supporting materials which cause the volume loss and influence the degree of thermal energy storages (TES). The capillary force is the reason of volume shrinkage that improve the flexibility or mechanical property is the effectively direction to solve the serious problem. The PDMS exhibits flexibility and recovery the initial shape completely. The PDMS embedded graphene aerogel can maintain a new flexible property and resist the capillary force to sustain the intrinsic porous structure. Hence, the increase weight of PCM composite can stored more thermal energy than before and efficiently applied to the thermoelectric energy harvesting system. In addition, the graphene /cysteamine aerogel (GCA) has an excellent mechanical properties and even tolerate the external force over the melting temperature, the GCA supported PCM composite are stable to utilize in various thermal energy applications and even control the temperature fluctuation during the phase transition process.

Chapter V.

PCMs for pyroelectric energy harvesting

5.1. Overview

In this chapter, the form stable phase change materials (PCMs) are utilized a new energy harvesting system to generate the electrical energy upon melting and cooling process. The pyroelectric materials can convert the thermal fluctuations into the electrical energy by their specific crystalline structures. In Section 5.2, the principles of phase change materials (PCMs) and the pyro-electrode are briefly described. The introduction of thermal energy device is performed in Section 5.2.1, and the research background is directly indicated in Section 5.2.2. Consider utilizing the pyro-electrode in the energy harvesting system instead of PN TEGs, the PCMs are correlated to the pyroelectric effect and the combination of these essential materials are presented in Section 5.2.3. The conclusions of pyroelectric energy harvesting system is indicated in Section 5.2.4.

Based on the two kinds of PCM composites for the thermal energy storage (TES) applications in the previous work, the PEG, and 1-TD composites are supposed to act as thermal energy collectors and transfer to the pyro-electrode. The change of temperature difference can develop the thermal fluctuation on the two sides of pyroelectric device and obtain the output electrical energy. The multiple PCM composites with pyro-electrode are designated to perform a new energy harvesting system as given in Section 5.3. Except the research introduction in Section 5.3.1, the design of the pyroelectric power generator is mentioned in Section 5.3.2, and the numerical analysis of temperature variations are described in Section 5.3.3. The pyroelectric energy harvesting results are referred to the Section 5.3.4 with the PEG, and 1-TD shape stabilized PCMs and the conclusions are defined in Section 5.3.5.

In order to combine with the practical applications, the sunlight irradiation is the

common heat source for the thermal energy harvesting. In addition, the glass is one of the popular materials utilized for the various applications. The window is the most widely used and manufactured by the glass in human life. Consider the transmission of sunlight across the glass, the pyro-electrode is able to lock in the window glass to generate the temperature variation between the two sides of window. Therefore, the glass transmission of light source is utilized immediately and the PCM composites act as a thermal blind in Section 5.4. There are some of the research background in Section 5.4.1, and the design of this new pyroelectric power generator is mentioned in Section 5.4.2. The numerical simulation is effectively estimate the temperature variation and described in Section 5.4.3. The PCM blind for pyroelectric energy harvesting is directly indicated in the results and discussion in Section 5.4.4, and conclusions are followed in Section 5.4.5. The summary of PCM composites for pyroelectric energy harvesting is completed in Section 5.5.

5.2. Review of PCMs for pyroelctric system

There are kinds of researches about the thermoelectric energy harvesting and the Seebeck effect is the conventional theory for the thermal energy applications. The PN cells are the popular thermoelectric device and the production of electrical current is obtained by the temperature difference between two sides of device. The hot side with high temperature can concentrate plenty of electrons to move toward the opposite side. The electron movement causes the electrical current in the circuit and utilized as a power generator. However, the new type of electrical device is attracted in these 2 years and the concept of pyroelectric effect is followed as below: (i) Need polarization by the external conditions, (ii) The change of temperature difference cause the electrical energy, and (iii) Construct the pyro-electrode with the substrates of great electrical properties. The change of temperature difference is exactly considered as the generation of thermoelectric energy harvesting and the PCM composites can control the temperature variation upon phase transition process. As a result, the shape stabilized PCMs are qualified for applying to the pyroelectric energy harvesting system.

5.2.1. Introduction

The crisis of energy depletion is the hot issue in human life and overcome the serious problem is a task in the science and engineering field. The Seebeck effect is kindly used for the power generation applications and many researched are reported in the thermoelectric energy harvesting system. In our previous work, the PN TEGs are selected as electrode to excite the electron movement. The temperature difference is the necessary condition for occurring the thermoelectric energy conversion. Hence, the two different PCM composites are placed at the sides of PN TEGs and successfully obtain the electrical current on the heating and cooling process.

However, the PN TEGs are relatively high cost with low output efficiency and hard to utilize for the smart control applications due to their rectification property. As mentioned before, the solar energy is a wonderful resource and widely employed to the tremendous applications. Compare with the PN TEGs, the pyroelectric device has a filmy structure, easy to control, and high light transmissions [232]. The most of pyroelectric device is film structure and less than 2 μm which can paste to some of typical materials for the energy harvesting. In addition, the electrical current generated from pyroelectric film depends on the temperature fluctuation and effectively utilized in a smart control of energy harvesting system.

As the temperature variation is affecting the pyroelectric effect, the form stable PCMs are able to adjust the thermal control upon their phase transition process and produce a stable electrical energy in the circuit. Owing to the high latent heat of PCMs, the change of temperature difference becomes regular and extends the time of energy harvesting. There are no report about the combination of PCM composites with pyroelectric film to measure the electrical production and the present research can lead a new approach for pyroelectric energy harvesting applications.

5.2.2. Theoretical background

Unlike the thermoelectric device especially the PN TEGs, the pyroelectric energy harvesters mainly require the change of temperature difference by an external light source or heat flux. The pyroelectric film needs the electrode materials to construct a pyro-effect system and the common used electrode materials are the copper films, sputtered aluminum films, and the indium tin oxide (ITO) glasses. These electrode materials have a high thermal and electrical conductivities which enable the effective heat transfer at the interface between the pyroelectric film and electrode materials. In addition, the optimization of thermal radiation is the main objective for improving the pyroelectric efficiency and increasing the thermal conductivity can contribute to the heat transfer and even energy harvesting efficiency.

In some researches of utilizing the pyroelectric films are mainly combining with the solar irradiation and even loading an external force to generate the piezoelectric effect. The irradiation is unstable and the continuous mechanical fluctuation lead to the damage of the electrode and restrict the broader applications. Thus, the pyro-electrode needs to combine the thermally stable materials to reduce the reflection and increase the efficiency of pyroelectric effect. According to the primary request, the shape stabilized PCMs are the candidate of resolving the main challenges under the phase transition process.

5.2.3. Pyroelectric effect by combination of PCMs

It is indicated that the pyroelectric researches focused on the thermal irradiation without any thermal energy storage (TES) materials. The irregular light fluctuation lead to the low efficiency and hard to utilize for the practical applications. There are combining with the carbon based coating films to increase the sunlight absorption and obtain the relatively high pyroelectric efficiency. In the present work, the PCM composites have large thermal storage capacity in which provides the stable thermal fluctuation and sufficiently controlled the change of temperature difference during the

phase transition process. The high latent heat can provide the continuous thermal irradiation to the pyro-electrode and the pyroelectric energy harvesting system could develop a stable electrical production with high pyroelectric conversion efficiency.

5.2.4. Conclusions

In this work, we attempt to observe the two kinds of new researches and find out that the PCMs are able to control the change of temperature difference and generate the continuous electrical voltage and current in both of melting and cooling process. The two different PCM composites placed at the each side of pyro-electrode exhibit high thermal stability and generate the electrical energy at the changer of external conditions. It is further demonstrated that the heat flux and solar irradiation become effectively utilized in the PCM composites and convert into the thermal stored energy. The PCMs with stored energy are able to prevent the heat reflection and insure the pyro-electrode generate the directional harvesting energy. For the glass transmission study, the sunlight is successfully transmitted to the window glass and aggregated in the PCM blind. The PCM composite absorbs the sunlight for the thermal energy storage (TES), and even releases the stored energy under the cooling process. The pyroelectric harvesting system is smart to control the electrical current under the Light-On/Off conditions.

5.3. Multiple PCM composites for pyroelectric applications

5.3.1. Introduction

Thermal energy storage (TES) is a popular method for the thermoelectric energy harvesting applications. There are several examples to utilize the thermoelectric device and collect the electrical energy in the circuit. The energy harvesting system is composed of working materials and electrodes which can lead to the electron movement. The PN TEGs are the representative device for measuring the thermoelectric effect and generate the induced current at the existence of temperature difference due to the Seebeck effect. The continuous temperature difference can provide the output electrical energy and sufficiently utilized in the practical energy harvesting system [233].

However, the limitation of the thermoelectric device could terminate the new approach for the smart control energy harvesting and a new type of electrode is required immediately. It is found out that the thermal energy is effectively converted to the electricity using pyroelectric device, which act as a smart power generator and providing a degree of electrical power [234]. The common used pyroelectric film is poly(vinylidene difluoride) (PVDF) and manufactured the electrode by the metallic materials [235]. The metallic materials such as copper films, and Silver films have a great electrical conductivity and contribute to the polarization of pyroelectric film. In addition, the PVDF film needs a stable and continuous change of temperature difference to develop the electron movement around the pyro-electrode and the PVDF with metallic materials are appropriate to provide the output electrics [236]. The previous research about the pyroelectrics are concentrated on the solar irradiation without any supporting materials. The low radiation absorption causes the decrease of pyroelectric efficiency and the thermal reflections are restricted the new applications. To provide the stable and continuous heat source, there are some of the supporting materials combined with the pyro-electrode to control the temperature fluctuations. As a result, the phase change materials (PCMs) with high thermal energy storage (TES) are employed to prevent the

main challenges.

The form stable phase change materials (PCMs) are fabricated using modified supporting materials in the previous work. The modified supporting materials especially the graphene /cysteamine aerogel (GCA) can prevent the volume shrinkage under the infiltration process and tolerate the external force over the melting temperature. The excellent thermal and mechanical properties of GCA supported PCMs are the candidate of constructing an effective pyroelectric energy harvesting system. There are no any reports about the pyroelectric effect with the PCM composites and combination of PCMs for the pyroelectric system could indicate a new applications for a smart energy harvesting.

5.3.2. Design of PCM based pyroelectric generator

The construction of PCM based pyroelectric power generator is similar to the thermoelectric energy harvesting system. The PEG, and 1-TD composites are utilized as thermal controller and the pyro-electrode is inserted between these two PCM composites. The schematic of the pyroelectric generator is shown in **Fig. 5.3.1**. There are three types of pyroelectric generator in this study, and the single PCM composite with heat sink is utilized for obtaining the possibility of pyroelectric effect under the change of temperature difference. After that, the multiple PCM composites support the pyro-electrode and confirm the electrical energy upon Light-On and cooling process. It is well known that the air flow affecting the degree of pyroelectric results and modify the heat flow for obtaining the energy harvesting is generally mentioned.

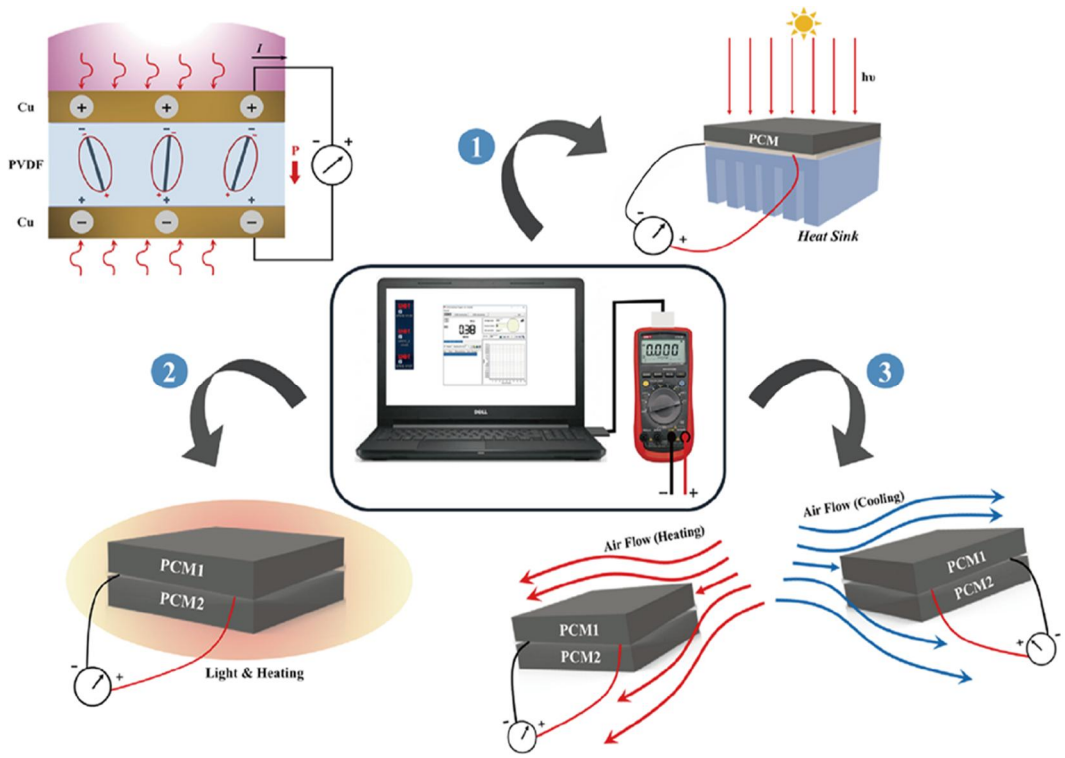

Figure. 5.3.1. The schematic of pyroelectric harvesting system and obtain the electrical energy by the change of external conditions.

5.3.3. Numerical analysis

The change of temperature profiles are predicted utilizing the COMSOL Multiphysics, a commercial software based on finite element method (FEM). The pyroelectric effect depends on the temperature fluctuation during the phase transition process. The pyroelectric energy harvesting system is consist of PCM composites, pyro-electrode (copper with PDVF), and solar lamp. The total mesh elements in this simulation is 30,956, and the pyroelectric current is determined to the change of temperature difference.

the governing equation is adopted the heat transfer model as follow:

$$\rho C_p \frac{\partial \mathbf{T}}{\partial t} + \rho C_p u \cdot \nabla \mathbf{T} + \nabla \cdot \mathbf{q} = Q \tag{1}$$

where ρ is the mass density, C_p represents the heat capacity, and the heat transfer rate $\mathbf{q}$, the heat transfer rate is affecting to the thermal conductivity k and temperature gradient as below:

$$\mathbf{q} = -k\nabla T \tag{2}$$

The density of phase change material (PCM) is given as:

$$\rho = \theta\rho_{phase1} + (1-\theta)\rho_{phase2} \tag{3}$$

where θ is a fill-factor of the mass fractions. The following equations in the numerical simulation are the functions of the fill-factor θ as below:

$$C_p = \frac{1}{\rho}\left(\theta\rho_{phase1}C_{p.phase1} + (1-\theta)\rho_{phase2}C_{p.phase2}\right) + L\frac{\partial \alpha_m}{\partial T} \tag{4}$$

$$k = \theta k_{phase1} + (1-\theta)k_{phase2} \tag{5}$$

$$\alpha_m = \frac{1}{2}\frac{(1-\theta)\rho_{phase2} - \theta\rho_{phase1}}{\theta\rho_{phase1} + (1-\theta)\rho_{phase2}} \tag{6}$$

where α_m shows the mass coefficient. The boundary condition is defined the external

natural convection as follow:

$$-\mathrm{n} \cdot \mathbf{q} = \mathbf{q_0} \tag{7}$$

where n means the normal vector and $\mathbf{q_0}$ is the heat flux by the external convections. The heat flux is the function of the heat transfer coefficient ($\mathrm{h_{air}}$) and the temperature difference as below:

$$\mathbf{q_0} = \mathrm{h_{air}} \cdot (\mathbf{T_{ext}} - \mathbf{T}) \tag{8}$$

The external temperature $\mathbf{T_{ext}}$ is corresponding to the external conditions and directly affecting the heat flux upon melting and cooling process. The pyroelectric current is defined as below [237]:

$$\mathrm{I} = p^* \mathrm{A} \cdot \mathrm{dT/dt} \tag{9}$$

Where the p^* means the pyroelectric coefficient, A is the surface area of pyro-electrode, and change of temperature difference is shown as $\mathrm{dT/dt}$. The electrical voltage is described as $\mathrm{V} = \mathrm{I} \cdot \mathrm{R}$ and R is the resistance of pyro-electrode.

5.3.4. Results and discussion

5.3.4.1. The confirmation of pyroelectric effect with PCM composite

To confirm the pyroelectric effect with the combination of PCM composite, the single PCM is directly placed at one side of the pyro-electrode and the other side is connected to the heat sink which can promote the heat flux at the temperature variation. The **Fig. 5.3.2** shows the change of temperature difference and profiles upon Light-On/Off process. In **Fig. 5.3.2a**, and **5.3.2b**, the temperature fluctuations are continuous and considered as providing the pyroelectric energy harvesting under the polarization of pyro-electrode. In addition, the **Fig. 5.3.2c**, and **5.3.2d** are generally indicated that the temperature difference is the main reason of motivating the temperature irradiation around the pyro-electrode. According to the temperature fluctuation result, the electrical voltage and current are easy to obtain in the closed circuit as shown in **Fig. 5.3.3**. It is well known that the current is just depended on the output voltage from the pyro-electrode and

corresponding to the temperature fluctuation upon Light-On/Off process. In **Fig. 5.3.3a**, and **5.3.3.b**, both of the energy harvesting is effectively occurred and the continuous results can briefly suggest that the PCM composite in the pyro-system prevents the thermal reflection and has a great ability to control the heat flux. To predict the temperature gradients sufficiently, the numerical simulation is mentioned and the modeling results are shown in **Fig. 5.3.4**, and **Fig. 5.3.5**. The numerical calculation is close to the experimental result and the **Fig. 5.3.4a** indicates the temperature profiles of PCM composite and heat sink. The temperature fluctuation is mentioned in the **Fig. 5.3.4b** upon Light-On process, and the change of temperature difference between the sides of pyro-electrode are able to produce the electrical energy in **Fig. 5.3.4c**, and **5.3.4d**. Furthermore, the **Fig. 5.3.5** illustrates the pyroelectric calculation as removing the heat source, and the cooling state of pyroelectric results are explained numerically and confirm that the PCM composite contributes to the generation of energy harvesting.

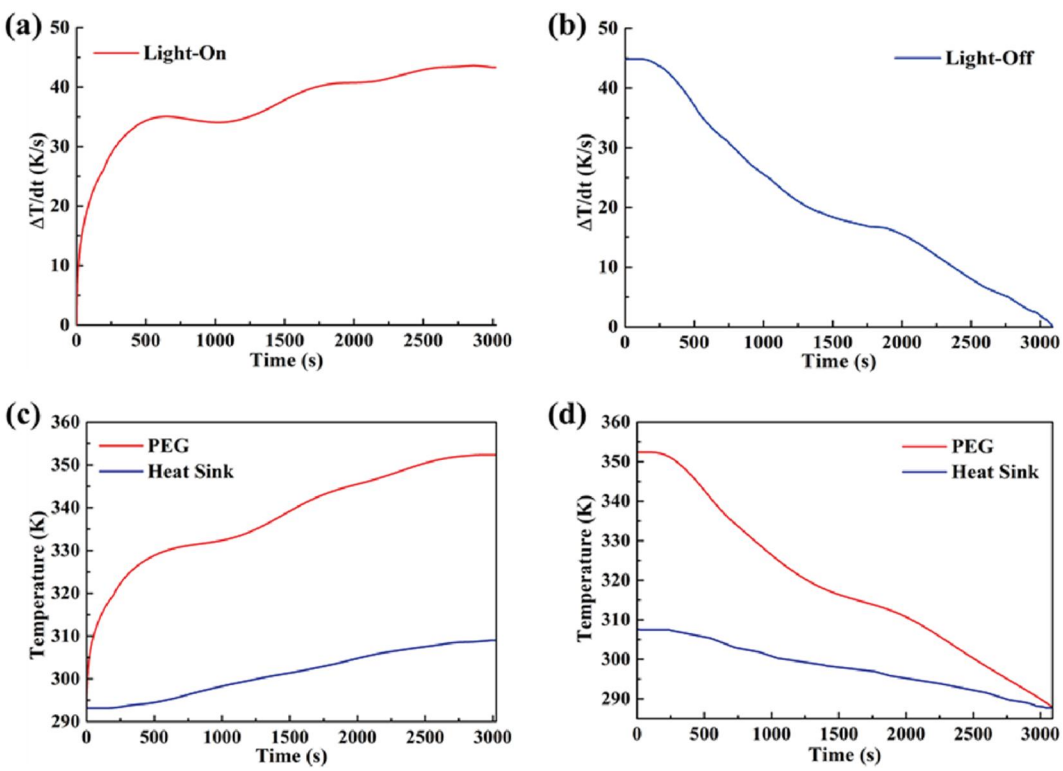

Figure. 5.3.2. The change of temperature difference upon (a) Light-On process, and (b) Light-Off process. The temperature curves of PEG and heat sink upon (c) Light-On process, and (d) Light-Off process.

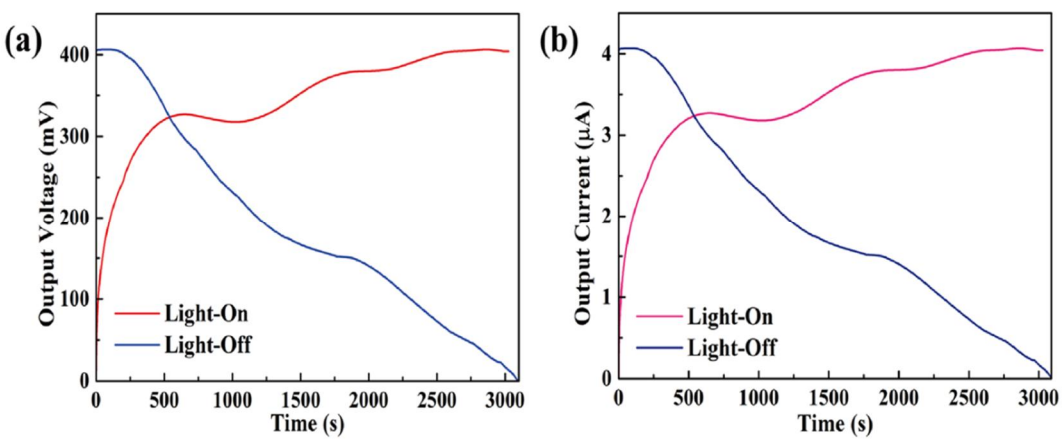

Figure. 5.3.3. The (a) output voltage, and (b) output current upon Light-On/Off process.

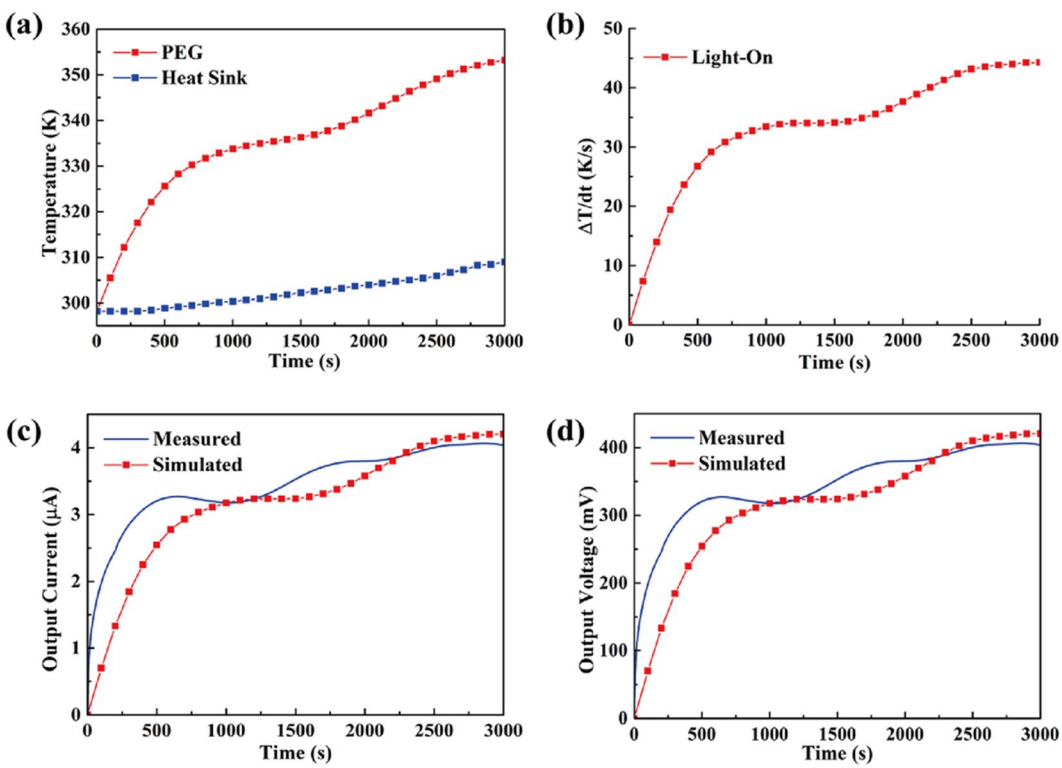

Figure. 5.3.4. The Light-On simulation results of (a) temperature profiles, (b) the change of temperature difference, (c) comparison of output current, and (d) output voltage.

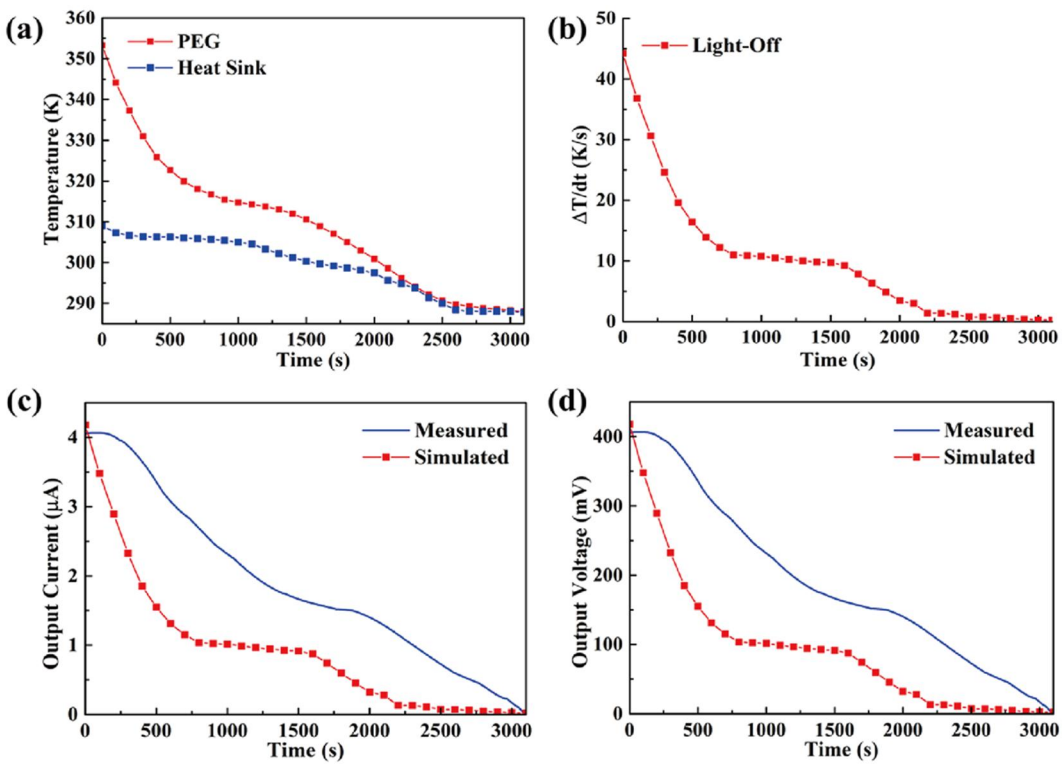

Figure. 5.3.5. The Light-Off simulation results of (a) temperature profiles, (b) the change of temperature difference, (c) comparison of output current, and (d) output voltage.

5.3.4.2. The multiple PCMs for pyroelectric energy harvesting

Based on the single PCM test in the pyroelectric system, the multiple PCM composites are directly employed in the pyroelectric generator and smartly control the thermal fluctuations on the melting and cooling process. The PCMs with high latent heat is one of prominent advantages and smoothly converts the external thermal energy to the pyro-electrode during the phase transitions. The results of multiple PCM pyroelectric energy harvesting are shown in **Fig. 5.3.6**. The electrical energy is collected at two steps due to the reversed temperature difference between two PCM composites. The multiple PCMs for pyroelectric system has effectively proceeded the temperature fluctuation under the control of PCM composites. The modeling results are presented in **Fig. 5.3.7**, and **5.3.8** to estimate the temperature profiles upon Light-On/Off process. The heating temperature gradients are illustrated in **Fig. 5.3.7a**, and the maximum change of temperature difference is close to 17 °C in **Fig. 5.3.7b**. It is indicated that the numerical modeling is appropriate to calculate the prediction of pyroelectric effect. The cooling state is well performed as shown in **Fig. 5.3.8**, and the multiple system is helpful to utilize the pyro-electrode in the thermal energy storage applications. Moreover, the natural condition is turned to the existence of heat flow and measuring the energy harvesting by the combination of PCM composites. The manufactured pyro-system is exposed at the heat flux of 1m/s, 3m/s, and 5m/s conditions to obtain the pyroelectric effect. The **Fig. 5.3.9** shows the output voltage and current under the heating and cooling air flow stations. In **Fig. 5.3.9a**, and **5.3.9b** is the main results of heat flux and the rate of harvesting transitions are rapidly increased due to the high thermal irradiations. In spite of the heating process has an effective change under the different rate of heat source, the cooling results merely occurs a slight deformation of curves in Fig. **5.3.9c**, and **5.3.9d** and it demonstrates the thermal fluctuation is the main reason for the production of pyroelectrics. To confirm the optimization of heat flux upon melting and cooling process, the peak area ratios are calculated as shown in **Fig. 5.3.10**, and the average ratio of

melting/cooling results are listed in **Table 5.3.1**. From the peak ratios, the 3m/s heat flux is the optimum external condition for the PCM based pyroelectric system to proceed the thermal energy harvesting.

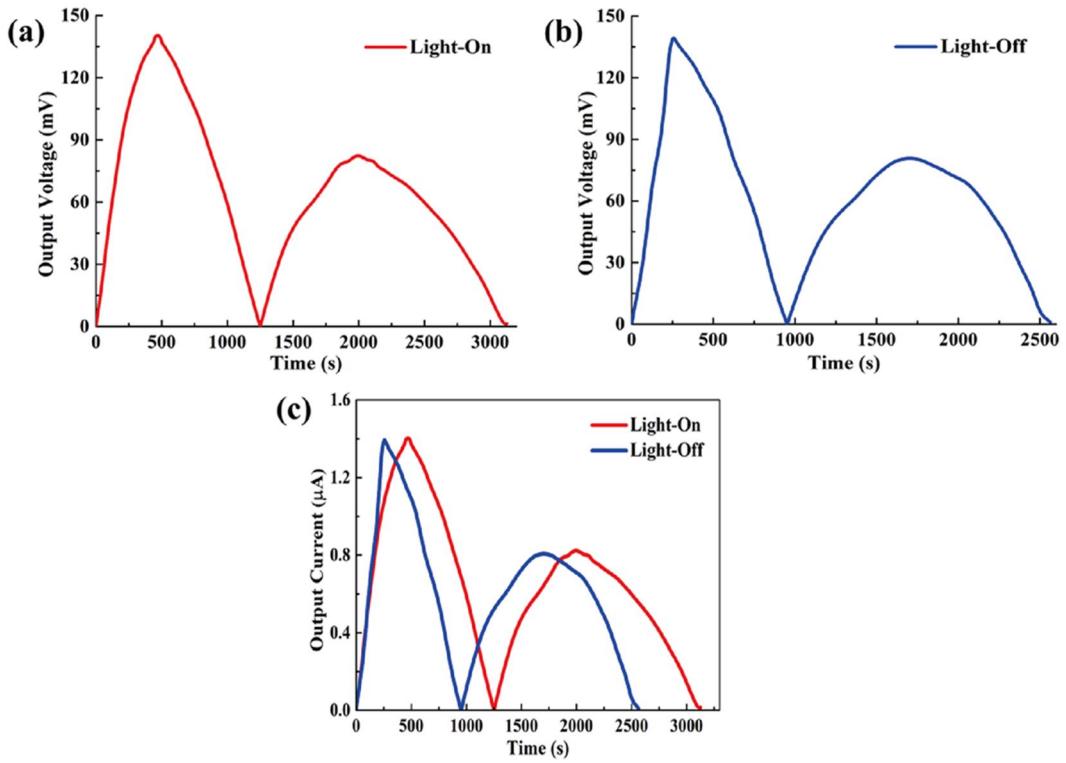

Figure. 5.3.6. The multiple PCMs for pyroelectric generator and the results of (a) output voltage upon Light-On, (b) output voltage upon Light-Off, and (c) output current upon Light-On/Off process.

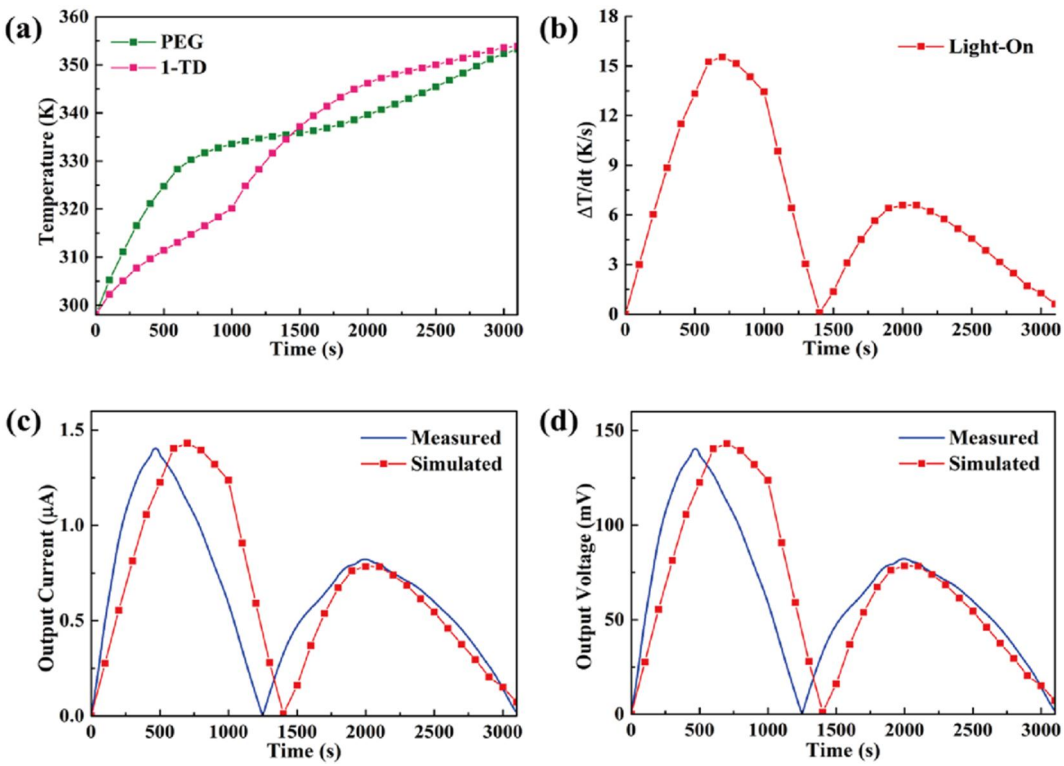

Figure. 5.3.7. The simulation results of (a) temperature profiles upon Light-On, (b) change of temperature difference upon Light-On, (c) the current comparison, and (d) the voltage comparison.

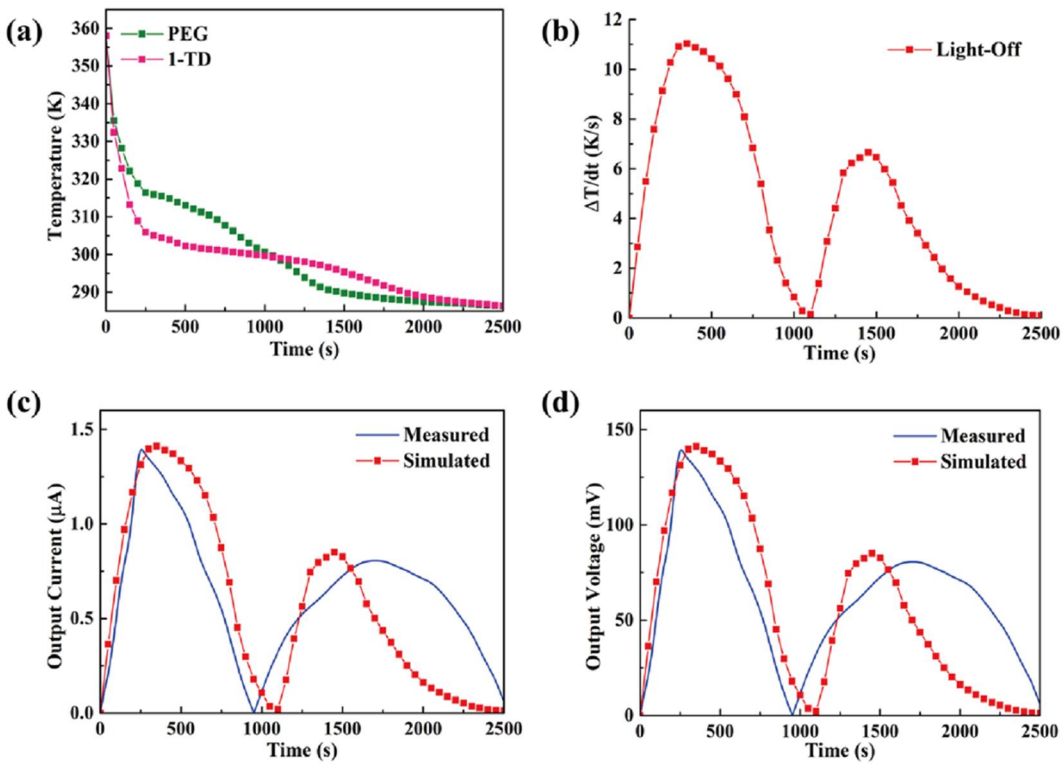

Figure. 5.3.8. The simulation results of (a) temperature profiles upon Light-Off, (b) change of temperature difference upon Light-Off, (c) the current comparison, and (d) the voltage comparison.

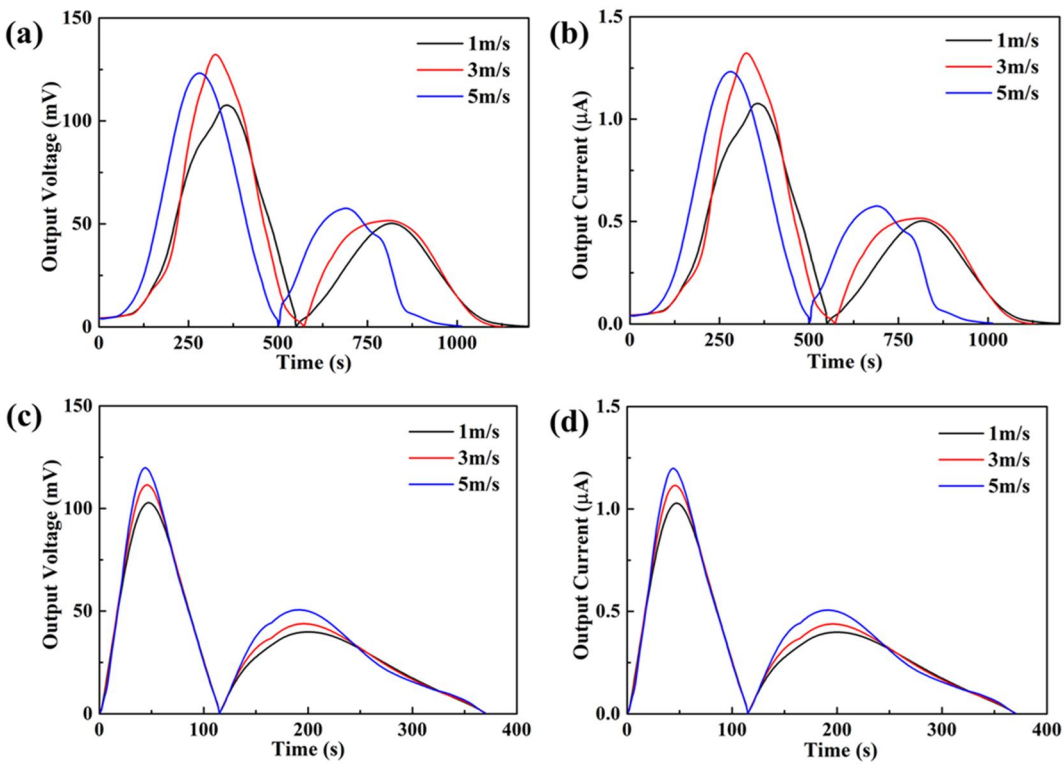

Figure. 5.3.9. The heat flux results of (a) output voltage upon heating, (b) output voltage upon cooling, (c) the current upon heating, and (d) current upon cooling.

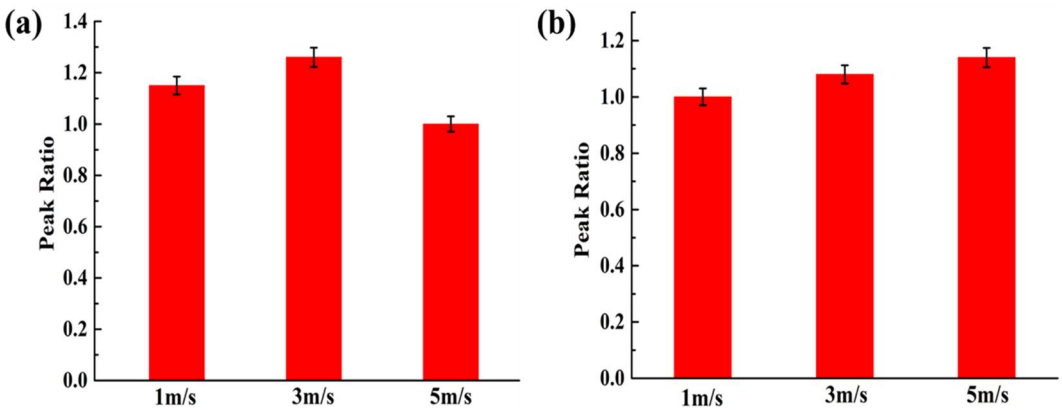

Figure. 5.3.10. The peak area ratios of (a) heating process, and (b) cooling process.

Table 5.3.1. The average ratios of peak area with different air flow conditions.

	1m/s	3m/s	5m/s
Average Ratio	1.08	1.17	1.07

5.3.5. Conclusions

In this work, the pyroelectric effect is successfully obtained using PEG, and 1-TD composites upon melting and cooling process. The PCMs act as a thermal controller and provide the stable and continuous heat source to the pyro-electrode. The single PCM confirms that the PCMs can hold the temperature fluctuations under the solar irradiation conditions and prevent the thermal reflection under Light-On/Off measurement. Furthermore, the multiple PCM composites construct the pyroelectric energy harvesting system is further indicated the change of temperature difference has an excellent result for the power generation system. The multiple PCM based system can be utilized to the different external conditions and the air flow test demonstrates the pyroelectric effect is effectively obtained under the heat flow observations. The numerical simulation is well agreement with the experimental result and directly performs the change of temperature profiles on the various melting and cooling process. Thus, the PCM composite with pyro-electrode system develop a new approach for thermal energy storage (TES) applications and would be widely utilized in the smart control of pyroelectric energy harvesting system.

5.4. Glass transmission of light source for pyro-generator

5.4.1. Introduction

The pyroelectric materials are able to produce the electrical energy under the thermal fluctuation, acting as a new type of power generator [238]. The utilization of power supply or thermal energy harvester become more and more attracted due to the energy depletion in the world. The thermoelectric effect is one of the popular method for electrical energy production under the temperature difference. Though the thermoelectric energy harvesting system is well mentioned, the smart control is the recent issue especially in these 2 years and the thermoelectric device have not approached to the new energy harvesting system [239]. Thus, the pyroelectric effect is considered as a potential design of constructing the smart control energy harvesting system.

In order to obtain the pyroelectric effect, the pyro-electrode is performed with the metallic nature materials which can exist the polarization in the pyroelectric device [240]. The poly(vinylidene difluoride) (PVDF) is one of the popular pyroelectric films due to the ferroelectric property. In addition, the PVDF film is transparent and easy to transmit the light source in the solar irradiation test [241]. Based on the PVDF features, the utilization of sunlight transmission across the pyro-electrode has a possibility of solar light conversion and pyroelectric energy harvesting applications. To construct the pyro-electrode, the indium tin oxide (ITO) is the appropriate electrode material and the pyroelectric device are effectively transmit the light source to obtain a new production of energy harvesting [242]. The glass especially window is normally used in various field and the transparency structure for solar irradiation is a new method to collect the thermal energy [243]. The window glass including that of pyro-electrode suggests the new smart control of sunlight application. However, the low efficiency and thermal reflection is the key challenge to complete the pyroelectric power generator. Hence, the phase change

materials (PCMs) are selected as a blind structure to combine with the window glass.

The shape stabilized phase change materials (PCMs) are successfully fabricated in previous work and significantly improved the thermal and mechanical properties. The form stable PCM composites are directly utilized as a thermal collector and even release the stored thermal energy due to the high latent heat. The PCMs placed at one side of window glass based pyro-electrode as a sunlight blind, it can sufficiently absorb the transmitted light source and convert into the thermal energy. After removing the light source, the PCM composite starts to release the stored energy and provide a stable change of temperature difference which can generate the pyroelectric effect upon Light-Off process. According to the construction of pyroelectric system, the PCM composite is utilized as a thermal blind and produce the electrical energy under the sunlight irradiation. This work extends the range of potential applications to the smart energy control, sunlight, and aerospace power supply fields.

5.4.2. Design of pyroelectric power generator

The pyroelectric energy harvesting system is correlated to the sunlight transmission across the window glass and pyro-electrode. The PCM composite is placed at the opposite side of window glass which acts as a sunlight blind and collect the solar energy under the Light-On process. The sunlight intensity at the surface of window glass is defined as 10 mW/cm^2, 15 mW/cm^2, and 20 mW/cm^2. The construction of pyroelectric power generator is given in **Fig. 5.4.1**. After removing the light source, the PCM composite are able to release the stored thermal energy and the current direction is reversed on the cooling process. The different intensity of solar irradiation requires the optimization system with PCM composite and this study are working out the appropriate PCM composites for the pyroelectric energy harvesting applications.

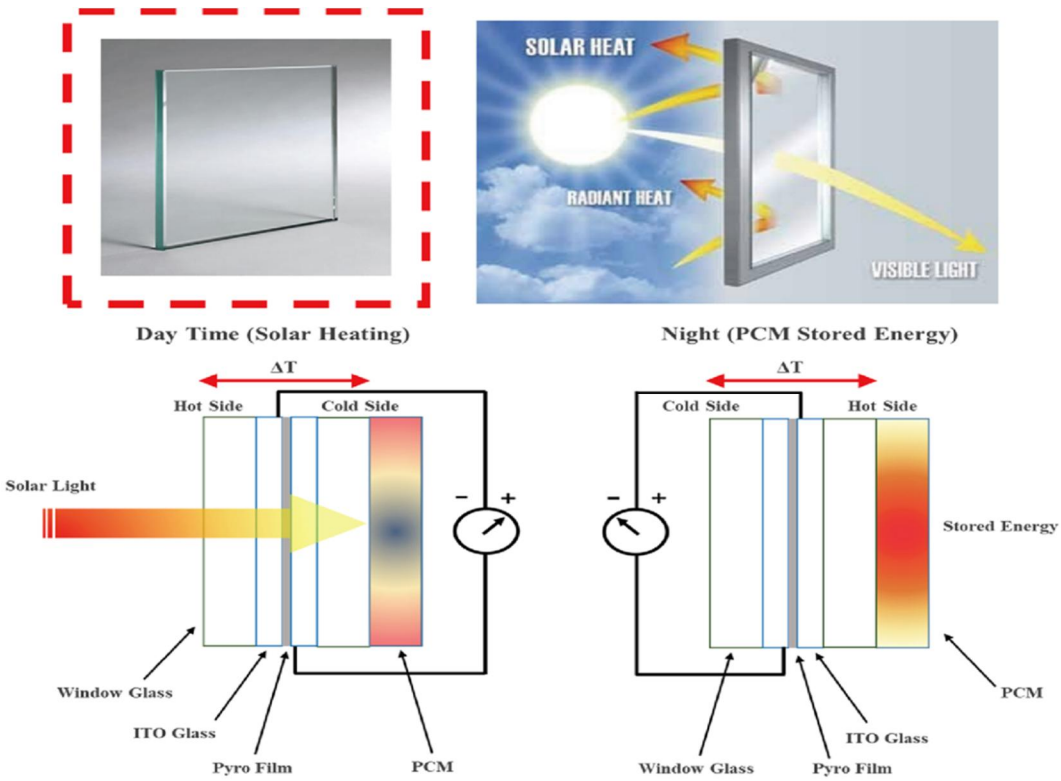

Figure. 5.4.1. The schematic of sunlight transmission and PCM blinds for pyroelectric energy harvesting.

5.4.3. Numerical analysis

The COMSOL Multiphysics, a commercial software based on finite element method (FEM) to estimate the change of temperature profiles upon Light-On/Off process. Based on the pyroelectric energy harvesting system, the geometry of unit cell is consist of PCM composites, normal glass, ITO, pyroelectric film (PDVF), and solar lamp. The total mesh elements in this numerical modeling is 31,034, and the pyroelectric current is calculated by the change of temperature variations.

The heat transfer governing equation is mentioned as below:

$$\rho C_p \frac{\partial \mathbf{T}}{\partial t} + \rho C_p u \cdot \nabla \mathbf{T} + \nabla \cdot \mathbf{q} = Q \tag{1}$$

where ρ shows the mass density, C_p is the heat capacity, and the heat transfer rate $\mathbf{q}$, the heat transfer rate is corresponding to the thermal conductivity k and temperature gradient as shown in Eqn (2). The PCM density is considered as the existence of two different phase as described in Eqn (3):

$$\mathbf{q} = -k\nabla T \tag{2}$$

$$\rho = \theta\rho_{phase1} + (1-\theta)\rho_{phase2} \tag{3}$$

where θ means a fill-factor of the PCM. The heat capacity equations are directly correlated to the fill-factor θ as below:

$$C_p = \frac{1}{\rho}\left(\theta\rho_{phase1}C_{p.phase1} + (1-\theta)\rho_{phase2}C_{p.phase2}\right) + L\frac{\partial \alpha_m}{\partial T} \tag{4}$$

$$k = \theta k_{phase1} + (1-\theta)k_{phase2} \tag{5}$$

$$\alpha_m = \frac{1}{2}\frac{(1-\theta)\rho_{phase2} - \theta\rho_{phase1}}{\theta\rho_{phase1} + (1-\theta)\rho_{phase2}} \tag{6}$$

where α_m is the mass coefficient. The boundary heat source is the B.C in the numerical modeling and defined as:

$$-\mathrm{n} \cdot \mathbf{q} = \mathbf{q_0} \tag{7}$$

where n still represents the normal vector and $\mathbf{q_0}$ is the general heat source by the sunlight intensity upon Light-On process. When the natural cooling after removing the light source, the $\mathbf{q_0}$ means the heat flux during the crystallization process. The heat flux is related to the heat transfer coefficient ($\mathrm{h_{air}}$) and the temperature difference as below:

$$\mathbf{q_0} = \mathrm{h_{air}} \cdot (\mathbf{T_{ext}} - \mathbf{T}) \tag{8}$$

The external temperature $\mathbf{T_{ext}}$ is changed by the degree of heat flux Light-On/Off process. The equation of pyroelectric current is given as below:

$$\mathrm{I} = p^* \mathrm{A} \cdot \mathrm{dT/dt} \tag{9}$$

where the p^* is the pyroelectric coefficient, A means the surface area of pyro-electrode, and $\mathrm{dT/dt}$ is the change of temperature difference by time. The electrical voltage is simple as $\mathrm{V} = \mathrm{I} \cdot \mathrm{R}$ and pyro-electrode resistance is R.

5.4.4. Results and discussion

5.4.4.1. The glass transmission with PCM blind for pyroelectric effect

The results of pyroelectric effect from the manufactured window glass system is obtained adequately and numerically to develop a new type of power generator. The sunlight intensities are composed of 10mW/cm^2, 15mW/cm^2, and 20mW/cm^2 to find out the optimum PCM blind to construct a smart control harvesting system. The UV-vis results can confirm the efficiency of sunlight transmittance and the thickness of glass is directly affecting the transmittance results on the basis of Lambert-Beer Law. The **Fig. 5.4.2** is the UV-vis peaks of glass electrode and the output sunlight transmittance is high enough for PCM composite to absorb the solar energy. In **Fig. 5.4.3** shows the temperature profiles and calculated temperature fluctuation under the 10mW/cm^2 solar irradiation. It is indicated that the relatively low light source are merely affecting the PCM composite with low melting temperature. Thus, the PEG composite is hard to proceed the phase transitions without any thermal energy storage. In contrast, the 1-TD

composite are sufficiently absorbed the external energy and release the thermal energy upon Light-Off process. The maximum temperature fluctuation is over the 30 °C and the 1-TD composite acts as an excellent thermal blind in this glass transmission system. When the intensity is increased to the 15mW/cm^2, the both of PEG, and 1-TD composites are occurring the phase transitions and stored light energy upon Light-On process. The PEG, and 1-TD composites exhibit each advantage of temperature fluctuation conditions as given in **Fig. 5.4.4**. It seems that the 1-TD still hold the optimum thermal energy harvesting, the average value of Light-On/Off process is important for the PCM blind and the PEG composite in this case is selected as an appropriate thermal collector for pyroelectric effect. As the sunlight intensity is up to 20mW/cm^2, the high intensity can promote the change of temperature and even the temperature fluctuations. The temperature profiles in this case are shown in **Fig. 5.4.5**, and the change of temperature difference is similar to each case of PCM blind. Consider the efficiency of energy harvesting, combination of PEG, and 1-TD composite to construct a multiple glass electrode system is considerable and the multiple pyro-system is presented in **Fig. 5.4.6**. In **Fig. 5.4.6a**, the PEG, and 1-TD combination system exhibits a relatively average temperature fluctuation and the ratios of peak area are mentioned in **Fig. 5.4.6b**. The multiple PEGs are relatively low while the multiple 1-TDs performs 1.1; the PEG with 1-TD system is obtained to 1.14 which is higher than that of multiple 1-TDs and the multiple pyro-electrodes with PEG and 1-TD blinds are the optimization system at the high sunlight intensity and effectively generate the pyroelectric energy harvesting.

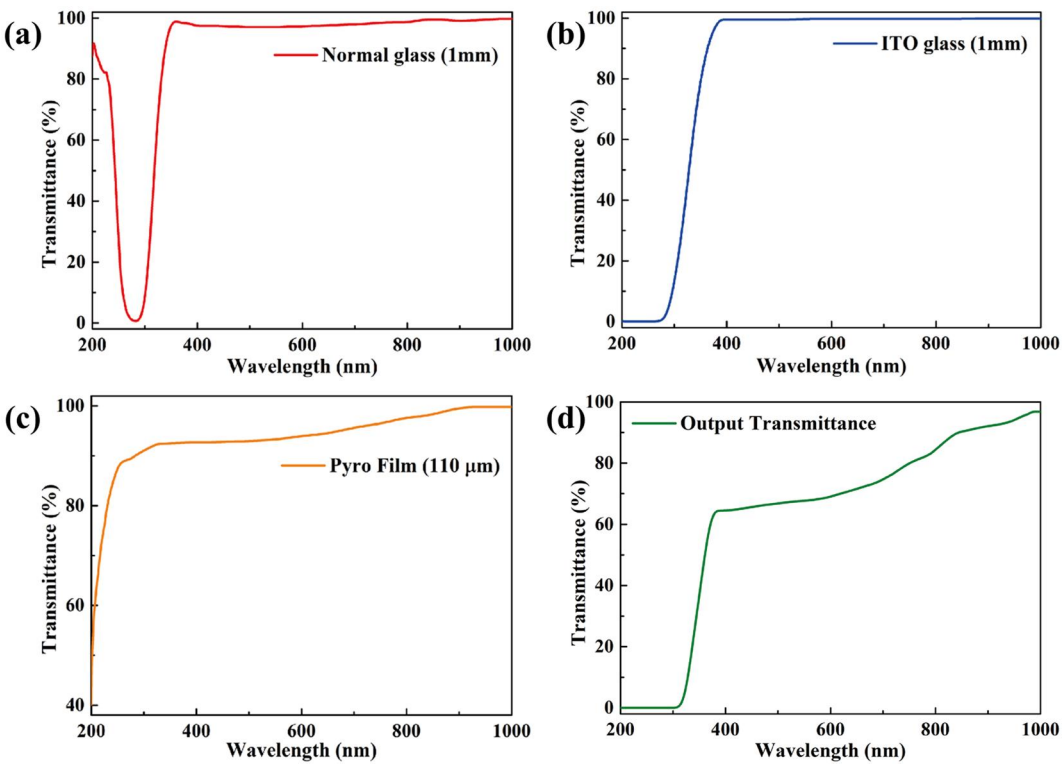

Figure. 5.4.2. The UV-vis transmittance results of (a) normal glass, (b) ITO glass, (c) pyro film, and (d) output transmittance.

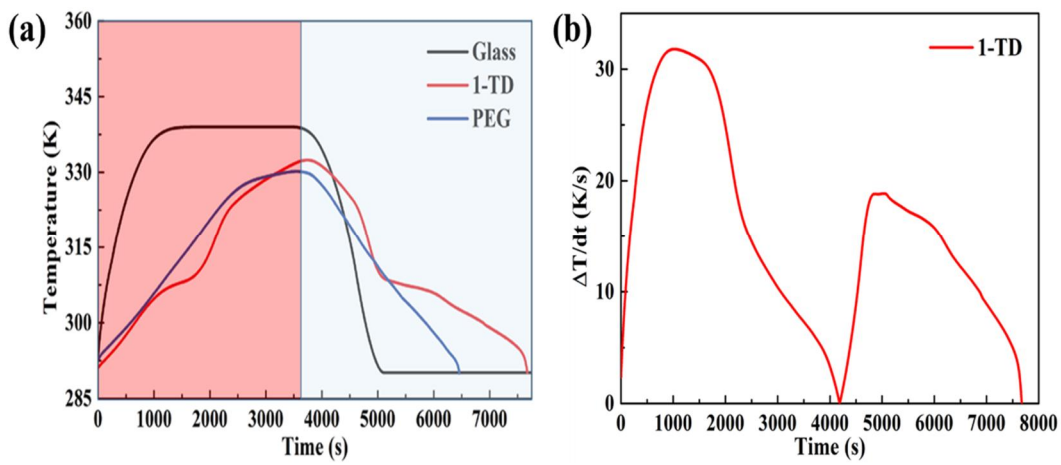

Figure. 5.4.3. (a) The temperature profiles, and (b) change of temperature difference at the 10 mW/cm^2.

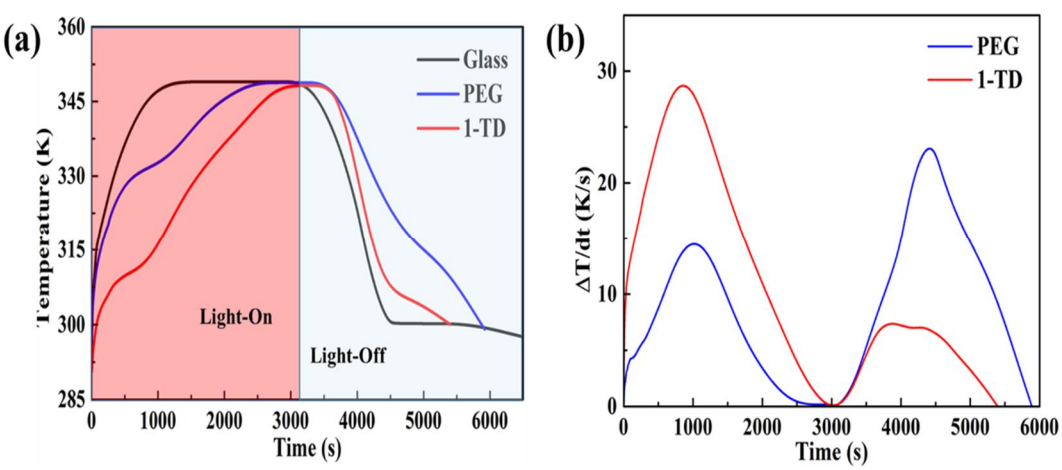

Figure. 5.4.4. (a) The temperature profiles, and (b) change of temperature difference at the 15 mW/cm^2.

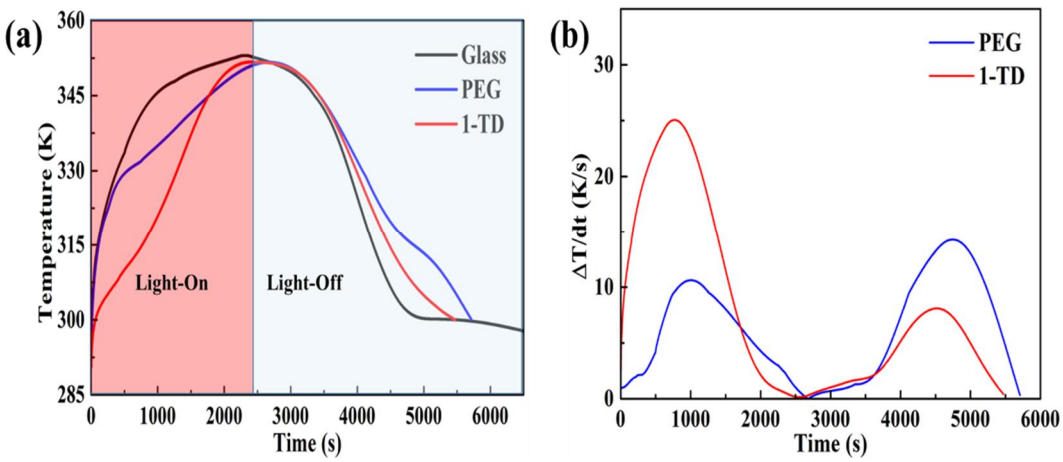

Figure. 5.4.5. (a) The temperature profiles, and (b) change of temperature difference at the 20 mW/cm^2.

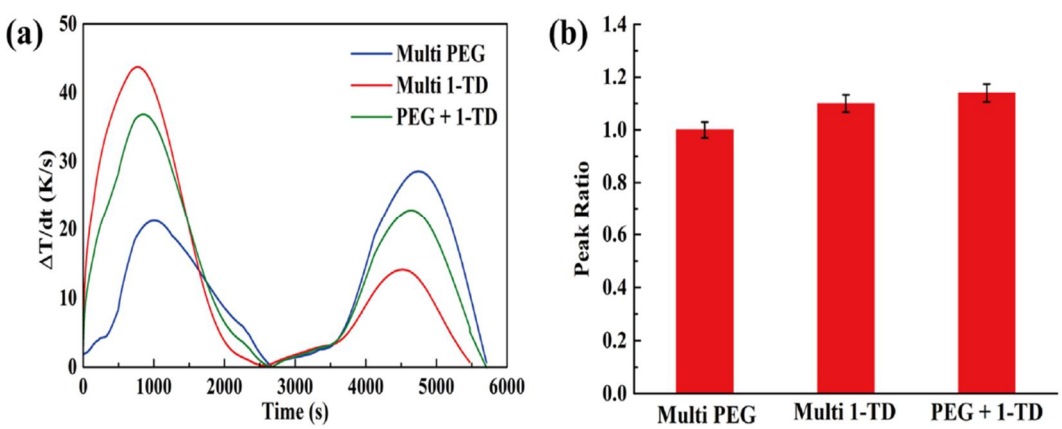

Figure. 5.4.6. (a) The multiple peaks of PCMs, and (b) ratios of peak area.

5.4.5. Conclusions

In this study, we fabricated a new structure of pyroelectric power generator with the light source across the window glass. The energy harvesting system has a great sunlight transmission by the UV-vis results and effectively utilized for a smart control of pyroelectric energy harvesting. Based on the Light-On measurement with different light intensities, the 1-TD composite exhibits an appropriate thermal blind than that of PEG composite at the 10mW/cm^2 conditions. The PEG composite is hard to approach the phase transition process due to the relatively high melting temperature. Furthermore, as the light intensity is increased to the 15 mW/cm^2, both of the PEG, and 1-TD composites show the large increase of the temperature change under the continuous solar irradiations. It demonstrates that the PEG composite in this solar intensity has the optimum pyroelectric effect by the Light-On/Off process. The multiple pyroelectric energy harvesting system is constructed at the 20 mW/cm^2 which combines with each advantage of PEG, and 1-TD composite. The multiple PCM blind system shows the better peak area than other constructions and sufficiently utilized in the high degree of thermal energy applications. The pyro-electrode of window glass implies a smart result with unprecedented design of pyroelectric energy harvesting. This work can briefly guide the neoteric research and provide an expansive occasion in the smart energy control utilizations.

5.5. Summary

The pyroelectric energy harvesting system is mentioned in this chapter and the two kinds of researches are successfully completed. The PCM composite combines with the pyro-electrode in Section 5.3 and demonstrated the PCM composites are able to control the change of temperature difference and provide the continuous thermal fluctuation upon melting and cooling process. In addition, the heat reflection is reduced and the pyroelectric energy harvesting efficiency become increased due to the existence of PCMs. The multiple PCM composites consist of pyroelectric power generator exhibits a various pyroelectric effect and further indicates the new approach of energy harvesting system.

The light transmission across the window glass of pyroelectric energy harvesting system is revealed and the PCM composites are employed as thermal blind upon Light-On process in Section 5.4. The different solar intensities are applied to obtain the degree of pyroelectric effect and the 1-TD composite is selected as an appropriate blind at the low solar intensity condition, and the PEG composite then replace the 1-TDs at the 15 mW/cm^2 of solar irradiations. The multiple PCM composites pyroelectric energy harvesting system is finally constructed and the multiple PCM blinds exhibit the optimum power generator at the relatively high Light-On/Off process. The PCM blind can develop a new opportunity of solar energy conversions and close to the practical energy harvesting applications.

Chapter VI.

Concluding Remarks

In the present researches, we fabricated the form stable phase change materials (PCMs) without any leakage during the phase transitions. The polyaniline is selected as a supporting material and construct the PCM microcapsules to obtain the volume change at the temperature variation. The PEG in the core is completely melted over the melting temperature while the microcapsules sustain their initial state which lead to the volume expansion on the heating process. The graphene filler embedded microcapsules are obviously changed their electrical conductivity due to the connection of graphene nano-sheets. Thus, the phase transition develops the magnitude variation of electrical conductivity in the PEG composite. The carbon nanotube (CNT) is used as a filler in the PEG composite and exhibits the better electrical conductivity than that of graphene powder due to the high aspect ratio. The microencapsulated PCM composites are effectively modified the physical structures under the temperature variations and utilized at the thermal sensing material applications.

the thermoelectric generator (TEG) with two different PCMs supply the controllable output current on the heating and cooling process, the PEG composite is placed on the hot-side of PN TEG and 1-TD is placed on the opposite cold-side plane. In general, the PEG rises the temperature as the 1-TD is under the solid-liquid phase transition. The

single energy harvesting system is a conventional device to obtain the thermoelectric energy conversion and the excess thermal energy is directly applied to the multiple system. The GNP fillers affecting the phase transition process is obtained and contributed to the thermoelectric energy conversion. The optimization of PCM composites are carried out by measuring the maximum peak area in both heating and cooling process. Thus, the smart control in the external condition is subsequently confirmed by the thermoelectric energy harvesting system.

The PDMS embedded graphene/GNP aerogel exhibits a flexible properties and reduce the volume shrinkage during the infiltration process. Therefore, the advanced PCM composites can possess more weight fraction of working material and increase the thermal energy storage upon melting and cooling. The porous aerogel structure could wrap the pure PEG, and 1-TD into the internal volume space, and keep the initial solid state during the phase transition process. In addition, the more mass of working material causes more excess thermal energy to utilize for the energy harvesting and increases the thermoelectric energy conversion efficiency. Novel highly stable graphene aerogels are prepared through facile covalent cross-linking of cysteamine under high temperature vapor method. The graphene aerogels can fully maintain their original morphology when exposed to the high temperature and external forces. The differences in the structure and chemical composition are also confirmed by the morphologies measurement and effectively utilized on the solar energy applications.

The pyroelectric effect is obtained by the combination of PCM composite and pyro-electrode. The PCM composite can prevent the thermal reflection and control the temperature fluctuation under the Light-On/Off process. In addition, the heat flux is applied to confirm the pyroelectric energy harvesting and the power generator system produces a stable electrical energy with the change of external condition. The sunlight transmission across the window glass is considered as a new concept of pyroelectric energy harvesting system and the PCM is placed at the opposite side of window glass and collects the thermal energy upon Light-On process. After removing the light source, the PCM blind releases the stored energy and generate the pyroelectric effect in the 2nd step. The optimization of PCM blind is obtained by the different light intensities and develops a new approach for pyroelectric energy harvesting applications.

Comparing with the previous researches, the energy harvesting system can sufficiently utilize the thermal energy transmission in both heating and cooling process, and confirmed the advanced result from the energy harvesting system with the PN TEGs. The multiple energy harvesting system utilizes the reversed temperature difference between two working materials and can effectively achieve the thermoelectric energy conversion upon phase transitions. The GNP fillers are affecting the degree of phase transition with the different ratios and increase the GNP contents can significantly increase the thermal conductivity and contribute to the phase transition process. Thus, the harvested energy could easy to export via melting and cooling cycles. The modified supporting materials are overcome the volume shrinkage and deformation via infiltrating method. The graphene/cysteamine aerogel (GCA) supported PCM composite exhibits high mechanical property and tolerates the external force over the melting temperature and increase the thermoelectric energy harvesting efficiency. The pyroelectric effect is well measured with the combination of PCM composite and the new concept of power generation system can effectively produce the electrical energy upon Light-On/Off process.

Bibliography

[1] A. Sharma, V.V. Tyagi, C. Chen, D. Buddhi. Review on thermal energy storage with phase change materials and applications. Renewable and Sustainable energy reviews. 13 (2009) 318-45.

[2] G.A. Lane. Solar Heat Storage: Volume II: Latent Heat Material. CRC press2018.

[3] R. Karami, B. Kamkari. Investigation of the effect of inclination angle on the melting enhancement of phase change material in finned latent heat thermal storage units. Applied Thermal Engineering. 146 (2019) 45-60.

[4] S. Seitz, H. Ajiro. Self-assembling weak polyelectrolytes for the layer-by-layer encapsulation of paraffin-type phase change material icosane. Solar Energy Materials and Solar Cells. 190 (2019) 57-64.

[5] K. Venkitaraj, S. Suresh. Effects of Al2O3, CuO and TiO2 nanoparticles son thermal, phase transition and crystallization properties of solid-solid phase change material. Mechanics of Materials. 128 (2019) 64-88.

[6] F. Yang, M.P. Gordon, J.J. Urban. Theoretical framework of the thermal memristor via a solid-state phase change material. Journal of Applied Physics. 125 (2019) 025109.

[7] I. Zarma, M. Ahmed, S. Ookawara. Enhancing the performance of concentrator photovoltaic systems using Nanoparticle-phase change material heat sinks. Energy Conversion and Management. 179 (2019) 229-42.

[8] F. Agyenim, N. Hewitt, P. Eames, M. Smyth. A review of materials, heat transfer and phase change problem formulation for latent heat thermal energy storage systems (LHTESS). Renewable and sustainable energy reviews. 14 (2010) 615-28.

[9] T. Ma, L. Li, Q. Wang, C. Guo. High-performance flame retarded paraffin/epoxy resin form-stable phase change material. Journal of Materials Science. 54 (2019) 875-85.

[10] A. Abhat, D. Heine, M. Heinisch, N. Malatidis, G. Neuer. Development of a

modular heat exchanger with integrated latent heat energy store. Final Report, Dec 1979 Institut fuer Kemtechnik und Energiewandlung eV, Stuttgart (Germany, FR). (1981).

[11] W. Wang, X. Fan, J. Qiu, M.M. Umair, B. Ju, S. Zhang, et al. Extracorporeal magnetic thermotherapy materials for self-controlled temperature through phase transition. Chemical Engineering Journal. 358 (2019) 1279-86.

[12] A. Vasu, F.Y. Hagos, R. Mamat, J. Kaur, M. Noor. The effect of thermal cyclic variation on the thermophysical property degradation of paraffin as a phase changing energy storage material. Applied Thermal Engineering. 149 (2019) 22-33.

[13] N. Mekaddem, S.B. Ali, M. Fois, A. Hannachi. Paraffin/Expanded Perlite/Plaster as Thermal Energy Storage Composite. Energy Procedia. 157 (2019) 1118-29.

[14] P. Wilson, S. Vijayan, K. Prabhakaran. Thermally Conducting Microcellular Carbon Foams as a Superior Host for Wax□Based Phase Change Materials. Advanced Engineering Materials. (2019) 1801139.

[15] A.T. Mohamad, N.A.C. Sidik. Nano-enhanced phase change material effects on the supercooling degree improvement: A review. IOP Conference Series: Materials Science and Engineering. IOP Publishing2019. p. 012036.

[16] S. Himran, A. Suwono, G.A. Mansoori. Characterization of alkanes and paraffin waxes for application as phase change energy storage medium. Energy Sources. 16 (1994) 117-28.

[17] X. Py, R. Olives, S. Mauran. Paraffin/porous-graphite-matrix composite as a high and constant power thermal storage material. International Journal of heat and mass transfer. 44 (2001) 2727-37.

[18] M. Hawlader, M. Uddin, H.J. Zhu. Preparation and evaluation of a novel solar storage material: microencapsulated paraffin. International Journal of Solar Energy. 20 (2000) 227-38.

[19] K. Cho, S. Choi. Thermal characteristics of paraffin in a spherical capsule during freezing and melting processes. International journal of heat and mass transfer. 43 (2000) 3183-96.

[20] R.J. Warzoha, R.M. Weigand, A.S. Fleischer. Temperature-dependent thermal properties of a paraffin phase change material embedded with herringbone style graphite nanofibers. Applied Energy. 137 (2015) 716-25.

[21] Z. Liu, D. Chung. Calorimetric evaluation of phase change materials for use as thermal interface materials. Thermochimica Acta. 366 (2001) 135-47.

[22] B. He, F. Setterwall. Technical grade paraffin waxes as phase change materials for cool thermal storage and cool storage systems capital cost estimation. Energy Conversion and Management. 43 (2002) 1709-23.

[23] A. Kürklü, A. Özmerzi, S. Bilgin. Thermal performance of a water-phase change material solar collector. Renewable Energy. 26 (2002) 391-9.

[24] B. He, V. Martin, F. Setterwall. Phase transition temperature ranges and storage density of paraffin wax phase change materials. Energy. 29 (2004) 1785-804.

[25] Z. Gu, H. Liu, Y. Li. Thermal energy recovery of air conditioning system—heat recovery system calculation and phase change materials development. Applied Thermal Engineering. 24 (2004) 2511-26.

[26] P. Lamberg. Approximate analytical model for two-phase solidification problem in a finned phase-change material storage. Applied Energy. 77 (2004) 131-52.

[27] G. Baran, A. Sari. Phase change and heat transfer characteristics of a eutectic mixture of palmitic and stearic acids as PCM in a latent heat storage system. Energy Conversion and Management. 44 (2003) 3227-46.

[28] J.L. Zuckerman, R.J. Pushaw, B.T. Perry, D.M. Wyner. Fabric coating containing energy absorbing phase change material and method of manufacturing same. Google Patents2003.

[29] X.-f. XIE, A.-y. CHEN. New Technology of Energy Storage-Phase Change Energy Storage [J]. Journal of Zhuzhou Teachers College. 5 (2003) 002.

[30] H. Hong, C.H. Park, J.H. Choi, J.H. Peck. Improvement of the T-history method to measure heat of fusion for phase change materials. International Journal of Air-Conditioning and Refrigeration. 11 (2003) 32-9.

[31] H. Inaba, P. Tu. Evaluation of thermophysical characteristics on shape-

stabilized paraffin as a solid-liquid phase change materialErmittlung thermophysikalischer Eigenschaften von form-stabilisiertem Paraffin, einem Material mit Phasenwechsel fest/flüssig. Heat and Mass Transfer. 32 (1997) 307-12.

[32] J. Fukai, M. Kanou, Y. Kodama, O. Miyatake. Thermal conductivity enhancement of energy storage media using carbon fibers. Energy Conversion and Management. 41 (2000) 1543-56.

[33] M. Pinelli, S. Piva. Solid/liquid phase change in presence of natural convection: a thermal energy storage case study. Journal of Energy resources technology. 125 (2003) 190-8.

[34] M.M. Farid, Y. Kim, A. Kansawa. Thermal performance of a heat storage module using PCM's with different melting temperature: experimental. Journal of Solar Energy Engineering. 112 (1990) 125-31.

[35] H.E. Fath. Thermal performance of a simple design solar air heater with built-in thermal energy storage system. Renewable energy. 6 (1995) 1033-9.

[36] S.R. Ovshinsky, W. Czubatyj, D.A. Strand, P.J. Klersy, S. Kostylev, B. Pashmakov. Memory element with memory material comprising phase-change material and dielectric material. Google Patents2000.

[37] J.-S. Cho, A. Kwon, C.-G. Cho. Microencapsulation of octadecane as a phase-change material by interfacial polymerization in an emulsion system. Colloid and polymer science. 280 (2002) 260-6.

[38] D. Zhang, K.-r. Wu. Tuning effect of porous structure on phase changing behavior of organic phase changing matters. JOURNAL-TONGJI UNIVERSITY. 32 (2004) 1163-7.

[39] F.Y.Z. Xinxiang. Progress in Studies of Solid-solid Phase Change Materials [J]. Materials Review. 7 (2003) 014.

[40] R. Rai, C. Lan. Crystal structure and properties of a new organic nonlinear optical material. Journal of materials research. 17 (2002) 1587-91.

[41] A.J. Fletcher, E.J. Cussen, T.J. Prior, M.J. Rosseinsky, C.J. Kepert, K.M. Thomas. Adsorption dynamics of gases and vapors on the nanoporous metal organic framework material Ni2 (4, 4 '-bipyridine) 3 (NO3) 4: guest

modification of host sorption behavior. Journal of the American Chemical Society. 123 (2001) 10001-11.

[42] M.K. Rathod, J. Banerjee. Thermal stability of phase change materials used in latent heat energy storage systems: a review. Renewable and Sustainable Energy Reviews. 18 (2013) 246-58.

[43] A. Hoshi, D.R. Mills, A. Bittar, T.S. Saitoh. Screening of high melting point phase change materials (PCM) in solar thermal concentrating technology based on CLFR. Solar Energy. 79 (2005) 332-9.

[44] A. Sarı. Thermal characteristics of a eutectic mixture of myristic and palmitic acids as phase change material for heating applications. Applied Thermal Engineering. 23 (2003) 1005-17.

[45] A. Sari, K. Kaygusuz. Thermal energy storage system using stearic acid as a phase change material. Solar Energy. 71 (2001) 365-76.

[46] A.M. Seayad, D.M. Antonelli. Recent advances in hydrogen storage in metal□ containing inorganic nanostructures and related materials. Advanced Materials. 16 (2004) 765-77.

[47] A.S. Kaygusuz, Kamil. Thermal energy storage system using some fatty acids as latent heat energy storage materials. Energy Sources. 23 (2001) 275-85.

[48] G. Suppes, M. Goff, S. Lopes. Latent heat characteristics of fatty acid derivatives pursuant phase change material applications. Chemical Engineering Science. 58 (2003) 1751-63.

[49] T. Tatsuma, S. Saitoh, P. Ngaotrakanwiwat, Y. Ohko, A. Fujishima. Energy storage of TiO2− WO3 photocatalysis systems in the gas phase. Langmuir. 18 (2002) 7777-9.

[50] K. Chen, X. Yu, C. Tian, J. Wang. Preparation and characterization of form-stable paraffin/polyurethane composites as phase change materials for thermal energy storage. Energy Conversion and Management. 77 (2014) 13-21.

[51] Y. Hong, G. Xin-shi. Preparation of polyethylene–paraffin compound as a form-stable solid-liquid phase change material. Solar Energy Materials and Solar Cells. 64 (2000) 37-44.

[52] J.-L. Zeng, F.-R. Zhu, S.-B. Yu, Z.-L. Xiao, W.-P. Yan, S.-H. Zheng, et al. Myristic acid/polyaniline composites as form stable phase change materials for thermal energy storage. Solar Energy Materials and Solar Cells. 114 (2013) 136-40.

[53] S. Yu, X. Wang, D. Wu. Microencapsulation of n-octadecane phase change material with calcium carbonate shell for enhancement of thermal conductivity and serving durability: synthesis, microstructure, and performance evaluation. Applied Energy. 114 (2014) 632-43.

[54] M. Mehrali, S.T. Latibari, M. Mehrali, T.M.I. Mahlia, H.S.C. Metselaar. Effect of carbon nanospheres on shape stabilization and thermal behavior of phase change materials for thermal energy storage. Energy Conversion and Management. 88 (2014) 206-13.

[55] H. Nazir, M. Batool, F.J.B. Osorio, M. Isaza-Ruiz, X. Xu, K. Vignarooban, et al. Recent developments in phase change materials for energy storage applications: A review. International Journal of Heat and Mass Transfer. 129 (2019) 491-523.

[56] M.M. Umair, Y. Zhang, K. Iqbal, S. Zhang, B. Tang. Novel strategies and supporting materials applied to shape-stabilize organic phase change materials for thermal energy storage–A review. Applied Energy. 235 (2019) 846-73.

[57] M. Delgado, A. Lázaro, J. Mazo, B. Zalba. Review on phase change material emulsions and microencapsulated phase change material slurries: materials, heat transfer studies and applications. Renewable and Sustainable Energy Reviews. 16 (2012) 253-73.

[58] Y. Wang, H. Ji, H. Shi, T. Zhang, T. Xia. Fabrication and characterization of stearic acid/polyaniline composite with electrical conductivity as phase change materials for thermal energy storage. Energy conversion and management. 98 (2015) 322-30.

[59] S.A. Atouei, A. Rezania, A. Ranjbar, L.A. Rosendahl. Protection and thermal management of thermoelectric generator system using phase change materials: An experimental investigation. Energy. 156 (2018) 311-8.

[60] Y. Kou, S. Wang, J. Luo, K. Sun, J. Zhang, Z. Tan, et al. Thermal analysis and heat capacity study of polyethylene glycol (PEG) phase change materials for thermal energy storage applications. The Journal of Chemical Thermodynamics. 128 (2019) 259-74.

[61] L. Zhang, F. Zhang, X. Yang, G. Long, Y. Wu, T. Zhang, et al. Porous 3D graphene-based bulk materials with exceptional high surface area and excellent conductivity for supercapacitors. Scientific reports. 3 (2013) 1408.

[62] M. Song, F. Niu, N. Mao, Y. Hu, S. Deng. Review on building energy performance improvement using phase change materials. Energy and Buildings. 158 (2018) 776-93.

[63] R. Wen, P. Jia, Z. Huang, M. Fang, Y. Liu, X. Wu, et al. Thermal energy storage properties and thermal reliability of PEG/bone char composite as a form-stable phase change material. Journal of Thermal Analysis and Calorimetry. 132 (2018) 1753-61.

[64] C.N. Markides. Low-concentration solar-power systems based on organic Rankine cycles for distributed-scale applications: Overview and further developments. Frontiers in Energy Research. 3 (2015) 47.

[65] C.-T. Hsu, G.-Y. Huang, H.-S. Chu, B. Yu, D.-J. Yao. Experiments and simulations on low-temperature waste heat harvesting system by thermoelectric power generators. Applied Energy. 88 (2011) 1291-7.

[66] B. Russ, A. Glaudell, J.J. Urban, M.L. Chabinyc, R.A. Segalman. Organic thermoelectric materials for energy harvesting and temperature control. Nature Reviews Materials. 1 (2016) 16050.

[67] W. Jiang, D. Yuan, S. Xu, H. Hu, J. Xiao, A. Sha, et al. Energy harvesting from asphalt pavement using thermoelectric technology. Applied Energy. 205 (2017) 941-50.

[68] Y. Jiang, Z. Wang, M. Shang, Z. Zhang, S. Zhang. Heat collection and supply of interconnected netlike graphene/polyethyleneglycol composites for thermoelectric devices. Nanoscale. 7 (2015) 10950-3.

[69] C. Li, B. Xie, D. Chen, J. Chen, W. Li, Z. Chen, et al. Ultrathin graphite sheets stabilized stearic acid as a composite phase change material for thermal

energy storage. Energy. 166 (2019) 246-55.

[70] Z. Wang, Y. Sun, H. Wu, C. Zhang. Low velocity impact resistance of bio-inspired building ceramic composites with nacre-like structure. Construction and Building Materials. 169 (2018) 851-8.

[71] M. Antonietti. Nacre replication: down to the bottom. Science Bulletin. 61 (2016) 1662-4.

[72] J.-Y. Hong, S. Yun, J.J. Wie, X. Zhang, M.S. Dresselhaus, J. Kong, et al. Cartilage-inspired superelastic ultradurable graphene aerogels prepared by the selective gluing of intersheet joints. Nanoscale. 8 (2016) 12900-9.

[73] P. Das, J.-M. Malho, K. Rahimi, F.H. Schacher, B. Wang, D.E. Demco, et al. Nacre-mimetics with synthetic nanoclays up to ultrahigh aspect ratios. Nature communications. 6 (2015) 5967.

[74] H. Wang, T. Maiyalagan, X. Wang. Review on recent progress in nitrogen-doped graphene: synthesis, characterization, and its potential applications. Acs Catalysis. 2 (2012) 781-94.

[75] P. Avouris, C. Dimitrakopoulos. Graphene: synthesis and applications. Materials today. 15 (2012) 86-97.

[76] S. Pei, H.-M. Cheng. The reduction of graphene oxide. Carbon. 50 (2012) 3210-28.

[77] S. Stankovich, D.A. Dikin, R.D. Piner, K.A. Kohlhaas, A. Kleinhammes, Y. Jia, et al. Synthesis of graphene-based nanosheets via chemical reduction of exfoliated graphite oxide. carbon. 45 (2007) 1558-65.

[78] M.S. Mauter, M. Elimelech. Environmental applications of carbon-based nanomaterials. Environmental Science & Technology. 42 (2008) 5843-59.

[79] G. Sebald, D. Guyomar, A. Agbossou. On thermoelectric and pyroelectric energy harvesting. Smart Materials and Structures. 18 (2009) 125006.

[80] S. Pandya, J. Wilbur, J. Kim, R. Gao, A. Dasgupta, C. Dames, et al. Pyroelectric energy conversion with large energy and power density in relaxor ferroelectric thin films. Nature materials. 17 (2018) 432.

[81] D. Zabek, J. Taylor, E.L. Boulbar, C.R. Bowen. Micropatterning of flexible and free standing polyvinylidene difluoride (PVDF) films for enhanced

pyroelectric energy transformation. Advanced Energy Materials. 5 (2015) 1401891.

[82] M. Arjmand, K. Chizari, B. Krause, P. Pötschke, U. Sundararaj. Effect of synthesis catalyst on structure of nitrogen-doped carbon nanotubes and electrical conductivity and electromagnetic interference shielding of their polymeric nanocomposites. Carbon. 98 (2016) 358-72.

[83] S. Gong, Z. Zhu, S. Meguid. Anisotropic electrical conductivity of polymer composites with aligned carbon nanotubes. Polymer. 56 (2015) 498-506.

[84] T. Ma, H.L. Gao, H.P. Cong, H.B. Yao, L. Wu, Z.Y. Yu, et al. A Bioinspired Interface Design for Improving the Strength and Electrical Conductivity of Graphene□Based Fibers. Advanced Materials. 30 (2018) 1706435.

[85] Q. Tang, M. Chen, C. Yang, W. Wang, H. Bao, G. Wang. Enhancing the energy density of asymmetric stretchable supercapacitor based on wrinkled CNT@ MnO2 cathode and CNT@ polypyrrole anode. ACS applied materials & interfaces. 7 (2015) 15303-13.

[86] M.M. Pour, A. Lashkov, A. Radocea, X. Liu, T. Sun, A. Lipatov, et al. Laterally extended atomically precise graphene nanoribbons with improved electrical conductivity for efficient gas sensing. Nature communications. 8 (2017) 820.

[87] X. Xia, Y. Wang, Z. Zhong, G.J. Weng. A frequency-dependent theory of electrical conductivity and dielectric permittivity for graphene-polymer nanocomposites. Carbon. 111 (2017) 221-30.

[88] N. Yousefi, M.M. Gudarzi, Q. Zheng, S.H. Aboutalebi, F. Sharif, J.-K. Kim. Self-alignment and high electrical conductivity of ultralarge graphene oxide–polyurethane nanocomposites. Journal of Materials Chemistry. 22 (2012) 12709-17.

[89] H. Pang, T. Chen, G. Zhang, B. Zeng, Z.-M. Li. An electrically conducting polymer/graphene composite with a very low percolation threshold. Materials Letters. 64 (2010) 2226-9.

[90] G. Ruschau, S. Yoshikawa, R. Newnham. Resistivities of conductive composites. Journal of applied physics. 72 (1992) 953-9.

[91] J.-L. Zeng, J. Gan, F.-R. Zhu, S.-B. Yu, Z.-L. Xiao, W.-P. Yan, et al.

Tetradecanol/expanded graphite composite form-stable phase change material for thermal energy storage. Solar Energy Materials and Solar Cells. 127 (2014) 122-8.

[92] P. Goli, S. Legedza, A. Dhar, R. Salgado, J. Renteria, A.A. Balandin. Graphene-enhanced hybrid phase change materials for thermal management of Li-ion batteries. Journal of Power Sources. 248 (2014) 37-43.

[93] H. Kim, Y. Miura, C.W. Macosko. Graphene/polyurethane nanocomposites for improved gas barrier and electrical conductivity. Chemistry of Materials. 22 (2010) 3441-50.

[94] A.K. Geim, K.S. Novoselov. The rise of graphene. Nanoscience and Technology: A Collection of Reviews from Nature Journals. World Scientific2010. pp. 11-9.

[95] Y. Zhu, S. Murali, W. Cai, X. Li, J.W. Suk, J.R. Potts, et al. Graphene and graphene oxide: synthesis, properties, and applications. Advanced materials. 22 (2010) 3906-24.

[96] B. Zalba, J.M. Marın, L.F. Cabeza, H. Mehling. Review on thermal energy storage with phase change: materials, heat transfer analysis and applications. Applied thermal engineering. 23 (2003) 251-83.

[97] M. Mehrali, S.T. Latibari, M. Mehrali, T.M.I. Mahlia, H.S.C. Metselaar, M.S. Naghavi, et al. Preparation and characterization of palmitic acid/graphene nanoplatelets composite with remarkable thermal conductivity as a novel shape-stabilized phase change material. Applied Thermal Engineering. 61 (2013) 633-40.

[98] T.M. Buckley. Flexible composite material with phase change thermal storage. Google Patents1999.

[99] E. Oró, A. De Gracia, A. Castell, M. Farid, L. Cabeza. Review on phase change materials (PCMs) for cold thermal energy storage applications. Applied Energy. 99 (2012) 513-33.

[100] B. Xu, Z. Li. Paraffin/diatomite composite phase change material incorporated cement-based composite for thermal energy storage. Applied Energy. 105 (2013) 229-37.

[101] Y. Fang, H. Kang, W. Wang, H. Liu, X. Gao. Study on polyethylene

glycol/epoxy resin composite as a form-stable phase change material. Energy Conversion and Management. 51 (2010) 2757-61.

[102] N. Zhang, Y. Yuan, Y. Yuan, T. Li, X. Cao. Lauric–palmitic–stearic acid/expanded perlite composite as form-stable phase change material: preparation and thermal properties. Energy and Buildings. 82 (2014) 505-11.

[103] C. Chen, L. Wang, Y. Huang. Morphology and thermal properties of electrospun fatty acids/polyethylene terephthalate composite fibers as novel form-stable phase change materials. Solar Energy Materials and Solar Cells. 92 (2008) 1382-7.

[104] J. Li, P. Xue, W. Ding, J. Han, G. Sun. Micro-encapsulated paraffin/high-density polyethylene/wood flour composite as form-stable phase change material for thermal energy storage. Solar Energy Materials and Solar Cells. 93 (2009) 1761-7.

[105] C. Alkan, A. Sarı, A. Karaipekli, O. Uzun. Preparation, characterization, and thermal properties of microencapsulated phase change material for thermal energy storage. Solar Energy Materials and Solar Cells. 93 (2009) 143-7.

[106] G. Leng, G. Qiao, Z. Jiang, G. Xu, Y. Qin, C. Chang, et al. Micro encapsulated & form-stable phase change materials for high temperature thermal energy storage. Applied Energy. 217 (2018) 212-20.

[107] K. Chi, Z. Zhang, J. Xi, Y. Huang, F. Xiao, S. Wang, et al. Freestanding graphene paper supported three-dimensional porous graphene–polyaniline nanocomposite synthesized by inkjet printing and in flexible all-solid-state supercapacitor. ACS applied materials & interfaces. 6 (2014) 16312-9.

[108] M. Silakhori, M.S. Naghavi, H.S.C. Metselaar, T.M.I. Mahlia, H. Fauzi, M. Mehrali. Accelerated thermal cycling test of microencapsulated paraffin wax/polyaniline made by simple preparation method for solar thermal energy storage. Materials. 6 (2013) 1608-20.

[109] D.C. Marcano, D.V. Kosynkin, J.M. Berlin, A. Sinitskii, Z. Sun, A. Slesarev, et al. Improved synthesis of graphene oxide. ACS nano. 4 (2010) 4806-14.

[110] H. Xia, Q. Wang. Ultrasonic irradiation: a novel approach to prepare conductive polyaniline/nanocrystalline titanium oxide composites. Chemistry

of materials. 14 (2002) 2158-65.

[111] E. Zelikman, M. Narkis, A. Siegmann, L. Valentini, J. Kenny. Polyaniline/multiwalled carbon nanotube systems: Dispersion of CNT and CNT/PANI interaction. Polymer Engineering & Science. 48 (2008) 1872-7.

[112] J. Wu, D. McLachlan. Percolation exponents and thresholds obtained from the nearly ideal continuum percolation system graphite-boron nitride. Physical Review B. 56 (1997) 1236.

[113] E. Ancona, R.Y. Kezerashvili. Temperature restrictions for materials used in aerospace industry for the near-sun orbits. Acta Astronautica. 140 (2017) 565-9.

[114] J. Stejskal, R. Gilbert. Polyaniline. Preparation of a conducting polymer (IUPAC technical report). Pure and Applied Chemistry. 74 (2002) 857-67.

[115] N.K. Jangid, N.P.S. Chauhan, P.B. Punjabi. Preparation and characterization of polyanilines bearing rhodamine 6-G and Azure B as pendant groups. Journal of Macromolecular Science, Part A. 52 (2015) 95-104.

[116] F. Du, R.C. Scogna, W. Zhou, S. Brand, J.E. Fischer, K.I. Winey. Nanotube networks in polymer nanocomposites: rheology and electrical conductivity. Macromolecules. 37 (2004) 9048-55.

[117] E. Flahaut, A. Peigney, C. Laurent, C. Marliere, F. Chastel, A. Rousset. Carbon nanotube–metal–oxide nanocomposites: microstructure, electrical conductivity and mechanical properties. Acta Materialia. 48 (2000) 3803-12.

[118] Q. Wang, J. Dai, W. Li, Z. Wei, J. Jiang. The effects of CNT alignment on electrical conductivity and mechanical properties of SWNT/epoxy nanocomposites. Composites science and technology. 68 (2008) 1644-8.

[119] G. Mittal, V. Dhand, K.Y. Rhee, S.-J. Park, W.R. Lee. A review on carbon nanotubes and graphene as fillers in reinforced polymer nanocomposites. Journal of Industrial and Engineering Chemistry. 21 (2015) 11-25.

[120] Y. Wang, H. Mi, Q. Zheng, Z. Ma, S. Gong. Flexible infrared responsive multi-walled carbon nanotube/form-stable phase change material nanocomposites. ACS applied materials & interfaces. 7 (2015) 21602-9.

[121] Y. Wang, H. Mi, Q. Zheng, Z. Ma, S. Gong. Graphene/phase change material

nanocomposites: light-driven, reversible electrical resistivity regulation via form-stable phase transitions. ACS applied materials & interfaces. 7 (2015) 2641-7.

[122] A. Sarı, A. Karaipekli. Thermal conductivity and latent heat thermal energy storage characteristics of paraffin/expanded graphite composite as phase change material. Applied Thermal Engineering. 27 (2007) 1271-7.

[123] J. Jaguemont, N. Omar, P. Van den Bossche, J. Mierlo. Phase-change materials (PCM) for automotive applications: A review. Applied Thermal Engineering. 132 (2018) 308-20.

[124] C. Alkan, A. Sari. Fatty acid/poly (methyl methacrylate)(PMMA) blends as form-stable phase change materials for latent heat thermal energy storage. Solar energy. 82 (2008) 118-24.

[125] A. Sarı. Form-stable paraffin/high density polyethylene composites as solid–liquid phase change material for thermal energy storage: preparation and thermal properties. Energy Conversion and Management. 45 (2004) 2033-42.

[126] J. Su, L. Wang, L. Ren. Fabrication and thermal properties of microPCMs: Used melamine□formaldehyde resin as shell material. Journal of applied polymer science. 101 (2006) 1522-8.

[127] J.-L. Zeng, S.-H. Zheng, S.-B. Yu, F.-R. Zhu, J. Gan, L. Zhu, et al. Preparation and thermal properties of palmitic acid/polyaniline/exfoliated graphite nanoplatelets form-stable phase change materials. Applied energy. 115 (2014) 603-9.

[128] A. Moisala, Q. Li, I. Kinloch, A. Windle. Thermal and electrical conductivity of single-and multi-walled carbon nanotube-epoxy composites. Composites science and technology. 66 (2006) 1285-8.

[129] J. Li, P.C. Ma, W.S. Chow, C.K. To, B.Z. Tang, J.K. Kim. Correlations between percolation threshold, dispersion state, and aspect ratio of carbon nanotubes. Advanced Functional Materials. 17 (2007) 3207-15.

[130] Y. Diao, L. Liang, Y. Zhao, Z. Wang, F. Bai. Numerical investigation of the thermal performance enhancement of latent heat thermal energy storage using longitudinal rectangular fins and flat micro-heat pipe arrays. Applied

Energy. 233 (2019) 894-905.

[131] C. Barreneche, A.L. Pisello, A.I. Fernández, L.F. Cabeza. Experimental Methods for the Characterization of Materials for Latent Thermal Energy Storage. Recent Advancements in Materials and Systems for Thermal Energy Storage. Springer2019. pp. 89-101.

[132] C.B. Vining. An inconvenient truth about thermoelectrics. Nature materials. 8 (2009) 83.

[133] T.Y. Kim, J. Kwak, B.-w. Kim. Energy harvesting performance of hexagonal shaped thermoelectric generator for passenger vehicle applications: An experimental approach. Energy Conversion and Management. 160 (2018) 14-21.

[134] J. Yang, L. Yang, C. Xu, X. Du. Experimental study on enhancement of thermal energy storage with phase-change material. Applied Energy. 169 (2016) 164-76.

[135] J. Mao, Z. Wu, H. Xie, A. Liu, Y. Wang, Y. Li, et al. Power Generation by Thermoelectric Generator Using Different Amounts of Phase Change Materials. Journal of Thermophysics and Heat Transfer. (2018) 1-7.

[136] S. Kahwaji, M.B. Johnson, A.C. Kheirabadi, D. Groulx, M.A. White. Fatty acids and related phase change materials for reliable thermal energy storage at moderate temperatures. Solar Energy Materials and Solar Cells. 167 (2017) 109-20.

[137] D. Su, Y. Jia, G. Alva, L. Liu, G. Fang. Comparative analyses on dynamic performances of photovoltaic–thermal solar collectors integrated with phase change materials. Energy Conversion and Management. 131 (2017) 79-89.

[138] S. Mondal. Phase change materials for smart textiles–An overview. Applied thermal engineering. 28 (2008) 1536-50.

[139] D. Zhou, C.-Y. Zhao, Y. Tian. Review on thermal energy storage with phase change materials (PCMs) in building applications. Applied energy. 92 (2012) 593-605.

[140] J. Shon, H. Kim, K. Lee. Improved heat storage rate for an automobile coolant waste heat recovery system using phase-change material in a fin–tube heat

exchanger. Applied Energy. 113 (2014) 680-9.

[141] R. Sharma, P. Ganesan, V. Tyagi, H. Metselaar, S. Sandaran. Developments in organic solid–liquid phase change materials and their applications in thermal energy storage. Energy Conversion and Management. 95 (2015) 193-228.

[142] M. Seitz, M. Johnson, S. Hübner. Economic impact of latent heat thermal energy storage systems within direct steam generating solar thermal power plants with parabolic troughs. Energy Conversion and Management. 143 (2017) 286-94.

[143] A. Karaipekli, A. Biçer, A. Sarı, V.V. Tyagi. Thermal characteristics of expanded perlite/paraffin composite phase change material with enhanced thermal conductivity using carbon nanotubes. Energy conversion and management. 134 (2017) 373-81.

[144] M.G. Li, Y. Zhang, Y.H. Xu, D. Zhang. Effect of different amounts of surfactant on characteristics of nanoencapsulated phase-change materials. Polymer bulletin. 67 (2011) 541.

[145] T. Qian, J. Li, H. Ma, J. Yang. The preparation of a green shape-stabilized composite phase change material of polyethylene glycol/SiO2 with enhanced thermal performance based on oil shale ash via temperature-assisted sol–gel method. Solar Energy materials and Solar cells. 132 (2015) 29-39.

[146] S. Ye, Q. Zhang, D. Hu, J. Feng. Core–shell-like structured graphene aerogel encapsulating paraffin: shape-stable phase change material for thermal energy storage. Journal of Materials Chemistry A. 3 (2015) 4018-25.

[147] J. Yang, E. Zhang, X. Li, Y. Zhang, J. Qu, Z.-Z. Yu. Cellulose/graphene aerogel supported phase change composites with high thermal conductivity and good shape stability for thermal energy storage. Carbon. 98 (2016) 50-7.

[148] Y. Xia, W. Cui, H. Zhang, F. Xu, L. Sun, Y. Zou, et al. Synthesis of three-dimensional graphene aerogel encapsulated n-octadecane for enhancing phase-change behavior and thermal conductivity. Journal of Materials Chemistry A. 5 (2017) 15191-9.

[149] G. Qi, J. Yang, R. Bao, D. Xia, M. Cao, W. Yang, et al. Hierarchical graphene foam-based phase change materials with enhanced thermal conductivity and

shape stability for efficient solar-to-thermal energy conversion and storage. Nano Research. 10 (2017) 802-13.

[150] L.-S. Tang, J. Yang, R.-Y. Bao, Z.-Y. Liu, B.-H. Xie, M.-B. Yang, et al. Polyethylene glycol/graphene oxide aerogel shape-stabilized phase change materials for photo-to-thermal energy conversion and storage via tuning the oxidation degree of graphene oxide. Energy Conversion and Management. 146 (2017) 253-64.

[151] R. Kiflemariam, M. Almas, C. Lin. Modeling Integrated Thermoelectric Generator-Photovoltaic Thermal (TEG-PVT) System. Proc 2014 COMSOL Conf2014.

[152] J. Kim, W.-H. Khoh, B.-H. Wee, J.-D. Hong. Fabrication of flexible reduced graphene oxide–TiO 2 freestanding films for supercapacitor application. Rsc Advances. 5 (2015) 9904-11.

[153] S. Kellici, J. Acord, J. Ball, H.S. Reehal, D. Morgan, B. Saha. A single rapid route for the synthesis of reduced graphene oxide with antibacterial activities. RSC Advances. 4 (2014) 14858-61.

[154] C.K. Chua, M. Pumera. Chemical reduction of graphene oxide: a synthetic chemistry viewpoint. Chemical Society Reviews. 43 (2014) 291-312.

[155] X. Huang, J. Guo, Y. Gong, S. Li, S. Mu, S. Zhang. In-situ preparation of a shape stable phase change material. Renewable Energy. 108 (2017) 244-9.

[156] L. Liu, H. Wang, X. Qi, L. Kong, J. Cui, X. Zhang, et al. Shape-stabilized phase change materials based on poly (ethylene-graft-maleic anhydride)-g-alkyl alcohol comb-like polymers. Solar Energy Materials and Solar Cells. 143 (2015) 21-8.

[157] B. Tang, C. Wu, M. Qiu, X. Zhang, S. Zhang. PEG/SiO 2–Al 2 O 3 hybrid form-stable phase change materials with enhanced thermal conductivity. Materials Chemistry and Physics. 144 (2014) 162-7.

[158] G.-Q. Qi, J. Yang, R.-Y. Bao, Z.-Y. Liu, W. Yang, B.-H. Xie, et al. Enhanced comprehensive performance of polyethylene glycol based phase change material with hybrid graphene nanomaterials for thermal energy storage. Carbon. 88 (2015) 196-205.

[159] B. Tang, Y. Wang, M. Qiu, S. Zhang. A full-band sunlight-driven carbon nanotube/PEG/SiO 2 composites for solar energy storage. Solar Energy Materials and Solar Cells. 123 (2014) 7-12.

[160] Q. Wei, M. Mukaida, K. Kirihara, Y. Naitoh, T. Ishida. Polymer thermoelectric modules screen-printed on paper. Rsc Advances. 4 (2014) 28802-6.

[161] H. Im, T. Kim, H. Song, J. Choi, J.S. Park, R. Ovalle-Robles, et al. High-efficiency electrochemical thermal energy harvester using carbon nanotube aerogel sheet electrodes. Nature communications. 7 (2016) 10600.

[162] B. Russ, A. Glaudell, J.J. Urban, M.L. Chabinyc, R.A. Segalman. Organic thermoelectric materials for energy harvesting and temperature control. Nature Reviews Materials. 1 (2016) 16050.

[163] X. Chen, H. Gao, M. Yang, W. Dong, X. Huang, A. Li, et al. Highly graphitized 3D network carbon for shape-stabilized composite PCMs with superior thermal energy harvesting. Nano energy. 49 (2018) 86-94.

[164] J.P. da Cunha, P. Eames. Thermal energy storage for low and medium temperature applications using phase change materials–a review. Applied energy. 177 (2016) 227-38.

[165] M. Jaworski, M. Bednarczyk, M. Czachor. Experimental investigation of thermoelectric generator (TEG) with PCM module. Applied Thermal Engineering. 96 (2016) 527-33.

[166] M.M.A. Khan, N.I. Ibrahim, I. Mahbubul, H.M. Ali, R. Saidur, F.A. Al-Sulaiman. Evaluation of solar collector designs with integrated latent heat thermal energy storage: A review. Solar Energy. 166 (2018) 334-50.

[167] S. Karaman, A. Karaipekli, A. Sarı, A. Bicer. Polyethylene glycol (PEG)/diatomite composite as a novel form-stable phase change material for thermal energy storage. Solar Energy Materials and Solar Cells. 95 (2011) 1647-53.

[168] Y. Wang, T.D. Xia, H.X. Feng, H. Zhang. Stearic acid/polymethylmethacrylate composite as form-stable phase change materials for latent heat thermal energy storage. Renewable Energy. 36 (2011) 1814-20.

[169] A. Sarı, A. Bicer, F. Al-Sulaiman, A. Karaipekli, V. Tyagi. Diatomite/CNTs/PEG composite PCMs with shape-stabilized and improved thermal conductivity: Preparation and thermal energy storage properties. Energy and Buildings. 164 (2018) 166-75.

[170] T. Wang, S. Wang, R. Luo, C. Zhu, T. Akiyama, Z. Zhang. Microencapsulation of phase change materials with binary cores and calcium carbonate shell for thermal energy storage. Applied energy. 171 (2016) 113-9.

[171] Z. Zhang, X. Fang. Study on paraffin/expanded graphite composite phase change thermal energy storage material. Energy Conversion and Management. 47 (2006) 303-10.

[172] G.V. Belessiotis, K.G. Papadokostaki, E.P. Favvas, E.K. Efthimiadou, S. Karellas. Preparation and investigation of distinct and shape stable paraffin/SiO 2 composite PCM nanospheres. Energy Conversion and Management. 168 (2018) 382-94.

[173] B. Mu, M. Li. Fabrication and thermal properties of tetradecanol/graphene aerogel form-stable composite phase change materials. Scientific reports. 8 (2018) 8878.

[174] L. Liu, K. Zheng, Y. Yan, Z. Cai, S. Lin, X. Hu. Graphene Aerogels Enhanced Phase Change Materials prepared by one-pot method with high thermal conductivity and large latent energy storage. Solar Energy Materials and Solar Cells. 185 (2018) 487-93.

[175] Y.S. Yun, S.Y. Cho, H.-J. Jin. Carbon aerogels based on regenerated silk proteins and graphene oxide for supercapacitors. Macromolecular Research. 22 (2014) 509-14.

[176] G.-Q. Qi, C.-L. Liang, R.-Y. Bao, Z.-Y. Liu, W. Yang, B.-H. Xie, et al. Polyethylene glycol based shape-stabilized phase change material for thermal energy storage with ultra-low content of graphene oxide. Solar Energy Materials and Solar Cells. 123 (2014) 171-7.

[177] A. Krittayavathananon, M. Sawangphruk. Electrocatalytic oxidation of ethylene glycol on palladium coated on 3D reduced graphene oxide aerogel paper in alkali media: Effects of carbon supports and hydrodynamic

diffusion. Electrochimica Acta. 212 (2016) 237-46.

[178] D. Li, G. Sur. Composites prepared by penetrating poly (ethylene oxide) chains into graphene interlayers. Macromolecular Research. 22 (2014) 113-6.

[179] D. Zou, X. Ma, X. Liu, P. Zheng, Y. Hu. Thermal performance enhancement of composite phase change materials (PCM) using graphene and carbon nanotubes as additives for the potential application in lithium-ion power battery. International Journal of Heat and Mass Transfer. 120 (2018) 33-41.

[180] J. Yang, L.-S. Tang, R.-Y. Bao, L. Bai, Z.-Y. Liu, B.-H. Xie, et al. Hybrid network structure of boron nitride and graphene oxide in shape-stabilized composite phase change materials with enhanced thermal conductivity and light-to-electric energy conversion capability. Solar Energy Materials and Solar Cells. 174 (2018) 56-64.

[181] W. Feng, M. Qin, Y. Feng. Toward highly thermally conductive all-carbon composites: Structure control. Carbon. 109 (2016) 575-97.

[182] C. Yu, S.H. Yang, S.Y. Pak, J.R. Youn, Y.S. Song. Graphene embedded form stable phase change materials for drawing the thermo-electric energy harvesting. Energy Conversion and Management. 169 (2018) 88-96.

[183] J. Yang, L.-S. Tang, R.-Y. Bao, L. Bai, Z.-Y. Liu, W. Yang, et al. Largely enhanced thermal conductivity of poly (ethylene glycol)/boron nitride composite phase change materials for solar-thermal-electric energy conversion and storage with very low content of graphene nanoplatelets. Chemical Engineering Journal. 315 (2017) 481-90.

[184] S.A. Atouei, A.A. Ranjbar, A. Rezania. Experimental investigation of two-stage thermoelectric generator system integrated with phase change materials. Applied Energy. 208 (2017) 332-43.

[185] W. He, G. Zhang, X. Zhang, J. Ji, G. Li, X. Zhao. Recent development and application of thermoelectric generator and cooler. Applied Energy. 143 (2015) 1-25.

[186] S. Kim. Analysis and modeling of effective temperature differences and electrical parameters of thermoelectric generators. Applied energy. 102 (2013) 1458-63.

[187] J. Choi, N.D. Tu, S.-S. Lee, H. Lee, J.S. Kim, H. Kim. Controlled oxidation level of reduced graphene oxides and its effect on thermoelectric properties. Macromolecular Research. 22 (2014) 1104-8.

[188] Y. Zhang, G.G. Gurzadyan, M.M. Umair, W. Wang, R. Lu, S. Zhang, et al. Ultrafast and efficient photothermal conversion for sunlight-driven thermal-electric system. Chemical Engineering Journal. 344 (2018) 402-9.

[189] T.H. Kwan, X. Wu, Q. Yao. Integrated TEG-TEC and variable coolant flow rate controller for temperature control and energy harvesting. Energy. 159 (2018) 448-56.

[190] R. Chavez, S. Angst, J. Hall, F. Maculewicz, J. Stoetzel, H. Wiggers, et al. Efficient pn junction-based thermoelectric generator that can operate at extreme temperature conditions. Journal of Physics D: Applied Physics. 51 (2017) 014005.

[191] R. Chavez. High Temperature Thermoelectric Device Concept Using Large Area PN Junctions.

[192] J. Yang, G.-Q. Qi, Y. Liu, R.-Y. Bao, Z.-Y. Liu, W. Yang, et al. Hybrid graphene aerogels/phase change material composites: thermal conductivity, shape-stabilization and light-to-thermal energy storage. Carbon. 100 (2016) 693-702.

[193] H. He, J. Klinowski, M. Forster, A. Lerf. A new structural model for graphite oxide. Chemical physics letters. 287 (1998) 53-6.

[194] J. Guerrero-Contreras, F. Caballero-Briones. Graphene oxide powders with different oxidation degree, prepared by synthesis variations of the Hummers method. Materials Chemistry and Physics. 153 (2015) 209-20.

[195] J. Song, X. Wang, C.-T. Chang. Preparation and characterization of graphene oxide. Journal of Nanomaterials. 2014 (2014).

[196] Q. Wei, M. Mukaida, K. Kirihara, Y. Naitoh, T. Ishida. Recent progress on PEDOT-based thermoelectric materials. Materials. 8 (2015) 732-50.

[197] H. Ji, D.P. Sellan, M.T. Pettes, X. Kong, J. Ji, L. Shi, et al. Enhanced thermal conductivity of phase change materials with ultrathin-graphite foams for thermal energy storage. Energy & Environmental Science. 7 (2014) 1185-92.

[198] W.-H. Chen, C.-C. Wang, C.-I. Hung, C.-C. Yang, R.-C. Juang. Modeling and simulation for the design of thermal-concentrated solar thermoelectric generator. Energy. 64 (2014) 287-97.

[199] T.M. Tritt. Thermoelectric phenomena, materials, and applications. Annual review of materials research. 41 (2011) 433-48.

[200] A.M. Khudhair, M.M. Farid. A review on energy conservation in building applications with thermal storage by latent heat using phase change materials. Energy conversion and management. 45 (2004) 263-75.

[201] G. Fang, H. Li, F. Yang, X. Liu, S. Wu. Preparation and characterization of nano-encapsulated n-tetradecane as phase change material for thermal energy storage. Chemical Engineering Journal. 153 (2009) 217-21.

[202] W. Wang, X. Yang, Y. Fang, J. Ding. Preparation and performance of form-stable polyethylene glycol/silicon dioxide composites as solid–liquid phase change materials. Applied Energy. 86 (2009) 170-4.

[203] Y. Konuklu, M. Unal, H.O. Paksoy. Microencapsulation of caprylic acid with different wall materials as phase change material for thermal energy storage. Solar Energy Materials and Solar Cells. 120 (2014) 536-42.

[204] A. Trigui, M. Karkri, I. Krupa. Thermal conductivity and latent heat thermal energy storage properties of LDPE/wax as a shape-stabilized composite phase change material. Energy Conversion and Management. 77 (2014) 586-96.

[205] Y. Zhong, M. Zhou, F. Huang, T. Lin, D. Wan. Effect of graphene aerogel on thermal behavior of phase change materials for thermal management. Solar Energy Materials and Solar Cells. 113 (2013) 195-200.

[206] S.-E. Jo, M.-S. Kim, M.-K. Kim, Y.-J. Kim. Power generation of a thermoelectric generator with phase change materials. Smart Materials and Structures. 22 (2013) 115008.

[207] Z. Zhang, W. Li, J. Kan, D. Xu. Theoretical and experimental analysis of a solar thermoelectric power generation device based on gravity-assisted heat pipes and solar irradiation. Energy Conversion and Management. 127 (2016) 301-11.

[208] R. Amirante, E. Cassone, E. Distaso, P. Tamburrano. Overview on recent

developments in energy storage: Mechanical, electrochemical and hydrogen technologies. Energy Conversion and Management. 132 (2017) 372-87.

[209] B. Zalba, J.M. Marín, L.F. Cabeza, H. Mehling. Review on thermal energy storage with phase change: materials, heat transfer analysis and applications. Applied thermal engineering. 23 (2003) 251-83.

[210] H. Akeiber, P. Nejat, M.Z.A. Majid, M.A. Wahid, F. Jomehzadeh, I.Z. Famileh, et al. A review on phase change material (PCM) for sustainable passive cooling in building envelopes. Renewable and Sustainable Energy Reviews. 60 (2016) 1470-97.

[211] P.B. Salunkhe, P.S. Shembekar. A review on effect of phase change material encapsulation on the thermal performance of a system. Renewable and Sustainable Energy Reviews. 16 (2012) 5603-16.

[212] Z. Lu, B. Xu, J. Zhang, Y. Zhu, G. Sun, Z. Li. Preparation and characterization of expanded perlite/paraffin composite as form-stable phase change material. Solar energy. 108 (2014) 460-6.

[213] L. Li, B. Li, J. Zhang. Dopamine-mediated fabrication of ultralight graphene aerogels with low volume shrinkage. Journal of Materials Chemistry A. 4 (2016) 512-8.

[214] Y. Cheng, S. Zhou, P. Hu, G. Zhao, Y. Li, X. Zhang, et al. Enhanced mechanical, thermal, and electric properties of graphene aerogels via supercritical ethanol drying and high-temperature thermal reduction. Scientific reports. 7 (2017) 1439.

[215] L. Ren, K. Hui, K. Hui, Y. Liu, X. Qi, J. Zhong, et al. 3D hierarchical porous graphene aerogel with tunable meso-pores on graphene nanosheets for high-performance energy storage. Scientific reports. 5 (2015) 14229.

[216] A. Safari, R. Saidur, F. Sulaiman, Y. Xu, J. Dong. A review on supercooling of Phase Change Materials in thermal energy storage systems. Renewable and Sustainable Energy Reviews. 70 (2017) 905-19.

[217] S.A. Mohamed, F.A. Al-Sulaiman, N.I. Ibrahim, M.H. Zahir, A. Al-Ahmed, R. Saidur, et al. A review on current status and challenges of inorganic phase change materials for thermal energy storage systems. Renewable and

Sustainable Energy Reviews. 70 (2017) 1072-89.

[218] W. Wang, B. Tang, B. Ju, Z. Gao, J. Xiu, S. Zhang. Fe 3 O 4-functionalized graphene nanosheet embedded phase change material composites: efficient magnetic-and sunlight-driven energy conversion and storage. Journal of Materials Chemistry A. 5 (2017) 958-68.

[219] M. Amin, N. Putra, E.A. Kosasih, E. Prawiro, R.A. Luanto, T. Mahlia. Thermal properties of beeswax/graphene phase change material as energy storage for building applications. Applied Thermal Engineering. 112 (2017) 273-80.

[220] N.I. Ibrahim, F.A. Al-Sulaiman, S. Rahman, B.S. Yilbas, A.Z. Sahin. Heat transfer enhancement of phase change materials for thermal energy storage applications: A critical review. Renewable and Sustainable Energy Reviews. 74 (2017) 26-50.

[221] W. Wu, W. Wu, S. Wang. Form-stable and thermally induced flexible composite phase change material for thermal energy storage and thermal management applications. Applied Energy. 236 (2019) 10-21.

[222] Y. Ma, Q. Xie, X. Wang, J. Lu. Synthesis and characterization of microencapsulated phase change materials with comb-like acrylic co-polymer shell as thermal energy storage materials. Solar Energy. 179 (2019) 410-23.

[223] S. Ramakrishnan, J. Sanjayan, X. Wang, M. Alam, J. Wilson. A novel paraffin/expanded perlite composite phase change material for prevention of PCM leakage in cementitious composites. Applied Energy. 157 (2015) 85-94.

[224] H. Hu, Z. Zhao, W. Wan, Y. Gogotsi, J. Qiu. Ultralight and highly compressible graphene aerogels. Advanced materials. 25 (2013) 2219-23.

[225] A.R. Akhiani, M. Mehrali, S. Tahan Latibari, M. Mehrali, T.M.I. Mahlia, E. Sadeghinezhad, et al. One-step preparation of form-stable phase change material through self-assembly of fatty acid and graphene. The Journal of Physical Chemistry C. 119 (2015) 22787-96.

[226] S. Yang, L. Zhi, K. Tang, X. Feng, J. Maier, K. Müllen. Efficient synthesis of heteroatom (N or S)□doped graphene based on ultrathin graphene oxide□ porous silica sheets for oxygen reduction reactions. Advanced Functional

Materials. 22 (2012) 3634-40.

[227] G. Zhou. Graphene–Pure Sulfur Sandwich Structure for Ultrafast, Long-Life Lithium-Sulfur Batteries. Design, Fabrication and Electrochemical Performance of Nanostructured Carbon Based Materials for High-Energy Lithium–Sulfur Batteries. Springer2017. pp. 75-94.

[228] X. Hu, W. Xu, L. Zhou, Y. Tan, Y. Wang, S. Zhu, et al. Tailoring Graphene Oxide□Based Aerogels for Efficient Solar Steam Generation under One Sun. Advanced materials. 29 (2017) 1604031.

[229] F. Wu, A. Xie, M. Sun, Y. Wang, M. Wang. Reduced graphene oxide (RGO) modified spongelike polypyrrole (PPy) aerogel for excellent electromagnetic absorption. Journal of Materials Chemistry A. 3 (2015) 14358-69.

[230] C. Chen, X. Zhu, B. Chen. Covalently cross-linked graphene oxide aerogel with stable structure for high-efficiency water purification. Chemical Engineering Journal. 354 (2018) 896-904.

[231] W. Lin, Z. Ma, H. Ren, S. Gschwander, S. Wang. Multi-objective optimisation of thermal energy storage using phase change materials for solar air systems. Renewable energy. 130 (2019) 1116-29.

[232] M. Shen, W. Li, M. Li, H. Liu, J. Xu, S. Qiu, et al. High room-temperature pyroelectric property in lead-free BNT-BZT ferroelectric ceramics for thermal energy harvesting. Journal of the European Ceramic Society. (2019).

[233] P. Korde, V. Kamble. Efficient Energy Harvesting Using Thermoelectric Module. Information and Communication Technology for Intelligent Systems. Springer2019. pp. 329-40.

[234] D. Zabek, K. Seunarine, C. Spacie, C. Bowen. Graphene ink laminate structures on poly (vinylidene difluoride)(pvdf) for pyroelectric thermal energy harvesting and waste heat recovery. ACS applied materials & interfaces. 9 (2017) 9161-7.

[235] B. Lin, Z.-T. Li, Y. Yang, Y. Li, J.-C. Lin, X.-M. Zheng, et al. Enhanced dielectric permittivity in surface-modified graphene/PVDF composites prepared by an electrospinning-hot pressing method. Composites Science and

Technology. (2019).

[236] M. Nisha, P.S.K. Reddy. Damage Sensing Through Electrical Resistive Measurement Using Electrospun PVDF-CNF Sensor. Advances in Manufacturing Processes. Springer2019. pp. 205-17.

[237] S. Binzaid, W.H. Dipon. Pyroelectric Simulation System-Advancing Programmability and Portability Concepts.

[238] Y. Yang, W. Guo, K.C. Pradel, G. Zhu, Y. Zhou, Y. Zhang, et al. Pyroelectric nanogenerators for harvesting thermoelectric energy. Nano letters. 12 (2012) 2833-8.

[239] S. Ravindran, T. Huesgen, M. Kroener, P. Woias. A self-sustaining micro thermomechanic-pyroelectric generator. Applied Physics Letters. 99 (2011) 104102.

[240] R. Sagar, S.S. Gaur, M. Gaur. Effect of BaZrO 3 nanoparticles on pyroelectric properties of polyvinylidene fluoride (PVDF). Journal of Thermal Analysis and Calorimetry. 128 (2017) 1235-9.

[241] M. Bobinger, S. Keddis, S. Hinterleuthner, M. Becherer, F. Kluge, N. Schwesinger, et al. Light and Pressure Sensors Based on PVDF With Sprayed and Transparent Electrodes for Self-Powered Wireless Sensor Nodes. IEEE Sensors Journal. 19 (2019) 1114-26.

[242] E.J. Ko, S.J. Jeon, Y.W. Han, S.Y. Jeong, C.Y. Kang, T.H. Sung, et al. Synthesis and Characterization of Nanofiber-type Hydrophobic Organic Materials as Electrodes for Improved Performance of PVDF-based Piezoelectric Nanogenerators. Nano Energy. (2019).

[243] A. Stapleton, M.R. Noor, E.U. Haq, C. Silien, T. Soulimane, S.A. Tofail. Pyroelectricity in globular protein lysozyme films. Journal of Applied Physics. 123 (2018) 124701.

Korean Abstract

초 록

상변이 물질은 상이 바뀜에 따라서 많은 에너지를 흡수하거나 방출하는 성질을 가지고 있고 저장된 열에너지를 우리는 잠열이라고 부른다. 잠열에너지 그리고 상변이 과정인 온도변화가 거의 없는 이 구간을 이용하여 많은 연구가 진행되고 있다. 우리는 상변이 물질이 저장하고 방출하는 에너지를 반도체 열전소자랑 같이 결부 시켜 열량을 흡수하거나 방출하는 과정에서 나타나는 에너지 하베스팅 연구를 진행하고자 하였고 거기에 따른 에너지 하베스팅 효율도 같이 탐구하고 결과를 나타냈다.

제 1 장에서는 상변이 물질에 대한 구체적인 서술을 진행하였고 상변이 물질 종류 및 가장 많이 사용하는 유기폴리머 상변이 물질에 대한 기능을 설명 하였고 상변이 물질이 상이 변하는 기본 원리 그리고 상변이 물질의 잠재적인 사용범위에 대한 서술을 하였고 마이크로 갭슐 구조에 대한 형상유지 그리고 상변이에 대한 전기전도도 변화를 보여주었고 반도체 열전소자의 원리 그리고 제백효과에 대한 간략한 서술도 진행 하였다. 또한 상변이 물질과 반도체 열전소자의 사용원인 응용역할에 대한 내용도 서술하였고 파이로 효과 그리고 파이로 전극을 이용한 에너지 하베스팅에 관한 간략한 설명을 진행 하였고 본 연구의 중요성 창의성에 대해서도 언급하였다.

제 2 장에서는 마이크로 캡슐 구조로 형상 유지 가능한 상변이 물질을 제조 하였고 캡슐 구조인 상변이 물질은 상전이 과정에서 볼륨 팽창을 발생 시킨다. 그래핀 그리고 카본 나노튜브가 들어간 상변이 복합재료는 온도변화에 대한 볼륨 팽창 그리고 볼륨 팽창에 대한 전기저항의 변화를 감지 하였고 상전이 과정에서 볼륨 변화가 많고 따라서 전기전도도의 변화도 상전이 변화에 비례한다는 것도 증명하였다.

제 3 장에서는 두가지 다른 상변이 물질을 사용한 에너지 하베스팅 연구에 대한 서술을 순서적으로 설명하였고 먼저 진행하게 된 반도체 열전소자가 하나만 들어있고 높은 온도구간대에서 상변이가 발생하는 상변이 물질과 낮은 온도 구간대에서 상변이가 발생하는 상변이 물질을 베이스로 온도차에 의한 에너지 하베스팅 결과를 설명 하였고 두번째 내용인 두 상변이 물질 온도가 서로 역전되는 현상을 주름 잡고 반도체 소자 두개를 사용하고 상변이 물질 위치를 서로 바뀌게 디자인 함과 동시에 온도차이가 역전되여도 여전히 에너지 하베스팅이 진행되는 것을 알 수 있다. 열전도도를 증가시켜 상변이 과정으로 빨리 진행됨과 동시에 에너지 하베스팅도 빨리 진행되는 연구를 진행함과 동시에 필러 농도가 증가됨에 따라서 에너지 하베스팅 효과도 변화가 발생하는 것을 확인 하게 되였다. 나중에는 여러 필러 농도가 다른 상변이 물질을 에너지 하베스팅에 결부 시켰고 결과 가장 적절한 두 조합을 얻는데 성공 하였다.

제 4 장에서는 기존 연구에 따른 적절한 두 조합을 베이스로 에너지 효율 관련 연구를 진행 하였고 결과 에너지 효율은 저장된 토탈 에너지 즉 함침된 상변이 물질 질량이 많을수록 저장하거나 방출하는 에너지가 더 많고 따라서 전기에너지로 전환되는 양도 많아짐을 알 수 있다. 함침된 상변이 물질 양을 증가시키는 것을 연구 목적으로 먼저 에어로겔이 상변이 물질을 함침하는 과정에서 모세관 힘에 의한 구조변화가 발생되고 볼륨 축소가 발생함으로서 함침되는 상변이 물질의 양도 어느 정도 손실을 보게 되는 것을 알 수 있다. 에어로겔이 볼륨 축소가 되는 것을 막기 위하여 일단은 PDMS 를 에어로겔 내부에 균일하게 분산시키고 따라서 분산된 PDMS 가 에어로겔 축에 접착 됨으로서 외부의 힘에 의한 탄성을 가지게 되고 따라서 볼륨을 유지시키게 된다. 함침된 상변이 물질 양도 증가되고 따라서 에너지 하베스팅 되는 효율도 증가 되는 것이다. 또한 에어로겔 기계적 물성을 어느 정도 증가시켜 더 안정적인 에어로겔 구조를 만들었고 함침된 상변이 물질 양도 또한 어느 정도 증가된다. 이는 전기에너지로 전환되는 효율을 증가 시키고 함침된

상변이 물질이 녹는 점보다 더 높은 온도환경에서도 더 안정적인 구조를 가질 수 도 있다.

제 5 장에서는 파이로 효과에 대한 간략한 서술과 상변이 물질을 파이로 전극에 대한 응용 원리 그리고 파이로 에너지 하베스팅에 대한 설명을 진행하였다. 서로 다른 상변이 물질을 사용한 파이로 시스템은 성공적으로 전기에너지를 하베스팅 하였고 외부조건이 다름에 따라서도 안정적인 파이로 효과를 유도하였다. 또한 태양빛의 투명한 유리에 대한 투과를 초점으로 투명한 파이로 전극 시스템을 구축 하였고 상변이 물질을 태양에너지를 흡수하고 외부에너지가 없는 상황에서는 저장된 잠열에너지를 방출하는 스마트한 파이로 에너지 효과를 관찰 하였다. 상변이 물질의 파이로 전극에 대한 응용은 새로운 잠재적인 사용가치를 언급할 수 있었고 더 간단하고 컨트롤이 스마트 한 시스템을 구축할 수 있음을 말해주고 있다.

제 6 장에서는 본 논문의 결론을 서술하였고 연구 결과 그리고 연구 목적 및 선행연구와는 어떤 차이점이 있는지를 설명 하였다. 또한 이런 연구를 진행함에 있어서 존재하는 문제점과 앞으로 더 연구를 진행해야 될 방향 그리고 극복해야 할 이론 베이스도 서술 하였고 연구를 통한 실제응용 전망에 대해서도 간략한 서술을 진행 하였다.

주요어: 상변이 물질, 잠열, 에너지 하베스팅, 마이크로 캡슐, 볼륨 팽창, 전기 전도도, 제백효과, 반도체 열전소자, 열전도도, 적절한 조합, 에너지 효율, 볼륨 축소, 기계적 물성, 파이로 효과,

학번: 2013-23814